

DESIGNING OF Ti-Mg COMPOSITES FOR VARIOUS APPLICATIONS

A THESIS SUBMITTED TO
THE GRADUATE SCHOOL OF NATURAL AND APPLIED SCIENCES
OF
MIDDLE EAST TECHNICAL UNIVERSITY

BY

EZGİ BÜTEV ÖCAL

IN PARTIAL FULFILLMENT OF THE REQUIREMENTS
FOR
THE DEGREE OF DOCTOR OF PHILOSOPHY
IN
METALLURGICAL AND MATERIALS ENGINEERING

JULY 2020

Approval of the thesis:

DESIGNING OF Ti-Mg COMPOSITES FOR VARIOUS APPLICATIONS

submitted by **EZGİ BÜTEV ÖCAL** in partial fulfillment of the requirements for the degree of **Doctor of Philosophy in Metallurgical and Materials Engineering, Middle East Technical University** by,

Prof. Dr. Halil Kalıpçılar
Dean, Graduate School of **Natural and Applied Sciences** _____

Prof. Dr. Cemil Hakan Gür
Head of the Department, **Metallurgical and Materials Eng.** _____

Prof. Dr. Arcan F. Dericioğlu
Supervisor, **Metallurgical and Materials Eng., METU** _____

Assoc. Prof. Dr. Ziya Esen
Co-Supervisor, **Materials Science and Eng., Çankaya Uni.** _____

Examining Committee Members:

Prof. Dr. Kadri Aydınol
Metallurgical and Materials Eng., METU _____

Prof. Dr. Arcan F. Dericioğlu
Metallurgical and Materials Eng., METU _____

Assoc. Prof. Dr. Zarife Göknur Büke
Materials Science and Nanotechnology Eng., TOBB-ETU _____

Assoc. Prof. Dr. Benat Koçkar
Mechanical Eng., Hacettepe University _____

Assist. Prof. Dr. Eda Aydoğan Güngör
Metallurgical and Materials Eng., METU _____

Date: 07.07.2020

I hereby declare that all information in this document has been obtained and presented in accordance with academic rules and ethical conduct. I also declare that, as required by these rules and conduct, I have fully cited and referenced all material and results that are not original to this work.

Name, Last name : Ezgi Btev cal

Signature :

ABSTRACT

DESIGNING OF Ti-Mg COMPOSITES FOR VARIOUS APPLICATIONS

Bütev Öcal, Ezgi
Doctor of Philosophy, Metallurgical and Materials Engineering
Supervisor : Prof. Dr. Arcan F. Dericioğlu
Co-Supervisor: Assoc. Prof. Dr. Ziya Esen

July 2020, 232 pages

In this study, galvanic corrosion of Ti-Mg based composites has been examined by combining different Mg-alloys with Ti6Al4V alloy and by addition of Na-rich layer between two dissimilar metals. After determining the wetting behavior of liquid unalloyed Mg, AZ91, and WE43 alloys on solid Ti6Al4V alloy, three different composites were manufactured via infiltration of liquid Mg/Mg-alloys into porous Ti6Al4V alloy skeletons. The same procedure was also repeated after coating the porous surfaces of Ti6Al4V alloy by alkali treatment. Electrochemical and non-electrochemical tests have been conducted in simulated body fluid (SBF) separately for bulk samples of Mg/Mg alloys, and their composite counterparts with and without Na-rich coating to reveal and compare corrosion mechanisms.

The composites containing unalloyed Mg and AZ91 alloy exhibited greater relative density due to their better wettability on Ti6Al4V alloy. Bulk Mg/Mg alloys displayed micro galvanic corrosion, and AZ91 had the highest corrosion resistance with its homogenously distributed Mg₁₇Al₁₂ intermetallics. On the other hand, the

coupling of Mg/Mg-alloys with Ti-alloy intensified the galvanic corrosion; however, the corrosion was not as severe as Ti6Al4V-Mg composites when AZ91 and WE43 alloys are used. In addition, formation of $TiAl_3$ phase in the Ti6Al4V-AZ91 composite reduced the galvanic effect significantly. The presence of Na-rich coating in the composites alleviated the galvanic effect. Although its impact was not visible in composites containing Mg-alloys, remarkable improvement in corrosion resistance was obtained in Ti6Al4V-Mg composite. Na-rich coatings not only reduced the galvanic corrosion but also enhanced the bioactivity of composites by allowing precipitation of Ca-P phases.

Keywords: Ti6Al4V-Mg Composites, Magnesium Alloys, Galvanic Corrosion, Wettability, In-vitro

ÖZ

ÇEŞİTLİ UYGULAMALAR İÇİN Ti-Mg KOMPOZİTLERİNİN DİZAYNI

Bütev Öcal, Ezgi
Doktora, Metalurji ve Malzeme Mühendisliği
Tez Yöneticisi: Prof. Dr. Arcan F. Dericioğlu
Ortak Tez Yöneticisi: Doç. Dr. Ziya Esen

Temmuz 2020, 232 sayfa

Bu çalışmada, farklı Mg alaşımlarının Ti6Al4V alaşımı ile birleştirilmesinin ve iki farklı metal arasında sodyum bakımından zengin bir kaplamanın varlığının, Ti-Mg bazlı kompozitlerin galvanik korozyonuna etkisi incelenmiştir. Sıvı Mg, AZ91 ve WE43 alaşımlarının katı Ti6Al4V alaşımı üzerindeki ıslatma davranışı incelendikten sonra, sıvı Mg/Mg-alaşımlarının gözenekli Ti6Al4V alaşımına emdirilmesi ile üç farklı kompozit elde edilmiştir. Aynı işlemler, Ti6Al4V alaşımının gözenekli yüzeylerinin alkali işlemleri ile kaplanmasından sonra da tekrarlanmıştır. Hacimli Mg/Mg alaşım numuneleri ile sodyum bakımından zengin kaplama içeren ve içermeyen kompozitlerin korozyon davranışları yapay vücut sıvısında (YVS) gerçekleştirilen elektrokimyasal ve elektrokimyasal olmayan testler ile belirlenmiştir.

Sıvı Mg ve AZ91 alaşımı katı Ti6Al4V alaşım yüzeyini daha iyi ıslatabildiği için Mg ve AZ91 içeren kompozitler göreceli olarak daha yüksek yoğunluğa sahip

olmuşlardır. Hacimli döküm Mg/Mg alaşımlarında mikro galvanik korozyon gözlemlenmiş ve AZ91 alaşımının, yapısında homojen dağılmış $Mg_{17}Al_{12}$ intermetaliklere bağlı olarak en yüksek korozyon direncine sahip olduğu tespit edilmiştir. Öte yandan, Mg/Mg alaşımlarının Ti alaşımı ile birleştirilmesi galvanik korozyonun hızlanmasına neden olmuş fakat AZ91 ve WE43 alaşımlarının kullanımı galvanik korozyonu Ti6Al4V-Mg kompozitine göre azaltmıştır. Ek olarak, Ti6Al4V-AZ91 kompozitinde $TiAl_3$ fazının oluşumu galvanik etkiyi önemli ölçüde azaltmıştır. Sodyum bakımından zengin kaplamanın varlığı ise kompozitlerde galvanik etkiyi azaltmıştır. Mg-alaşımı içeren kompozitlerde sodyumca zengin kaplamanın galvanik korozyona etkisi çok olmasa da, Ti6Al4V-Mg kompozitinin korozyon direncinde dikkate değer bir iyileşme elde edilmiştir. Sodyum bakımından zengin kaplama sadece galvanik korozyonu azaltmakla kalmamış, aynı zamanda Ca-P fazlarının oluşmasına olanak sağlayarak kompozitlerin biyoaktivitesini de arttırmıştır.

Anahtar Kelimeler: Ti6Al4V-Mg Kompozitleri, Magnezyum Alaşımları, Galvanik Korozyon, Islatılabilirlik, In-vitro

To my family

ACKNOWLEDGMENTS

I would like to sincerely thank my supervisor Prof. Dr. Arcan Dericiođlu for sharing his valuable knowledge and experiences and for giving me the opportunity to work under his supervision.

I heartly thanks my supervior Assoc. Prof. Dr. Ziya Esen for his guidance, endless patience and valuable support. His positive attitude always motivated me to carry out my research successfully. His personality and dedication himself to his students always impressed me. I am forever grateful and indebted to him.

I appreciate to Prof. Dr. Kadri Aydınol for giving me a chance to use the laboratory facilities and sharing his valuable knowledge. I also thank members of Energy Storage Devices and Battery Laboratory, especially Özgün Köse and Cansu Savaş.

I would like to thank Dr. Elif Tarhan Bor for her support and guidance.

I am also grateful to Serkan Yılmaz and Dr. Süha Tirkeş for their support and sharing their knowledge.

I warmly thank my laboratory mates Merve Nur Dođu, Seren Özer, Merve Özkan and Erdil Akar. The achievement of experiments and completion of this study would not have been possible without their help.

I specially thank to Nazan Kara, Nazan Taşkıran and Simge Tülbez for their understanding, endless support and their lovely friendship.

Last, but not least, I would like to express my sincere appreciation to my husband, and best friend, Arda, for his endless support and encouragement. He has always motivated me to overcome difficulties and he has never left me alone.

TABLE OF CONTENT

ABSTRACT.....	v
ÖZ	vii
ACKNOWLEDGMENTS	x
TABLE OF CONTENT	xi
LIST OF TABLES	xvi
LIST OF FIGURES	xviii
CHAPTERS	
1 INTRODUCTION	1
2 LITERATURE REVIEW	7
2.1 Biomaterials	7
2.2 Classification of biomaterials.....	11
2.2.1 Biopolymers.....	11
2.2.2 Bioceramics.....	11
2.2.3 Biometals	13
2.2.3.1 Degradable biometals	13
2.2.3.1.1 Magnesium.....	16
2.2.3.1.2 Magnesium as a biomaterial	18
2.2.3.1.3 Corrosion of Mg and its alloys.....	21
2.2.3.1.4 Proposed corrosion models for Mg and its alloys.....	25
2.2.3.1.5 Factors that affect the corrosion of Mg alloy.....	30
2.2.3.1.6 Corrosion rate measurement for Mg	37
2.2.3.2 Permanent biometals.....	46

2.2.3.2.1	Titanium as a biomaterial	48
2.2.3.2.2	Production methods for porous titanium and its alloys	49
2.2.3.2.3	Loose Powder Sintering Method	50
2.2.3.2.4	Surface modification of titanium and its alloys	51
2.2.4	Biocomposites	53
3	EXPERIMENTAL	57
3.1	Raw Materials	57
3.1.1	Ti6Al4V Powders	57
3.1.2	Bulk Ti6Al4V Alloy	58
3.1.3	Bulk unalloyed Mg, AZ91 and WE43 Alloys	58
3.2	Production of Porous Ti6Al4V Alloy	59
3.3	Production of Ti6Al4V-Mg/Mg-alloy Composites	60
3.4	Interface Formation.....	61
3.5	Wetting Test.....	61
3.6	In-vitro studies	62
3.7	Corrosion Rate Determination Techniques.....	65
3.7.1	Non-Electrochemical Techniques	65
3.7.1.1	Hydrogen evolution test	65
3.7.1.2	Weight Loss Test.....	67
3.7.2	Electrochemical Techniques.....	68
3.7.2.1	Galvanic corrosion test.....	69
3.7.2.2	Potentiodynamic Polarization Test	70
3.7.2.3	Electrochemical Impedance Spectroscopy (EIS)	71

3.8	Characterization	71
3.8.1	Particle Size Determination	71
3.8.2	Chemical Composition Analysis.....	72
3.8.3	X-ray Diffraction Analysis (XRD)	72
3.8.4	Microstructural Analysis.....	72
3.8.5	Atomic Force Microscopy (AFM)	73
3.8.6	Density Measurement	73
3.8.7	Mechanical Characterization	75
4	RESULTS	77
4.1	Composite production	77
4.1.1	Wetting behavior of liquid Mg/Mg-alloy on the Ti6Al4V alloy	78
4.1.2	Structure and chemical analysis of the composites.....	94
4.1.3	Mechanical characterization	99
4.2	Composites with Na-rich coating	103
4.2.1	Formation of Na-rich coating by alkali treatment.....	103
4.2.2	Wetting behavior of liquid Mg/Mg-alloy on Na coated Ti6Al4V alloy	107
4.2.3	Structure and chemical analysis of composite containing Na-rich .	112
4.3	Corrosion Properties.....	120
4.3.1	As-cast bulk Mg/Mg-alloy	120
4.3.1.1	Structure and chemical analysis.....	120
4.3.1.2	Corrosion behaviors.....	123

4.3.1.2.1	Short-term degradation characteristics	123
4.3.1.2.2	Long-term degradation characteristics	136
4.3.1.2.3	Electrochemical tests	148
4.3.2	Composites	155
4.3.2.1	Macro-structural examination	155
4.3.2.2	Microstructural changes	157
4.3.2.2.1	Cross-sectional examination.....	159
4.3.2.2.2	Corrosion products	161
4.3.2.3	Hydrogen evolution.....	166
4.3.2.4	pH change of SBF solution	168
4.3.2.5	Electrochemical tests.....	169
4.3.2.5.1	Galvanic Corrosion.....	169
4.3.2.5.2	Potentiodynamic polarization tests.....	171
4.3.2.5.3	Electrochemical Impedance Spectroscopy (EIS) tests	174
4.3.2.6	Proposed corrosion mechanism.....	177
4.3.3	Composites containing Na-rich coating	180
4.3.3.1	Microstructural changes	180
4.3.3.2	pH change of SBF solution	188
4.3.3.3	Hydrogen evolution.....	190
4.3.3.4	Electrochemical tests.....	192
4.3.3.4.1	Galvanic corrosion test	192
4.3.3.4.2	Potentiodynamic polarization test	193
5	CONCLUSION	197
	REFERENCES	201

APPENDICES

A. PERMISSON LICENCES	229
CIRRICULUM VITAE	231

LIST OF TABLES

TABLES

Table 2.1 Properties of various metallic biomaterials and natural bone [50].....	20
Table 3.1 The chemical composition analysis of Ti6Al4V alloy in powder and bulk form, and ASTM F 1580-01 standard [181].....	57
Table 3.2 Chemical compositions of unalloyed Mg, AZ91, and WE43 alloys.	59
Table 3.3 Ion concentration of blood plasma and SBF [182].....	63
Table 3.4 Molecular weight and amount of chemicals added during the preparation of one liter SBF [182].....	64
Table 4.1 Average density and porosity values of different metals and manufactured composites.	96
Table 4.2 Compressive properties of manufactured porous and composite samples compared with bone [195].....	102
Table 4.3 EDS spot analysis taken from Na-rich coating.	105
Table 4.4 EDS spot analysis of different regions taken from Figure 4.43.	116
Table 4.5 EDS results of various phases in the starting microstructure of as-cast AZ91 and WE43 alloys.	123
Table 4.6 EDS analysis of unalloyed Mg, AZ91, and WE43 alloys after two hours of immersion in SBF.	129
Table 4.7 EDS analysis of the regions shown by yellow, black, and red arrows in Figure 4.61.....	142
Table 4.8 Corrosion parameters measured from polarization curves of Mg/Mg alloys.....	150
Table 4.9 Fitting parameters of Mg/Mg-alloys in SBF for after 1, 2, and 4 h.	153
Table 4.10 EDS analysis of composites taken from different regions labeled in Figure 4.73.....	163

Table 4.11 EDS analysis taken from the rod-like structures seen in Figure 4.75.	165
Table 4.12 Galvanic corrosion parameter of unalloyed Mg, AZ91, and WE43 alloys.	171
Table 4.13 Corrosion parameters obtained from the polarization curves of the composites [195].	173
Table 4.14 Fitting parameters of composites in SBF solution for 1, 2, 4, and 6 hours [195].	177
Table 4.15 EDS analysis taken from the corroded Mg regions in Figure 4.82 and Figure 4.83.	183
Table 4.16 EDS analysis taken from the Mg region in Figure 4.85.	186
Table 4.17 Galvanic corrosion parameters of unalloyed Mg, AZ91 coupled with uncoated and Na-coated Ti6AlV alloy.	193
Table 4.18 Corrosion parameters obtained from polarization curves of the composites.	195

LIST OF FIGURES

FIGURES

Figure 2.1. Evolution of biomaterials science and technology [6].	8
Figure 2.2. Dental implants with various designs, (b) A hip prosthesis containing titanium alloy femoral stem, alumina-zirconia ceramic femoral head, and UHMWPE acetabular cup, (c) mechanic metallic heart valve, and (d) intraocular lenses [6].	12
Figure 2.3. The schematic diagram of degradation behavior and the change of mechanical integrity of biodegradable metallic stents during the vascular healing process [31].	14
Figure 2.4. (a) Iron stent, (b) SEM images of Zn-based stent produced by selective laser melting method, and (c) tungsten embolization coils.	15
Figure 2.5. (a) Schematic representation of magnesium HCP showing principal planes and directions [49] and (b) Mg ion in octahedral coordination with six water molecules [50].	17
Figure 2.6. Biodegradable magnesium alloys; (a) headless screw, (b) compression screw, and (c) BIOTRONIK stent [60].	20
Figure 2.7. Galvanic series of some metals in the seawater environment [66].	23
Figure 2.8. Schematic representation of (a) macro-galvanic and (b) micro-galvanic corrosion [65].	23
Figure 2.9. Schematic representation of the negative difference effect (NDE) [65].	27
Figure 2.10. Model of the partially protective surface film; (a) low E or I and (b) high E or I nad (c) Mono-valent magnesium ion model [65].	28
Figure 2.11. Schematic representation of particle undermining model at (a) low and (b) high current density/potential and (c) magnesium hydride model [65].	29

Figure 2.12. Development of magnesium with various alloying elements [80].	31
Figure 2.13. Phase diagram of the Mg-Al system [81].	33
Figure 2.14. (a) μ CT images of the vertical section of a screw and (b) the schematic images of the original screw and residual screw after 1, 4, and 18 months after implantation. [96].	36
Figure 2.15. Surface morphologies of WE43 alloy samples after immersion in SBF for (a) 6 h and (b) 12 h [97].	37
Figure 2.16. Schematic representation of H ₂ evolution test setup [54].	39
Figure 2.17. Comparison of hydrogen gas evolution in the SBF for bare and HA-coated magnesium [110].	40
Figure 2.18. Schematic representation of a three-electrode electrochemical cell. . .	41
Figure 2.19. Schematic plot of current density (I) versus potential (E) curves obtained from the Tafel extrapolation method [119].	42
Figure 2.20. (a) Nyquist plot (b) Equivalent circuit of a parallel R-C circuit [128].	44
Figure 2.21. (a) Nyquist plot (b) Equivalent circuit of a simplified Randles cell model [128].	45
Figure 2.22. Schematic representation of typical Nyquist plots [114].	46
Figure 2.23. (a) Stainless steel knee and hip implant [133], (b) Co-Cr removable partial dentures [137], (c) Ti-Ni root canal files [136], and (d) Ti-Ni dental braces [30].	47
Figure 2.24. Three stages of loose powder sintering of copper powders detected by in-situ micro-tomography [157].	51
Figure 2.25. (a) the surface of porous titanium after alkali-heat treated, and (c) the apatite formatted titanium surfaces after immersion in SBF [166].	53

Figure 2.26. (a) Porous titanium has entangled structure, (b) Ti-Mg composite having 30% Ti and 70% Mg, and (c) the comparison of the compressive strengths and Young's moduli of different Ti-Mg composites and the natural bone [179]. ..	56
Figure 3.1. (a) Particle size distribution and (b) SEM images of Ti6Al4V alloy powders.....	58
Figure 3.2. Schematic representation of (a) porous Ti6Al4V alloy structure, (b) cross-section of the furnace showing the stainless steel crucible, porous Ti6Al4V rods, and liquid Mg alloys and (c) Ti6Al4V-Mg composite in which pores are filled with Mg alloys.....	60
Figure 3.3. Schematic illustrations of the wetting furnace.....	62
Figure 3.4. Experimental set-up used for measurement of H ₂ evolution rate.	67
Figure 3.5 Experimental set-up of galvanic corrosion test.....	68
Figure 3.6. The electrochemical cell containing three electrodes.	69
Figure 4.1. Schematic representation of Mg/Mg alloy on the Ti6Al4V substrate; (a) side and (b) top views.....	79
Figure 4.2. Change in shape of unalloyed magnesium on Ti6Al4V alloy substrate with time.....	80
Figure 4.3. Change in the contact angle and diameter of molten unalloyed Mg alloy at 800 °C.....	81
Figure 4.4. Schematic representation of wetting of molten pure Mg on solid titanium substrate [186].....	82
Figure 4.5. (a) SEM image, (b) EDS spot analysis, and (c) EDS line scan analysis taken along the reaction layer.....	82
Figure 4.6. XRD analysis of Ti6Al4V alloy substrate wetted by unalloyed Mg. ...	83
Figure 4.7. Change in shape of liquid AZ91 alloy on Ti6Al4V alloy substrate with time.....	84

Figure 4.8. The changes in contact angle and diameter of the molten AZ91 alloy at 800 °C.	84
Figure 4.9. SEM analysis showing the reaction layer formed on Ti6Al4V alloy... ..	85
Figure 4.10. EDS dot map analysis across the reaction layer and Ti6Al4V alloy.. ..	85
Figure 4.11. Cross-sectional examination of AZ91 alloy; (a) showing reaction layer, and (b) EDS analysis taken from the points in part (a).	86
Figure 4.12. Phase diagram of Ti and Al [190].	87
Figure 4.13. XRD analysis of Ti6Al4V alloy substrate wetted by AZ91 alloy.....	87
Figure 4.14. Change in the shape of liquid WE43 alloy on Ti6Al4V alloy substrate with time.	88
Figure 4.15. The changes in contact angle and diameter of molten WE43 alloy at 800 °C.	89
Figure 4.16. SEM analysis showing the reaction layer formed on Ti6Al4V alloy.	90
Figure 4.17. EDS dot map analysis across the reaction layer and Ti6Al4V alloy.. ..	90
Figure 4.18. (a-b) The closer examination of the reaction layer and (c) EDS results.	91
Figure 4.19. (a-b) SEM images of the interface layer, and (c) EDS spot analysis taken from the number shown in part (a-b).	92
Figure 4.20. XRD analysis of Ti6Al4V alloy substrate wetted by WE43 alloy.....	92
Figure 4.21. Schematic representation of equilibrium contact angle, θ	93
Figure 4.22. Macro images of (a) porous Ti6Al4V alloy rod and (b) manufactured Ti6Al4V-Mg composite rod.....	95
Figure 4.23. Microstructure of (a-b) porous Ti6Al4V alloy and (c) polished cross-section of Ti6Al4V-Mg composite.	95
Figure 4.24. Microstructure of (a) Ti6Al4V-Mg, (b) Ti6Al4V-AZ91, and (c) Ti6Al4V-WE43 composites [195].	97

Figure 4.25. EDS maps showing the elemental distribution of various elements in the Ti6Al4V-AZ91 composite [195].	97
Figure 4.26. (a-b) The microstructure of cuboidal Ti-Al rich particles and (c) EDS line analysis taken along reaction layer between Ti6Al4V particle and AZ91 alloy [195].	98
Figure 4.27. EDS maps showing the distribution of various elements in the Ti6Al4V-WE43 composite [195].	98
Figure 4.28. XRD analysis of (a) Ti6Al4V-Mg, (b) Ti6Al4V-AZ91, and (c) Ti6Al4V-WE43 composites [195].	99
Figure 4.29. (a) Stress-strain diagram and (b) macro images of compression tested porous Ti6Al4V alloy and Ti6Al4V-Mg/AZ91/WE43 composites.	100
Figure 4.30. Fractured surfaces of (a) Ti6Al4V-Mg, (b) Ti6Al4V-AZ91, and (c) Ti6Al4V-WE43 composites.	101
Figure 4.31. SEM images of (a) starting surface (uncoated) and (b-d) NaOH treated porous Ti6Al4V surfaces at different magnifications.	104
Figure 4.32. (a-b) SEM images of fracture surface showing the Na-rich coating layer and (c) EDS line analysis taken along the interface between Ti6Al4V and Na rich layer (indicated by the white line).	105
Figure 4.33. SEM images of (a) starting surface (uncoated) and (b-d) Na-coated Ti6Al4V surface, and AFM 3D micro-topography (a) uncoated and (b) Na-coated Ti6Al4V alloy.	106
Figure 4.34. Change in shape of unalloyed Mg on Na-coated Ti6Al4V alloy substrate with time.	108
Figure 4.35. Change in shape of AZ91 on Na-coated Ti6Al4V alloy substrate with time.	108
Figure 4.36. The change of contact angle for (a) unalloyed liquid Mg and (b) liquid AZ91 alloy on coated Ti6Al4V substrate at 800 °C.	109

Figure 4.37. (a) SEM and (b) EDS analysis of the interface layer taken from the yellow arrow in part (a), and (c-d) EDS line scan analysis taken along the yellow line in part (c).	110
Figure 4.38. XRD analysis taken along the reaction layer of (a) unalloyed liquid Mg and (b) liquid AZ91 alloy on coated Ti6Al4V substrate.	110
Figure 4.39. (a-b-c) SEM analysis showing the reaction layer formed on Ti6Al4V alloy, and (d) EDS spot analysis taken from the numbered points in part (c).	112
Figure 4.40. The polished surfaces of (a-b) Ti6Al4V-Na-Mg and (c-d) Ti6Al4V-Na-AZ91 composites with Na-rich interface.	113
Figure 4.41. XRD analysis of (a) porous Ti6Al4V alloy, (b) Ti6Al4V-Na-Mg and (c) Ti6Al4V-Na-AZ91 composites.	114
Figure 4.42. EDS dot map showing the elemental distribution of various elements in the Ti6Al4V-Na-Mg composite (SE: Secondary electron image).	115
Figure 4.43. (a-b) SEM images and (c) EDS line scan analysis of region B.	115
Figure 4.44. EDS dot map showing the elemental distribution of various elements in the Ti6Al4V-Na-AZ91 composite (SE: Secondary electron image).	117
Figure 4.45. SE-image showing the interface between coated Ti6Al4V and AZ91 alloy in Ti6Al4V-Na-AZ91 composites.	117
Figure 4.46. (a) Polished cross-section of Ti6Al4V-Na-AZ91 composite, and (b) EDS line analysis taken along the Ti-alloy-coating and AZ91 alloy, indicated by the white line in (a).	118
Figure 4.47. (a) Fractured surface of Ti6Al4V-Na-AZ91 composites and EDS analysis taken from the different regions. (b) EDS analysis of regions shown in (a).	119
Figure 4.48. (a-b) The starting microstructure and (c) XRD of unalloyed Mg.	121
Figure 4.49. The starting microstructure of as-cast AZ91 alloy.	121
Figure 4.50. The starting microstructure of as-cast WE43 alloy.	122

Figure 4.51. XRD results of as-cast (a) AZ91 and (b) WE43 alloys.....	122
Figure 4.52. Surface morphology change of unalloyed Mg after various immersion time in SBF.....	126
Figure 4.53. Surface morphology change of AZ91 alloy after various immersion time in SBF.....	127
Figure 4.54. Surface morphology change of WE43 alloy after various immersion time in SBF.....	128
Figure 4.55. XRD results of (a) unalloyed Mg, (b) AZ91, and (c) WE43 alloys after various immersion times. 0h indicates starting as-cast samples.....	130
Figure 4.56. Cross-section analysis of Mg/Mg-alloys after various times of immersion. A: Epoxy resin, B: Corrosion layer, C: Mg/Mg-alloys substrate.	132
Figure 4.57. ICP-OES analysis of SBF solution for (a) unalloyed Mg, (b) AZ91, and (c) WE43 alloys after 1, 8, and 24 h, and (d) change in pH of the SBF solution during first 24 h.	134
Figure 4.58. Macro images of the corroded surfaces of Mg/Mg-alloys after different time intervals in SBF.	137
Figure 4.59. XRD results of (a) unalloyed Mg, (b) AZ91, and (c) WE43 alloys after various time intervals in SBF. 0d indicates the XRD of uncorroded as-cast samples.	138
Figure 4.60. Macro-structural changes of Mg/Mg-alloys after immersion in SBF.	139
Figure 4.61. BSE images of (a–d) unalloyed Mg, (b–e) AZ91 and (c–f) WE43 alloys after two days of immersion.	141
Figure 4.62. Relative amount of the intermetallics in the AZ91 and WE43 alloys during in-vitro test.	143
Figure 4.63. (a) Weight loss percentage and (b) cumulative hydrogen gas produced during the in-vitro test in SBF.	145

Figure 4.64. pH change measurement of Mg/Mg-alloys during the in-vitro test in SBF.	148
Figure 4.65. Polarization curves of as-cast unalloyed Mg, AZ91 and WE43 alloys in SBF at 37 °C.	150
Figure 4.66. Nyquist diagrams of Mg/Mg-alloys for (a) 1, (b) 2, and (c) 4 h, and (d) equivalent circuit for EIS data fitting.....	151
Figure 4.67. Schematic corrosion mechanism of bulk Mg/Mg-alloys.....	155
Figure 4.68. Macro-structural changes of composites during in-vitro tests [195].	156
Figure 4.69. SEM images of corroded surfaces in composites in SBF for various immersion times [195].	158
Figure 4.70. SEM images of corroded surfaces in composites for various immersion times in SBF (A: Ti6Al4V powder, B: prior Mg/Mg-alloy regions) [195]......	159
Figure 4.71. Cross-sections of the polished surface of Ti6Al4V-Mg/AZ91/WE43 composites showing corrosion depth at different time intervals of immersion in SBF [195]......	160
Figure 4.72. The change of average corrosion depths of Ti6Al4V-Mg/Mg-alloy composites with time.	160
Figure 4.73. SEM images of corroded surfaces of (a-c) Ti6Al4V-Mg, (d-f) Ti6Al4V-AZ91, and (g-i) Ti6Al4V-WE43 composites after one hour of immersion in SBF [195]......	162
Figure 4.74. XRD of (a) Ti6Al4V-Mg, (b) Ti6Al4V-AZ91, and (c) Ti6Al4V-WE43 composites after 1, 2, 5, and 10 days of immersion in SBF [195]......	164
Figure 4.75. SEM images of the corroded surface of (a) Ti6Al4V-Mg, (b) Ti6Al4V-AZ91, and (c) Ti6Al4V-WE43 composites showing Cl rich rod-like structure [195]......	165

Figure 4.76. Cumulative hydrogens produced the Ti6Al4V-Mg/AZ91/WE43 composites during the in-vitro test [195].....	167
Figure 4.77. pH change of the SBF solution containing Ti6Al4V-Mg/AZ91/WE43 composites [195].	169
Figure 4.78. The change in (a) potential and (b) current density of Mg/Mg-alloys coupled with Ti6Al4V alloy.....	171
Figure 4.79. Polarization curves of Ti6Al4V-Mg/Mg-alloy composites in SBF at 37 °C [195].	172
Figure 4.80 Nyquist diagrams and corresponding equivalent circuits of (a-b) Ti6Al4V-Mg, (c-d) Ti6Al4V-AZ91, (e-f) Ti6Al4V-WE43 composites.....	176
Figure 4.81 Schematic representation of corrosion mechanism for composite samples.	179
Figure 4.82 Surface morphological changes of Ti6Al4V-Na-Mg composites after immersion in SBF for 1-24 h.....	181
Figure 4.83 Surface morphological changes of Ti6Al4V-Na-AZ91 composites after immersion in SBF for 1-24 h.....	182
Figure 4.84 Microstructure showing the region between Ti6Al4V powder and AZ91 alloy of (a) Ti6Al4V-AZ91 and (b) Ti6Al4V-Na-AZ91 composites after immersion in SBF for two hours.	184
Figure 4.85 Surface morphological changes after immersion in SBF for 1-10 days (a) Ti6Al4V-Na-Mg, (b) Ti6Al4V-Na-AZ91 composites.....	185
Figure 4.86 XRD analysis of (a) Ti6A4V-Na-Mg and (b) Ti6Al4V-Na-AZ91 composites after immersion in SBF for 1- 10 days.	186
Figure 4.87 Ca/P ratio of the corroded surface in all the composites after immersion in SBF for 1, 2, 5, and 10 days.	188
Figure 4.88 pH variations of composites during in-vitro tests.	189

Figure 4.89 The comparison of hydrogen evolution of two different composite couples; (a) Ti6Al4V-Mg and Ti6Al4V-Na-Mg, and (b) Ti6Al4V-AZ91 and Ti6Al4V-Na-AZ91 composites.	191
Figure 4.90 The change in (a) potential and (b) current density of Mg/Mg-alloys coupled with uncoated and Na-coated Ti6Al4V alloy.	193
Figure 4.91 Polarization curves of composites in SBF at 37 °C.	195

CHAPTER 1

INTRODUCTION

Recent studies have focused on the development of biodegradable materials having acceptable degradation characteristics with time without releasing toxic elements. Among the biomaterials, the usage of biodegradable metals has several advantages such that secondary surgery is not needed after implantation since they spontaneously degrade in the human body and replace with bone tissues when they are used as bone substitutes. Therefore, biodegradable metals are considered as alternatives to permanent bioinert metals, which remain in the body even after healing and sometimes cause adverse reactions. Although they degrade over time, biodegradable material should stay enough time in the body and preserve its mechanical integrity to provide sufficient strength during the first few weeks of the healing stage.

Over the last years, magnesium (Mg) and Mg alloys are considered as appropriate candidates for biomedical applications because of their degradable characteristics in an aqueous environment, together with their low densities ($1.75\text{-}2.00\text{ gr/cm}^3$) comparable to those of bone. Additionally, magnesium and its alloys possess excellent mechanical compatibility (elastic moduli (41-45 GPa)) with the bone, thereby alleviating the stress-shielding problem associated with the remarkable difference between the elastic moduli of implant and bone.

Besides its usage as an implant material, the presence of Mg in the human body contributes to many biological reactions, bone strength, and growth of bone tissues.

Therefore, the deficiency of Mg in the body causes an increase in the risk of cardiovascular disease and neurological problems.

Despite their numerous favorable properties, the high corrosion rate of magnesium and Mg alloys causes deterioration of their mechanical integrities shortly after implementation, before complete healing. In addition, Mg generates the hydrogen gas bubbles adjacent to the implant during its degradation, which could delay the healing of the damaged tissue. Accordingly, research about magnesium and Mg alloys implants have focused on controlling and slowing down the corrosion rate.

The surface treatment and alloying are two different approaches used for reducing the degradation rates of Mg and Mg alloys. The surface modification of magnesium enables controlling the corrosion rate and improves the biocompatibility by adding a corrosion resistant biocompatible coating. On the other hand, by alloying, newly designed magnesium alloys for biomedical applications such as Mg-Ca, Mg-Sr, Mg-Zn, Mg-Al, and Mg-Ag have been developed with enhanced mechanical properties and corrosion resistance. Moreover, the addition of rare earth (RE) elements such as Gd, Nd, and Y have commonly used in Mg alloying, which are designed as biodegradable stents in cardiovascular applications. In addition, the solid solution effect of alloying elements, the presence, and distribution of second phases/intermetallics formed as a result of alloying determine the corrosion behavior of the alloy with its rate. Therefore, to minimize the micro galvanic corrosion in the alloy, both types of the elements and resultant phases/intermetallics should be carefully controlled with their size and distribution.

In contrast to Mg and Mg alloys, titanium and Ti-alloys, popular metallic biomaterials, display bioinert character and preferred to be used especially in artificial joints owing to their excellent corrosion resistance, high fatigue strength, and good biocompatibility. However, mismatch of elastic moduli differences between titanium-based implants and bone lead uneven load distribution, which

results finally stress-shielding and loss of implant by bone resorption. Thus, the problem related to the mismatch of elastic moduli between bone and Ti-alloy should be overcome by either modifying the chemical composition or structure/geometry of Ti-alloys. One of the possible solutions is to manufacture porous titanium foams with relatively lower elastic modulus so that the mechanical stability between bone and implant can be achieved. Additionally, the open porous structure of titanium foams provides a suitable place for bone growth and enables the transfer of body fluid. As a result, several studies have been focused on the production of porous titanium foams through the use of different techniques such as loose powder, space holder, gas entrapment, and additive manufacturing techniques. Among the aforementioned techniques, loose powder sintering is one of the most cost effective and practical methods, which is based on the partial sintering metal powders at elevated temperatures to control pore size, distribution, and interconnectivity of pores.

Although generating pores in the structure alleviates the stress-shielding problem by reducing the elastic moduli and provides a place for ingrowth of bone tissues, a porous structure is vulnerable and cannot be loaded before ingrowth of bone tissues. Therefore, filling the pores of titanium alloy with biodegradable magnesium may be an alternative solution to increase the strength of the implant under repetitive loading. In addition, elastic modulus can be tuned easily by changing the relative amounts of titanium and magnesium in the composite. Moreover, combining porous bioinert titanium with biodegradable magnesium can also enhance bioactivity since magnesium promotes the formation of new bone and accelerate precipitation of calcium phosphate phase. During *in vivo*, dissolved magnesium is expected to be replaced by new bone tissues. Accordingly, a dynamic balance between the degradation of magnesium and the new bone ingrowth could be achieved so that no dramatic decrease will be observed in the strength; therefore, the implant can also be loaded even in the degradation stage of the magnesium. However, it has been reported that galvanic corrosion occurring between dissimilar metals like Ti and Mg

accelerates the dissolution rate of magnesium, thereby increasing the hydrogen gas evolution rate. Replacement of Ti and Mg with their alloy form counterparts and eliminating the direct contact of Ti and Mg by the formation of an interlayer between two metals may be used as an approach to alleviate the galvanic effect.

In the present study, three different magnesium alloys, namely, unalloyed Mg, AZ91, and WE43 alloys, were impregnated into porous Ti6Al4V skeletons with pressureless liquid infiltration method to observe the effect of coupling of Ti6Al4V alloy with unalloyed Mg and Mg-alloys with different chemical compositions. Ti6Al4V-Mg/Mg alloy composites were tested by non-electrochemical and electrochemical techniques to compare the corrosion behaviors and mechanisms of composites with the bulk alloys constituting the composites. As a second approach, Na-rich coating was applied on porous surfaces of Ti6Al4V alloy prior to Mg infiltration with the aim of decreasing the galvanic effect in the composite samples. Na-rich coating was especially preferred since it is known to enhance osseointegration in Ti-alloys as well. Therefore, after the degradation of Mg/Mg-alloy regions in the composites over time, Na-rich coating on Ti-alloys is supposed to allow direct bonding of the bone tissues, which is rarely seen in uncoated Ti-alloys. The effect coating layer on corrosion behaviors of the composites was also investigated by electrochemical techniques as well as non-electrochemical techniques like hydrogen evolution test.

This thesis comprises of five main chapters. In the first chapter, the introduction, the current state of the subject is summarized, and the motivation of the study is presented. On the other hand, a detailed literature review has been given in Chapter 2, which is subdivided into various parts. Firstly, definitions and classifications of biomaterials are given. Then, the proposed corrosion models of biodegradable Mg/Mg-alloys are discussed in detail. Apart from these, the production methods of porous titanium alloys and their surface modification techniques are also briefly

introduced. The information about biocomposites, including Ti-Mg, is given at the end of Chapter 2. The properties of materials used in the present study, the details of the composite production methods and coating techniques are given in Chapter 3. Furthermore, this chapter also includes the details of test methods used to characterize the corrosion behaviors (non-electrochemical and electrochemical tests), the wettability tests, in-vitro studies, and characterization techniques. The results of the work and discussion are presented in Chapter 4, which is subdivided into three main sections. In the first section, important findings of the wetting behavior of liquid unalloyed Mg, AZ91, and WE43 alloys on the Ti6Al4V alloy is given. Subsequently, the structure and mechanical properties of Ti6Al4V-unalloyed Mg/AZ91/WE43 composites have been investigated. The second section includes the results about the formation and characterization of Na-rich coating layers between Ti6Al4V alloy and Mg-Mg alloy in the composites and its effect on the wetting behavior of liquid Mg/Mg-alloys. In the last part of Chapter 4, the experimental results about the corrosion behaviors, and corrosion mechanisms of as-cast bulk Mg/Mg-alloys, Ti6Al4V-Mg/Mg-alloy composites, and Na-rich coated Ti6Al4V-Mg/Mg-alloy composites have been investigated after immersion in SBF. Finally, in Chapter 5, important findings of the current work are listed with the proposed future studies

CHAPTER 2

LITERATURE REVIEW

2.1 Biomaterials

The biomaterial is defined as a material that is designed to interact with the body and to replace a part of the body in a reliable, economical, and physiologically acceptable way [1]. Therefore, biomaterials can be used for replacing a missing part of the body part by improving its function or by duplicating the structure that no longer exists. Also, the researchers have stated that the main objective of biomaterials is the improvement of human health by repairing the function of the tissue in the body [2–4]. Therefore, it is essential to understand the relationship between the structure-property relationships of biomaterials to use them successively in biomedical applications. Nowadays, the usage of biomaterials has been growing by incorporating the knowledge and ideas from diverse disciplines such as medicine, chemistry, biology, material, and engineering sciences.

For thousands of years, there have been attempts to replace or correct damaged or diseased body parts. The first biomaterials used were the linen sutures seen in Egypt, which dates back to 3000 BC, and the seashells used as an artificial tooth [5]. However, ancient biomaterials had been failed mainly because of the toxicity and the lack of knowledge about infection control [1,6]. Witte et al. [4] stated that the development of biomaterials has evolved through three generations. The objective of the first-generation biomaterials was to obtain a proper combination of functional properties to match those of the tissue without considering the tissue response.

Therefore, most of the first-generation biomaterials were designed to be bioinert. Some of the examples were the joint prosthesis implemented by Charnley in 1958 [7], vascular graft invented by Vorhess in the early 1950s [8], kidney dialysis introduced by Kolff in 1943 [9], and stent and heart valves invented by Hufnagel in the early 1950s [5]. In the mid to late 1800s, H.S. Levert [6] examined the various metal implants such as silver, gold, and platinum for bone fixation plates in dogs. At the end of the 1940s, the number of biomaterials with acceptable medical principles had been grown because of the increased life expectancy in developing countries.

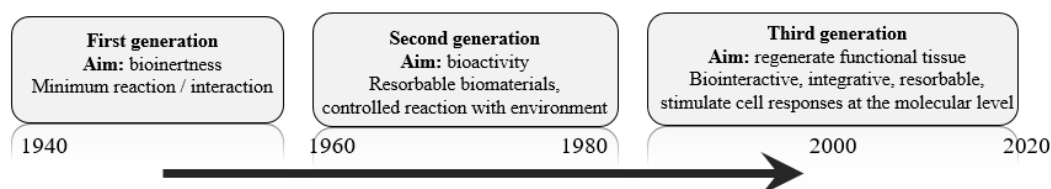


Figure 2.1. Evolution of biomaterials science and technology [6].

On the other hand, the second generation of biomaterials mainly consists of resorbable biomaterials, which degrades with a specific rate that can be regulated according to the need for desired applications. For example, a biodegradable suture made up of polyglycolic acid (PGA) has been widely used in clinical applications. Another application area is controlled drug delivery, which targets specific tumors, blood vessels, etc. [10].

The third generation of biomaterials aims to support and stimulate the improvement of functional tissue at the molecular level [5,6,11]. For instance, bioactive glasses and porous foams are being designed to activate genes in order to reconstruct the living tissues [12]. As a result, a better understanding of biocompatibility at a molecular level can allow the improvement of advanced biomaterials.

In recent years, the number of using implantable biomaterials has been growing due to the increasing older people population and the desire for maintaining the same life quality of patients after surgery [13]. Thus, the need for high performance biomaterials has also steadily increased in different areas such as cardiology, orthopedics, vascular therapy, and dental implants. The variety of biomaterials that can meet the various needs required for different applications allows the selection and usage of the materials, such as biodegradable materials for temporary tissue healing, bioinert materials used for permanent replacement of lost body parts, and the metals with high electroconductivity to be used in artificial organs [1,13]. The biomaterials used in all of the aforementioned areas should possess unique properties such as excellent biocompatibility, high corrosion/wear-resistant, low toxicity, and sufficient mechanical property, which are defined below.

Biocompatibility: The capability of a material to be accepted by surrounding tissue with an appropriate response in the specific applications is defined as biocompatibility [5]. Two key factors that determine the biocompatibility of biomaterials are the host response induced by the biomaterial and the corrosion of the material in the human body [5,14,15]. A biocompatible material is desired to behave with a suitable host response leading to minimum disturbance of standard body function. Therefore, no toxic and allergic response is expected to occur during the healing process if the material used is classified as biocompatible.

Corrosion and wear resistance: The corrosion and wear resistance affect the mechanical integrity of biomaterial and healing time of tissue [2]. Insufficient corrosion and wear resistance may induce the release of toxic elements in an extended period. Similarly, in some cases, high corrosion rate may induce formation of gas pockets around the tissue and causes loss of mechanical integrity before healing process. Although unalloyed magnesium is one of the biodegradable materials, it has high degradation rate in the aggressive environment, especially in a

biological fluid [15]. Because of its rapid corrosion rate, the large amount of hydrogen gas is released around the implant. Although excess hydrogen is removed by the blood flow or by the usage of a syringe, a high amount of retained hydrogen gas can cause toxicity in the body [16,17]. Another example is plain carbon steel, which can corrode and cause allergic reactions because of the high degradation rate [18]. Therefore, the selection of suitable biomaterials should be cautiously made.

Toxicity: A biomaterial should not be toxic on the local and systemic levels [19]. For example, the usage of leachable polymers can cause the unintentional release of the elements from the substance, which affect the biological system. Besides, most of the metallic implant materials like low carbon steel, and Nitinol (Ti-Ni alloy) having low corrosion and wear resistance, can cause the release of unwanted metallic ions. For example, nickel may be released from Nitinol and may induce local tissue damage and also inflammatory reactions. On the other hand, the release of the iron oxide, which is the corrosion by-product of iron (Fe) stents, should be controlled because iron overdose may cause toxicity and inflammation around the implant [20].

Mechanical property: Biomaterials or devices should match sufficient mechanical requirements in order to perform a physiological function for a specific application. For example, a hip prosthesis, which is desired to carry body load partly, must be strong and rigid in order not to fail under heavy loads for long term periods, and it should also possess elastic modulus similar to that of bone to lessen stress-shielding effect [6]. On the other hand, a leaflet in a heart valve must be flexible and tough enough to flex four thousand times per hour without tearing for the life span of the patient [6]. Therefore, depending on the type of applications, biomaterials used for substituting the human tissue or organ should match the desired specific mechanical properties.

2.2 Classification of biomaterials

Depending on the type of materials, biomaterials can be classified into four major groups, which are biopolymers, bioceramics, biometals, and biocomposites.

2.2.1 Biopolymers

Since the beginning of the twentieth century, a wide variety of polymers have been started to be used in biomedical applications. They are mainly preferred for hard and soft tissue applications such as vascular prosthesis, intraocular prosthesis, Figure 2.2(d), catheters, drug delivery aids [5,6,21]. For example, ultra-high molecular weight polyethylene (UHMWPE) is used as an acetabular cup in the hip prosthesis, Figure 2.2(b). Although polymeric biomaterials are not appropriate for screws, plates, or other fixations devices that require high mechanical strength, they are mainly used as fibers for repairing the damaged tissue and wrapping biodegradable stents [22]. In addition, smart polymers have been used in order to clarify bio-separation problems in drug delivery systems. For instance, flexible hydrogels having 3D structures and not dissolving in the water help the process of bio-separation by changing its volume in response to the external stimulus [23]. Moreover, polylactide-*co*-glycolide (PLGA) is another example of degradable polymers used for biomedical applications. PLGA has widely used in sutures, tissue engineering scaffolds, and drug delivery devices due to its rapid degradation rate compared to other polyesters [24].

2.2.2 Bioceramics

Bioceramics have been preferred due to their excellent compressive strength, good biocompatibility, high corrosion, and wear resistance. However, they cannot be used

in load-bearing applications because they are hard and brittle and prone to fatigue failure. Common bio-ceramics are alumina (Al_2O_3), zirconia (ZrO_2), and a form of calcium phosphate named as hydroxyapatite ($\text{Ca}_{10}(\text{PO}_4)_6(\text{OH})_2$) [25,26]. Bioceramics can be utilized in the replacement materials for malfunctioning joints as well as bones and teeth due to bioinert characteristic, high resistance to friction, and their high hardness. Besides, they are integrated with metals in dentistry, such as teeth root, Figure 2.2(a), and orthopedic applications like a hip prosthesis as alumina-zirconia ceramic femoral head, Figure 2.2 (b), where high wear resistance is required. Alumina, which is most widely used as bioceramics in the biomedical applications, is used as electrical insulation for pacemakers, and inner ear ossicles due to their high lifespan [6,25,27]. Besides, bioactive ceramics such as bio-glass, and sintered hydroxyapatite can allow the formation of direct bonding to surrounding tissue. These types of ceramics can stimulate healing and are utilized as essential bone substitutes in the biomedical field [5].

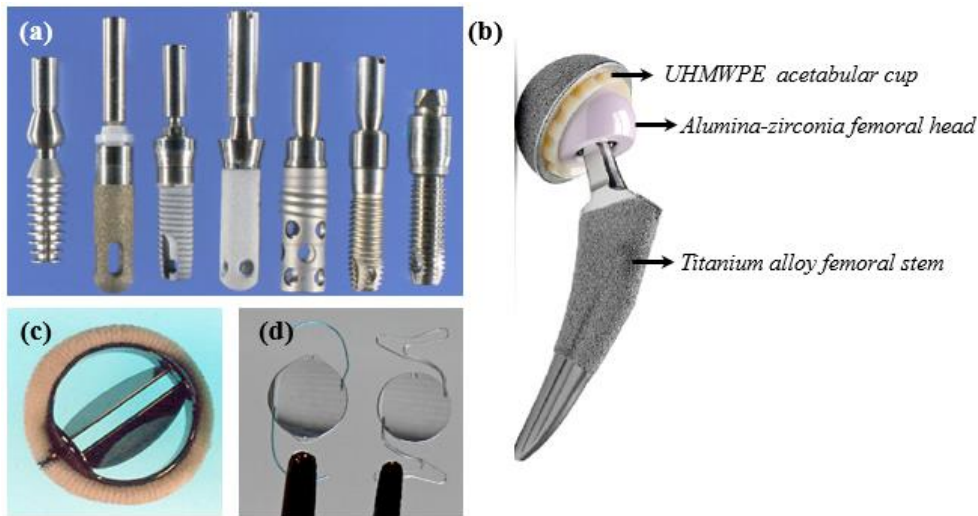


Figure 2.2. Dental implants with various designs, (b) A hip prosthesis containing titanium alloy femoral stem, alumina-zirconia ceramic femoral head, and UHMWPE acetabular cup, (c) mechanic metallic heart valve, and (d) intraocular lenses [6].

2.2.3 Biometals

Biometals have an essential role in biomedical applications such that in the last decades, around 70 % of implants are made from metallic materials [28]. They have a wide range of usages in the human body, such as cardiovascular devices (stents, staples, and artificial hearts [13,29]), dental implants (orthodontics [30], dental braces [3]), and orthopedic applications (hip and knee joint implants).

Biometals can be examined in two main groups, which are degradable and permanent biometals.

2.2.3.1 Degradable biometals

The biodegradable metals are defined as the metals which should dissolve completely without any residue and corrode gradually in vivo with a suitable surrounding tissue response induced by the released corrosion products [23]. The usage of biodegradable metals has various advantages such that secondary surgery is not needed after implantation because of their spontaneous degradation in the human body environment. In addition, degradable biomaterials are alternative to permanent implants, which may induce long-term complications.

However, biodegradable metals should keep their mechanical integrity during the healing of surrounding tissue, and they should dissolve without causing any toxicity. However, it is reported that biodegradable metals, for example, metallic stents, have a relatively faster degradation rate than expected during the tissue remodeling process, Figure 2.3 [31]. For instance, Mg-based stents completely degrade within four months, which causes the loss of mechanical integrity before complete healing. Therefore, there should be an optimum degradation rate that allows sufficient time for the healing of the damaged tissue. Surface coating [32–34] and alloying [35–37]

are two different approaches used to maintain mechanical integrity during healing by slowing down the degradation rate of biodegradable metals.

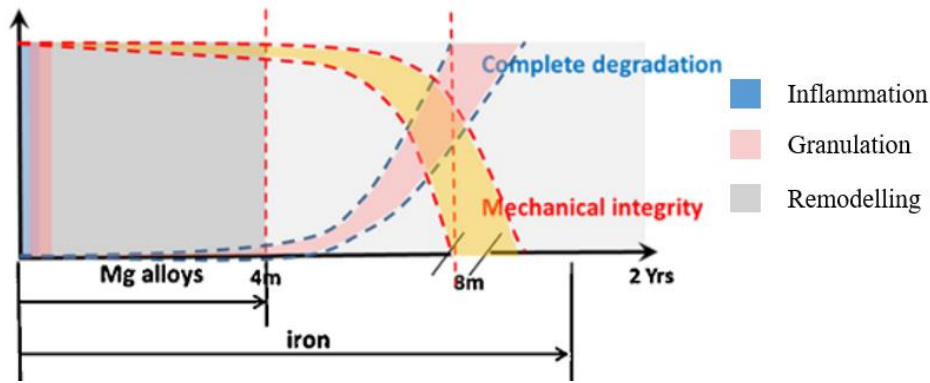


Figure 2.3. The schematic diagram of degradation behavior and the change of mechanical integrity of biodegradable metallic stents during the vascular healing process [31].

Iron (Fe), zinc (Zn), tungsten (W), and magnesium (Mg) based implant materials are commonly used biodegradable metallic materials. Therefore, in the following paragraphs, Fe, Zn, and W-based bio metals are described briefly, while magnesium and its alloys, which are the subject of the present study, will be explained in detail.

The first usage of Fe implant was a dental implant, and then Fe wires were used as a suture in the seventeenth century; however, infections were observed around the implant [38]. In the 1900s, Fe-based plates and screws have been preferred for the fracture fixation devices [31]. In recent years, compared to other biodegradable metals, they have become more popular from a structural point of view because iron-based alloys have similar mechanical properties to those of stainless steel. Besides, Waksman et al. [39] have shown that the biodegradable iron stent, Figure 2.4(a), is safe for implantation in coronary arteries because there is no inflammation around

the stent. On the other hand, in vivo test results revealed that a large portion of Fe stent remained intact in the blood vessel even after long immersion days [31]. Also, it was reported that the Fe implant exhibited a slow degradation rate in the preliminary animal test [4]. The ferromagnetic property is another limitation of Fe-based implant materials, which directly affects the imaging devices like magnetic resonance imaging (MRI). As a result, the researchers have focused on the modification of the composition, microstructure, and ferromagnetic properties by developing new kinds of Fe-based biodegradable metals such as Fe-Mn, Fe-Mn-Si, Fe-W and Fe-Fe₂O₃ [31]. New production methods such as powder metallurgy, casting, and inkjet 3D printing have gained attention to obtain Fe-base stents with a slower degradation rate and diminished ferromagnetic properties. Besides, alloying [40], surface modification [41,42], and heat treatment [20,43] of are the common approaches to slow down the degradation and for improvement of the surface biocompatibility of Fe-base stents.

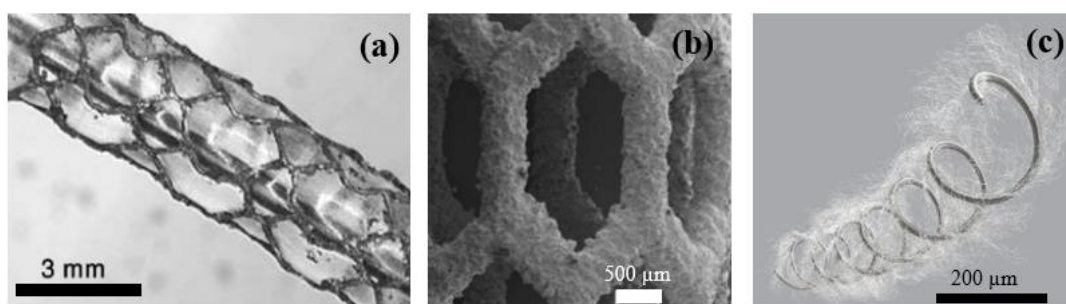


Figure 2.4. (a) Iron stent, (b) SEM images of Zn-based stent produced by selective laser melting method, and (c) tungsten embolization coils.

On the other hand, Zn-based biodegradable metals have become popular due to their high biocompatibility and suitable corrosion rate. For example, Vojtech et al. [44] have investigated the mechanical properties and corrosion behavior of binary Zn-Mg

alloys containing 3% wt. Mg as a bone fixation device. Moreover, Xie et al. [45] produced the porous Zn-Ag scaffolds by gas pressure infiltration method. They found that Zn-Ag scaffolds showed excellent bioactivity due to high biocompatibility and good antibacterial ability of silver (Ag). In addition, the corrosion rate of Zn was reduced upon the addition of Ag, which resulted in grain refinement. In recent years, by the advancement in additive manufacturing technology, Zn cardiovascular stents, Figure 2.4(b), have been produced by the selective laser melting method and shown to be replaced by their traditional counterparts because of their superior mechanical properties with fine-grained microstructure [46].

Likewise, Tungsten (W) can be considered to be a safe, biodegradable metal since it has no toxic effect during dissolution in the human body. Various studies made use of tungsten as biodegradable metal. For example, Peuster et al. [19] placed embolization tungsten coil into the arteries of rabbits, Figure 2.4(c). They found that increased tungsten serum level did not cause any local toxicity, while long-term studies are necessary to understand the effect of tungsten levels in the blood. Also, Butler et al. [47] stated that only long-term follow-up would answer this question whether elevated levels of tungsten are harmful to health or not.

2.2.3.1.1 Magnesium

Magnesium (Mg) is one of the lightest metals with a density of 1.74 g/cm^3 . It is an alkaline earth metal having an atomic number and atomic weight of 12 and 24.305 g/mol, respectively. It was first recognized as hydrated magnesium sulfate and magnesium chloride. Then, Humphry Davy isolated magnesium in 1808 to obtain an elemental form entitled as Magnesia of Greek mythology [48].

Magnesium has a hexagonal closed packed (hcp) structure, and its lattice parameters are a: 0.3209 nm, c: 0.5210 nm, and c/a ratio: 1.624 at room temperature, Figure 2.5.

Besides, alloying elements can easily dissolve in the magnesium, and magnesium tends to form solid solutions with other elements because of its small atomic diameter of 0.320 nm [49].

Also, positively charged magnesium ions, Mg^{2+} , can bind electrostatically to negatively charged molecules like nucleic acids and proteins [50]. Ionized magnesium favors the attraction of water molecules due to the high hydration energy, leading to a large ionic radius. The coordination between Mg and H_2O molecules occurs in octahedral conformation, Figure 2.5(b), with six rigid coordination bonds.

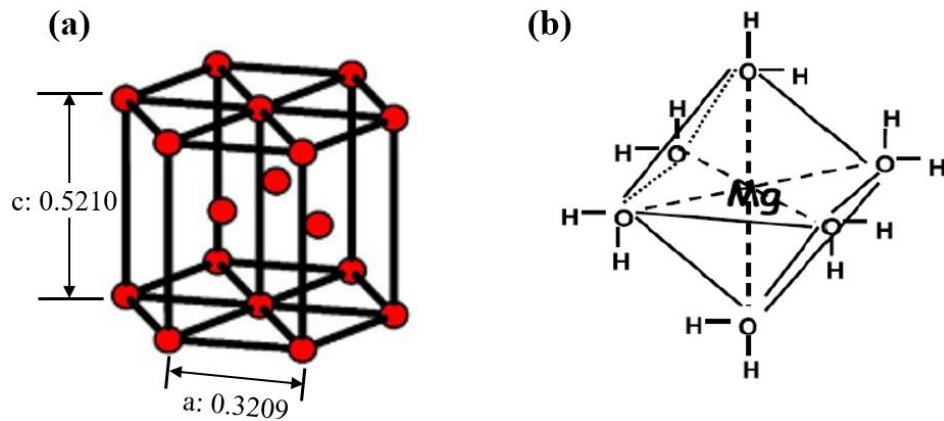


Figure 2.5. (a) Schematic representation of magnesium HCP showing principal planes and directions [49] and (b) Mg ion in octahedral coordination with six water molecules [50].

Two main production methods exist for extraction of Mg named as a thermal reduction and electrolysis. The thermal reduction process is conducted at elevated temperatures (1200-1600°C), in which magnesium oxide is reduced with silicon and then produced magnesium vapor is condensed at a lower temperature in the

converter. Subsequently, condensed magnesium is then re-melted, refined, and poured. This process is called the Pidgeon process, which is one of the least efficient, the most straightforward, and oldest production methods [51]. Another production method to obtain magnesium in elemental form is the electrochemical technique. First, magnesium chloride, $MgCl_2$, is obtained by the precipitation of magnesium hydroxide from brine or seawater. Then, $MgCl_2$ is dissolved in the hydrochloric acid (HCl) and then melted and electrolyzed. At the cathode, the molten magnesium is deposited; on the other hand, the chlorine gas is released at the anode [4].

The usage of magnesium has been extensively increased owing to its lightweight, excellent biocompatibility, good machinability, good heat dissipation, and high damping capacity [35,52–54]. Several studies have been conducted about the usage of magnesium in biomedical applications. Therefore, in the following section, bio-characteristic and related applications of magnesium and its alloy will be discussed in detail.

2.2.3.1.2 Magnesium as a biomaterial

Mg is the fourth most abundant cation in the human body, and it is naturally found in bone tissues, which contains approximately 67% of the magnesium found in the body.

Moreover, Mg is widely distributed throughout the world only as a divalent cation (Mg^{2+}) or in salt or mineral form because of its high level of reactivity. Therefore, it took time for magnesium to be found in its elemental form, and it was discovered in 1755 by Joseph Black [55]. The first usage of magnesium in the biomedical application was in 1878 by Edward C. Huse, who used magnesium wire successfully to stop bleeding vessels [4]. Then, in 1900, the Australian-German physician Erwin Payr believed that Mg wires were brittle to be a suture; therefore, Mg was used in a thin-walled cylinder form as a bone fracture fixation device [56,57]. Mg sheets were

also used for restoring joint motion in both animals and humans [4,56]. In the following years, magnesium and magnesium alloys have been used as a plate, screws, wire, and sheets to heal fractured bone for orthopedic applications, Figure 2.6(a-b). In recent years, commercial Mg alloys are preferred as cardiovascular stents because of their controllable degradation rate. BIOTRONIC® performed successful implantation of a commercial magnesium alloy containing 93 wt. % Mg and 7 wt. % RE metals, Figure 2.6(c), in a coronary artery [57]. In addition, Eggebrecht et al. [58] believed that Mg stents possessed excellent biocompatibility and good mechanical properties compared to those of conventional stainless steel. Both chemical and physical properties make magnesium the most functional cation and lead to the interaction of Mg ion in a broad range of enzymatic reactions and biological functions [50].

Mg has a high strength to weight ratio, low density of 1.74 g/cm^3 , and it can be easily cast. Although its high corrosion rate seems to be a disadvantage, degradable characteristics in an aqueous environment, together with its low density, enable Mg and its alloys to be used for orthopedic applications. Moreover, lightweight Mg implants have elastic moduli closer to that of bone than commercially used titanium alloys and stainless steel, Table 2.1 [55]. The comparatively low elastic moduli make possible reducing the stress-shielding problem observed in load-bearing metallic implants. For example, for temporary orthopedic devices, magnesium alloys match the elastic moduli of bone better than other metallic alloys (like titanium and stainless steel). Therefore, they can be used not only as temporary orthopedic fixtures but also as stents, where a high strength to weight ratio is necessary [59].

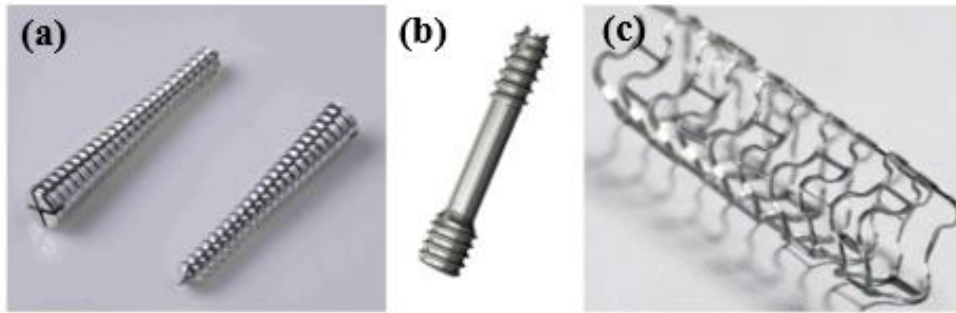


Figure 2.6. Biodegradable magnesium alloys; (a) headless screw, (b) compression screw, and (c) BIONTRONIK stent [60].

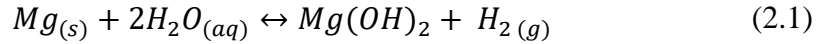
Table 2.1 Properties of various metallic biomaterials and natural bone [50].

	Density (g/cm ³)	Elastic Modulus (GPa)
Natural bone	1.8-2.1	3-20
Magnesium-magnesium alloys	1.74-2.0	41-45
Titanium alloys	4.4-4.5	110-117
Stainless Steels	7.9-8.1	189-205

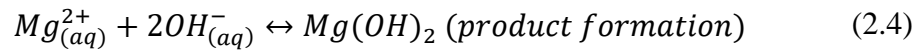
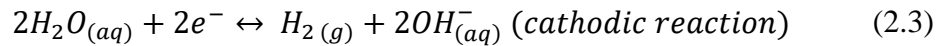
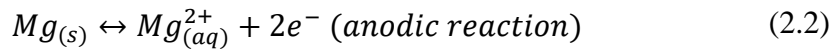
The main drawback of using magnesium is the evolution of hydrogen gas and its rapid corrosion in an aqueous environment. Since the primary function of biomaterials is to maintain its mechanical stability during the healing period, it is essential to control the corrosion rate of magnesium alloy by understanding its corrosion mechanism and corrosion products when exposed to an aqueous solution like in the body fluid.

2.2.3.1.3 Corrosion of Mg and its alloys

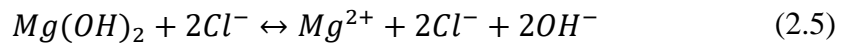
Magnesium dissolution in aqueous environments occurs via an electrochemical reaction with water to produce magnesium hydroxide and hydrogen gas. The overall corrosion reaction of magnesium in aqueous environments is given below:



This overall reaction includes the following partial reactions:



During the dissolution of magnesium, magnesium hydroxide, $Mg(OH)_2$, Eq. 2.4, accumulated on the magnesium substrate, forming a protective corrosion layer. However, corroding of magnesium continues when metallic impurities or aggressive electrolyte species like Cl^- exist in the environment. In the physiological environment (pH: 6.8-7.4), magnesium hydroxide starts to dissolve and convert into highly soluble magnesium chloride, Eq.(2.5), when the concentration of Cl^- ion is above 30 mmol/l [15,31]. As a result, the surface of a magnesium substrate can undergo severe pitting corrosion [61].



Moreover, the corrosion of Mg-alloys, which is a kinetic phenomenon, depends on the alloy composition, impurity content, distribution and amount of the phases in the alloy, and the environmental factors like temperature and pH of the aqueous environment are also effective on the corrosion of Mg-alloys.

Magnesium and its alloys can undergo various forms of corrosion, such as galvanic corrosion, intergranular, and localized corrosion [62], which are explained in the following sections of the thesis.

1) Galvanic Corrosion

Galvanic corrosion is an electrochemical reaction of two dissimilar metals in the presence of an electrolyte and electrical continuity [63]. When two different types of metals are in contact, and the difference in their electrical potential is at least 100 mV, galvanic corrosion occurs [64]. The metal with an electronegative potential becomes an anode, while more noble metal acts as a cathode.

Galvanic corrosion is commonly seen as severe local corrosion of the magnesium adjacent to the cathode [63,65]. For example, galvanic corrosion can occur when stainless steel bone plates are connected to degradable magnesium screws in the body fluid because magnesium is located in the most active metal in the galvanic series, Figure 2.7.

There are two kinds of galvanic corrosion observed for magnesium and its alloys. The first one is the macro-galvanic corrosion in which cathodes can be externally in contact with magnesium, Figure 2.8(a). In micro-galvanic corrosion, on the other hand, the second phase or impurities present in Mg and its alloys could be internally in contact with magnesium, Figure 2.8(b).

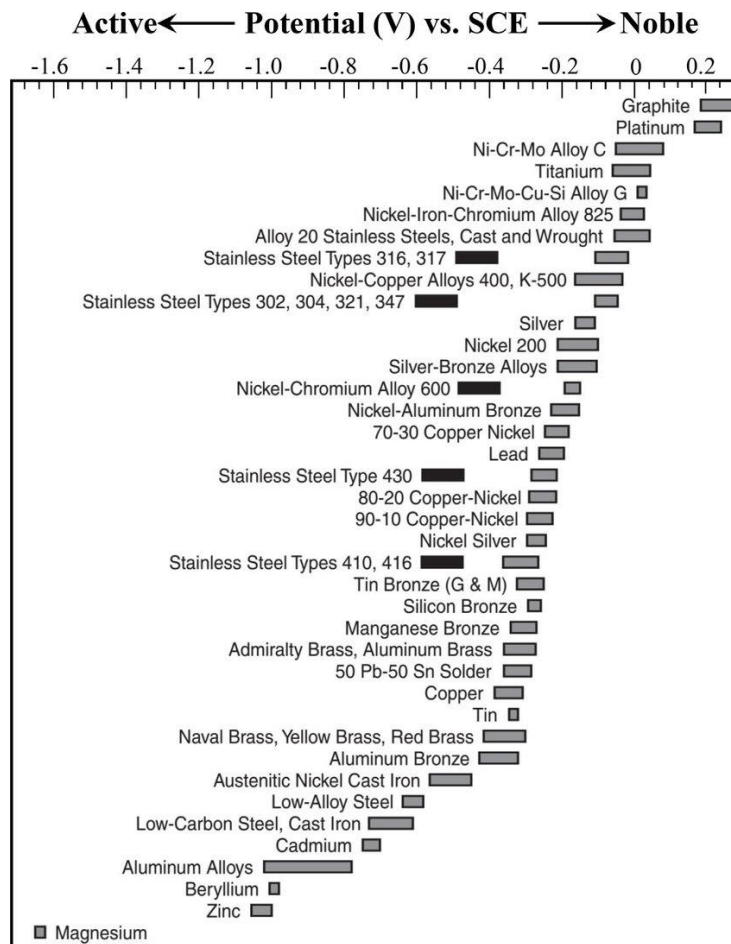


Figure 2.7. Galvanic series of some metals in the seawater environment [66].

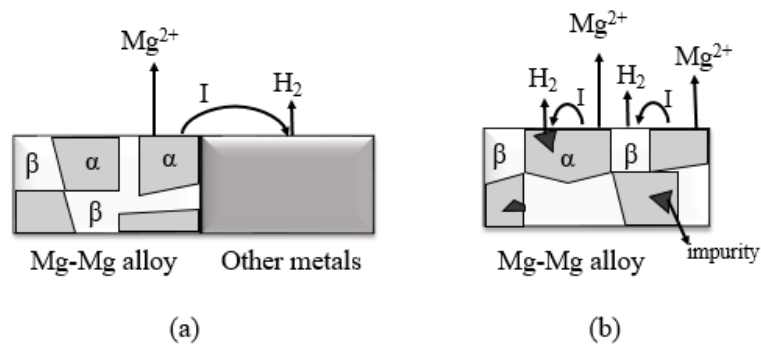


Figure 2.8. Schematic representation of (a) macro-galvanic and (b) micro-galvanic corrosion [65].

- **Macro-galvanic corrosion**

Figure 2.8 shows the galvanic series for metals in the order of their relative activities in ambient seawater [66]. The list starts with the noble metal (cathode) and reaches the most active metals (anode). It is seen that magnesium is at the bottom of the list, meaning that it is the most active metal among alloys listed, Figure 2.7. Therefore, when coupled with one of the metals listed, magnesium becomes the anode and corrodes preferentially in any galvanic couple.

Figure 2.8(a) shows the schematic illustration of macro-galvanic corrosion of magnesium coupled with a less active metal. Severe galvanic corrosion occurs when the magnesium is in contact with less active metals such as stainless steel, Ni-Cr-Mo alloy, and titanium, Figure 2.7. Because these metals have low hydrogen overpotential and act as cathodes. Therefore, the potential difference between Mg and other metals can produce galvanic current, I , which causes the magnesium dissolution at the anode and hydrogen evolution at the cathodic site, Figure 2.8(a).

- **Micro-galvanic corrosion**

Micro galvanic corrosion takes place between the α -Mg matrix having a lower free corrosion potential and second phases or metallic impurities (Fe, Ni, and Cu) with a higher free corrosion potential [67]. Therefore, the anodic α -Mg matrix is corroded preferentially, and hydrogen evolution is observed at the cathodic secondary phase, Figure 2.8(b). Secondary phases such as Al_8Mn_5 and $Mg_{17}Al_{12}$ are cathodic to α -Mg matrix [68,69], while the other types of secondary in the rare earth (RE) containing magnesium Mg alloys like WE43 (Mg-Y-Nd), GW93 (Mg-Y-Gd), are found to be more active than Mg matrix [70].

2) Pitting Corrosion

Magnesium undergoes pitting corrosion when exposed to chloride ions in neutral or alkaline solution [53]. The reasons for the formation of pits may be related to several reasons, such as the chemical composition, surface condition, and grain size of Mg alloy, and the environmental conditions (i.e., pH, temperature) [53,63,71]. For example, the discontinuous oxide film on the AM60 alloy causes the adsorption of Cl⁻ anion in the α phase. Therefore, after the dissolution of α -phase, the passivation film is collapsed, and subsequently, pitting corrosion takes place [71].

3) Intergranular Corrosion

Magnesium and its alloy are not susceptible to intergranular corrosion. Grain boundaries are always cathodic relative to the grain interior; therefore, corrosion does not penetrate the grain along the grain boundaries [63]. Accordingly, grains are anodic to grain boundary so that corrosion focuses on an area adjacent to grain boundaries [65].

4) Stress Corrosion Cracking

Stress corrosion cracking (SCC) of magnesium alloys results from the combined effect of electrochemistry and the tension forces. SCC is expected to occur when Mg alloy is exposed to stress in wet conditions. In the presence of hydrogen, SCC initiation stress decreases below the operation value so that catastrophic failure occurs. Although the addition of aluminum and zinc enhance the SCC, alloying with tin decrease the stress corrosion sensitivity of Mg alloy [72].

2.2.3.1.4 Proposed corrosion models for Mg and its alloys

The negative difference effect (NDE) is an extraordinary phenomenon affecting especially magnesium and its alloy dissolution. Generally, electrochemistry categorizes corrosion reactions in either anodic or cathodic [73]. By increasing

applied potential or current density, the anodic reaction rate increases and simultaneously a decrease is observed in the cathodic hydrogen evolution for traditional metals like copper, steel, and zinc. However, the hydrogen evolution behavior of magnesium appears to be different from the basics of the electrochemical theory. Figure 2.9 shows a schematic illustration for the NDE, in which solid lines labeled as I_a and I_c , the normal anodic and the cathodic partial reactions, respectively, are assumed to obey Tafel kinetics [65]. At the corrosion potential, E_{corr} , the rates of both reactions are equal to I_o . Typically, increasing the applied potential from E_{corr} to E_{appl} causes a decrease in cathodic rate from I_o to $I_{H,e}$, and an increase in anodic reaction rate from I_o to $I_{Mg,e}$. However, it is experimentally found for Mg and its alloy that increasing the potential leads to an increase in the dissolution rate and hydrogen evolution rate, shown by dashed lines, I_{Mg} and I_H , Figure 2.9. Therefore, for an applied potential, E_{appl} , the actual hydrogen evolution rate (HER), corresponds to the $I_{H,m}$, which is higher than the expected current $I_{H,e}$. Also, the anodic Mg dissolution current can increase faster than expected from the polarization curve, I_{Mg} , meaning that the actual dissolution rate, $I_{Mg,m}$ is significantly higher than the expected current, $I_{Mg,e}$.

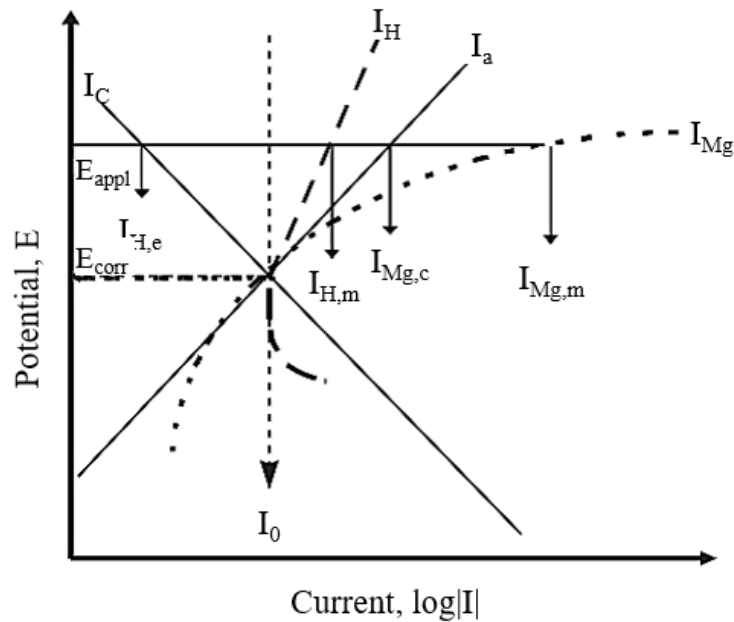


Figure 2.9. Schematic representation of the negative difference effect (NDE) [65].

Several authors have tried to explain the NDE phenomena via developing four different models described below:

i. Partially protective surface film

This model purposed that NDE is referred to as the breakdown of the partially protective layer on the surface during the dissolution of magnesium. Divalent magnesium ions, Mg^{2+} , dissolve into the solution near the metal/electrolyte interface, experience hydrolysis, resulting in lowering the pH of the solution and enhance the corrosion rate. Also, the thickness of the protective film decreases as the potential/current is increased [65], as given in Figure 2.10(a-b).

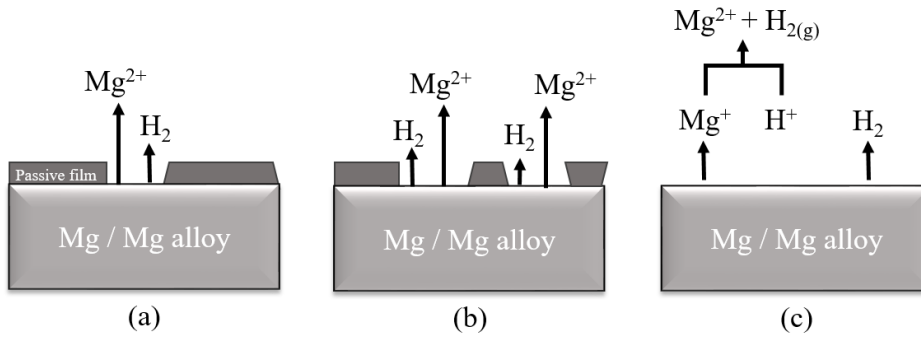


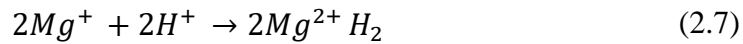
Figure 2.10. Model of the partially protective surface film; (a) low E or I and (b) high E or I and (c) Mono-valent magnesium ion model [65].

ii. Mono-valent magnesium ion model

In this model, Mg^+ monovalent ion may be involved in the NDE as schematically given in Figure 2.10(c). It is believed that the Mg^+ monovalent ion is produced electrochemically, according to Eq. 2.6:



Then, intermediate mono-valent Mg^+ ion chemically reacts to evolve hydrogen gas by the following Eq. 2.7.



Song et al. [65] stated that this mechanism is consistent with the experimental results in which the hydrogen evolution rate increase with an increase of applied anodic potential.

iii. Particle undermining model

This model proposes the NDE in terms of the undermining and falling away of second phase particles, especially at high anodic current potential or current, Figure 2.11 (a-b). Also, this model can be explained by the micro-galvanic corrosion

mechanism [63]. Second phase particles (i.e., impurities in pure Mg or $Mg_{12}Al_{17}$ phase in Mg-Al alloys) are more cathodic to surrounding magnesium matrix so that local galvanic corrosion occurs at the particle boundary [65,74]. Also, a particle can be undermined by corrosion of the adjoining Mg matrix, resulting in particles fall out and increased mass loss. Also, more undermining of particles can occur at the higher current densities, Figure 2.11(a-b).

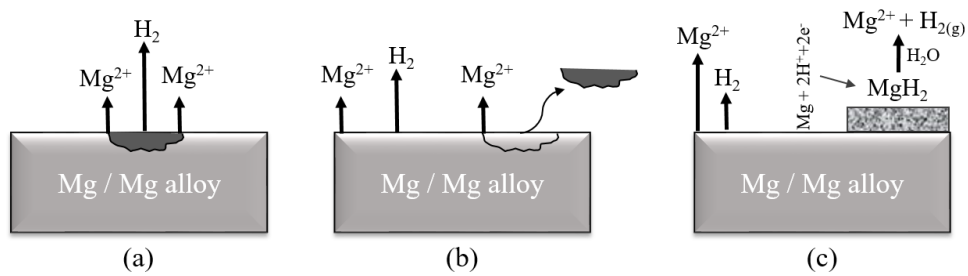


Figure 2.11. Schematic representation of particle undermining model at (a) low and (b) high current density/potential and (c) magnesium hydride model [65].

iv. Magnesium hydride (MgH_2) model

This model suggests that the NDE can be explained by the formation of magnesium hydride, MgH_2 , layer on the specimen's surface [65,74], as shown in Figure 2.11(c). MgH_2 is quite reactive in water and produces H_2 by the following reaction:



Although this model is based on thermodynamics, predicting the stability of MgH_2 , it is a contradiction to basic electrochemistry. Because Eq. (2.8) is a cathodic reaction, HER should decrease with an increase of potential or current. However, there is still debate on the existence of the NDE for Mg and its alloy. Maker et al. [75] stated that there was no NDE for corrosion of the as-cast AZ61 alloy. In contrast, Chen et al. [76] concluded that magnesium hydride, partially protective

film, monovalent magnesium ion model, and particle undermining model were the primary mechanism for the NDE as-cast AZ91 alloy. Also, Zhang et al. [77] showed that HER increased with increasing potential for AZ91 alloy based on the partial breakdown of the passive film.

Furthermore, the NDE is associated with the corrosion performance of the magnesium alloy. An alloy having a higher degradation rate performed a severe NDE. If magnesium can form a stable surface film, NDE can be prevented, and corrosion resistance of the alloy can be enhanced.

2.2.3.1.5 Factors that affect the corrosion of Mg alloy

Several parameters affect the corrosion of magnesium alloys, which are chemical composition (impurities, alloying elements), microstructure (second phase, grain size), and environment (solution, temperature, atmosphere). In the following section, the effect of impurity elements, alloying elements, and the role of the second phase in the microstructure will be discussed in detail.

- The impurity content

The type and concentration of the impurities have various effects on the corrosion characteristics of magnesium. Hanawalt et al. [78] studied the effect of different impurity elements on the corrosion rate of magnesium alloy in the saltwater. They have divided 14 elements into three main groups. The first group includes Fe, Ni, Cu, and Co elements, which are extremely detrimental to the corrosion when their concentrations are below 0.2 wt. %. The second group of elements was containing Ag, Ca, and Zn, which do not have a significant influence on corrosion between the concentrations of 0.5 and 5 wt. %. On the other hand, the last group (Al, Sn, Cd, Mn, Si, and Na) had rarely effect on the corrosion of Mg at the concentration below 5 wt. %. Moreover, recent studies have also revealed that the most critical issue in the

dissolution of Mg is its purity. Especially, Fe, Ni, and Cu elements have detrimental effects because of their low solid-solubility limit. They become the active cathodic sites and accelerate the corrosion rate because of micro galvanic coupling with anodic Mg-matrix. For example, the FeAl₃ intermetallics acts as a cathodic site so that they cause degradation of magnesium [79]. Therefore, it is essential to control the quantity and types of impurity elements to control the corrosion of magnesium.

- **Types of alloying elements**

Magnesium alloys are usually alloyed to get the desired mechanical property and corrosion rate for specific applications. The first step in the designing of magnesium with a lower corrosion/degradation rate is the careful selection of alloying elements. Various alloying elements like Al, Zn, Mn, Ca lead to the formation of the different microstructures and enhance the corrosion behavior of resultant magnesium alloy. Commercial Mg-alloys used as biodegradable materials in biomedical applications includes mainly AZ (Mg-Al-Zn), WE (Mg-RE), and ZK (Mg-Zn-Zr) series alloys [80], Figure 2.12.

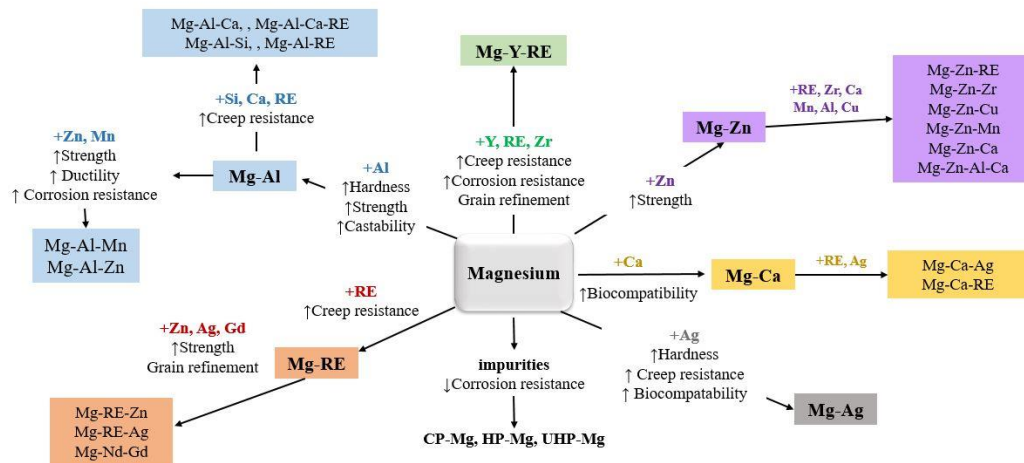


Figure 2.12. Development of magnesium with various alloying elements [80].

Aluminum (Al)

Aluminum (Al) has been mostly preferred alloying element for magnesium with a maximum solubility of 12.7 wt. %, Figure 2.13 [81]. Various Mg-Al based alloy systems, such as AZ and AM alloys, have been developed for various applications to understand the corrosion mechanism of Mg alloys [82–86]. Aluminum addition results in β -phase ($\text{Mg}_{17}\text{Al}_{12}$) precipitation, which enhances the corrosion resistance by acting as a corrosion barrier. Moreover, aluminum contributes to solid solution strengthening and precipitation of the second phase in the form of $\text{Mg}_{17}\text{Al}_{12}$ along grain boundaries as a continuous phase [87] and the formation of a lamellar structure [65].

Gusieva et al. [37], on the other hand, believed that Al with an amount of above 3 wt. % raises the degradation rate of Mg-Al alloy by the formation of $\text{Mg}_{17}\text{Al}_{12}$ phase. Esmaily et al. [88] stated that the amount and distribution of Al are responsible for the increase in the corrosion rate. Moreover, Lunder et al. [89] found that 8 wt. % aluminum accelerates anodic dissolution, while aluminum improves the corrosion resistance when its content is above 10%. According to Winzer et al. [72], $\text{Mg}_{17}\text{Al}_{12}$ phase has two different influence on the corrosion of Mg and Mg alloy. It is believed that it acts either as a corrosion barrier or as a galvanic cathode depending on its amount and distribution. When $\text{Mg}_{17}\text{Al}_{12}$ has a lower volume fraction compared to α -matrix, it acts as a galvanic cathode and increases the dissolution rate of magnesium. On the other hand, if the volume fraction of β - $\text{Mg}_{17}\text{Al}_{12}$ is relatively high and it has an interconnected network layer, the overall corrosion of the alloy can be reduced since $\text{Mg}_{17}\text{Al}_{12}$ phase acts as a barrier. The effect of the quantity and distribution of the second phase on corrosion of magnesium behavior will be discussed in detail in the following sections.

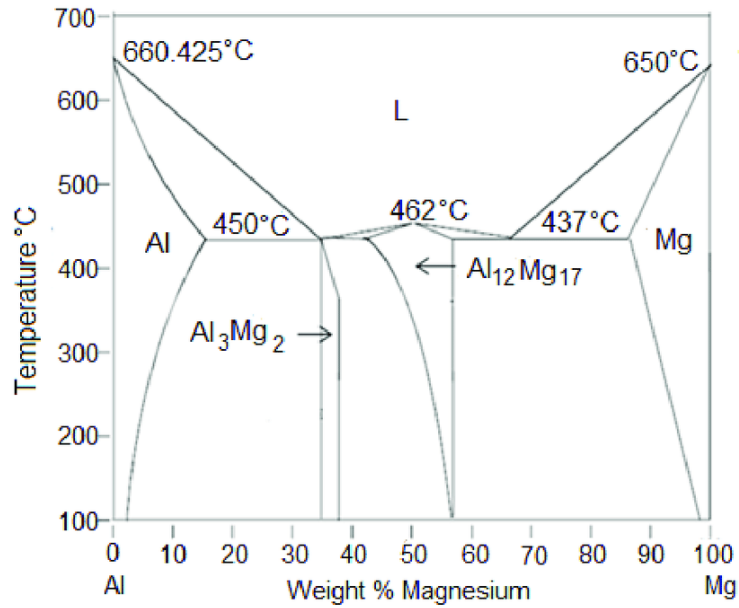


Figure 2.13. Phase diagram of the Mg-Al system [81].

Manganese (Mn)

The addition of Mn to the Al-containing magnesium alloy causes the formation of Al-Mn intermetallic phases. Accordingly, these intermetallics can control the corrosion of Mg alloy by picking up iron (Fe), which has a detrimental effect on the corrosion resistance of magnesium alloy [65].

Calcium (Ca)

The human body needs calcium to maintain growth and healing of the bones, and therefore, it has been extensively used as an alloying element for biodegradable Mg alloys. Although Ca has a limited solubility of about 1 wt. % in Mg, the formation Mg_2Ca secondary phase in the grain boundaries and grain interior improve the corrosion resistance of Mg and its alloy [74]. Bornapour et al. [17] found that the corrosion resistance of magnesium enhanced by the addition of a small amount of Ca and Sr (0.3 wt. % Sr and 0.3 wt. % Ca).

Zinc (Zn)

Zinc, one of the most abundant nutrients in the body, is essential alloying elements with relatively high solubility of 6.2 wt. % in Mg [31]. Increasing the mass fraction of Zn in magnesium alloy enhances the corrosion resistance of Mg. Even a small amount of zinc (Zn) can provide a solid solution and precipitation strengthening that can lessen the dissolution rate of Mg alloy. Cai et al. [90] believed that the corrosion resistance improved with increasing Zn content by grain boundary, solid solution, and secondary phase strengthening.

Rare Earth (RE) Elements

The RE group contains 17 different elements that can be divided into two groups according to their solid solubility in magnesium. The first group includes elements having high solid solubility in Mg, which are yttrium (Y), Dysprosium (Dy), Gadolinium (Gd), Terbium (Tb), Thulium (Tm), Holmium (Ho), Erbium (Er), Ytterbium (Yb), and Lutetium (Lu). On the other hand, the second group contains elements with limited solid solubility in Mg (Neodymium (Nd), Lanthanum (La), Cerium (Ce), Samarium (Sm) and Europium (Eu)) [15,31,91]. In recent years, Mg-RE-based alloys have been gained attention due to their controllable degradation rate.

Rare earth elements can form complex intermetallic phases with Al and Mg. These intermetallic phases may enhance the corrosion resistance of magnesium alloy by solid solution strengthening. Zhang et al. [92] found that the degradation of magnesium alloys having Y can be slowed down because of the formation of the $Mg_{24}Y_5$ intermetallic phase. Moreover, Chen et al. [91] believed that the Nd element, with limited solubility of 3.6 wt. %, forms the $Mg_{12}Nd$ phase, thereby lowering the corrosion rate of the alloy [91]. Additionally, Peron et al. [74] stated that the improved corrosion rate of EV31A (2.8 Nd-1.3 Gd-0.56 Zr-0.29 Zn-other RE in wt.

%) is due to the formation of mixed oxides of Nd and Gd on the surface, which is more stable than that of RE free magnesium alloy.

However, Feyereband et al. [93] stated that the addition of the small amount of La and Ce elements in WE43 alloy (Mg-3.5Y-2.3Nd-0.5Zr in wt. %) caused the formation of the gas bubbles and the high cytotoxicity effect. Besides, Chino et al. [94] conducted showed that La and Ce elements localized in a small area around the implant, although they improved the corrosion resistance of WE43 alloy.

On the other hand, Willbold et al. [95] investigated the corrosion behavior of WE43 and LAE442 (Mg-4%Li-3.6%Al-2.4%RE, in wt. %) and conducted in-vitro experiments by inserted the implants into the bodies of rabbits. They revealed that hydrogen gas bubbles existed around both implants and subsequently disappeared after two weeks. Finally, the surgical sites were recovered four weeks later, and there was no adverse effect of gas bubbles [95].

Moreover, Niu et al. [96] implanted Mg-Nd-Zn-Zr screws in the rabbit mandible. They observed the formation of new bone around the screw, and there was no inflammation around the implant after 18-month implantation, Figure 2.14(a). The degradation process of Mg-Nd-Zn-Zr implants is shown in Figure 2.14(b) [96]. They stated that the screw did not lose its integrity after four mounts, while; a large part of the screw has degraded, and only a small piece remained in the center after 18 mounts. As a result, new bone tissues, such as osteoblasts and osteocytes, were observed around Mg-alloy screws in the rabbit's mandible [96].

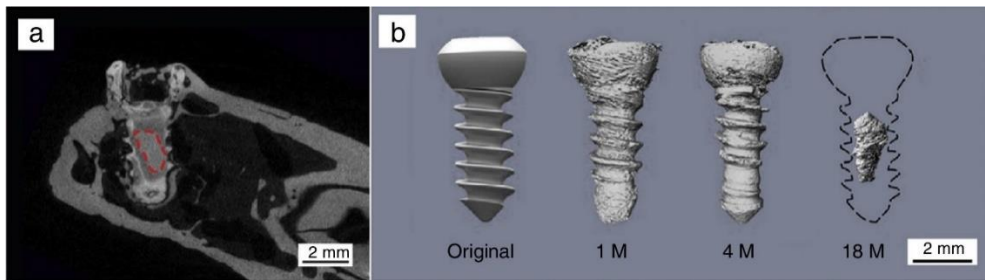


Figure 2.14. (a) μ CT images of the vertical section of a screw and (b) the schematic images of the original screw and residual screw after 1, 4, and 18 months after implantation. [96].

- Second Phases

The amount and the distribution of the second phase may have a pronounced effect on the degradation characteristics of magnesium alloys. Because the second phases act as cathodic centers, which are known to be less active than anodic α -Mg matrix when immersed in the aqueous environment. This type of corrosion is called micro galvanic corrosion, in which α -matrix dissolved preferentially.

If the volume fraction of the intermetallic phase, i.e., β -intermetallic phase in AZ91 alloy, is relatively low compared to α -matrix, the undermining of the second phase occurs. The preferential dissolution of α -matrix occurs at or along the grain boundary so that the second phase is undermined (fall out), causing an increase in the corrosion rate. On the other hand, the high-volume fraction of the secondary intermetallic phase can enhance the corrosion resistance by acting as a barrier against the corrosion of the alloy. For instance, Song et al. [65] believed that AZ91 alloy was improved when it contained homogeneously distributed $Mg_{12}Al_{12}$ intermetallic phases along the grain boundary, which acted as a corrosion barrier. Therefore, secondary phases with the homogenous distribution in the microstructure contribute to the decrease of the corrosion rate.

In the study of Cao et al. [97], they investigated the corrosion rate of WE43 alloy by an in-vitro test using simulated body fluid (SBF). They realized that the coarse, secondary particles were undermined, leaving the deep holes after immersion of 12 h, Figure 2.15(b), although there was no sign of falling out the intermetallics after six hours of immersion, Figure 2.15(a). This phenomenon was due to the low amount of the second phase and its discontinuous distribution in the microstructure, leading to a severe increase in the corrosion rate of WE43 alloy.

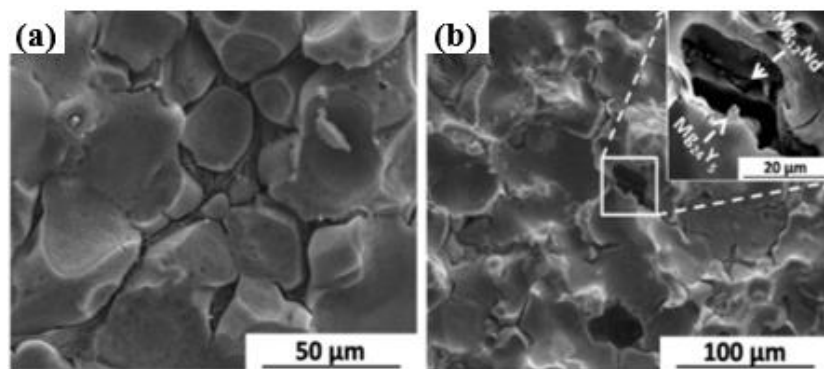


Figure 2.15. Surface morphologies of WE43 alloy samples after immersion in SBF for (a) 6 h and (b) 12 h [97].

2.2.3.1.6 Corrosion rate measurement for Mg

Corrosion of magnesium and its alloys is a complex process so that the combination of various techniques should be conducted to support the results of different tests used for revealing the corrosion kinetics and mechanism of Magnesium alloys. Kirkland et al. [98] and Esmaily et al. [54] provide a summary of the main advantages and drawbacks of various corrosion rate measurement techniques. This section includes the test methods used to determine the corrosion resistance and the

degradation rate of magnesium and its alloys, which are categorized into two groups:

(i) non-electrochemical and (ii) electrochemical techniques.

i) Non-electrochemical techniques

- Weight loss measurement

In the weight loss experiments, only a sample, corrosion medium, and a precision balance are needed to assess the corrosion behavior of magnesium. Firstly, the sample is immersed in the corrosive medium for a while and then removed from the aqueous solution. Before measuring the resultant change in mass and mass loss, a cleaning solution like chromic acid (Cr_3O) is preferred to remove corrosion products (i.e., magnesium hydroxide, $\text{Mg}(\text{OH})_2$) from the surface. Different acid solutions such as chromic acid, CrO_3 [86,99–101], a mixture of CrO_3 and AgNO_3 solution [102], and a mixture of nitric acid and CrO_3 [103] can be used as cleaning solutions. The corrosion rate of magnesium is calculated according to ASTM G31-72 [104] as given in Eq. (2.9);

$$CR = \frac{\Delta W}{A_o \times t \times \rho} \quad (2.9)$$

Where CR is the corrosion rate, ΔW is the difference between the initial and final weight of the sample (after removal of the corrosion products), A_o is the initial surface area, t is the exposure time, and ρ is the density of the sample.

- Hydrogen evolution measurement

The rate of the magnesium dissolution directly corresponds to the amount of H_2 evolution, Eq. (2.1). According to H_2 evolution tests, the evolution of 1 mole of hydrogen gas directly proportional to the dissolution of 1 mole of magnesium,

meaning that measuring the volume of H_2 gas is equivalent to measuring the weight loss of the Mg.

Numerous studies have been performed to determine the in-vitro performance of magnesium alloy by hydrogen evolution experiments [54,67,71,73,82,105–109]. Figure 2.16 shows the typical experimental setup, which contains a collector, an inverted funnel, and a burette. Initially, a sample is immersed in the corrosion medium, i.e. simulated body fluid, and a collector is placed in the medium directly above the sample to capture evolved H_2 gas during Mg corrosion. The hydrogen gas accumulates as bubbles that detach from the surface. H_2 bubbles are collected at the top of the burette by displacement of the solution in it. Subsequently, the volume of the H_2 gas is measured by noting the level of the solution in the burette at different time intervals [54,98].

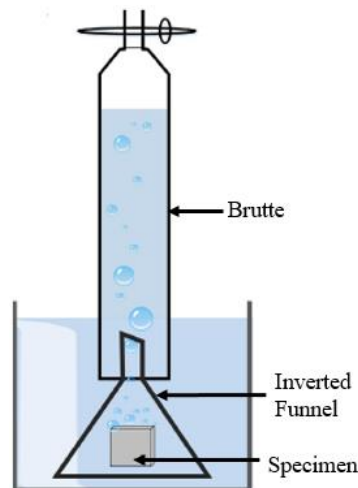


Figure 2.16. Schematic representation of H_2 evolution test setup [54].

However, similar to weight loss experiments, H_2 evolution experiments do not provide any information about the corrosion mechanism. Besides, Esmaily [54] et al. stated that H_2 bubbles usually attached to the walls of the inverted funnel and the

burette; therefore, they were not added to the gas volume at the top of the funnel. Thus, it causes misleading results in the calculation of the hydrogen evolution rate. Also, Kirkland et al. [98] stated that the H₂ evolution technique is not a suitable method for the study of alloys with high corrosion resistance and the study of corrosion in time intervals less than one hour because there is an insufficient volume of evolved gas at the early stage of corrosion. Figure 2.17 displays the representative graph of the hydrogen evolution test, in which the y-axis shows the amount of hydrogen gas evolved with respect to immersion time (x-axis).

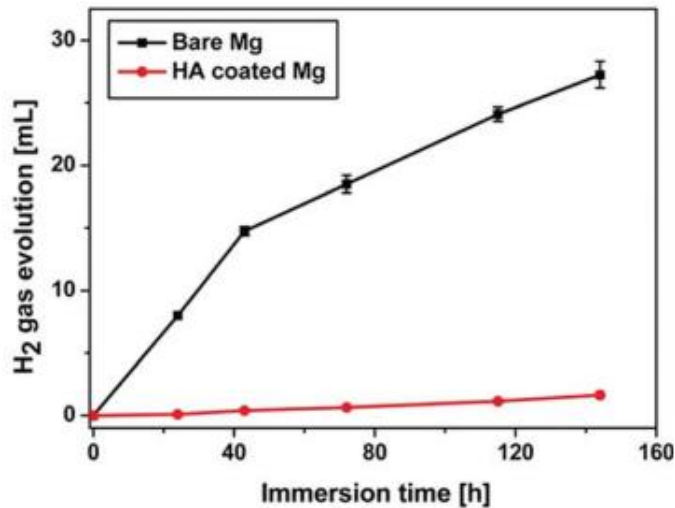


Figure 2.17. Comparison of hydrogen gas evolution in the SBF for bare and HA-coated magnesium [110].

ii) Electrochemical techniques

- Potentiodynamic polarization (PDP) test

Potentiodynamic polarization (PDP) test is an electrochemical technique that can be used to study in vitro corrosion of Mg alloys. The PDP test gives information about

corrosion potential, E_{corr} (in volt), corrosion current density, i_{corr} (mA/cm^2) and, relative anodic and cathodic reactions at a specific time. Figure 2.18 shows the schematic representation of a three-electrode electrochemical cell containing counter electrode (CE), reference electrode (RE), working electrode (WE), and the electrolyte.

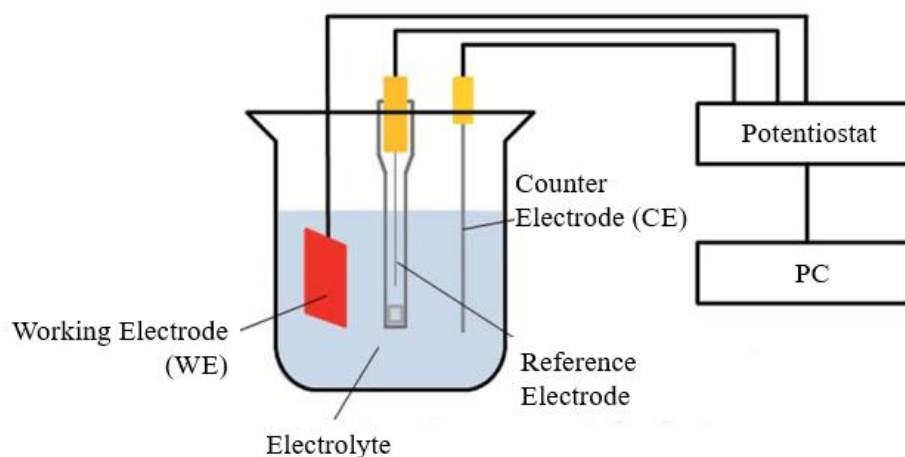


Figure 2.18. Schematic representation of a three-electrode electrochemical cell.

A reference electrode provides information about the potential applied to the working electrode. The suitable reference electrodes for specific applications are saturated calomel electrode (SCE) [32,111], the silver-silver chloride (Ag/AgCl) [112] and the copper/copper sulfate [113,114] electrodes. Besides, the counter electrode provides the applied current to the system and should be made up of corrosion-resistant materials such as platinum [33,62,114–116] and graphite [61,117] because the dissolution of the electrode changes the solution chemistry and may cause complication during measurement. Also, the size of the counter electrode is an important parameter such that it should be equal or larger than that of the working electrode as the size of the electrode directly related to the amount of current formed [118].

Before starting the PDP test, open circuit potential (OCP) is recorded for a while. Then, potential is increased with the controlled rate (i.e., 0.5 mVs^{-1}) via adjusting the current flowing between two electrodes. Usually, the initial voltage is set to start at values more negative than the OCP, and subsequently, the scan continues to increase more positive values [98].

Figure 2.19 shows the schematic plot of current density (I) versus potential (E) curves, which are named as a Tafel plot. The E_{corr} and i_{corr} values can be estimated by using the Tafel extrapolation method. Also, anodic (β_a) and the cathodic (β_c) Tafel slopes are the other important parameters, which can be found from the slopes of the anodic and cathodic branches, Figure 2.19. Then, the corrosion rate (CR) can be calculated using i_{corr} value according to Eq. (2.10) in ASTM G102-89 as follow:

$$CR = \frac{K \times i_{\text{corr}} \times EW}{\rho} \quad (2.10)$$

Where CR is given in mm/yr, i_{corr} is in $\mu\text{A}/\text{cm}^2$, K is a constant and equal to $3.27 \times 10^{-3} \text{ mm g}/\mu\text{A cm.yr}$, ρ is the density of the sample in g/cm^3 .

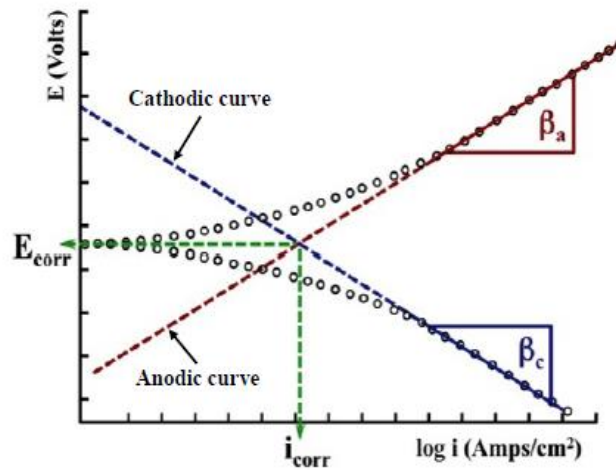


Figure 2.19. Schematic plot of current density (I) versus potential (E) curves obtained from the Tafel extrapolation method [119].

- **Electrochemical impedance spectroscopy (EIS)**

EIS is one of the useful techniques for understanding the electrochemical corrosion process and surface film formation on the surfaces of metals in corrosive environments. Besides, EIS is a non-destructive technique that characterizes the bulk and interfacial properties of materials. In recent years, EIS has been widely used in the characterization of coatings, batteries, and fuel cells and the determination of corrosion behavior of the materials due to its simplicity and relative ease of use [59,62,98,120–122].

In this technique, the response of AC polarization, as a function of the frequency, can be monitored, when an excitation signal with a small amplitude is applied to the system [98,123]. The impedance, $Z(\omega)$, of the system is a complex quantity with a magnitude and a phase shift which depends on the frequency of the signal [124,125]. Moreover, the impedance of the system can be obtained by changing the frequency of the applied signal. For the electrochemical cells, a frequency range of 100 kHz–0.1 Hz has been widely preferred [124]. Besides, the impedance, $Z(\omega)$, is a complex quantity that can be described in Cartesian coordinates and it is represented by $Z(\omega) = Z'(\omega) - j \cdot Z''(\omega)$. $Z'(\omega)$ and $Z''(\omega)$ are the real and imaginary parts, respectively, and j equals to $\sqrt{-1}$ [124,126].

The characterization of electrochemical systems with impedance spectroscopy requires an understanding of the data by using a suitable equivalent circuit model. The model predicts parameters that can describe the experimental data adequately and estimate the behavior of the system under different conditions [127].

The circuit model for EIS consists of electrical circuit elements which are resistors (R), capacitors (C) and inductance (L). The various elements of the equivalent circuit are then assigned a specific physical meaning [124,126]. The resistance, R, has an impedance that is independent of frequency, while the capacitance, C, has an impedance, which is a function of frequency. Also, the double-layer capacitance,

Cdl, forms at the electrode/electrolyte interface when oppositely charged ions separated from each other at the electrode surface [128]. While it behaves like the non-ideal capacitor due to inhomogeneities in the electrode or the electrolyte. Thus, the non-ideal behavior of the capacitor can be compensated by using the concept of a constant phase element (CPE) in the modeling of an electrical double layer. The CPE is usually defined by the n value, which is a dimensionless constant between -1 and +1. When n is equal to +1, CPE is identical to a capacitor [59]. As a result, these circuit elements can be combined in series and parallel to yield complex equivalent circuits.

For a simple parallel R-C circuit, the Nyquist plot and equivalent circuit model are given in Figure 2.20. The impedance spectrum can be shown by the Nyquist diagram having real (Z_{real}) and imaginary (Z_{img}) parts of $Z(\omega)$ using cartesian coordinates, respectively. The diameter of semicircle along the x-axes (Z_{real}) represents the resistance of R_1 , and the capacitance value can be found from the maximum point of the semicircle in the Nyquist plot in Figure 2.20(a) and shown as C_1 in the equivalent circuit in Figure 2.20(b).

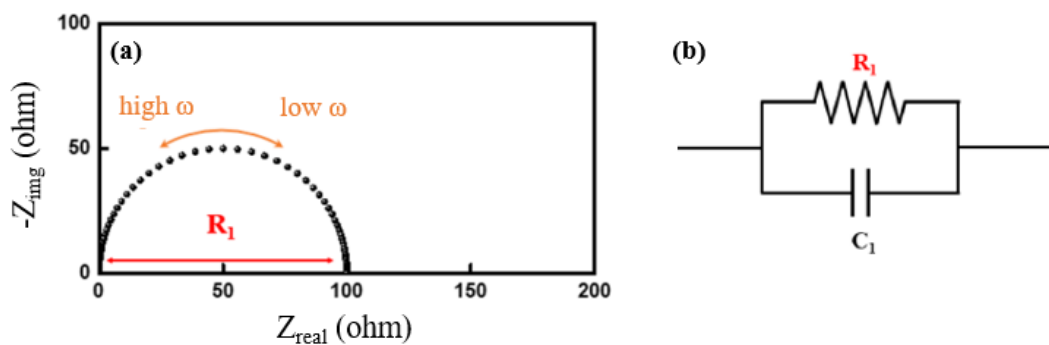


Figure 2.20. (a) Nyquist plot (b) Equivalent circuit of a parallel R-C circuit [128].

The simplified Randles circuit has been commonly used to model the corrosion processes by EIS. In Figure 2.21(a), the polarization resistor, R_1 , is connected in series with the bulk resistor, R_2 , and at the same time in parallel with the double layer capacitor, C_1 [128]. In the Nyquist plot of a simplified Randles cell, Figure 2.21(b), the starting point of the semicircle is shifted to a higher value of Z_{real} , which is called as R_2 and the diameter of the semicircle equals to R_1 .

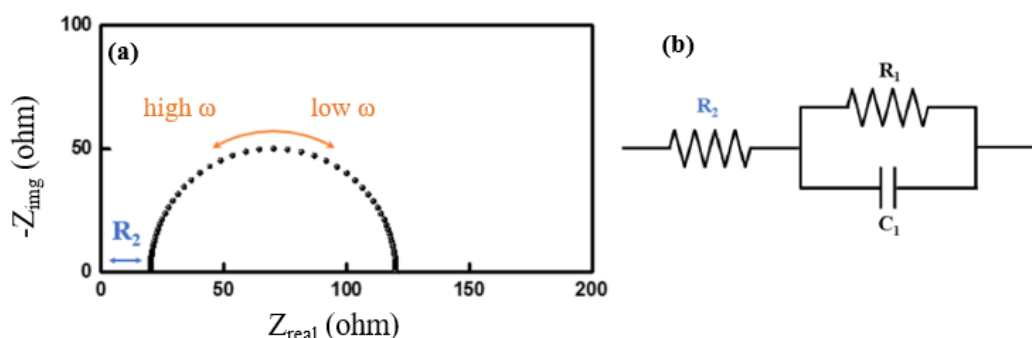


Figure 2.21. (a) Nyquist plot (b) Equivalent circuit of a simplified Randles cell model [128].

On the other hand, the Nyquist plot of pure Mg, Figure 2.22, consists of three different loops named as capacitive loop at the high and low-frequency region and inductive loop at the low-frequency region. The capacitive loop at the high-frequency region, Figure 2.22 is related to the charge transfer process due to the degradation of the sample [61,129]. On the other hand, the low-frequency region, Figure 2.22, is associated with the mass transport in the solid electrode because of the diffusion of ions to the metal surface from the electrolyte [130]. Moreover, the existence of the inductive loop at low frequencies may result from the intense microgalvanic corrosion between magnesium matrix and intermetallic phases [123] or the relaxation process of intermediate Mg^+ species [59].

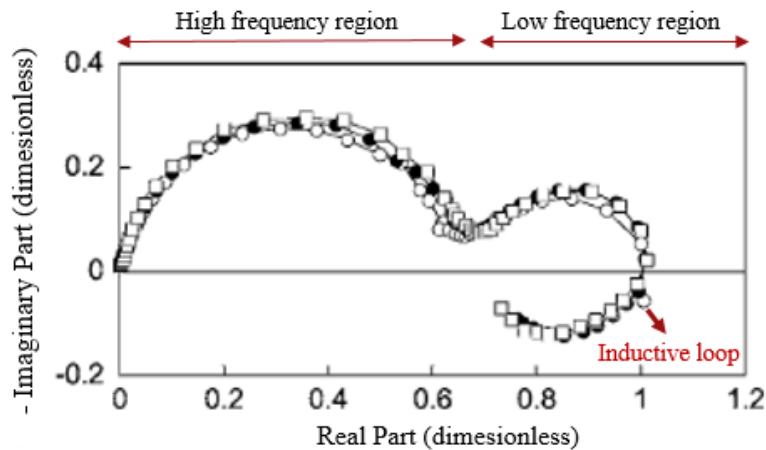


Figure 2.22. Schematic representation of typical Nyquist plots [114].

2.2.3.2 Permanent biometals

Stainless steel, titanium and titanium alloys, cobalt-chromium (Co-Cr) alloys and titanium-nickel (Ti-Ni) alloys are some of the examples of the bioinert metallic materials that remain as a permanent fixture by conserving their structures [131]. They have been extensively used in load-bearing applications because of their excellent combination of high mechanical strength and fracture toughness compared to ceramic and polymeric counterparts.

Stainless steel is an iron-based alloy consisting minimum of 11 % chromium (Cr) that prevents iron from rusting [132]. Conventional stainless steel and Ni-free stainless steel are preferred for biomedical applications because possible Ni ion release causes allergic reactions in the human body [133]. Most of the stainless-steel implants used routinely in hip and knee replacement, Figure 2.23(a) and stents that sustain the flow of blood in an artery [13].

Co-based implant alloys have higher wear resistance compared to other permanent biometals, which warrants their extensive use in artificial hip joints. Generally, Co-Cr-Mo alloys are the most commonly used alloy owing to their great combination of

high strength and high ductility [13,133,134]. Besides, they exhibit a high cyclic fatigue resistance and modulus of elasticity, which are an essential requirement for dental implants. They have been extensively used as a metal framework for removal dental partials, Figure 2.23(b), which is a well-known brand called Vitallium (65% Co, 30% Cr, and 5 % Mo) [135]. However, the possible release of Cr and Co ions through corrosion or wear processes cause inflammation and toxicity in the human body [13]. Besides, in vivo studies reported that Co ion release from Co-Cr alloy could cause carcinogenicity [52,134].

The use of Ti-Ni (Nitinol) shape memory alloys has grown over the last years, especially in the dentistry area. One of the examples that made up of Ti-Ni alloy is the endodontic root canal files, Figure 2.23(c), which was developed by Harmeet D. Walia [136]. Another example of Ti-Ni alloy used in dentistry is the dental braces, Figure 2.23(d), which is used to align and straighten teeth.

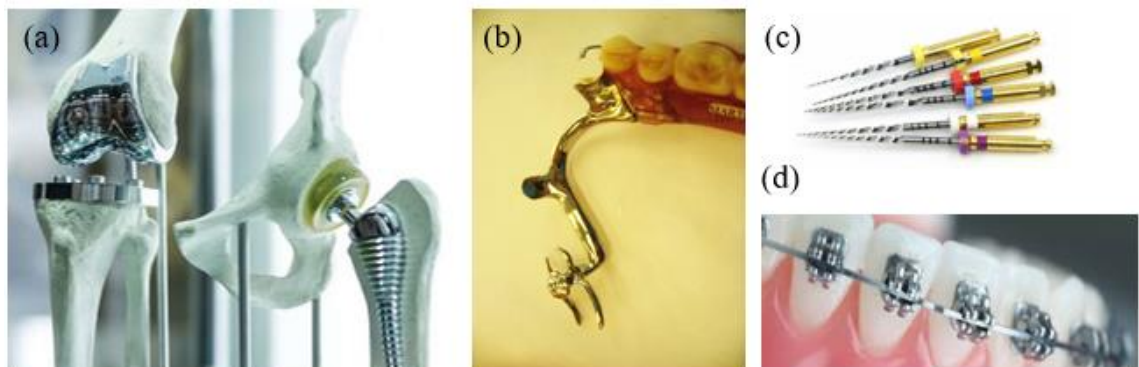


Figure 2.23. (a) Stainless steel knee and hip implant [133], (b) Co-Cr removable partial dentures [137], (c) Ti-Ni root canal files [136], and (d) Ti-Ni dental braces [30].

2.2.3.2.1 Titanium as a biomaterial

Titanium and its alloys served as the first choice of metallic biomaterials showed the outstanding combinations of high specific strength), great corrosion resistance, excellent bioinert characteristic, and sufficient biocompatibility [6,138].

Compared to ceramics and polymers, bioinert metals have exceptional mechanical strength under repetitive loading. However, they have tendencies to fail after long term usage because of the stress shielding problem, which is caused by the elastic moduli differences between the implant and bone [131]. The load cannot be transferred effectively to the bone, and the stress concentration is observed around the implant. Therefore, implant materials should have similar elastic modulus to that of bone (1-40 GPa) in order to achieve a homogenous distribution of stress between the implant and bone [139]. Titanium and its alloys possess relatively smaller elastic moduli (110 GPa) compared to stainless steel (210 GPa) and Co-Cr alloy (240 GPa) [11,131,140]. However, their elastic moduli should be reduced more.

The mismatch of elastic moduli between a titanium implant and bone can lead to failure in load transmission for long term usage under repetitive loading. Thus, the inconsistency in elastic moduli causes to a stress-shielding problem over the surrounding bone, inducing the bone resorption, and finally implant loosening. Alloying titanium is one of the solutions to decrease elastic modulus and to alleviate stress shielding.

Dunand et al. [141] stated that the introduction of pores to the dense titanium structure could alleviate the stress shielding problem because porous titanium having comparatively lower elastic moduli helps to balance the mechanical stability between bone and implants. Accordingly, porous titanium alloys can provide desired mechanical properties at the same time, yielding an appropriate place for bone growth. Thereby, the researches have stated that pore structure, connectivity, and

also its diameter affect the mechanical properties and biological performance of porous titanium implants [131,142–146].

2.2.3.2.2 Production methods for porous titanium and its alloys

Porous titanium can be manufactured through the use of many different techniques, which are the replication method, hollow sphere sintering, gas entrapment technique, space holder method, and loose powder sintering [146–149]. Brief information will be given for these methods, while detailed information about the loose powder sintering method, the subject of the current work, will be presented in the following section.

In the replication method, highly porous materials have been produced through the use of open-cell polyurethane (PU) foam or sponge as a template. The pattern preparation, infiltration, and pattern removal are the three main steps of this method. Li et al. [143] produced porous Ti6Al4V alloy having porosity content higher than 80% by thermal evaporation of polyurethane and subsequent sintering of titanium alloy powders. On the other hand, the final product may contain irregular porous structure due to the starting structure of the polymeric foam. In addition, titanium powders can be oxidized during the evaporation of the polymeric template [147,148].

For the high temperature applications, porous titanium alloys are produced by the hollow sphere method, in which nickel, steel, copper, or titanium having hollow sphere shape are bonded together by sintering [150]. One of the advantages of this method is that the pore size distribution is homogeneous, and porous structures have orderly distributed porosity content [150].

Another technique to produce porous titanium is the gas entrapment method, which is widely used in the aerospace industry by the aircraft manufacturer Boeing to produce porous titanium sandwich panels [151]. In this technique, titanium alloy

powders are compressed to the dense precursor, and argon gas is allowed to be entrapped in the material. Then, a precursor is heated at elevated temperatures, and as a result of the expansion of argon gas, isolated pores are formed in the structure. However, the resultant structure has a low amount of porosity (< 40 %) with closed and irregular shaped pores [148,150].

The space holder method enables direct manufacturing of porous structure with relatively homogenous and interconnected porosities by the evaporation of spacer particles during heating. Space holder materials can be carbamide [152,153], polymeric granules [154], ammonium hydrogen carbonate [150], and metallic powders such as magnesium [145]. Moreover, the space holder technique allows great control over pore size, porosity content, and distribution by using suitable spacers because the shape, size, and amount of the spacers greatly affect the morphology and structure of the pores.

2.2.3.2.3 Loose Powder Sintering Method

Loose powder sintering method is the simplest way to manufacture metallic foams, which depends on the partial densification of metal powders during sintering [144]. This technique consists of three main steps, which are powder preparation, compaction, and sintering of metal powders at elevated temperatures. The sintering time and temperature mainly affect the pore size, distribution, and interconnectivity of pores. The final product has irregularly shaped and randomly oriented porosities with maximum achievable porosity around 50% [147,150,154–156].

Lame et al. [157] observed three different stages during loose powder sintering of copper powders by using in-situ micro-tomography, Figure 2.24. In the stage 1, initial bonding occurs between particles, and neck formation started at 1000°C. In stage 2 (between 1000 °C-1050 °C), the main changes in the neck areas were observed, in which particles come closer to each other. At the final stage (stage 3),

neck growth causes the closing of the pore channel, and the contact area between the powders increases, Figure 2.24.

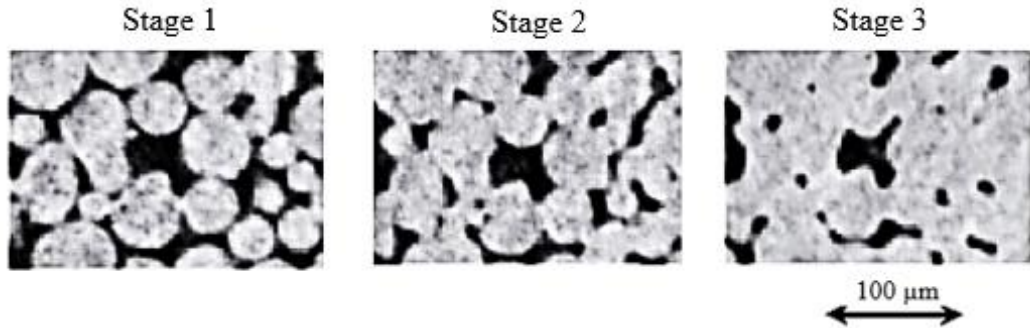


Figure 2.24. Three stages of loose powder sintering of copper powders detected by in-situ micro-tomography [157].

Moreover, Esen et al. [154] found that Ti6Al4V alloy samples produced by loose powder sintering at various sintering temperatures have porosity content between 30-37.5 vol. %. Besides, Oh et al. [156] stated that porous unalloyed titanium having 30 % porosity content was appropriate to maintain close mechanical properties to that of bone. In addition, Cabezas-Villa et al. [158] investigated the mechanical properties of loosely sintered Ti6Al4V alloy powders. They found that the pore characteristic strongly affects the compression strength of porous titanium.

2.2.3.2.4 Surface modification of titanium and its alloys

While the interconnected pores of titanium provide the biomechanical stability, the main concern for biomedical applications is the inadequate bonding ability of the surfaces with the living tissue, named as insufficient osseointegration [6,18,159]. Therefore, surface modification of titanium and its alloy should be carried out to

enhance the bioactivities and to attain both physical and chemical attachment of bone tissues to the porous surfaces.

Different surface modification methods, which are physical, mechanical, and chemical treatments, have been performed in order to improve the osseointegration ability of porous titanium surfaces.

Mechanical methods: Mechanical methods are the most straightforward technique to modify or change the surface properties of Titanium and its alloys. Increased surface roughness allows the attachment, growth, and deposition of living tissues easily on Titanium. The surface of the surgical bone plates, fixation screws, and dental implant made of Titanium are treated via mechanical methods, including machining, polishing, and blasting [160].

Physical methods: In these methods, it is aimed to enhance the corrosion resistance, biocompatibility, wear resistance of titanium by the formation of films or coating having micro or nanometer thickness. Thermal spray, physical vapor deposition (PVD), and ion deposition are some of the examples of physical methods [161].

Chemical methods: The most frequently used method for the surface modification of titanium is the chemical method because stronger adhesion between modified surface and bones is obtained compared to other methods. Moreover, the main purpose is to modify the surface by chemical reactions occurring at the interface between the solution and the titanium. Some of the examples of chemical methods are hydrogen peroxide, sol-gel, anodic oxidation, acid etching, and hydrothermal method [18].

Due to its simplicity and easy to apply on a complex structure, the hydrothermal method has been gained attention to get the homogenous and uniform coating on the surface of Ti and its alloy. NaOH-alkali heat treatment is one of the most widely used hydrothermal methods to obtain sodium titanate layer, which induces the apatite formation on the surface of titanium [162–165]. The method contained two major

steps. Initially, titanium alloys are immersed in NaOH solution having various concentrations (1-10 M) at different temperatures (40-120 °C) so as to obtain sodium titanate hydrogel, $\text{Na}_x\text{H}_{2-x}\text{Ti}_y\text{O}_{2y+1}\cdot n\text{H}_2\text{O}$. Then, the heat treatment at various temperatures (600-800 °C) was conducted to obtain a mechanically stable crystalline bioactive titanate layer, $\text{Na}_2\text{Ti}_y\text{O}_{2y+1}$ [163].

Moreover, Pattanayak et al. [166] found that titanium surface having a porous network structured Na-rich coating layer, Figure 2.25(a) enhanced the apatite precipitation on the surface of porous titanium, Figure 2.25(b). They stated that alkali heat-treated porous titanium was found to be a useful bone substitute [166]. It is known that the osseointegration of titanium and its alloy improved by the formation of the bioactive titanate phase, which inhibits the precipitation of hydroxyapatite in the body environment.

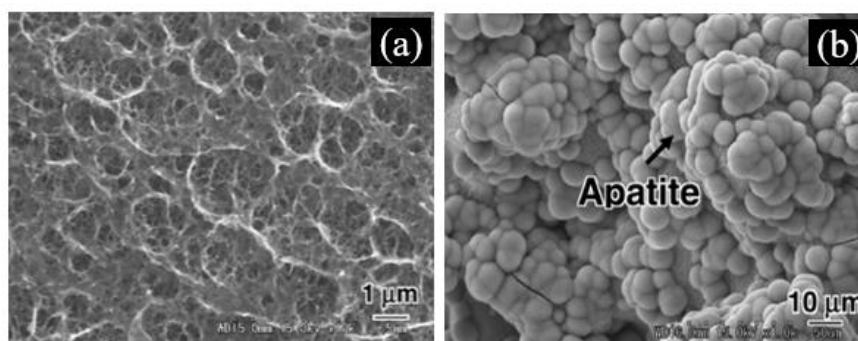


Figure 2.25. (a) the surface of porous titanium after alkali-heat treated, and (c) the apatite formatted titanium surfaces after immersion in SBF [166].

2.2.4 Biocomposites

Composite is defined as the combination of two or more materials having different composition and morphology. In addition, they are designed to produce materials

with properties adapted to meet the specific chemical, physical, or mechanical needs. Thus, the composite usually shows significant properties that the single constituents do not have and sometimes exhibits the best qualities of each constituent [167].

In the human body, bones, tendons, ligaments, and teeth are the natural composites, and their distribution, amount, and morphology determine the final behavior of tissue or organ [167]. On the other hand, man-made composites can be used to make implant or prostheses that can mimic these living tissues, match their mechanical behavior, and improve the mechanical functions of damaged tissues.

Various types of composites have already been studied for different biomedical applications such as cardiovascular applications, dentistry, oral surgery, tissue engineering, and orthopedics [168–171]. There are various types of composites that are used in biomedical applications, such as polymer-ceramic, metal-ceramic, and metal-metal composites.

Polymer-Ceramic Composite: In the last decade, the use of composites materials in dentistry, mainly polymer-ceramic composites, has been progressively increasing. Salernitano et al. [169] stated that composite composed of polymeric acrylic or methacrylic matrix reinforced with ceramic particles are used in restorative dentistry such as filling cavities, improving fractured teeth and replacing the missing teeth. Polylactic acid (PLA) is used in biomedical applications due to its biodegradability, biocompatibility, and ease of processing, while degradation products of PLA in the human body can cause toxic reactions [172]. Therefore, PLA is combined with ceramics to eliminate the inflammatory effect and to improve the biocompatibility of ceramics. Because of their poor mechanical properties, PLLA-HA composites are suitable for non-load bearing applications such as bone fracture fixations: sutures, interference screws, and meniscus repair [173–175]. Moreover, PEEK, polyetherimide (PEI), and liquid crystalline polymer (LCP) containing composites

are also used as femoral stems due to their inherent advantages like high corrosion resistance and excellent flexibility [176].

Metal-Ceramic Composite: Another composite type used in the biomedical application is the metal-ceramic composites such that Titanium-HA composites are used in dental implants due to their high mechanical stability and excellent biocompatibility [177]. Dezfuli et al. [178] manufactured the magnesium-based biocomposite for orthopedic applications. They stated that magnesium (metal)–bredigite (ceramic) composites could enable effective control over their mechanical and corrosion behavior in physiological solutions. A biodegradable and bioactive ceramic bredigite was preferred as a reinforcing phase in the composite in order to hinder fast corrosion of magnesium and increase the bioactivity of the composite.

Metal-Metal Composite: The newly designed functional composite has been produced in order to diminish the limitation of conventional metallic biomaterials. Since degradable metals do not conserve their integrity during corrosion, they are combined with the alternative metals to sustain mechanical stability by producing metal-metal composite [28]. For instance, Jiang et al. [179] manufactured Mg-based composite by infiltration casting method in which Mg melt infiltrated into the porous titanium having entangled structure, Figure 2.26(a-b). They found that both elastic moduli and compressive strength of composites were comparable with cortical bone, Figure 2.26(c) [179]. Therefore, Ti-Mg composites were suitable for load-bearing applications. However, they stated that galvanic corrosion between Ti and Mg accelerated the degradation rate; therefore, the mechanical stability of composites could not be established. As a result, additional treatments like alloying magnesium or surface treatments, should be done. The presence of an oxide-based interlayer, which is biocompatible as well, may reduce the galvanic effect between titanium and

magnesium, and may improve the attachment of bone tissue during degradation of magnesium.

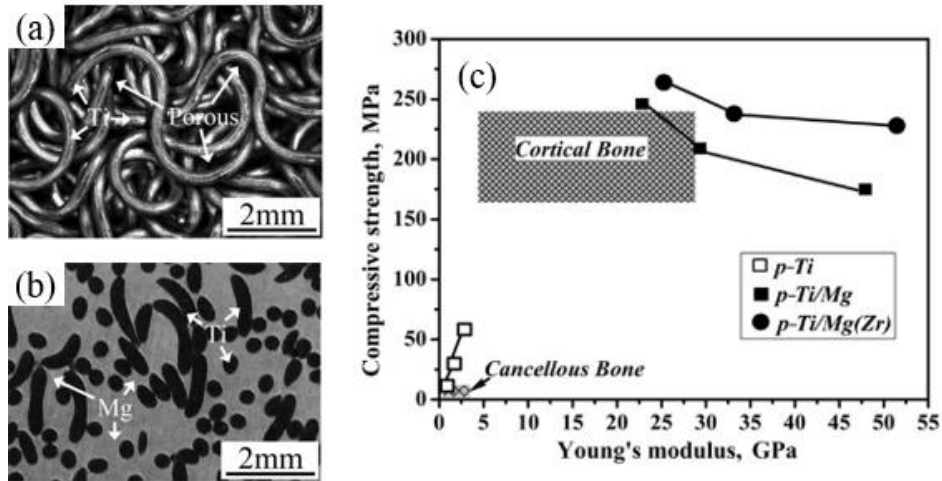


Figure 2.26. (a) Porous titanium has entangled structure, (b) Ti-Mg composite having 30% Ti and 70% Mg, and (c) the comparison of the compressive strengths and Young's moduli of different Ti-Mg composites and the natural bone [179].

Moreover, Balog et al. [180] investigate the titanium-magnesium bioactive composite having commercial named BIACOM. Ti-12 vol.% Mg composite manufactured by hot extrusion method had the capability of withstanding fatigue limits defined in the ISO 14801 standard for dental implants. They also conducted in-vitro experiments by using Ti-Mg screws and revealed that magnesium gradually corroded and enhanced the surface roughness. Therefore, they stated that bioactive composite could be used as a dental implant with improved mechanical compatibility [180].

CHAPTER 3

EXPERIMENTAL

3.1 Raw Materials

3.1.1 Ti6Al4V Powders

Spherical Ti6Al4V powders (99.9% purity) supplied from Phelly Materials, U.S.A., were used as starting materials during the production of the porous Ti6Al4V samples. The powders conforming to ASTM F 1580-01 standard [181], Table 3.1, had particle size in the range of 150-300 μm with an average particle size of around 200 μm , Figure 3.1.

Table 3.1 The chemical composition analysis of Ti6Al4V alloy in powder and bulk form, and ASTM F 1580-01 standard [181].

Chemical Composition (wt. %)			
Element	Ti6Al4V alloy powder	Bulk Ti6Al4V alloy	ASTM F 1580-01 Standard
Al	6.20 \pm 0.20	6.20	5.50 – 6.75
V	4.10 \pm 0.10	4.10	3.50 – 4.50
Fe	0.095 \pm 0.006	0.06	0.30 max.
Cu	0.002 max.	-	0.10 max.
Sn	-	-	0.10 max.
C	-	0.01	0.08 max.
H	0.006	0.004	0.015 max.
N	0.034	0.1	0.05 max.
O	0.162	0.1	0.20 max.
Ti	balance	balance	balance

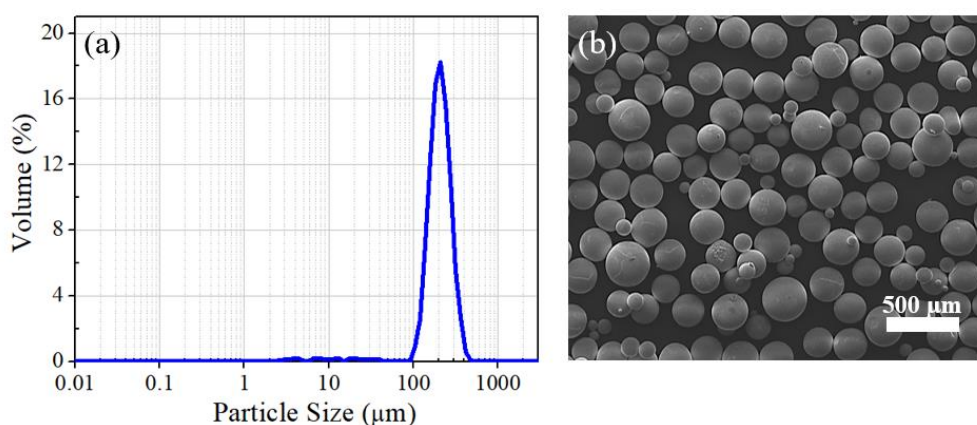


Figure 3.1. (a) Particle size distribution and (b) SEM images of Ti6Al4V alloy powders.

3.1.2 Bulk Ti6Al4V Alloy

Bulk Ti6Al4V alloy bars having 5.5 mm diameter were supplied from Phelly Materials. The chemical compositions of the alloy bars meet the ASTM F 1580-01 standard [181] (Table 3.1). Titanium alloys in bulk form were used in both galvanic corrosion tests by coupling with bulk Mg and Mg-alloys and the wetting tests of liquid Mg/Mg-alloys on them.

3.1.3 Bulk unalloyed Mg, AZ91 and WE43 Alloys

Bulk samples of unalloyed magnesium (Mg, 99.5% purity), AZ91, and WE43 alloys with the chemical compositions given in Table 3.2 were supplied in as-cast condition from the Changchun Institute of Applied Chemistry, Chinese Academy of Sciences, China. To determine their corrosion behaviors, bulk Mg/Mg-alloy samples were used in the wetting test, weight loss, hydrogen evolution rate measurements, galvanic corrosion, potentiodynamic polarization (PDP), and electrochemical impedance spectroscopy (EIS) tests. Bulk samples of Mg/Mg-alloys were also used for the

production of chips, which were used in the production of Ti6Al4V-Mg/Mg-alloy composite samples via pressureless infiltration method.

Table 3.2 Chemical compositions of unalloyed Mg, AZ91, and WE43 alloys.

Elements (wt. %)											
	Al	Zn	Mn	Y	Nd	Zr	Cu	Fe	Ni	Si	Mg
Unalloyed Mg	0.025	0.057	0.071	-	0.027	-	0.0356	0.0176	0.072	0.035	99.50
AZ91 alloy	9.0	0.8	0.2	-	-	-	-	-	-	-	balance
WE43 alloy	-	-	-	4.0	6.2-7.2	0.5	-	-	-	-	balance

3.2 Production of Porous Ti6Al4V Alloy

For the production of porous Ti6Al4V alloy, a loose powder sintering method has been preferred in which spherical Ti6Al4V powders were sintered at an elevated temperature under high purity argon (Ar) gas atmosphere in loose condition. Initially, one end closed cylindrical quartz tubes having 5.5 mm diameter and 100 mm length have been used to fill the spherical Ti6Al4V alloy powders. After that, powder filled tubes were placed in the tubular furnace, which was evacuated by using a rotary vacuum pump and then filled with high purity argon gas. Before the sintering process, the vacuum-gas purging cycles were repeated three times to ensure that the furnace was filled entirely with argon gas. Subsequently, Ti6Al4V alloy powders filled quartz tubes were heated to 1100 °C with a heating rate of 10 °C/min and kept at this temperature for 90 min to obtain desired porosity content by allowing partial sintering of powders. Then, as-produced porous surfaces of Ti6Al4V samples were gently ground with 2500 SiC paper in order to remove possible surface contamination caused by silica tubes.

3.3 Production of Ti6Al4V-Mg/Mg-alloy Composites

The pressureless infiltration method was performed via penetration of liquid unalloyed Mg, AZ91, and WE43 alloys into porous Ti6Al4V structure through capillary action under a controlled atmosphere. The composite manufacturing was started by inserting of porous Ti6Al4V alloy rods (5.5 mm diameter and 100 mm long) into stainless steel crucibles having 15 mm diameter. Next, liquid unalloyed Mg, AZ91, and WE43 alloy were filled around the porous rods, Figure 3.2(b). Then, stainless steel crucibles were heated to 800 °C, above the melting temperature of magnesium (650 °C), at which samples were kept for 20 min under high purity Ar gas to allow infiltration of liquid magnesium through the pores. Subsequently, samples were cooled down to room temperature slowly. All of the manufactured composites were machined to remove excess magnesium stuck on the surfaces during infiltration and to obtain desired smooth and clean surfaces for corrosion and mechanical tests. Figure 3.2(c) shows the schematic representation of a final product produced by a pressureless infiltration method.

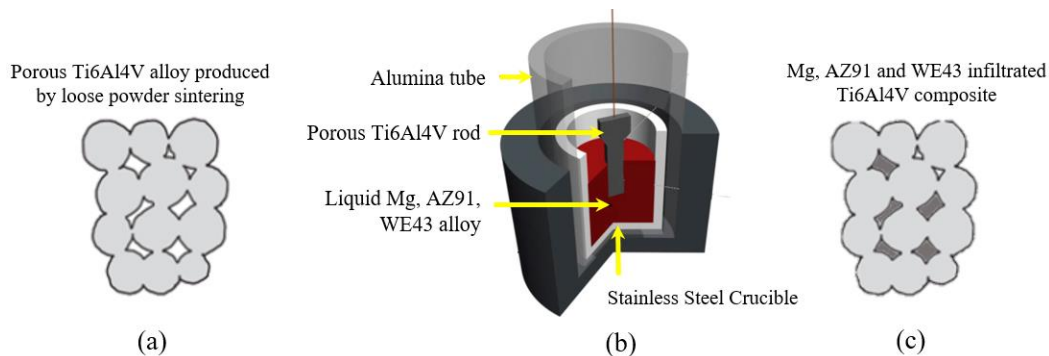


Figure 3.2. Schematic representation of (a) porous Ti6Al4V alloy structure, (b) cross-section of the furnace showing the stainless steel crucible, porous Ti6Al4V rods, and liquid Mg alloys and (c) Ti6Al4V-Mg composite in which pores are filled with Mg alloys.

3.4 Interface Formation

Galvanic corrosion is expected to occur between titanium and magnesium, which promotes increment of the degradation rate of magnesium. Therefore, to lessen the galvanic effect encountered in Ti6Al4V-Mg/Mg-alloy composites, sodium (Na)-rich ceramic coating was deposited on the pore surfaces of the Ti6Al4V alloy by NaOH-alkali treatment process prior to the magnesium infiltration step. Na-rich coating layer not only enhanced the bioactivity of the titanium alloy surfaces but also was supposed to decrease the galvanic corrosion between titanium alloy and magnesium during in-vitro tests. Initially, porous Ti-alloy samples were immersed in the 5 M NaOH solution at 60 °C for 24 h. Subsequently, alkali-treated porous rods were kindly cleaned with deionized water (DI) and then dried at 40 °C for 24 h. Some of the surface-treated porous Ti6Al4V alloys were kept in as-coated conditions as reference samples, while the remaining samples were used in the infiltration process as described in Section 3.3 for production of Ti6Al4V-Mg alloy composites with Na-rich interface layer.

3.5 Wetting Test

The wetting behavior of molten magnesium on the Ti6Al4V substrate is an essential issue in designing of Ti6Al4V-Mg composites for ensuring full penetration of liquid magnesium into open pores of Ti6Al4V alloy. Therefore, the contact angle measurement was performed in order to examine the wetting behavior of magnesium and the presence of chemical reactions at the interface between liquid magnesium and the coated and uncoated titanium alloy substrates. Figure 3.3 shows a schematic view of the experimental set-up used for wetting tests. For the wetting experiments, initially, a set-up was designed and constructed after the production of an atmosphere controlled tube furnace in the laboratory, Figure 3.3. Experiments were conducted

by heating the samples with a heating rate of 10 °C/min up to 800 °C under high purity Ar gas. The raw materials were in the shape of disc of bulk unalloyed Mg, AZ91, and WE43 alloy (diameter: 6 mm, height: 4.4 mm) and Ti6Al4V alloy (diameter 16 mm and height: 4 mm) as a substrate. Wetting behaviors of liquid Mg/Mg alloys were investigated on two different Ti6Al4V alloy surfaces, namely, untreated, and 5 M NaOH- treated Ti6Al4V alloys. The thickness of the Na-rich layer obtained on the Ti-alloy substrate after treatment in 5 M aqueous solution of NaOH at 60 °C is critical as it directly affects the wetting characteristics of molten magnesium. For the measurement of the contact angle, the morphological changes of the droplet were monitored by a CCD camera.

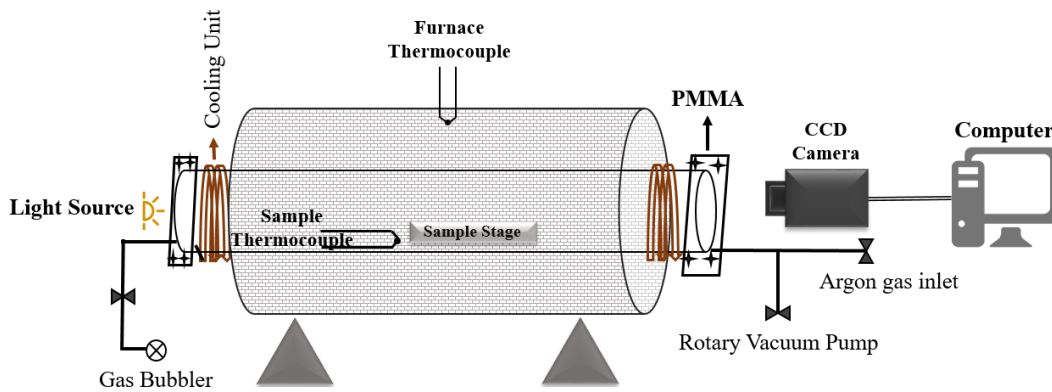


Figure 3.3. Schematic illustrations of the wetting furnace.

3.6 In-vitro studies

In the present study, both as-cast unalloyed Mg, AZ91, WE43 alloy, and Ti6Al4V-Mg/AZ91/WE43 composites (with and without Na-rich interface) were immersed in simulated body fluid (SBF, 36.5 ± 0.5 °C, 7.4 pH) for different immersion times to check possible apatite formation and to monitor the degradation behavior of Mg/Mg-

alloys. SBF, which has similar ion concentration to that of the human blood plasma, Table 3.3, was prepared according to Kokubo's recipe [182].

Table 3.3 Ion concentration of blood plasma and SBF [182].

	Ion Concentration (mM)								pH
	Na ⁺	K ⁺	Mg ²⁺	Ca ²⁺	Cl ⁻	HCO ³⁻	HPO ₄ ²⁻	SO ₄ ²⁻	
Blood plasma	142.0	5.0	1.5	2.5	103.0	27.0	1.0	0.5	7.2-7.4
SBF	142.0	5.0	1.5	2.5	147.8	4.2	1.0	0.5	7.4

Before the preparation of the SBF solution, 700 ml DI with a stirring bar was put into a 1000 ml polyethylene bottle, which was placed on a temperature-controlled magnetic stirrer. Next, the temperature of the solution was set to 36.5 ± 0.5 °C, and stirring speed was fixed to moderate mode. Then, the reagents, numbered as one to eight were dissolved one by one in the order given in Table 3.4. Tris-hydroxymethyl aminomethane (Tris, (HOCH₂)₃CNH₂) and the small amount of hydrochloric acid, HCl, were dissolved in order to adjust the final pH of the solution. Special attention is required during dissolving calcium chloride, CaCl₂, because it has a significant effect on precipitation of apatite. Therefore, small amounts of CaCl₂ granules were added part by part after allowing enough time for the dissolution of the previous granules.

After the complete dissolution of each reagent, additional DI water was added to increase the volume of the solution up to 900 ml. When the pH of the solution was measured around 2.0 ± 1.0 , the reagent Tris was added into solution little by little to avoid a sudden increase in the pH value. The addition of Tris was continued until the pH of the solution reached 7.3 ± 0.1 at 36.5 ± 0.5 °C. The final pH was adjusted to 7.4 by the addition of Tris and 1 M HCl alternately into the solution. After the pH

was adjusted to 7.4 at 36.5 °C, the volume of the solution was increased to 1000 ml. Finally, the prepared solution was allowed to cool down to room temperature and then put it into the refrigerator at a temperature of 5-10 °C.

Table 3.4 Molecular weight and amount of chemicals added during the preparation of one liter SBF [182].

	Chemicals	Molecular Weight (g/mol)	Amount (in L⁻¹)
1	NaCl	58.44	8.035 g.
2	NaHCO ₃	84.01	0.355 g.
3	KCl	74.56	0.225 g.
4	K ₂ HPO ₄ .3H ₂ O	228.22	0.231 g.
5	MgCl ₂ .6H ₂ O	203.30	0.311 g.
6	1 M HCl	36.46	39 ml.
7	CaCl ₂	110.99	0.292 g.
8	Na ₂ SO ₄	142.04	0.072 g.
9	Tris	121.14	6.118 g.
10	1 M HCl	36.46	0-5 ml.

After preparation of SBF, as-cast Mg/Mg-alloys having 7 x 6.5 x 4 mm rectangular dimensions and as-manufactured Ti6Al4V-Mg/Mg-alloy composites with and without Na-rich interface (cylindrical shape having 5 mm length and 5.5 diameter) were immersed in 30 ml SBF (36.5 ± 0.5 °C, 7.4 pH) for various time intervals in order to investigate the apatite formation abilities of all samples and compare their corrosion and degradation characteristics. SBF was refreshed every three days to stabilize ion concentration. After each immersion test, samples were cleaned gently

with DI water and then dried at room temperature for 24 h. The pH of the solution was recorded after removing the samples from the solution. Besides, electrolyte concentration of magnesium, calcium, and phosphate ions in SBF before and after in-vitro tests were measured to reveal degradation of Mg/Mg alloys and precipitation of calcium phosphates on bulk Mg Mg/Mg alloys. The details of the tests used for monitoring the corrosion behaviors of bulk Mg alloys and composites by the use of SBF is given below.

3.7 Corrosion Rate Determination Techniques

3.7.1 Non-Electrochemical Techniques

3.7.1.1 Hydrogen evolution test

Corrosion behavior of both Mg/Mg-alloy and Ti6Al4V-Mg/Mg-alloy composites (with and without Na-rich interface) have been investigated and compared extensively by weight loss and hydrogen evolution tests by immersion in SBF. Corrosion initiation points were also examined during immersion in SBF for 1, 2, 4, 8, and 24 hours, and structural changes of the samples at the micro and macro levels were also monitored after immersion in SBF for 1, 2, 5, and 10 days.

For immersion experiments, as-cast Mg, AZ91, and WE43 samples were cut into a rectangular shape and ground with SiC papers (400-600-800-1000) and subsequently cleaned with DI water and ethanol. The final dimension of the bulk samples was 7 mm x 6.5 mm x 4 mm. Besides, composite samples were cut into a cylindrical shape having 10 mm long and 5.5 mm diameters. All of the immersion tests were conducted in SBF, having temperature and pH of 36.5 ± 0.5 °C and 7.4, respectively.

The hydrogen gas evolution tests have been performed to understand both short and long-term corrosion behavior of samples. Hence, the degradation rate of bulk Mg/Mg-alloys and Ti6Al4V-Mg/Mg-alloy composites was correlated with the volume of collected hydrogen gas (H_2) during the in-vitro test. All the samples were placed in a beaker containing 250 ml of SBF. The collector, consisting of an inverted funnel and burette shown in Figure 3.4, was placed above the samples to capture evolved hydrogen gas. Then, the volume of the evolved gas in the burette was recorded at specific time intervals. All of the experiments were conducted at a temperature of 36.5 ± 0.5 °C. The hydrogen evolution was monitored for 7 and 14 days for composite and bulk samples, respectively.

The volume of H_2 was directly determined by reading the variation of solution level in the burette at different time intervals. Thus, the corrosion rates of the various Mg alloys (unalloyed Mg, AZ91, and WE43 alloys) compared by measuring the evolved H_2 gas volume, which is proportional to the degradation of magnesium according to Eq. (3.1).



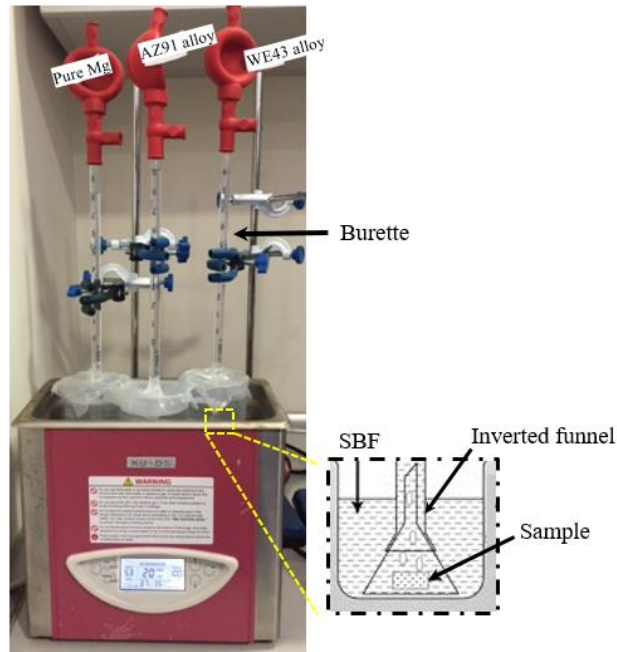


Figure 3.4. Experimental set-up used for measurement of H₂ evolution rate.

3.7.1.2 Weight Loss Test

Weight loss measurement was utilized to investigate the long-term corrosion behaviors of the samples by calculating the weight loss percentage. The technique was successfully applied to only bulk Mg/Mg-alloy samples. In this technique, the initial weight, W_0 , of the sample was measured, and then the samples were immersed in 30 ml SBF solution kept at 36.5 ± 0.5 °C for 1, 2, 5, 10, and 20 days. After they have taken out of the solution, samples' surfaces were cleaned with a chromic acid solution (200 g/l CrO₃) in order to remove the corrosion products. Finally, the final weight of the samples was measured after they were washed gently with DI water and ethanol, respectively, and dried in an open atmosphere. After the calculation of the difference between initial and final weight, ΔW , weight loss percentage was determined according to Eq. (3.2).

$$\text{Weight Loss \%} = \frac{\Delta W}{W_0} \times 100 \quad (3.2)$$

3.7.2 Electrochemical Techniques

Electrochemical experiments include three different tests, namely galvanic corrosion, potentiodynamic polarization (PDP), and electrochemical impedance spectroscopy (EIS) tests. Galvanic corrosion experiments were carried out using a Solartron Analytical model 1480 Multistat. The experimental set-up contained three electrodes; two of these were working electrodes (Ti6Al4V alloy as the cathode, and Mg/Mg alloys as the anode) and another one was the reference saturated calomel electrode (SCE), Figure 3.5. Prior to the galvanic corrosion test, both bulk M/Mg-alloy and Ti6Al4V alloy were embedded in the epoxy resin and ground with SiC (400-1200) and subsequently cleaned with DI water and ethanol.

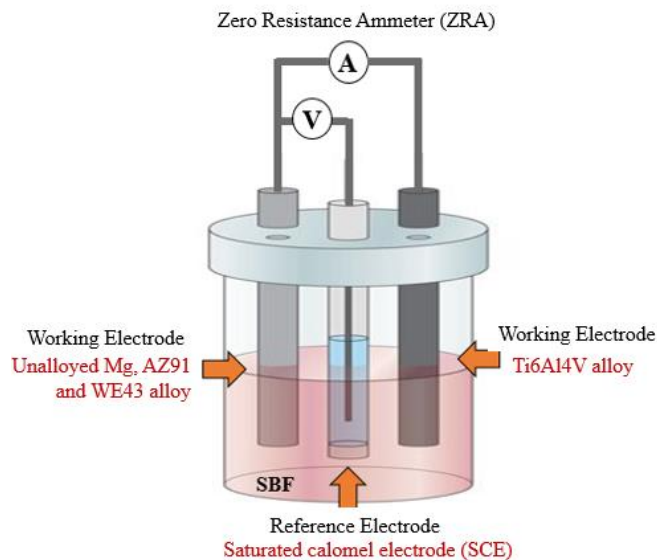


Figure 3.5 Experimental set-up of galvanic corrosion test.

Potentiodynamic polarization and electrochemical impedance tests were conducted by using a potentiostat (Versastat3, Princeton Applied Research) in a three-electrode electrochemical cell, Figure 3.6. Both Ti6Al4V-Mg/Mg alloy composites and bulk Mg/Mg alloy samples were used as working electrodes. On the other hand, graphite rod and saturated calomel electrode (SCE) were counter and reference electrodes, respectively. All potentials were measured by referring to the SCE. Before the electrochemical experiments, both as-cast bulk Mg/Mg-alloy and composite samples were machined to get cylindrical shapes with a diameter of 5 mm and length 20 mm, and then subsequent cleaning was done in an ultrasonic cleaner using ethanol.



Figure 3.6. The electrochemical cell containing three electrodes.

3.7.2.1 Galvanic corrosion test

All galvanic corrosion tests were carried out for 600 seconds in the SBF solution (pH 7.4) at room temperature. The surface area ratio of Ti6Al4V alloy to that of Mg/Mg-

alloy was 1:1. The random fluctuations of current were measured by the zero resistance ammeter (ZRA). Simultaneously, the random fluctuations in potential at the coupled electrodes were computed relative to SCE. The galvanic potential, current density, and resistance were analyzed by a statistical approach. The standard deviations (σ) over constant periods for potential, σ_E , and current density, σ_I were calculated by quantification of noise data. Also, galvanic resistance (R_g) was determined as the standard deviation of the potential noise divided by the standard deviation of the current noise ($R_g = \sigma_E / \sigma_I$).

3.7.2.2 Potentiodynamic Polarization Test

Potentiodynamic polarization tests were performed in order to understand the corrosion kinetics of both as-cast bulk Mg/Mg alloys and Ti6Al4V-Mg/Mg-alloy composites. The polarization scans were utilized at a potential scanning rate of 0.2 mV/s over the potential range from -250 to 350 mV. Then, the corrosion potential, E_{corr} , and corrosion current density, i_{corr} ($\mu A/cm^2$), were calculated according to the Tafel extrapolation method. The corrosion rate (CR) in $mm \cdot year^{-1}$ was calculated according to ASTM G102 [183] and Eq. (3.3) given below;

$$CR = \frac{K \times i_{corr} \times EW}{\rho} \quad (3.3)$$

Where K is the corrosion constant ($3.27 \times 10^{-3} \mu A/cm^2$), and ρ is the density (g/cm^3) of samples. The equivalent weight (EW) of pure elements is calculated according to Eq. (3.4), where W is the atomic weight, and n is the valence of the element. On the other hand, in order to calculate the EW of the alloy, Eq. (3.5) in ASTM G102 [183] is used. Where f_i is the mass fraction of the i th element in the alloy, W_i shows the atomic weight of the i th element in the alloy, and n_i is equal to the valence of the i th element of the alloy. Thus, the equivalent weight of alloy, EW, is the reciprocal of

this quantity, Eq. (3.5). Moreover, the rule of mixture given in Eq. 3.6 was used to determine the EW of Ti6Al4V-Mg composites by knowing the volume fraction (V_f) of each constituent, Eq. (3.4).

$$EW = \frac{W}{n} \quad (3.4)$$

$$EW = \frac{1}{\sum \frac{n_i f_i}{W_i}} \quad (3.5)$$

$$EW_{composite} = (EW_{Mg-Mg \text{ alloy}} \times V_{f,Mg-Mg \text{ alloy}}) + (EW_{Ti6Al4V} \times V_{f,Ti6Al4V}) \quad (3.6)$$

3.7.2.3 Electrochemical Impedance Spectroscopy (EIS)

The electrochemical impedance spectroscopy (EIS) tests of both as-cast bulk Mg, AZ91 and WE43 alloys, and Ti6Al4V-Mg/AZ91/WE43 composites were carried out in SBF at 36.5 ± 0.5 °C in the electrochemical cell containing three electrodes, Figure 3.6. The EIS spectra were recorded at different time intervals of 1, 2, 4, 6, and 24 h for each sample in the frequency range between 100 kHz and 100 MHz with a 10 mV sinusoidal perturbation signal at open circuit potential.

3.8 Characterization

3.8.1 Particle Size Determination

Particle size analyses of Ti6Al4V alloy powders were utilized by using “Malvern Mastersizer 2000”. The analyzer uses Helium-neon laser as a source for a red light to determine the size of coarser particles; on the other hand, the solid-state light

source (blue light) for finer particle size measurement. At the end of the experiment, the frequency versus logarithmic particle size graph was obtained.

3.8.2 Chemical Composition Analysis

Inductively coupled plasma optic emission spectroscopy (ICP-OES, Perkin Elmer Optima 4300DV) analysis was performed in order to identify the ion concentration change of SBF used in immersion tests. In this technique, argon plasma at a temperature of 6000-10000 °K is used to break the molecular bonds so that atoms and ions are formed. Immediately after stimulating in plasma, atoms and ions irradiate at characteristic wavelengths and return to their former energy levels. Therefore, elements are analyzed by measuring the characteristic radiation released from the excited atoms.

3.8.3 X-ray Diffraction Analysis (XRD)

X-ray diffraction analyses (XRD) was performed so as to examine the phase constituents in the starting bulk Mg/Mg-alloys, porous Ti6Al4V alloy, and as-manufactured Ti6Al4V-Mg/AZ91/WE43 composites as well as corroded composites exposed to SBF. XRD analysis was conducted via an X-ray diffractometer, “Rigaku D/Max 2200/PC, Tokyo, Japan” with Cu K α radiation having a current and voltage of 30 mA and 40 kV, respectively. Continuous scanning was performed between 10° and 90°, 2 θ angles with a scan speed of 2 °/min.

3.8.4 Microstructural Analysis

Morphological and microstructural investigation of the starting as-cast bulk Mg/Mg-alloys and porous Ti6Al4V alloy and their corroded surfaces were characterized by

optical microscope (OM) “Nikon Eclipse LV150” and scanning electron microscope (SEM) “FEI 430 Nano Scanning Electron Microscope” equipped with energy-dispersive X-ray spectroscopy (EDS). Sample surfaces were examined with the etched condition after grinding by SiC papers (400-2000 grit size) and polishing via diamond (1 and 0.3 μm) suspensions. On the other hand, in order to examine the thickness of the corroded layer, both bulk Mg/Mg alloys and Ti6Al4V-Mg composite samples were embedded in the epoxy resin, and the cross-sections of the samples were analyzed. 5% Nital (5-HNO₃ and 98-ethanol ml) solution was used to reveal the microstructures of bulk Mg/Mg alloys and Mg/Mg alloy regions in composites. On the other hand, for the examination of the microstructure of bulk Ti6Al4V alloys and Ti6Al4V alloy regions in composites, Kroll’s reagent (10-HF, 5-HNO₃ and 85-H₂O ml) was used.

3.8.5 Atomic Force Microscopy (AFM)

The surface roughness and three dimensional topography of starting (uncoated) and sodium rich coated bulk Ti6Al4V surface were examined with Atomic Force Microscope (AFM, Veeco MultiMode V) on 50 μm by 50 μm scans using tapping mode.

3.8.6 Density Measurement

The porosity contents and densities of both porous Ti6Al4V alloys and Ti6Al4V-Mg/Mg alloy composites were evaluated based on the Archimedes’ principle via “Precisa XB220A” precision balance equipped with a density determination kit by using Xylol solution (CH₃C₆H₄CH₃). Firstly, all samples were weighed in dry condition, m_a , and then immersed into a xylol solution in a beaker. Samples were kept in the solution for 24 h to ensure full penetration of the xylol solution into the

pores. Next, the weight of the xylol impregnated samples, $m_{x,x}$, was measured in the beaker filled with the xylol solution. Finally, samples were taken out of the solution, and immediately, the weights of the xylol impregnated samples were measured in air, $m_{a,x}$.

The volume of the porous Ti6Al4V and Ti6Al4V-Mg composites, V_{sample} , were calculated according to Eq. (3.7). Then, the densities of the samples, ρ_{sample} , were determined via Eq. (3.8), where the densities of bulk Ti6Al4V alloy ($\rho_{Ti6Al4V}$) and xylol (ρ_{xylol}) were taken as 4.429 g/cm³ and 0.861 g/cm³, respectively. Percentage of the total, P_{total} (%), open, P_{open} (%), and closed, P_{closed} (%), porosities of the samples were calculated by the Eqs. (3.9), (3.10), and (3.11), respectively.

$$V_{sample} = \frac{m_{a,x} - m_{x,x}}{\rho_{xylol}} \quad (3.7)$$

$$\rho_{samples} = \frac{m_a}{V_{sample}} \quad (3.8)$$

$$P_{total}(\%) = 100 - \left(\frac{\rho_{samples}}{\rho_{Ti6Al4V}} \right) \quad (3.9)$$

$$P_{open}(\%) = \frac{\text{volume of xylol in pores}}{\text{volume of the samples}}$$

$$P_{open}(\%) = \left\{ \frac{\left(\frac{m_{a,x} - m_a}{\rho_{xylol}} \right)}{\left(\frac{m_{a,x} - m_{x,x}}{\rho_{xylol}} \right)} \right\} \times 100 \quad (3.10)$$

$$P_{closed}(\%) = P_{total}(\%) - P_{open}(\%) \quad (3.11)$$

3.8.7 Mechanical Characterization

Mechanical properties of the samples were determined by compression tests under quasi-static conditions by a 100 kN capacity "MTS Universal Testing Machine, MTS Criterion Model 45" at a crosshead speed of 0.5 mm/min. Quasi-static compression tests were performed for both as-manufactured porous Ti6Al4V alloys and Ti6Al4V-Mg/AZ91/WE43 composites, according to ASTM E9-89a standard designed for compression testing of metallic materials at room temperature [184]. The height to diameter ratio (H/D) of the samples was kept at around one to avoid buckling and non-homogenous deformation. From the stress-strain diagram, elastic moduli of the samples were calculated by using the slope of the graph in the linear region, and compressive yield strength values were measured by a 0.2% offset method.

CHAPTER 4

RESULTS

This part of the thesis is composed of three main sections, namely, composite production with and without Na-rich coating, and their corrosion properties. In the first section, the results about the production and characterization of 3 different bio-composites, in which Ti6Al4V alloy coupled with unalloyed Mg, AZ91, and WE43 alloys, have been presented. Prior to composite production, the wetting behavior of liquid unalloyed Mg, AZ91 and WE43 alloys on solid Ti6Al4V alloy has been investigated. Second section presents the results about formation of chemically and morphologically different Na-rich coating layers between Ti6Al4V alloy and Mg-Mg alloy regions in the composites. Additionally, wettability of liquid Mg/Mg-alloys on Na-coated bulk Ti6Al4V alloy was examined as well. In the last section, corrosion behaviors and corrosion mechanisms of bulk Mg/Mg-alloys, and Ti6Al4V-Mg/Mg-alloy composites with and without Na-rich coating have been investigated separately by soaking the samples in SBF for different time intervals. Non-electrochemical and electrochemical tests have been utilized to understand the corrosion rates of composites and bulk Mg/Mg-alloy counterparts.

4.1 Composite production

Since corrosion of magnesium and magnesium alloys is too fast in an aqueous environment, they cannot maintain their mechanical stability during the healing period when they are used as biodegradable implant materials. Accordingly, there needs to be additional support, or their corrosion rates should be minimized to carry the loads effectively until the patient heals. One of the approaches is the coupling of

biodegradable Mg/Mg-alloy with bioinert Ti-alloy. Ti-alloy, i.e., Ti6Al4V alloy, skeleton is assumed to support the composite implant during degradation of Mg regions and replacement with newly formed bone tissues. Additionally, composite production by combining Mg and Ti-alloys helps to alleviate the stress-shielding problem by reducing the elastic modulus and makes the resultant implant more suitable for load-bearing applications with elastic modulus close to that of bone. However, combining two different materials causes the formation of a galvanic couple and intensifies the corrosion rate. Therefore, in the present study, Ti6Al4V alloy was combined with alloy forms of Mg (AZ91 and WE43 alloys) in addition to unalloyed Mg so as to reveal the effect of coupling alloyed Mg with Ti-alloy on galvanic corrosion. Accordingly, wetting behavior of liquid Mg/Mg-alloys on the surface of Ti6Al4V alloy has been investigated before composite production. Then, structural and mechanical characterization of Ti6Al4V-Mg/Mg-alloy composites were studied.

4.1.1 Wetting behavior of liquid Mg/Mg-alloy on the Ti6Al4V alloy

The wetting behavior of liquid unalloyed Mg, AZ91, and WE43 alloys on Ti6Al4V alloy surface is a crucial factor during the infiltration of liquid Mg/Mg-alloys into porous Ti6Al4V structure. Therefore, prior to the production of Ti6Al4V-Mg/Mg-alloy composites, the wettability of Ti6Al4V alloy substrate by molten Mg/Mg-alloy have been studied using bulk alloys. The wetting tests were performed by heating the samples under high purity argon gas slowly up to 800 °C, at which they held for a maximum 30 minutes as in the composite production by infiltration. Figure 4.1 shows the schematic placement of cylindrical samples of bulk Mg/Mg alloy on the bulk Ti6Al4V alloy prior to the wetting test.

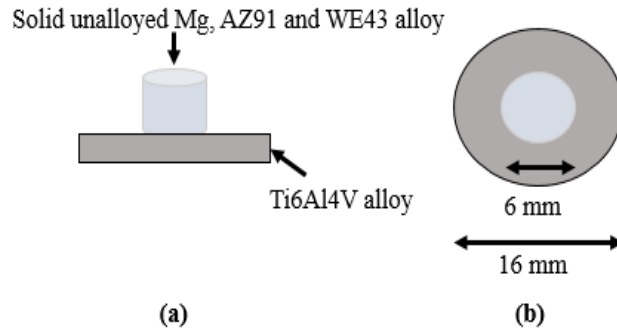


Figure 4.1. Schematic representation of Mg/Mg alloy on the Ti6Al4V substrate; (a) side and (b) top views.

Figure 4.2 shows the morphological changes of molten unalloyed Mg on the Ti6Al4V substrate at different stages of holding at 800 °C. There was no detectable change in the shape of unalloyed Mg in the first five minutes of the test. Then, melting started in the center of the sample and subsequently, the edges collapsed towards the center within seconds (at $t=5.58$ min). Afterwards, all of the magnesium melted and completely wetted the surface of Ti6Al4V alloy rapidly. Kumar et al. [185] stated that magnesium displays a relatively slow oxidation rate up to temperatures of about 450 °C, while the rate of oxidation increased suddenly beyond 450 °C. In the present study, the oxide layer was thought to be formed on solid magnesium because of the observed delayed melting. As can be seen in Figure 4.2, although samples started to collapse at the central region, the outer case, possibly the magnesium oxide, preserved its continuity for a while, until all liquid magnesium spread out on Ti-alloy surface.

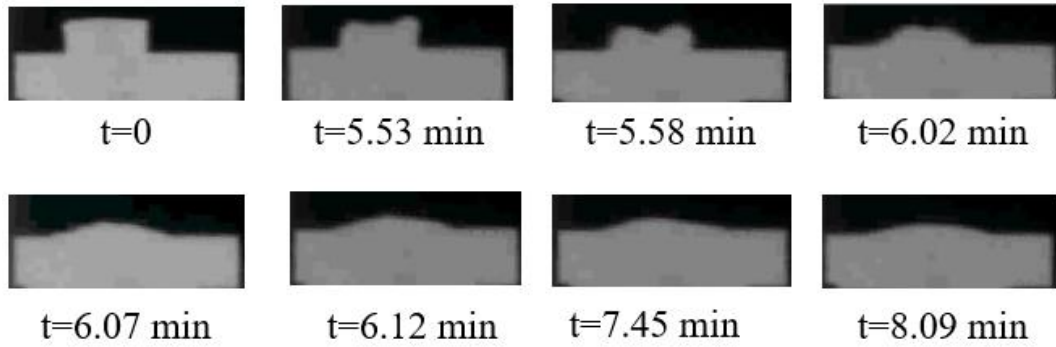
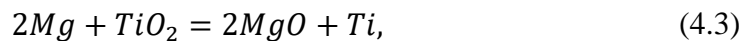
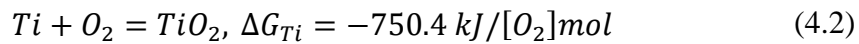
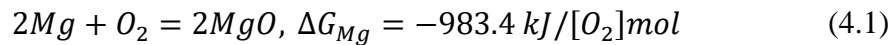


Figure 4.2. Change in shape of unalloyed magnesium on Ti6Al4V alloy substrate with time.

Figure 4.3 shows the change in measured contact angles of molten unalloyed Mg in which three different stages were observed. In the first five minutes, almost no change was detected in the wetting angle. A similar observation was detected in the study of Kondoh et al. [186]. They stated that initially contact angle remained unchanged due to the reduction of native TiO_2 layer on pure titanium by liquid magnesium according to reactions given through Eqs. 4.1-4.3 [186,187].



$$\Delta G = -233 \text{ kJ}/mol \text{ } (\Delta G, \text{standard free energy})$$

In the second region, the contact angle suddenly decreased to approximately 12° in one minute, Figure 4.3. Then, the contact angle remained constant at the remaining stages of the wetting experiment. The rapid reduction of wetting angle was attributed to sudden flow of liquid magnesium as a result of cracking of the oxide layer, which

encapsulated molten magnesium [186,188]. As a result of flowing out of liquid magnesium, nearly complete wetting was observed on solid Ti6Al4V substrate. Unfortunately, as stated in the previous studies [186,188], sudden evaporation of unalloyed magnesium directly affects the contact angles. However, the effect of Mg evaporation on the contact angle change is not the subject of the current study.

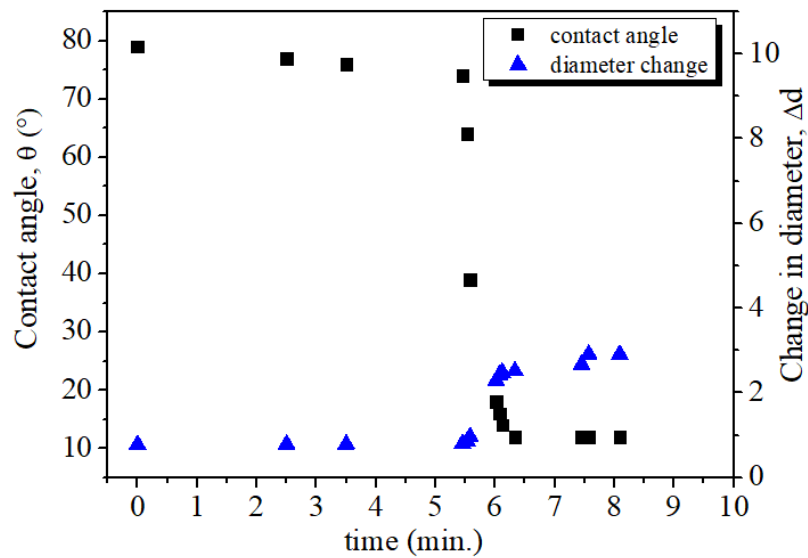


Figure 4.3. Change in the contact angle and diameter of molten unalloyed Mg alloy at 800 °C.

Additionally, the diameter of unalloyed magnesium remained constant at the initial stage, where there was no change in the contact angle. On the other hand, it increased rapidly when a sudden change in the contact was observed. Kondoh et al. [186] stated that the evaporation of pure Mg at a relatively high temperature could cause an increase in the dimension of molten droplet, Figure 4.4, due to its high vapor pressure of 2×10^3 Pa at 800 °C [186]. Similarly, in the current study, simultaneous melting and evaporation of Mg were followed by wetting and dimension change of liquid magnesium.

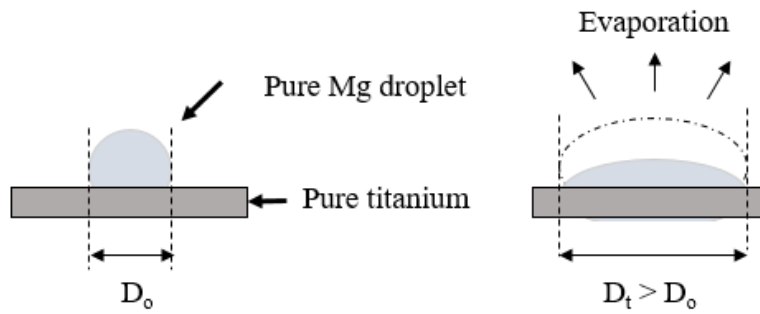


Figure 4.4. Schematic representation of wetting of molten pure Mg on solid titanium substrate [186].

Figure 4.5 shows SEM images of the reaction layer formed on solid Ti6Al4V alloy when contacted with liquid magnesium. The reaction layer had a porous structure having 2-5 μm thickness, and it was mainly composed of magnesium (5.57 wt. %) and oxygen (13.39 wt. %) elements according to EDS spot analysis. The presence of Mg and O elements on the surface of Ti-alloy supports the idea of TiO_2 reduction by liquid Mg, which results in MgO formation according to Eqs. 4.1-4.3. XRD analysis taken from the reaction layer consisted of only α -Ti and titanium oxide phases (TiO_3 and TiO), Figure 4.6, which were formed possibly during the cooling stage of the experiment.

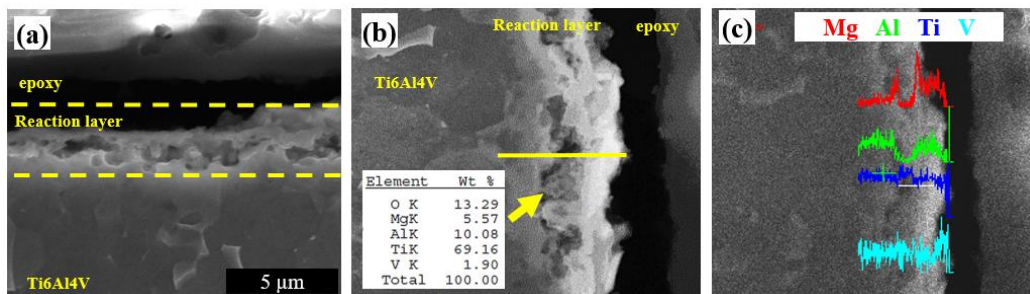


Figure 4.5. (a) SEM image, (b) EDS spot analysis, and (c) EDS line scan analysis taken along the reaction layer.

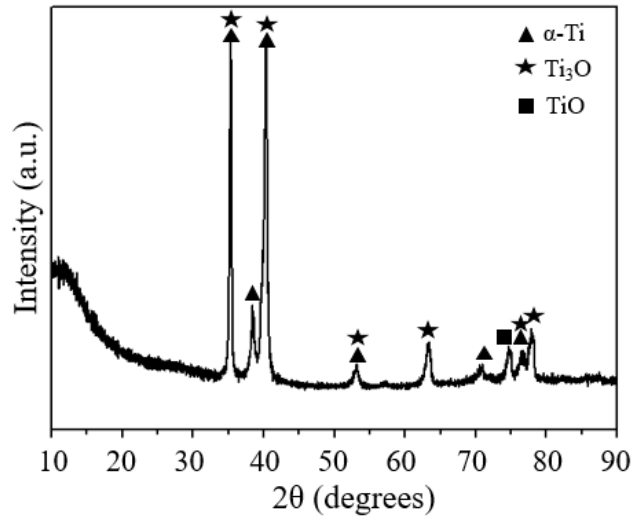


Figure 4.6. XRD analysis of Ti6Al4V alloy substrate wetted by unalloyed Mg.

Figure 4.7 shows the variation in the shape of AZ91 alloy placed on the Ti6Al4V alloy substrate during wetting test. The point where the AZ91 alloy began to melt was accepted to be the reference point at which time, t , was taken as zero. Molten AZ91 homogeneously wetted the Ti6Al4V substrate surfaces at the end of 22 minutes. In contrast to unalloyed Mg, the contact angle between liquid AZ91 alloy and Ti6Al4V alloy decreased gradually, Figure 4.8. It is known that Zn decreases the oxidation resistance of Mg-alloy, and the presence of Mg-Zn intermetallic phases with low melting temperature may cause significant evaporation of Mg. Moreover, Zn tends to sublime, thereby, accelerating the cracking of the oxide scale [189]. Accordingly, the melt pool of AZ91 alloy was seen in the earlier stages of wetting experiments compared to pure magnesium due to distorted oxide scale, which normally envelops the liquid magnesium. After the complete melting of AZ91 alloy, the wetting angle values were measured, Figure 4.8. The contact angle of liquid AZ91 alloy was observed to decrease gradually. At the end of 22 minutes, liquid AZ91 droplet wetted the Ti6Al4V alloy surface with a wetting angle of about 12° ,

which was similar to that of unalloyed Mg. On the other hand, in contrast to unalloyed Mg, the diameter of the melt pool decreased possibly due to a higher evaporation rate of magnesium because of the presence of Zn element in AZ91 alloy.

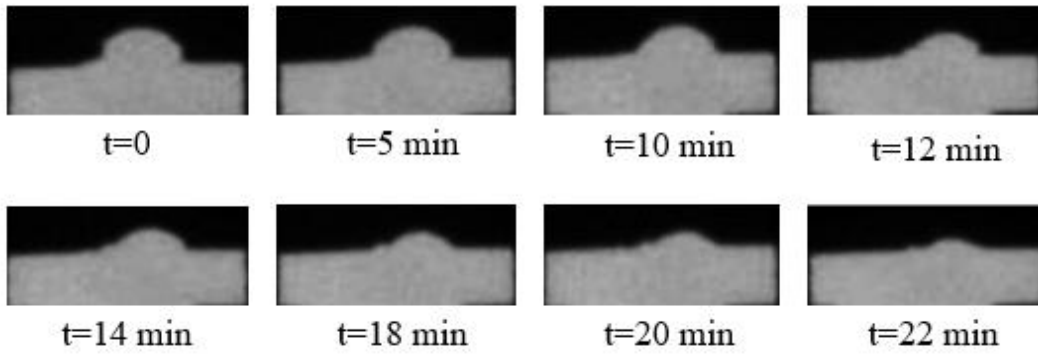


Figure 4.7. Change in shape of liquid AZ91 alloy on Ti6Al4V alloy substrate with time.

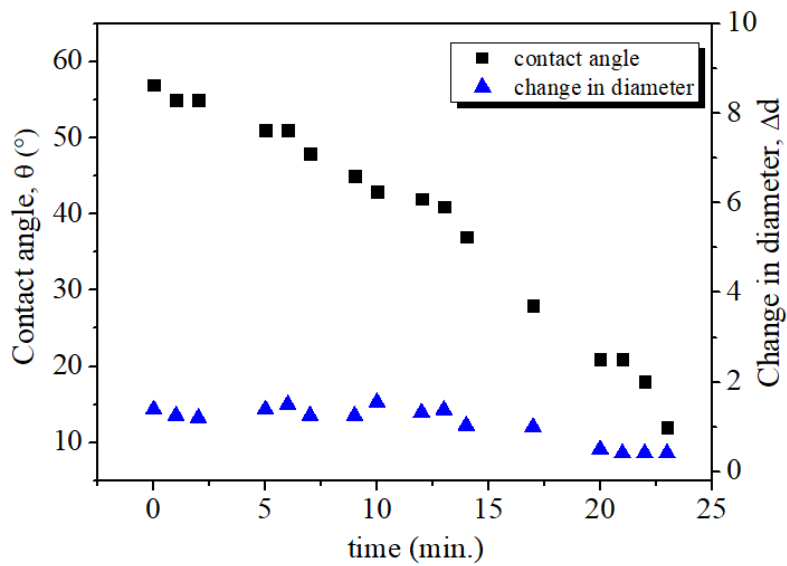


Figure 4.8. The changes in contact angle and diameter of the molten AZ91 alloy at 800 °C.

Figure 4.9 shows the SEM image of the reaction layer formed at the end of the wetting experiment when molten AZ91 was in contact with the solid Ti6Al4V alloy. The microstructure of Ti6Al4V alloy (at the bottom) contained Al-rich α -phase (dark region) and V rich β -phase (bright region). In contrast to unalloyed Mg, a reaction layer having approximately 70 μm thickness was formed on the Ti-alloy surface. In addition, the EDS dot map analysis showed that the porous reaction layer was rich in Al and Ti elements, Figure 4.10.

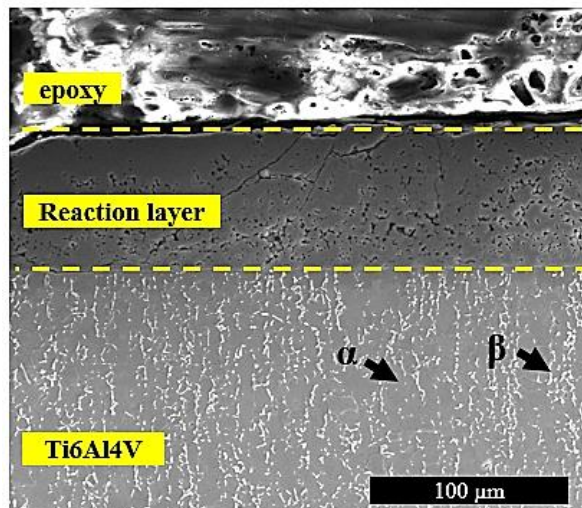


Figure 4.9. SEM analysis showing the reaction layer formed on Ti6Al4V alloy.

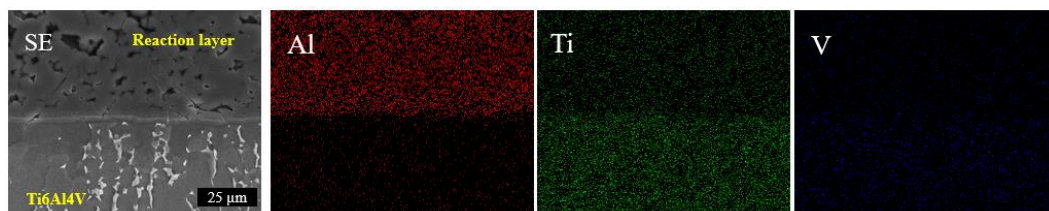


Figure 4.10. EDS dot map analysis across the reaction layer and Ti6Al4V alloy.

Moreover, closer examination of the reaction layer exhibited an additional interface layer with 2-3 μm thickness. EDS spot analysis results taken from different points were given in Figure 4.11(b). It was thought that aluminum in AZ91 alloy diffused through the Ti6Al4V substrate at elevated temperature, thereby, causing the formation of Ti and Al rich phases. The regions labeled as point 1 had around 73 at. % Al and 27 at. % Ti, Figure 4.11(b), corresponding to the TiAl_3 phase, which was also verified with XRD analysis, Figure 4.13.

On the other hand, as moving towards to titanium substrate, the concentration of the Al element decreased. The regions (labeled as points 2 and 3) were thought to be TiAl_2 and TiAl phases according to EDS spot analysis, Figure 4.11(b), and Ti-Al phase diagram given in Figure 4.12. Skolavo et al. [190] also stated that the existence of TiAl and TiAl_2 phases could be explained by the series of solid-liquid reactions of Ti and Al in which the TiAl phase is starting phase and subsequently, TiAl_2 phase formed. Since the thickness of the TiAl_3 phase was relatively thicker, it was hard to detect the TiAl and TiAl_2 phases by XRD analysis.

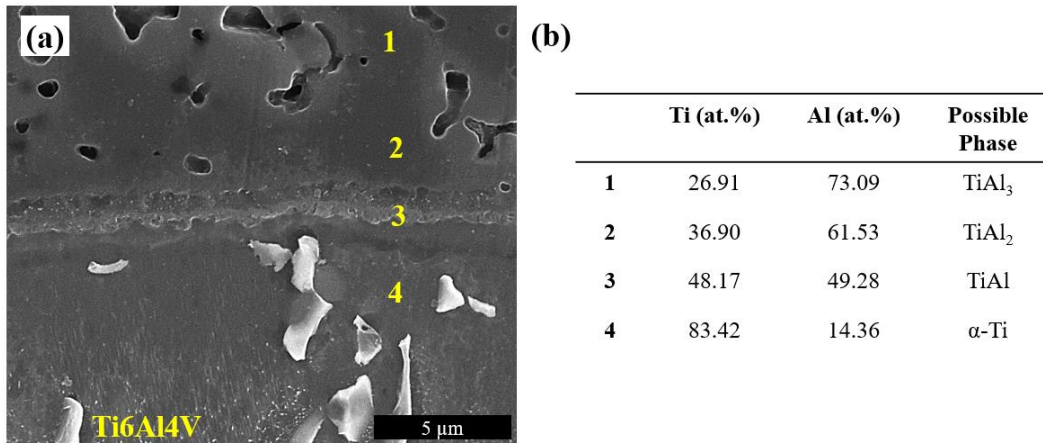


Figure 4.11. Cross-sectional examination of AZ91 alloy; (a) showing reaction layer, and (b) EDS analysis taken from the points in part (a).

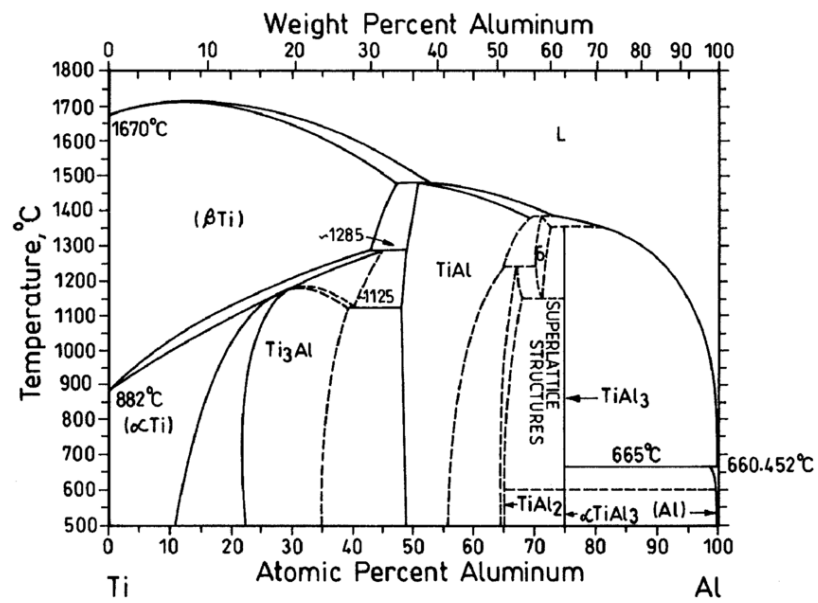


Figure 4.12. Phase diagram of Ti and Al [190].

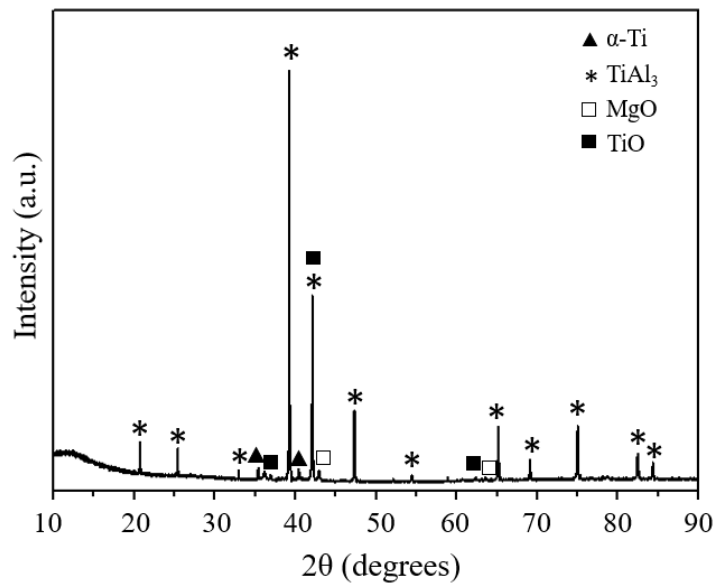


Figure 4.13. XRD analysis of Ti_6Al_4V alloy substrate wetted by AZ91 alloy.

Figure 4.14 shows the change in the shape of molten WE43 alloy on the Ti6Al4V substrate during the wetting test. The initial shape of molten WE43 alloy (at $t=0$) was changed at the end of the 8 minutes, and the liquid WE43 alloy took the form of a droplet. Then, inhomogenous melting was observed, possibly due to the non-uniform evaporation of Mg in the alloy.

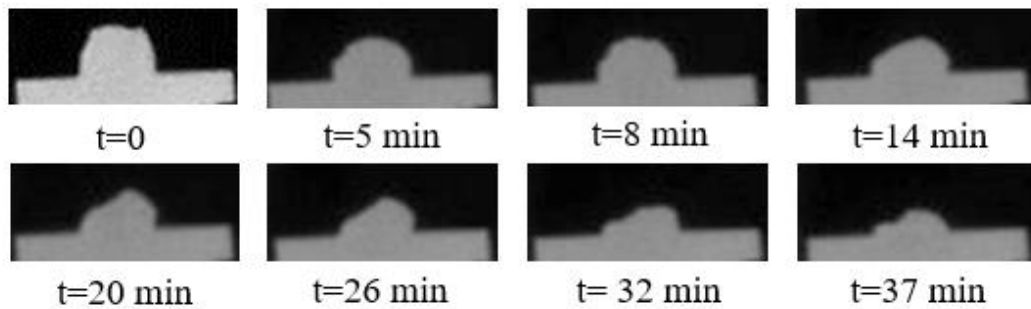


Figure 4.14. Change in the shape of liquid WE43 alloy on Ti6Al4V alloy substrate with time.

Figure 4.15 displays the time-dependent change of wetting angles for molten WE43 alloy on the Ti6Al4V alloy substrate at 800 °C. Initially, the contact angle decreased rapidly from 67 to 53° in 6 minutes, and subsequently, it decreased to 40° in 30 minutes at a relatively slower rate. The sudden decrease in the contact angle may be explained by the dissolution of Y and Nd elements into titanium [188]. At the end of 35 minutes, the contact angle of liquid WE43 alloy became stable at about 25°, which was much larger than those found in both unalloyed Mg and AZ91 alloy.

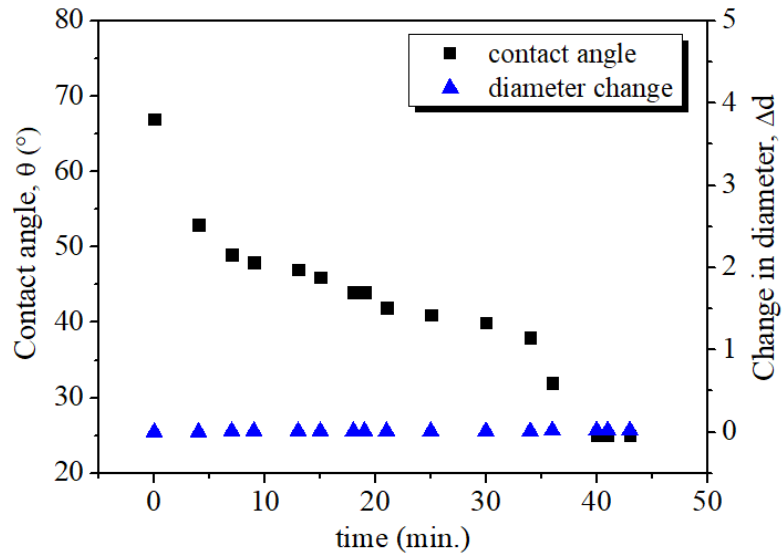


Figure 4.15. The changes in contact angle and diameter of molten WE43 alloy at 800 °C.

Figure 4.16 shows the porous reaction layer having approximately 35 μm thickness formed on the Ti6Al4V substrate when it was in contact with liquid WE43 alloy. According to the EDS dot map analysis, Figure 4.17, the reaction layer was rich in Y and Nd elements. The closer examination, Figure 4.18(a-b), showed that different regions rich in Y and Nd elements (regions A, B, and C) have formed. EDS spot analysis, Figure 4.18(c), revealed that regions A and C contained relatively higher amounts of Y and Nd elements. However, region B possessed higher amount of Ti while the quantity of Nd and Y was relatively low in the region, Figure 4.18(c). Interestingly, magnesium element was not detected in both the reaction layer and titanium substrate, possibly due to the evaporation of Mg at the end of wetting experiments.

Additionally, relatively rough surfaces were detected, Figure 4.18(a-b), at the reaction layer on the Ti6Al4V substrate. It is known that surface roughness directly affects the wetting phenomena of molten metals [191]. The high surface energy of

the rough surfaces causes the wetting angle to increase. Therefore, in the present study, the wetting angle of WE43 alloy was comparatively higher, 25°. One of the possible reasons for the delay in the wetting of WE43 alloy was attributed to the reaction between liquid WE43 alloy and solid Ti6Al4V alloy by the formation of Nd and Y rich phases.

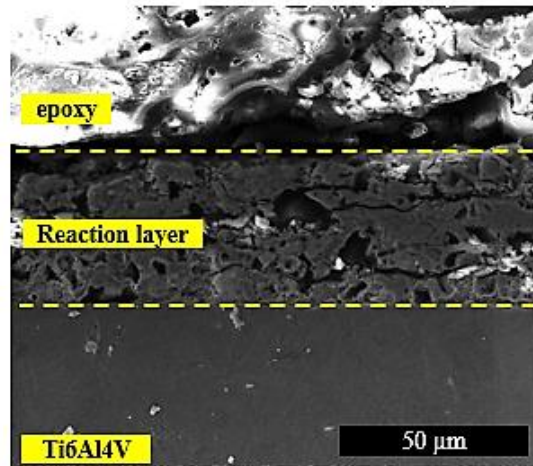


Figure 4.16. SEM analysis showing the reaction layer formed on Ti6Al4V alloy.

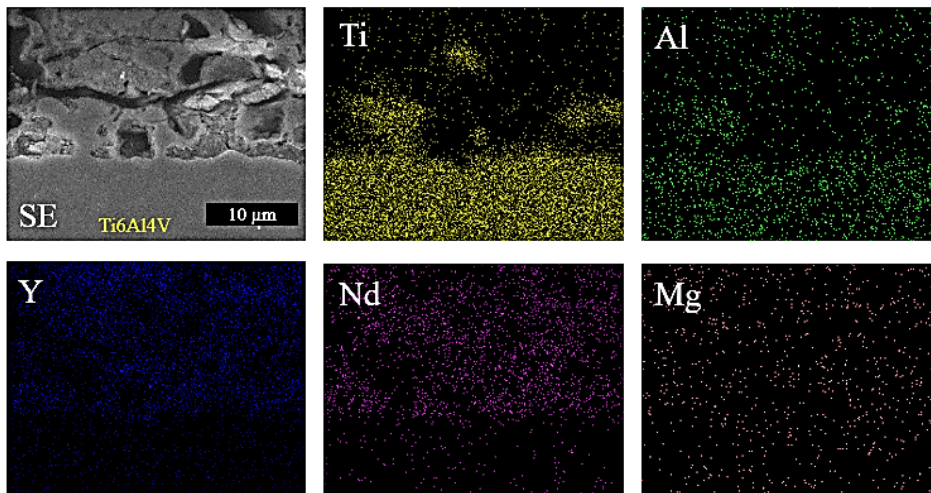


Figure 4.17. EDS dot map analysis across the reaction layer and Ti6Al4V alloy.

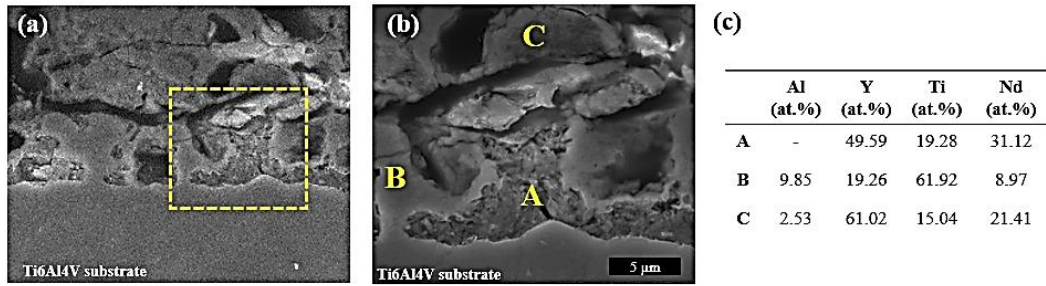


Figure 4.18. (a-b) The closer examination of the reaction layer and (c) EDS results.

Further investigations of the interface layer was conducted at the cross-sections prepared by etching. Three distinct regions were detected, Figure 4.19(a). The first region was the reaction layer rich in Y, Nd and O elements, Figure 4.19(c), which was defined as yttrium oxide phase, Y_2O_3 , by XRD analysis, Figure 4.20. It was stated that above 650 °C, the oxide film on the WE43 alloy was cracked and regenerated rapidly, which was resulted in the formation of the Y_2O_3 phase [189]. In the present study, the oxide layer was a mixture of Nd_2O_3 and Y_2O_3 phases after the wetting experiment according to XRD analysis. In addition, the presence of titanium oxide phases was attributed to oxidation during cooling stage. Interface region (region 2) with around 50 μm thickness contained Ti, Al, and Y elements according to EDS spot analysis, Figure 4.19(c). Moreover, Y and Al rich phase, Figure 4.19(c), having rod-like shape were identified as Al_3Y by XRD analysis.

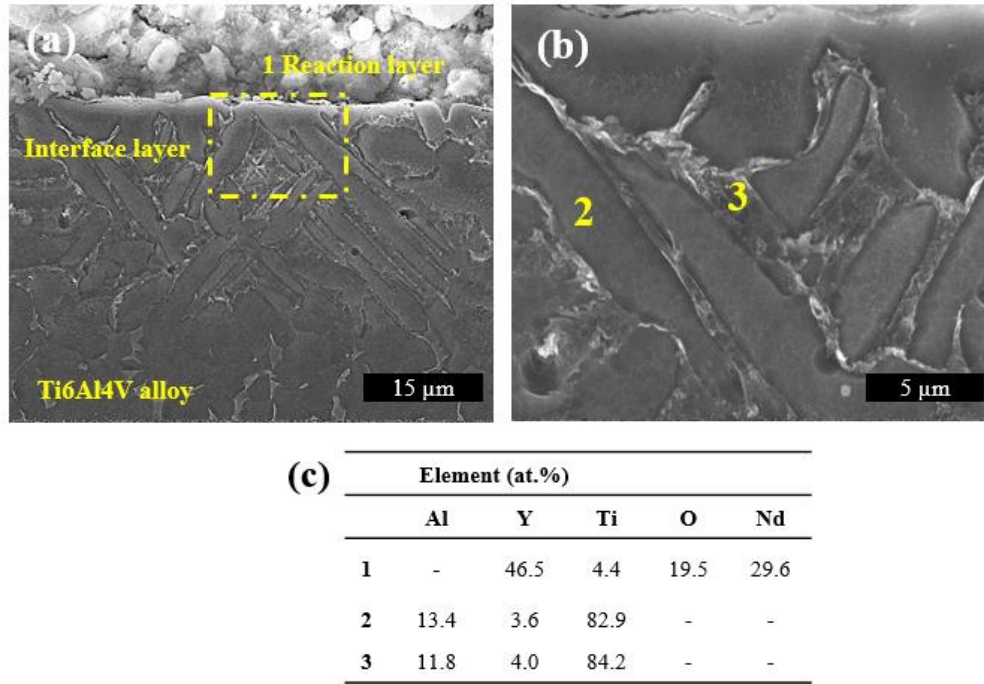


Figure 4.19. (a-b) SEM images of the interface layer, and (c) EDS spot analysis taken from the number shown in part (a-b).

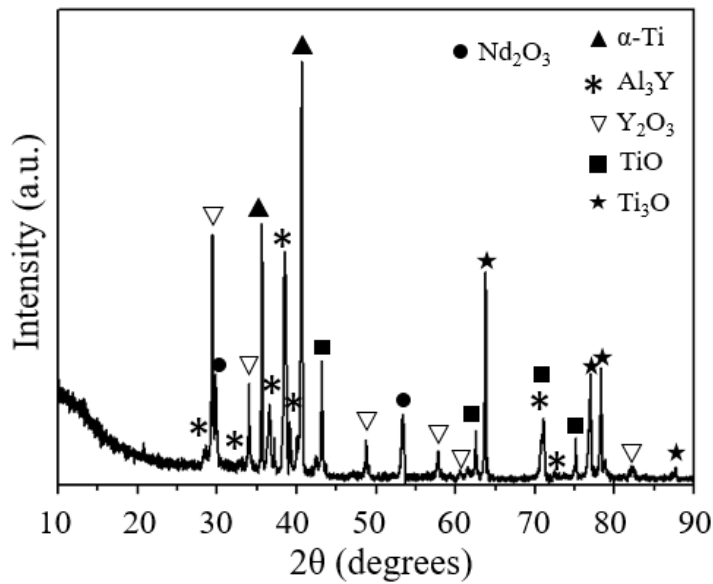


Figure 4.20. XRD analysis of Ti6Al4V alloy substrate wetted by WE43 alloy.

It is known that the contact angle measurement is a common way to understand the wettability of solid surface by liquid [192]. The contact angle, θ , is determined by interaction and repulsion forces between the liquid and solid and by a thermodynamic equilibrium between three phases (solid, liquid, and gas), Figure 4.21. This contact angle is described by Young's equation given in Eq. (4.4), where σ_{LV} and σ_{SV} are the surface energy between liquid and vapor, and solid and vapor phases, respectively, and σ_{SL} is the solid/liquid interface energy [191].

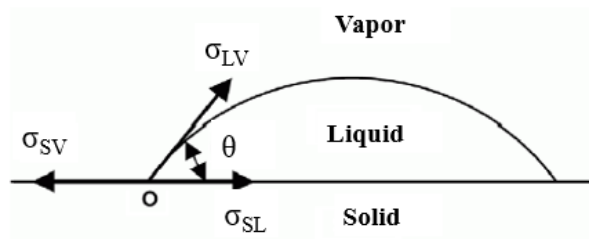


Figure 4.21. Schematic representation of equilibrium contact angle, θ .

$$\cos\theta = \frac{(\sigma_{SV} - \sigma_{SL})}{\sigma_{LV}} \quad (4.4)$$

When the contact angle is smaller than 90° ($\theta < 90^\circ$), the surface is favorable for wetting. Conversely, a non-wetting liquid creates a contact angle between 90° and 180° with the solid substrate. The Young's equation is valid for the non-reactive systems, where the interfacial energies remain unchanged during wetting experiments [193]. On the other hand, it is not applicable for the reactive systems, in which all surface tensions vary with time and undergoes the complex morphological changes during the spreading of liquid [193]. Similarly, in the present study, the reaction between liquid Mg/Mg-alloy and Ti6Al4V caused the formation of compounds in the porous reaction layer. Since surface tension change is not stationary in the reactive wetting system, Young's equation was not considered to be criteria for evaluation of the wetting of Mg/Mg-alloys on solid Ti6Al4V alloy.

According to the results of wetting tests, it was concluded that the wettability of molten Mg/Mg-alloys on solid Ti6Al4V alloy was very good in which the equilibrium contact angles were measured as 12° for unalloyed Mg and AZ91 alloy, and 25° for WE43 alloy. Therefore, liquid magnesium can be successfully infiltrated into a porous Ti6Al4V structure.

4.1.2 Structure and chemical analysis of the composites

Figure 4.22 shows the cylindrical porous Ti6Al4V alloy and composite rods manufactured by loose powder sintering and pressureless liquid infiltration methods, respectively. The resultant microstructure of porous Ti6Al4V alloy after sintering had lamellar Widmanstätten structure, Figure 4.23(a-b). Dark regions displayed aluminum-rich α plates (8.7 wt. % Al, 1.4 wt. % V) grown in different orientations with β lathes (bright area) rich in vanadium (7.4 wt. % Al, 9.5 wt. % V). The porosity and density of the manufactured porous Ti6Al4V alloy, which was used for the infiltration of Mg during composite production, were around 42.5 % and 2.55 g/cm³, respectively. After infiltration of liquid unalloyed Mg, AZ91, and WE43, almost all of the pores in the starting porous Ti6Al4V rods were filled with Mg/Mg-alloy, Figure 4.23(c). There were trace amounts of porosity after Mg infiltration. The content of the residual porosity in the Ti6Al4V-AZ91 composite was around 0.4 %, while it reached around 1.2 % for Ti6Al4V-Mg and 1.3 % for Ti6Al4V-WE43 composites, Table 4.1. Moreover, the density of the manufactured composites were calculated to be between 3.24 and 3.29 gr/cm³, which was closer to that of bone (1.8-2.1 g/cm³ [16]), Table 4.1.



Figure 4.22. Macro images of (a) porous Ti6Al4V alloy rod and (b) manufactured Ti6Al4V-Mg composite rod.

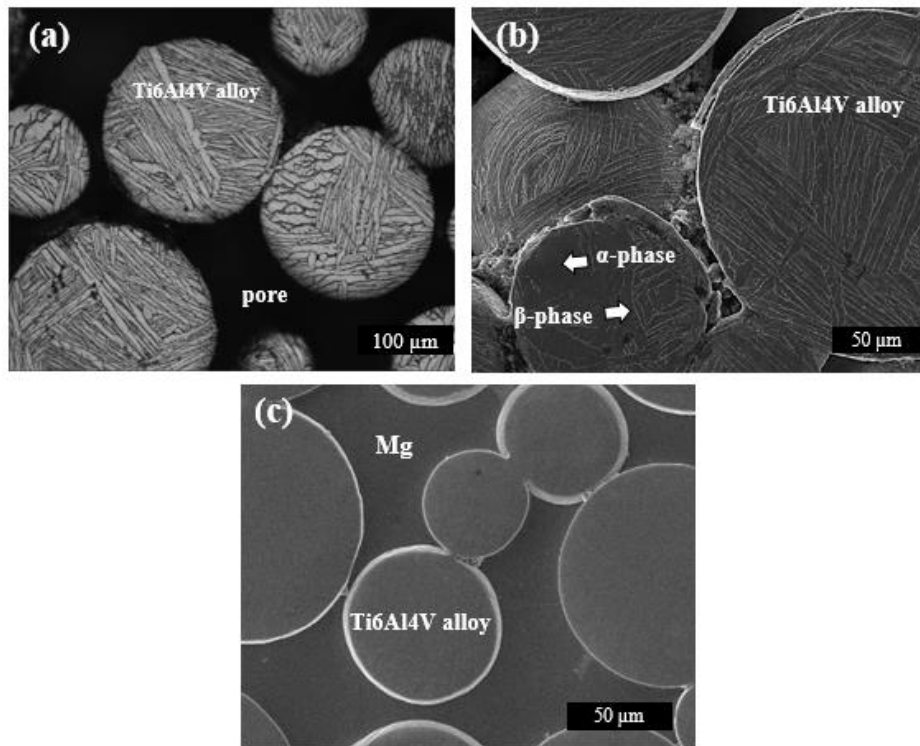


Figure 4.23. Microstructure of (a-b) porous Ti6Al4V alloy and (c) polished cross-section of Ti6Al4V-Mg composite.

Table 4.1 Average density and porosity values of different metals and manufactured composites.

Materials	Density (g/cm³)	Porosity content (%)
Bulk Ti6Al4V alloy	4.43	-
Bulk unalloyed Mg	1.74	-
Bulk AZ91 alloy	1.9	-
Bulk WE43 alloy	1.8	-
Porous Ti6Al4V alloy	2.55 ± 0.05	42.5 ± 0.7
Ti6Al4V-Mg composite	3.14 ± 0.1	1.2 ± 0.3
Ti6Al4V-AZ91 composite	3.41 ± 0.1	0.4 ± 0.2
Ti6Al4V-WE43 composite	3.49 ± 0.1	1.3 ± 0.3

Figure 4.24 shows the microstructures of Ti6Al4V-Mg, Ti6Al4V-AZ91, and Ti6Al4V-WE43 composites after infiltration process. Magnesium infiltrated porous Ti6Al4V composites were composed of only α -Mg, Figure 4.28(a). On the contrary, AZ91 alloy containing composites had both α -Mg matrix and intermetallic phases, Mg₁₇Al₁₂, indicated by white arrows in Figure 4.24(b). The presence of intermetallics was also verified with the XRD analysis given in Figure 4.28(b).

The EDS dot map of the Ti6Al4V-AZ91 composite displayed enrichment of Al and depletion of Mg close to the Ti6Al4V/AZ91 interface, Figure 4.25. In the closer examination of the interface layer, new cuboidal particles were observed, which stuck on the Ti6Al4V powders as shown by yellow arrows in Figure 4.26(a-b). Moreover, EDS line and spot analysis taken along the interface revealed that these particles were Ti and Al rich phases having 28.2 at. % Ti and 71.8 at. % Al, Figure 4.26(c). According to XRD analysis, cuboidal particles were identified as titanium aluminide, TiAl₃, Figure 4.28(b). Possibly, the diffusion of Al elements from AZ91

melt through the Ti-alloy during infiltration caused the formation of cuboidal particles [194].

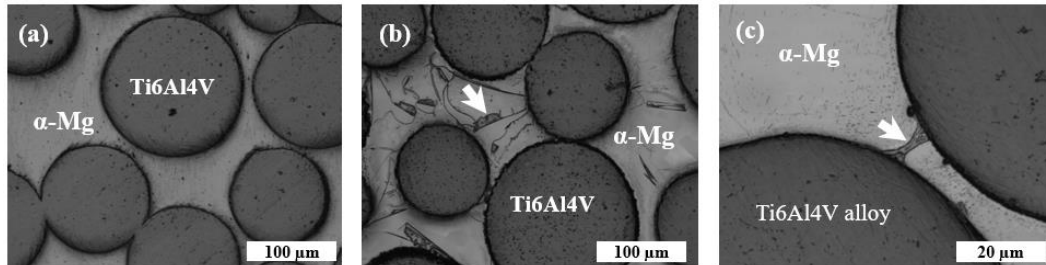


Figure 4.24. Microstructure of (a) Ti6Al4V-Mg, (b) Ti6Al4V-AZ91, and (c) Ti6Al4V-WE43 composites [195].

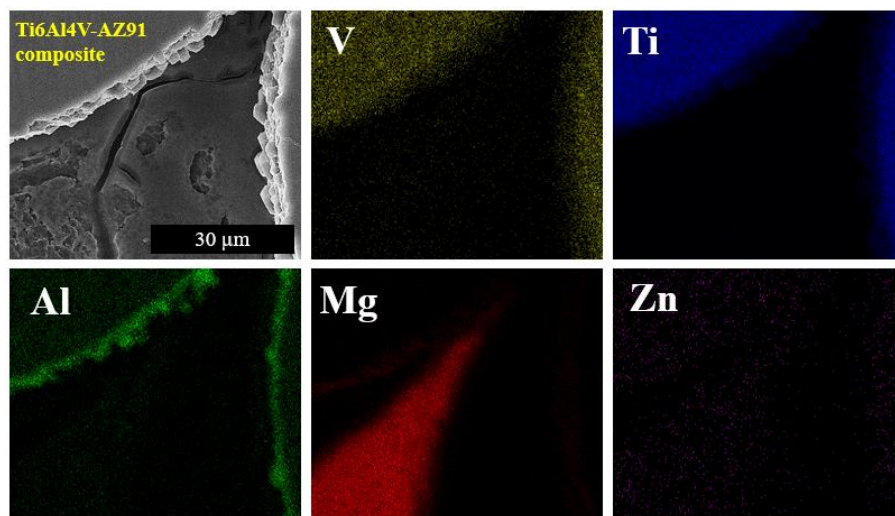


Figure 4.25. EDS maps showing the elemental distribution of various elements in the Ti6Al4V-AZ91 composite [195].

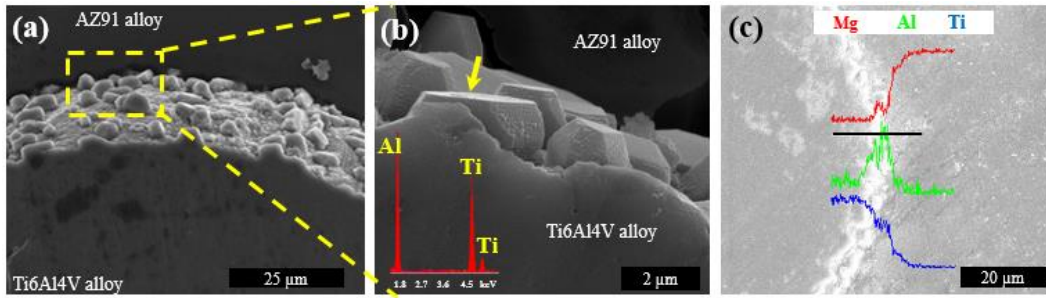


Figure 4.26. (a-b) The microstructure of cuboidal Ti-Al rich particles and (c) EDS line analysis taken along reaction layer between Ti6Al4V particle and AZ91 alloy [195].

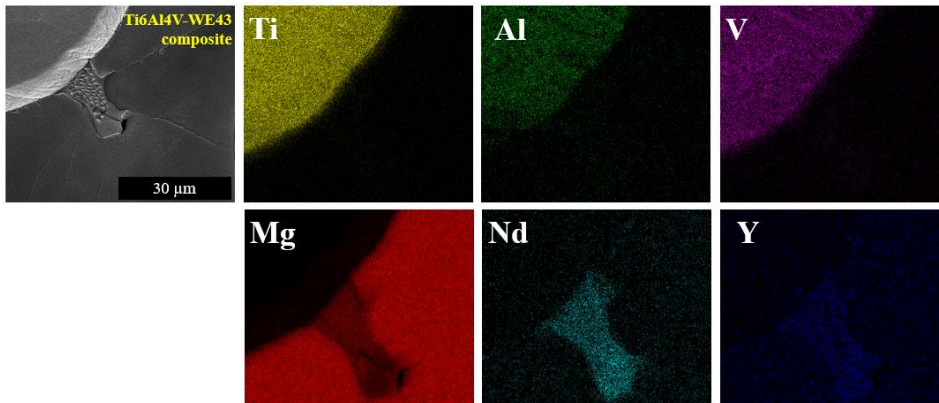


Figure 4.27. EDS maps showing the distribution of various elements in the Ti6Al4V-WE43 composite [195].

On the other hand, WE43 alloy containing composites were found to be composed of eutectic phase mixture (white arrow in Figure 4.24(c)) in the α -Mg matrix, between the Ti-alloy powders. EDS analysis and mapping have shown that the magnesium regions of the composites were composed of an α -Mg matrix with around 6.95 wt. % dissolved Y element and the eutectic mixture made up of mainly

Mg, Y, and Nd elements, respectively, Figure 4.28. The EDS spot analysis has shown that the eutectic phase mixture contained around 8.4 wt. % Y and 20.6 wt. % Nd (balance Mg) element. XRD analysis, Figure 4.28(c), revealed that the phases in Ti6Al4V-WE43 composite were mainly $Mg_{41}Nd_5$, $Mg_{24}Y_5$, and α -Mg in addition to α -Ti.

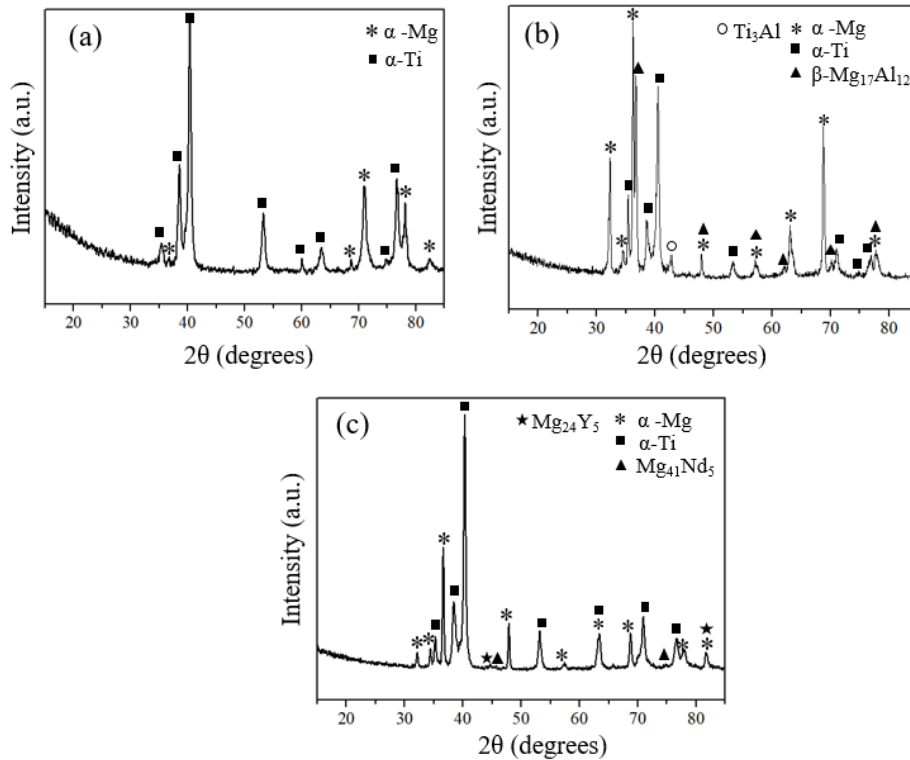


Figure 4.28. XRD analysis of (a) Ti6Al4V-Mg, (b) Ti6Al4V-AZ91, and (c) Ti6Al4V-WE43 composites [195].

4.1.3 Mechanical characterization

Figure 4.29(a) shows the compression stress-strain diagrams of porous Ti6Al4V alloy and magnesium infiltrated composites. It is clearly seen that infiltration improved the mechanical properties of porous samples. In all samples, the stress-

strain curves exhibited three distinct regions commonly observed in wrought bulk materials, which are linear elastic, strain hardening, and fracture regions. Both porous Ti6Al4V and magnesium infiltrated composite samples fractured at angles 45° to the compression axis, Figure 4.29(b). For all of the composite samples, fracture occurred not only by tearing of the necks between the titanium alloy powder particles but also by smearing of surrounding magnesium and its alloys, Figure 4.30. The fracture surfaces of Ti6Al4V-Mg/AZ91/WE43 composites were composed of equiaxed dimples, shown by white arrows and magnified images in Figure 4.30, indicating ductile failure.

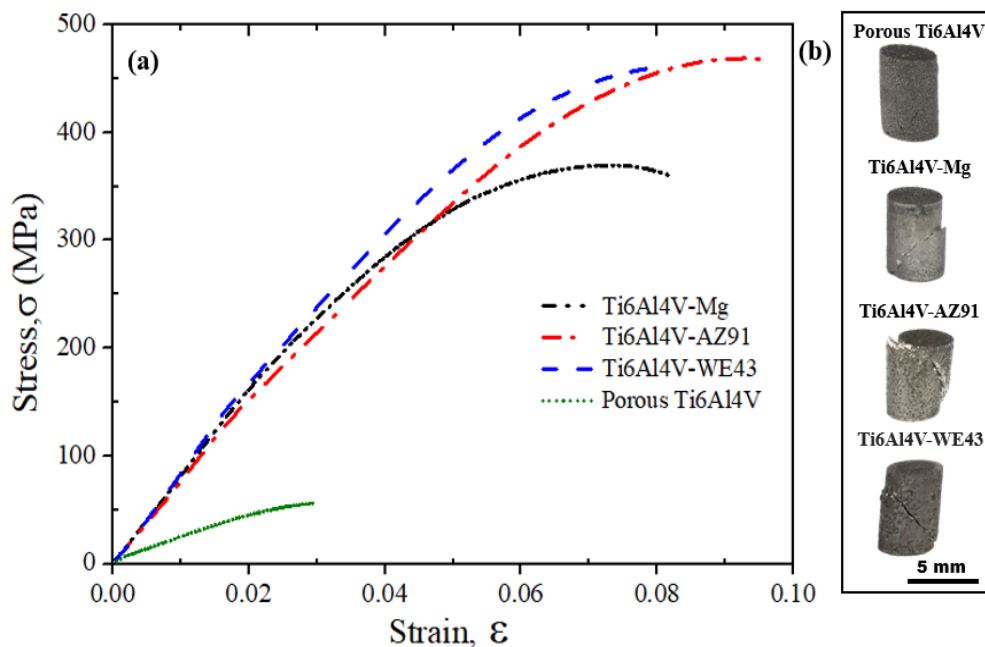


Figure 4.29. (a) Stress-strain diagram and (b) macro images of compression tested porous Ti6Al4V alloy and Ti6Al4V-Mg/AZ91/WE43 composites.

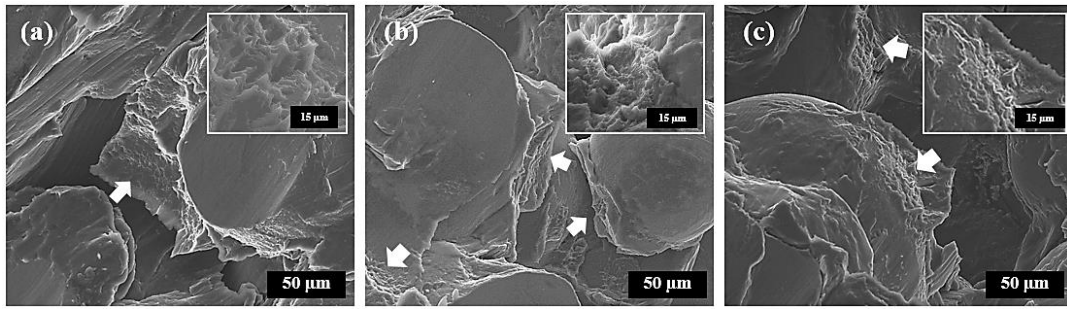


Figure 4.30. Fractured surfaces of (a) Ti6Al4V-Mg, (b) Ti6Al4V-AZ91, and (c) Ti6Al4V-WE43 composites.

Table 4.2 displays the mechanical properties of porous Ti6Al4V alloy and manufactured composites. Infiltration of Mg/Mg-alloys improved the elastic moduli, yield, and peak strength of porous Ti6Al4V samples. For example, the peak strength (σ_{ps}) of the porous Ti-alloy, which was around 57 MPa, reached to 365, 470 and 460 MPa for unalloyed Mg, AZ91 and WE43 alloy containing composites, respectively. Besides, yield strength values increased by around ten times compared to starting porous Ti-alloy as the load-bearing capacity of composites was supported by magnesium.

The strength of the porous Ti6Al4V-alloy skeleton determines both mechanical stability and integrity of the composite because magnesium in the composite corrodes over time. H_2 gas, formed during the corrosion of Mg, generates high pressure, especially on the neck regions of Ti6Al4V powders rather than the whole section of the composite. The neck regions encounter different amounts of hydrogen gas pressure depending on the degradation rates of unalloyed and alloyed magnesium matrix. Thus, the quantity of H_2 gas and the resultant stress on the neck regions determine the mechanical integrity of the bio-composites. The mechanical integrities of the composites in SBF will be presented in the following section 4.3.2.1.

The elastic modulus is another essential mechanical property to understand the composite's in vivo performance. As can be seen in Table 4.2, magnesium infiltration improved the elastic moduli of porous Ti6Al4V samples and the elastic modulus of porous sample (4 GPa) raised to the values between 7.5 - 9.8 GPa, which is comparable to elastic modulus of bone [163]. Although the peak strengths of the manufactured composites were higher than that of cortical bones, elastic modulus values were in the range of cortical bone, which is crucial for the lessening of the stress shielding effect.

Table 4.2 Compressive properties of manufactured porous and composite samples compared with bone [195].

	Elastic Modulus, E (GPa)	Yield Strength, σ_y (MPa)	Peak strength, σ_{ps} (MPa)	Strain at Fracture (%), ϵ
Cortical Bone [163]	7-30	-	100-230	-
Cancellous Bone [163]	0.05-5	-	2-12	-
Porous Ti6Al4V	4.0 ± 0.9	14.0 ± 0.8	57.0 ± 1.4	4.0 ± 1.0
Ti6Al4V-Mg	8.0 ± 0.7	200.0 ± 8.0	365.0 ± 7.5	8.0 ± 0.1
Ti6Al4V-AZ91	7.5 ± 0.9	220.0 ± 9.0	470.0 ± 8.2	9.5 ± 0.2
Ti6Al4V-WE43	9.8 ± 1.1	180.0 ± 6.2	460.0 ± 4.5	8.0 ± 0.3

4.2 Composites with Na-rich coating

It is expected that galvanic corrosion occurring between dissimilar metals like Ti6Al4V and Mg/Mg-alloys accelerates dissolution rate of magnesium. Therefore, sodium-rich phase on the porous surfaces was obtained by NaOH-alkali treatment to decrease the galvanic effect by eliminating direct contact between Ti-alloy and Mg/Mg-alloys. Subsequently, liquid Mg and its alloys were impregnated into surface coated porous Ti6Al4V alloy skeleton. Unalloyed magnesium and AZ91 alloy have been chosen for infiltration into Na-coated porous Ti6Al4V structures due to their relatively better wetting on solid Ti6Al4V. Moreover, before the infiltration, wetting behavior of unalloyed Mg and AZ91 alloyed on Na-coated Ti6Al4V alloy has been also investigated.

4.2.1 Formation of Na-rich coating by alkali treatment

Figure 4.31 shows the SEM images of untreated and NaOH alkali treated porous Ti6Al4V alloy surfaces. The starting (untreated) surface of Ti6Al4V alloy was relatively smooth, Figure 4.31(a). NaOH-alkali treated surfaces, on the other hand, exhibited non-uniform surface structure, Figure 4.31(b-c). The coating layer formed on the powders had a fine porous network structure composed of feather-like structures, Figure 4.31(c-d). Although Na-rich layer was uniform throughout the porous surface, it was found as small islands in some regions. The EDS analysis conducted at different regions revealed similar chemical composition with around 20.4 ± 2.0 at. % O and 9.9 ± 2.0 at. % Na in addition to Ti, Al and V elements coming from porous substrate (Table 4.3).

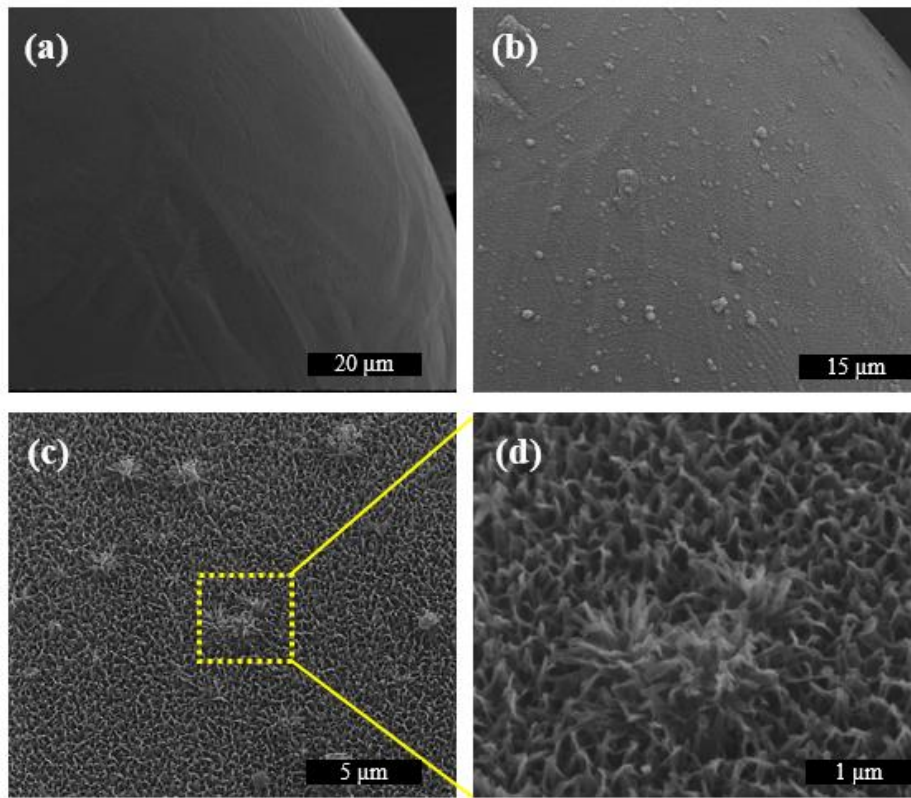


Figure 4.31. SEM images of (a) starting surface (uncoated) and (b-d) NaOH treated porous Ti6Al4V surfaces at different magnifications.

The thickness of the coating layer was also examined using the fractured samples. Figure 4.32(a-b) displays the fracture surface of partially sintered Ti6Al4V powders. A homogenous and thin layer of Na-rich coating was detected throughout the surface, Figure 4.32(a). The thickness of the coating layer was found to be around 500 nm, Figure 4.32(b). In addition to spot analysis (Table 4.3), the EDS line scan was taken along the Ti6Al4V substrate and Na-rich layer (Figure 4.32(c)). It was revealed that Ti6Al4V powders were rich in Ti, Al and V elements, while the concentration of Na increased in the coating layer as expected.

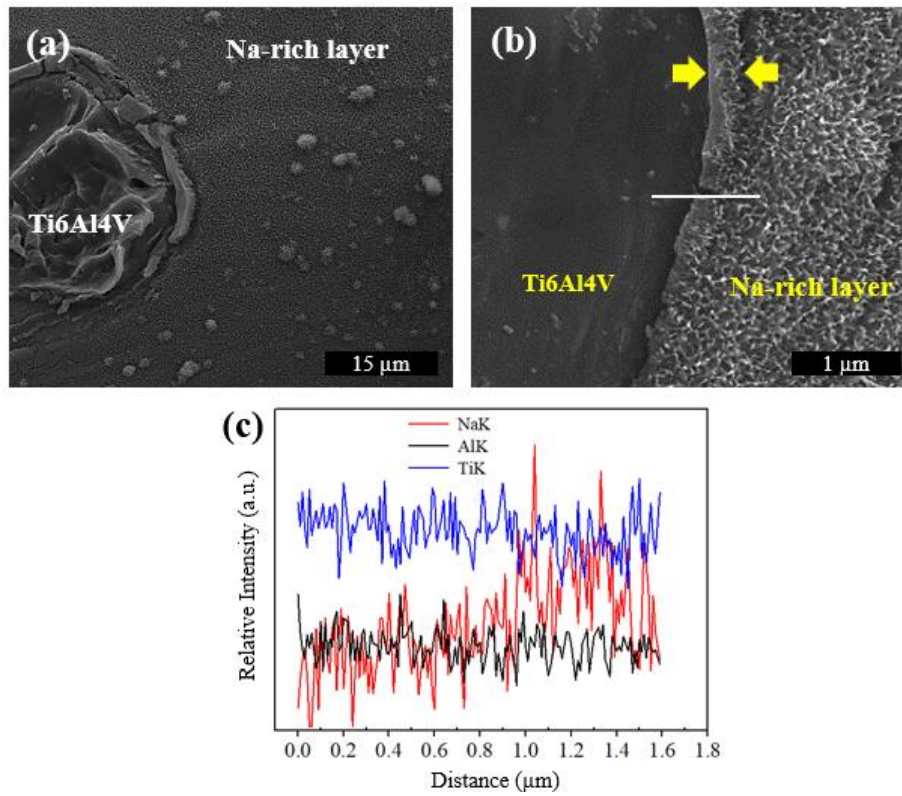


Figure 4.32. (a-b) SEM images of fracture surface showing the Na-rich coating layer and (c) EDS line analysis taken along the interface between Ti6Al4V and Na rich layer (indicated by the white line).

Table 4.3 EDS spot analysis taken from Na-rich coating.

Region	Elements (in at. %)				
	O	Na	Al	Ti	V
Na-rich layer	20.4 ± 2.0	9.9 ± 2.0	4.6 ± 1.0	61.4 ± 2.0	3.7 ± 0.5

Bulk Ti6Al4V alloy samples were also coated with NaOH-alkali treatment by using the same process parameters applied to porous Ti-alloy to investigate wetting of liquid Mg/Mg-alloys on solid Ti-alloy. Figure 4.33(a) shows the relatively smooth

surface of starting solid Ti-alloy with rarely observed grinding scratches, which was completely changed after alkali treatment. Ti6Al4V alloy surface with Na-rich coating (3.66 at. % Na, 28.54 wt. % O) exhibited relatively homogenous and fine porous network structure with pores around 400 nm size, Figure 4.33(b). It is known that the surface condition of substrate directly affects wetting behavior of liquid [191]. Therefore, surface roughness of both uncoated and coated Ti6Al4V alloy was measured by AFM three-dimensional (3D) micro-topography, Figure 4.33(c-d). The average roughness values were found to be 146 ± 40 nm and 100 ± 30 nm for uncoated and coated Ti6Al4V surfaces, respectively. Since the Na-rich coating layer filled grinding scratches on uncoated Ti-alloy surfaces, the average surface roughness of starting the Ti-alloy surface was observed to be decreased after alkali treatment. However, formation of nano-porous coating layer increased the local surface roughness of the samples.

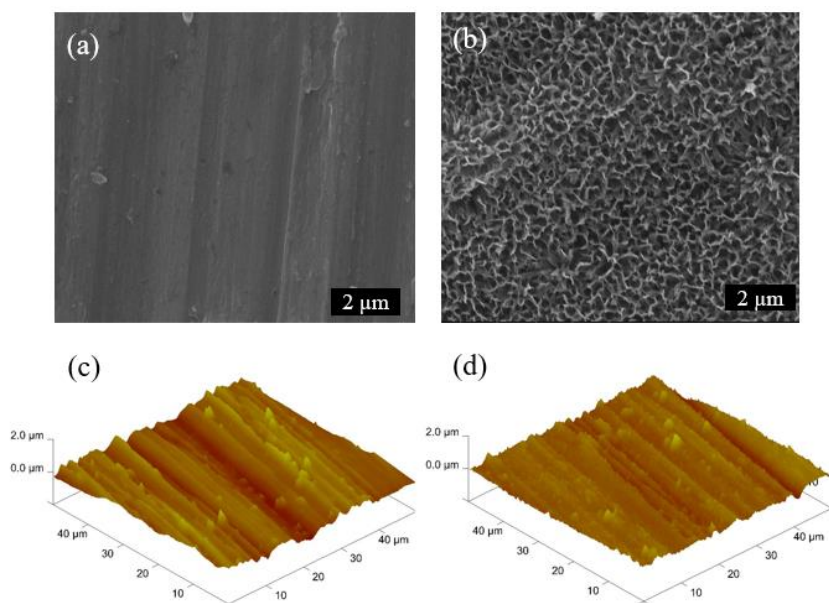


Figure 4.33. SEM images of (a) starting surface (uncoated) and (b-d) Na-coated Ti6Al4V surface, and AFM 3D micro-topography (a) uncoated and (b) Na-coated Ti6Al4V alloy.

4.2.2 Wetting behavior of liquid Mg/Mg-alloy on Na coated Ti6Al4V alloy

As it will be presented in the following sections, the effect of Na-rich coating on the corrosion behaviors of composites was investigated for two composites, namely, Ti6Al4V-unalloyed Mg and Ti6Al4V-AZ91 alloy, which displayed two different extreme corrosion behavior. Therefore, wetting experiments were conducted by use of only unalloyed magnesium and AZ91 alloy on Na-coated bulk Ti6Al4V alloys.

Figure 4.34 shows the shape change of molten unalloyed Mg on Na-coated Ti6Al4V substrate. The point where the melting of unalloyed Mg started was accepted as reference point where time was equal to zero. Similar to uncoated samples, the midpoint of unalloyed magnesium started to collapse firstly. The initial irregular shape of molten Mg was changed after 8 minutes. Although the height of the molten droplet decreased possibly because of the evaporation of Mg, inhomogeneous melting was detected after 21 minutes. In contrast to the wetting of liquid Mg on uncoated Ti6Al4V samples, the diameter of the molten Mg droplet was almost constant until the end of the experiment, which may be explained by the formation of a reaction between magnesium and coated titanium surface.

A similar melting behavior was also observed for liquid AZ91 alloy on the coated Ti6Al4V alloy, Figure 4.35. Initially, AZ91 alloy started to melt from one corner non-homogeneously, and the midpoint of the AZ91 alloy collapsed simultaneously. However, after 22 minutes, the liquid magnesium alloy became relatively flat. Similar to unalloyed Mg, the height of the samples decreased, possibly due to the evaporation of magnesium. Although the wetting experiments were repeated several times, unalloyed Mg and AZ91 alloy samples did not melt homogeneously.

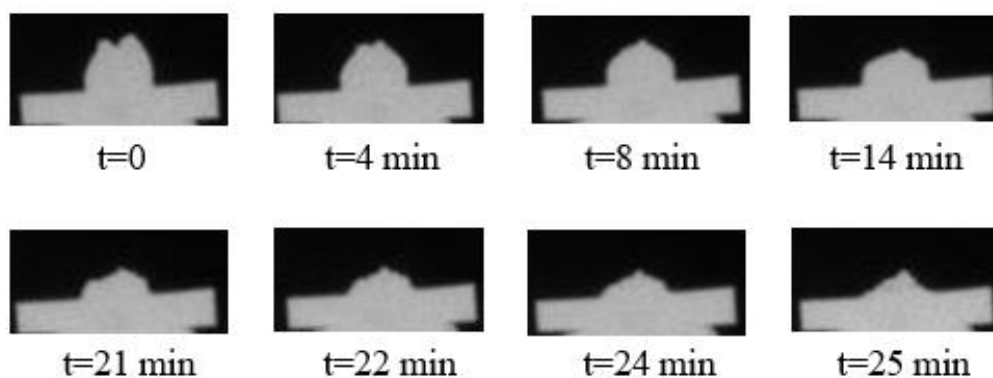


Figure 4.34. Change in shape of unalloyed Mg on Na-coated Ti6Al4V alloy substrate with time.

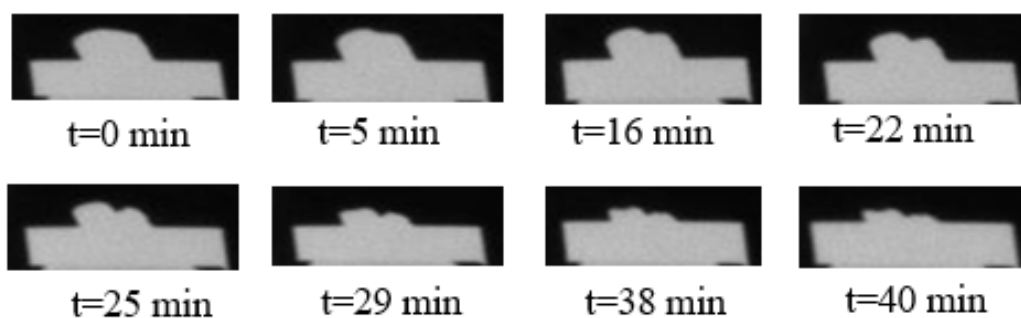


Figure 4.35. Change in shape of AZ91 on Na-coated Ti6Al4V alloy substrate with time.

Since the melting of unalloyed Mg and AZ91 alloy was nonhomogeneous on the coated Ti-alloys, the contact angle between liquid Mg/Mg-alloys and Ti-alloy was measured only from one side of Mg/Mg-alloy at which melting started initially. Figure 4.36(a) shows the change of contact angle for unalloyed liquid Mg on both uncoated and coated Ti6Al4V substrates. As previously found, despite sudden change of the wetting angle of unalloyed liquid Mg on uncoated titanium alloy, the wetting angle of unalloyed liquid was observed to decrease gradually when there was

Na-rich coating on the Ti6Al4V alloy. After 20 minutes, the contact angle decreased down to 25° and remained nearly constant until the end of the experiment. The presence of Na-rich coating on Ti6Al4V decreased the wettability of unalloyed liquid magnesium, possibly due to the highly porous structure of the coating and the reaction between unalloyed liquid magnesium and Na-rich coating.

Figure 4.37 shows the cross-sectional analysis of the reaction layer formed on Na-coated Ti6Al4V alloy. The reaction layer had approximately 1 μm thickness and contained mainly Mg (23.74 at. %) and O (22.79 at. %) elements, which was supported with the EDS line scan, Figure 4.37(c-d), taken along the reaction layer. XRD analysis given in Figure 4.38(a) verified the formation of the magnesium oxide, MgO, layer on the coated Ti6Al4V substrate surface in addition to Ti₃O and TiO phases, which were thought to be formed during cooling stage of the wetting experiment.

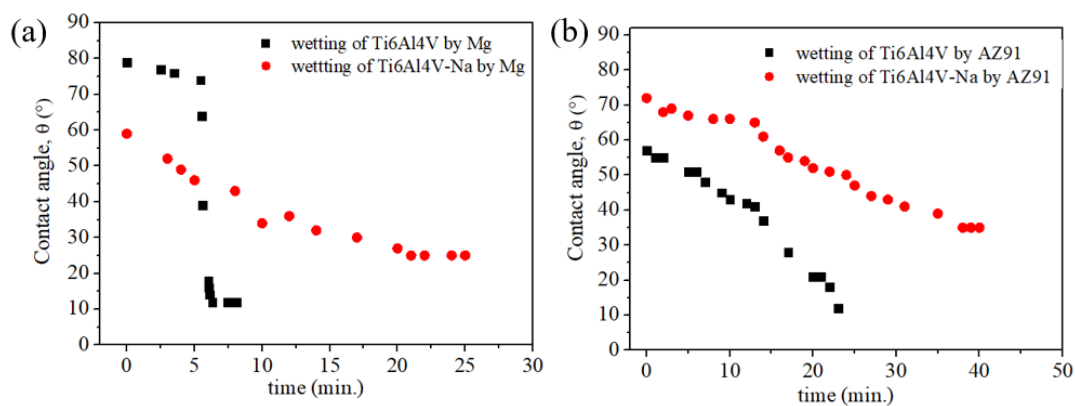


Figure 4.36. The change of contact angle for (a) unalloyed liquid Mg and (b) liquid AZ91 alloy on coated Ti6Al4V substrate at 800 °C.

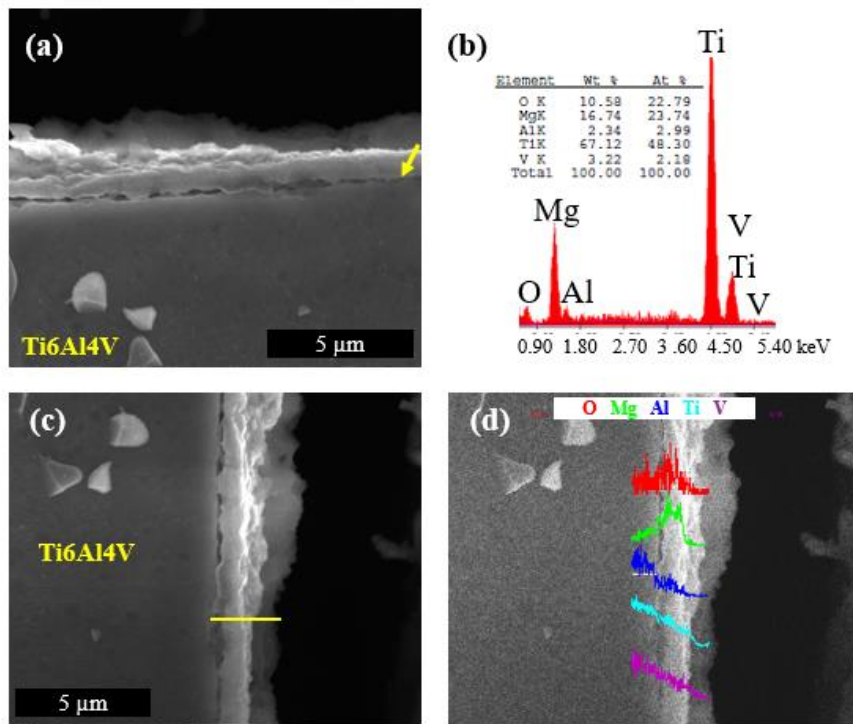


Figure 4.37. (a) SEM and (b) EDS analysis of the interface layer taken from the yellow arrow in part (a), and (c-d) EDS line scan analysis taken along the yellow line in part (c).

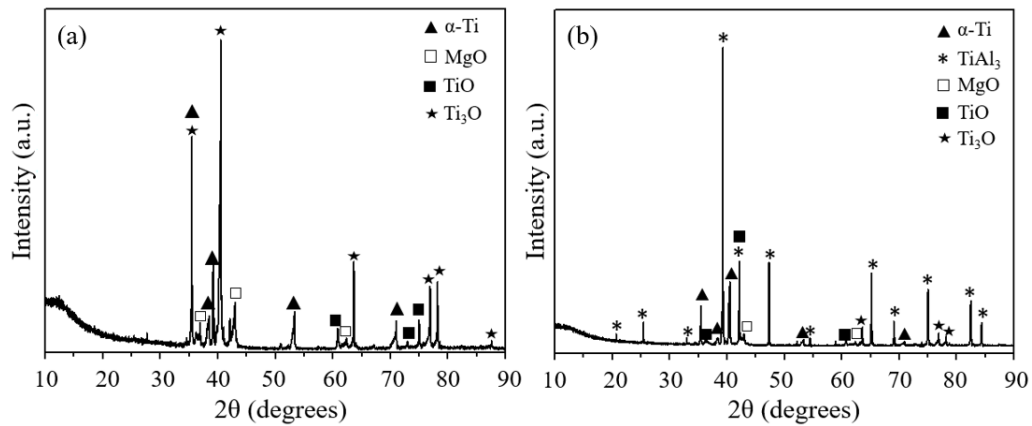


Figure 4.38. XRD analysis taken along the reaction layer of (a) unalloyed liquid Mg and (b) liquid AZ91 alloy on coated Ti6Al4V substrate.

The change of contact angle values for liquid AZ91 alloy on the Na coated Ti6Al4V alloy is given in Figure 4.36(b). Initially, the contact angle was nearly constant at around 65° during the first 13 minutes. Subsequently, a gradual decrease was observed, and the contact angle reached a stable value at around 35° , Figure 4.36(b). The presence of Na-rich coating on Ti6Al4V alloy degraded the wetting of AZ91 alloy, and a higher contact angle was observed. Additionally, the wetting of AZ91 alloy delayed when there was a coating on Ti6Al4V alloy. Similar to wetting tests of unalloyed Mg on coated Ti-alloys, the porous rough surface of the coating and possible reaction took place between liquid Mg-alloy and the coating deteriorated the wettability.

Figure 4.39(a) shows the cross-sectional examination of the Na-coated Ti6Al4V substrate after the wetting test conducted using liquid AZ91 alloy. On the Na-coated Ti6Al4V substrate, a porous reaction layer was detected, which was relatively thicker (around $150\ \mu\text{m}$) compared to that of uncoated Ti6Al4V substrate, Figure 4.9. The closer examination displayed a wave-like interface layer between the reaction layer and the Ti6Al4V substrate, Figure 4.39(b). EDS spot analysis taken from the different regions, Figure 4.39(c), revealed mainly Ti and Al elements with variable concentrations. For example, in region 1, which was close to liquid Mg-alloy, TiAl_3 was detected by XRD analysis, Figure 4.38(b). Besides, the composition analysis corresponded to TiAl_2 and TiAl phases in regions of 2 and 3, respectively, Figure 4.39(d). These results were similar to those found in the wetting tests conducted by liquid AZ91 alloy on uncoated Ti6Al4V alloy, Figure 4.11(b). However, the reaction layer was observed to be rougher (wave-like) when there was a coating on Ti6Al4V alloy, Figure 4.39(b). Additionally, cracks were detected between regions 1 and 2, containing different intermetallics, which possibly formed during cooling because of the difference in thermal expansion coefficients of phases.

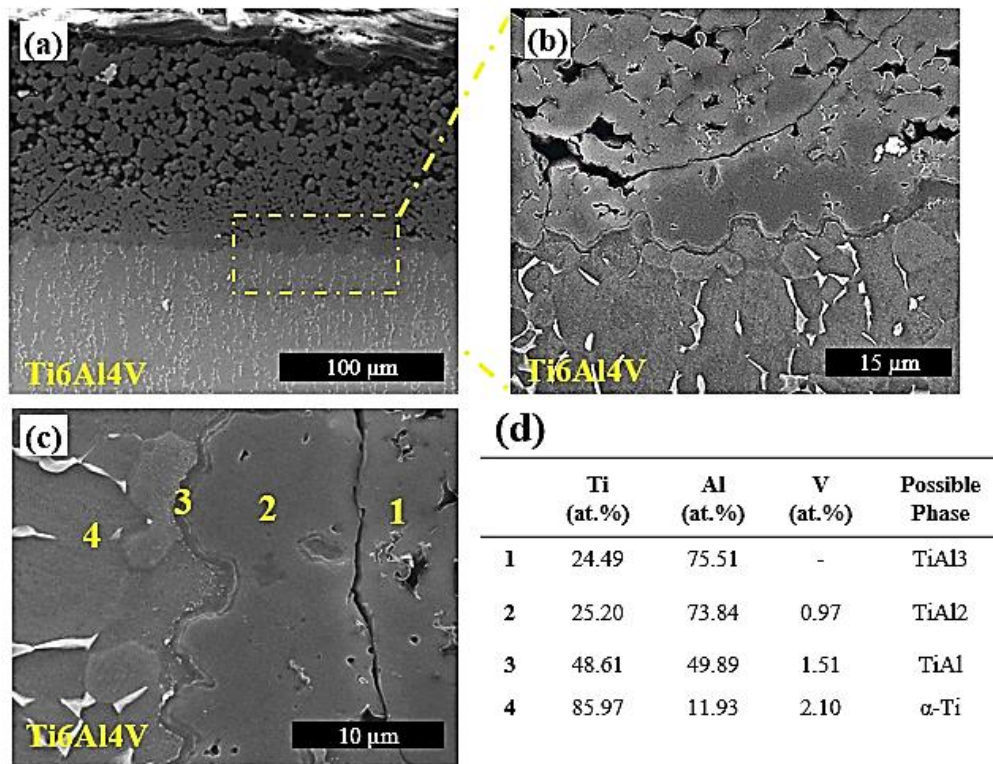


Figure 4.39. (a-b-c) SEM analysis showing the reaction layer formed on Ti6Al4V alloy, and (d) EDS spot analysis taken from the numbered points in part (c).

4.2.3 Structure and chemical analysis of composite containing Na-rich

Cylindrical Ti6Al4V-Na-Mg and TiAl4V-Na-AZ91 composites with 5.5 mm diameter and 100 mm length were produced. After infiltration, liquid unalloyed Mg and AZ91 alloy filled almost all the pores in the Na-rich coated porous Ti6Al4V structure, Figure 4.40(a), and (c). The residual porosity reached about 2.2 % and 1.5 % in Ti6Al4V-Na-Mg and Ti6Al4V-Na-AZ91 composites, respectively. The dark gray regions in Figure 4.40 belong to Mg/Mg-alloys, while the light grey regions were Ti6Al4V alloy. Although the interface region between coated Ti-alloy powders and Mg was mostly uniform, the residual porosities formed at the interface region

partly distorted the continuity of the interface (shown by arrows in Figure 4.40(b-d)). It was found that coating did not alter the composite density significantly and the coated composites displayed densities around 3.21 and 3.37 gr/cm³, which was similar to those found in their uncoated counterparts. Moreover, no intermediate compound or secondary phase formation was detected as confirmed by XRD analysis, Figure 4.41.

It is known that the sodium titanate hydrogel layer formed due to treatment in aqueous solution of NaOH is transformed into a more dense sodium titanate layer when subjected to heat treatment at elevated temperatures (like 500-700°C) [159,163,196]. Similarly, in the present study, the Na-rich hydrogel layer was thought to be transformed into a more dense titanate layer during infiltration at 800 °C. However, the presence of the coating layer was not detected by XRD analysis due to being very thin and because of rough surfaces caused by partially sintered powders.

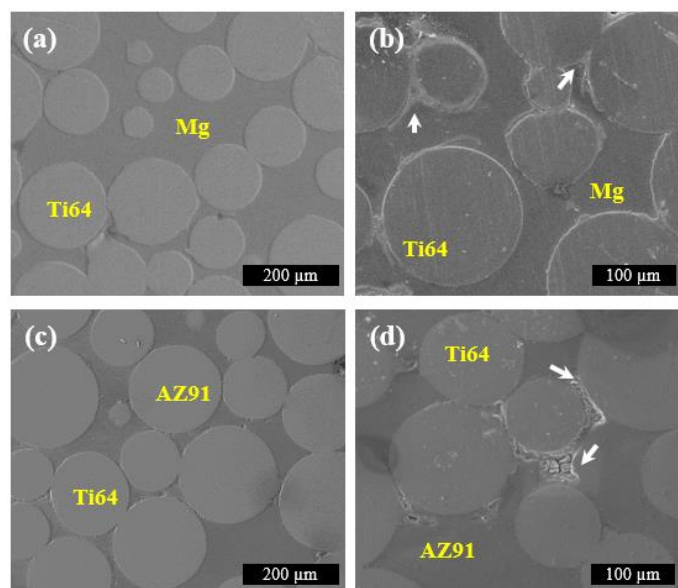


Figure 4.40. The polished surfaces of (a-b) Ti6Al4V-Na-Mg and (c-d) Ti6Al4V-Na-AZ91 composites with Na-rich interface.

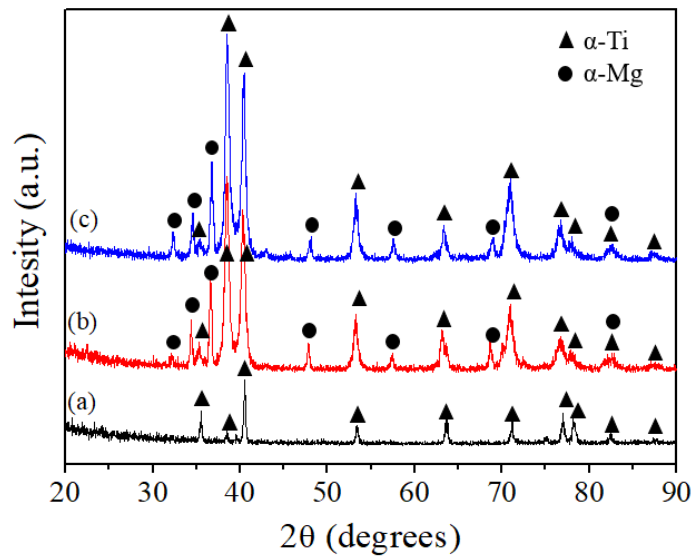


Figure 4.41. XRD analysis of (a) porous Ti6Al4V alloy, (b) Ti6Al4V-Na-Mg and (c) TiAl4V-Na-AZ91 composites.

2D elemental distribution was also obtained by EDS dot map, Figure 4.42, across the polished cross-sections of composites to reveal the elemental distribution clearly. Although its content was relatively low, Na-rich coating, between the Mg and Ti6Al4V regions, can be seen clearly. Despite its homogeneity in terms of thickness and bonding characteristics, the Na-rich coating has been observed to slightly peeled off in some regions of Ti6Al4V-Mg composites, Figure 4.42. The coating layer and the gap between the coating layer and Ti-alloy powder was labelled by letters of “A” and “B”, respectively, Figure 4.43(b). The EDS spot analysis taken from both regions, Table 4.4, revealed Na and O elements in addition to Mg, Ti and Al signals coming from Mg regions and Ti6Al4V powders underneath of the coating layer. The EDS line analysis taken along the region B, Figure 4.43(c), displayed similar elements and no secondary phase formation was detected. Although a gap was formed in some regions between Ti6Al4V and coating layer, the coating did not completely peel off and it mostly preserved its continuity. Partial distortion of

continuity of the coating layer was attributed to mechanical forces created during sample preparation step and due to difference in co-efficient of thermal expansions.

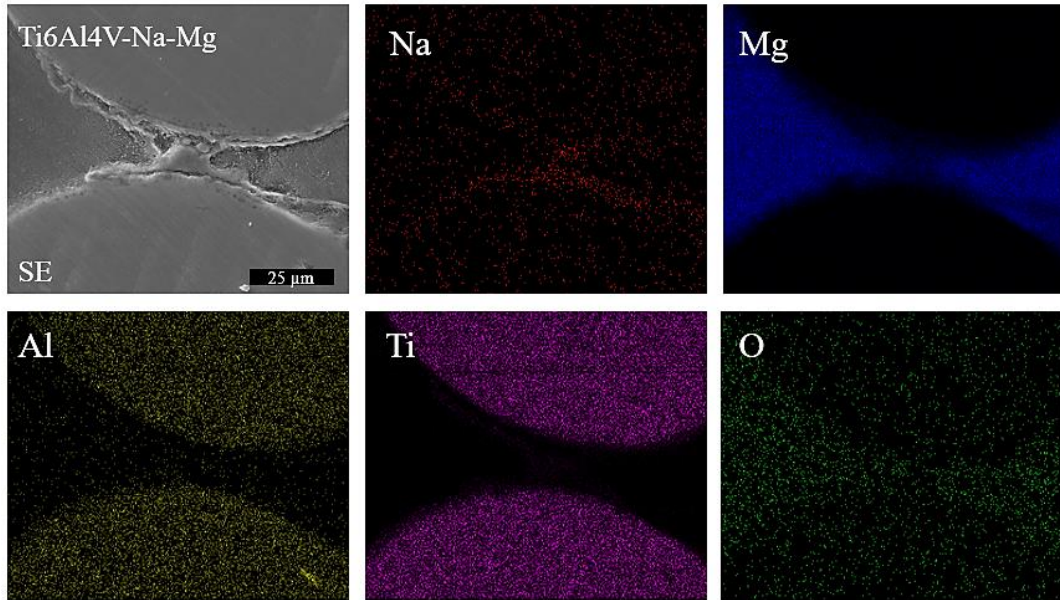


Figure 4.42. EDS dot map showing the elemental distribution of various elements in the Ti6Al4V-Na-Mg composite (SE: Secondary electron image).

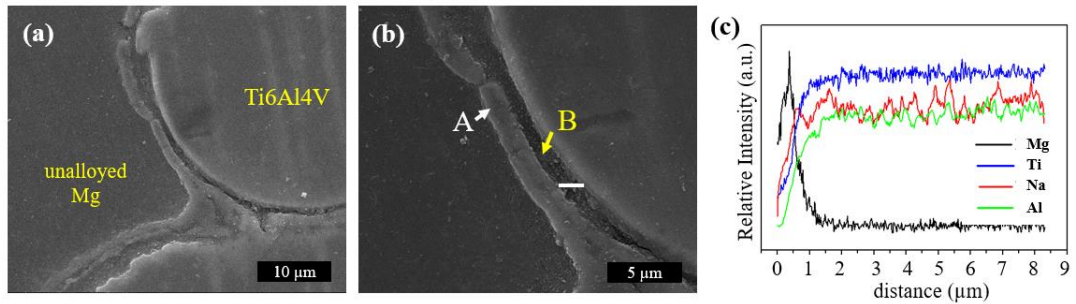


Figure 4.43. (a-b) SEM images and (c) EDS line scan analysis of region B.

Table 4.4 EDS spot analysis of different regions taken from Figure 4.43.

Region	Element (at. %)				
	O	Na	Mg	Al	Ti
A	19.8 ± 2.0	1.3 ± 0.1	74.7 ± 3.5	0.9 ± 0.1	balance
B	15.0 ± 2.2	3.0 ± 0.5	68.8 ± 4.0	1.8 ± 0.1	balance

The presence of coating layer rich in Na and O elements were also detected in the EDS dot map of Ti6Al4V-AZ91 composites, Figure 4.44. However, the quantity of regions containing distorted coating layers (SE-image in Figure 4.44) was relatively higher compared to Ti6Al4V-Mg composites. Additionally, enrichment of aluminum element was detected on the Ti6Al4V alloy powder surfaces similar to those seen in uncoated Ti6Al4V-AZ91 composites in which the Al-rich particles were identified as TiAl₃ phase. Figure 4.45 clearly shows the presence of irregular Al rich phase on the coated Ti6Al4V powders. It was observed that the quantity of Al-rich particles has been decreased as a result of coating the Ti-alloy particles. Relative decrease in the quantity of such particles with respect to uncoated composites was attributed to the presence of Na-rich layer between AZ91 and Ti6Al4V alloys. Na-rich layer possibly limited the reaction between aluminum in AZ91 and titanium coming from Ti6Al4V alloy. Secondly, a possible reaction between sodium and aluminum in AZ91 alloy may lead to reduction of Al-rich layer.

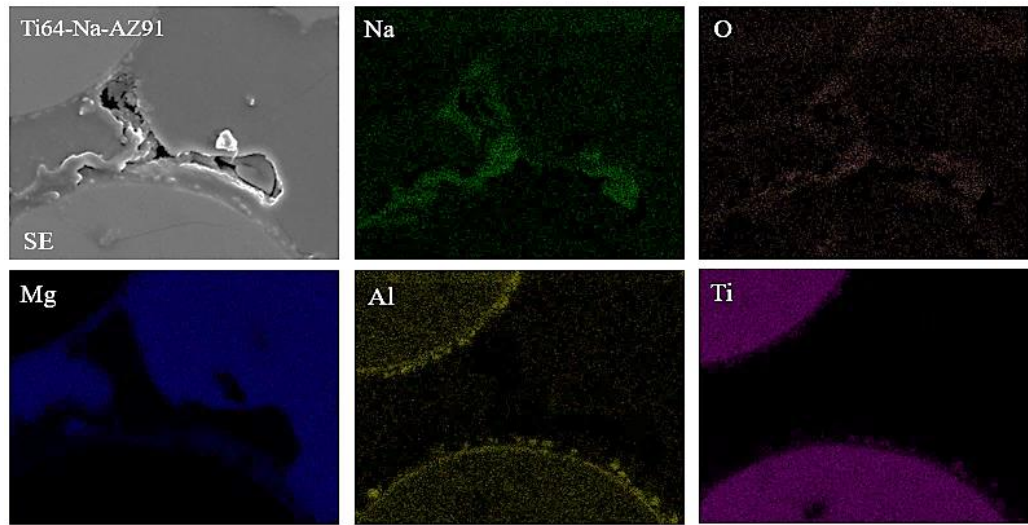


Figure 4.44. EDS dot map showing the elemental distribution of various elements in the Ti6Al4V-Na-AZ91 composite (SE: Secondary electron image).

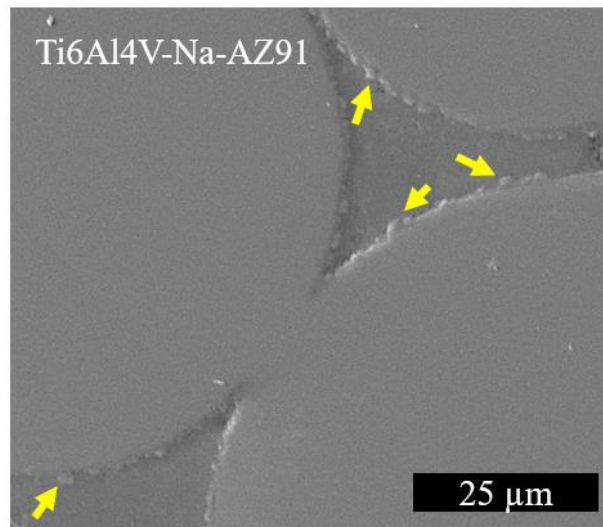


Figure 4.45. SE-image showing the interface between coated Ti6Al4V and AZ91 alloy in Ti6Al4V-Na-AZ91 composites.

Enrichment of the interface regions with Al, Na and O elements can also be seen in Figure 4.46. Interestingly, the relative quantity of Na and O didn't drop to zero when analysis was taken from AZ91 alloy region. Accordingly, it was believed that there is a slight of diffusion sodium and oxygen from coating to AZ91 alloy region. However, the interface region is need to be examined in detail to reveal diffusional transformation across the interface.

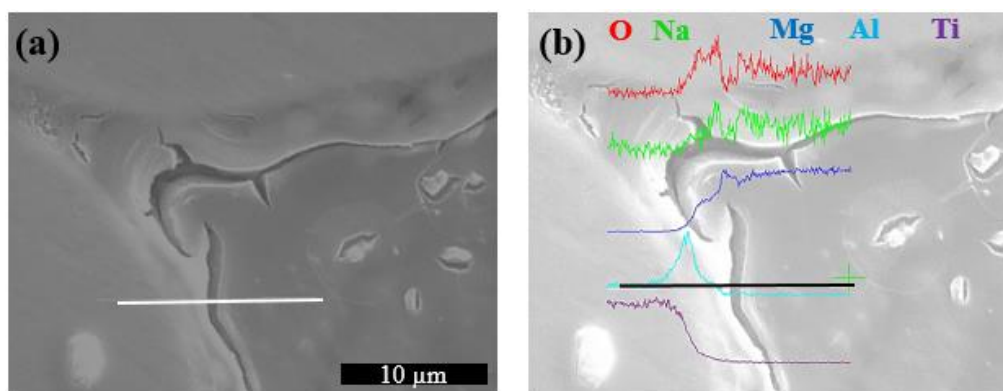


Figure 4.46. (a) Polished cross-section of Ti6Al4V-Na-AZ91 composite, and (b) EDS line analysis taken along the Ti-alloy-coating and AZ91 alloy, indicated by the white line in (a).

Figure 4.47(a) shows the fractured surface of Ti6Al4V-Na-AZ91 composites. The fracture surface was observed to contain three different regions, namely, AZ91, Na-rich, and Ti6Al4V alloy regions. Since it was hard to detect Na element because of Mg and Ti signals coming from AZ91 and Ti6Al4V regions, EDS analysis revealed relatively low amount of Na element on the surface, Figure 4.47(b).

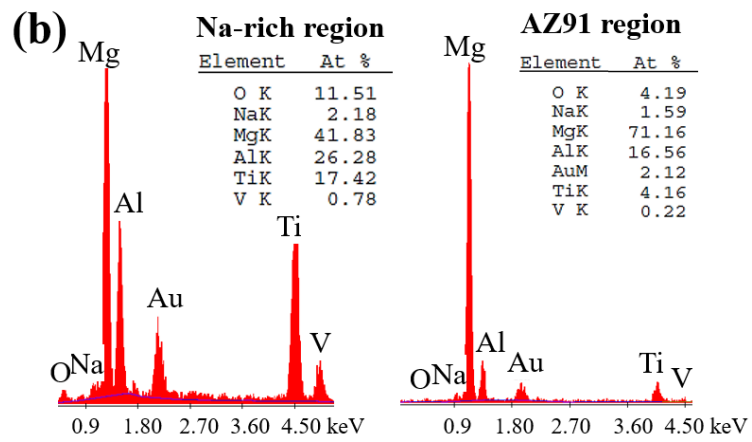
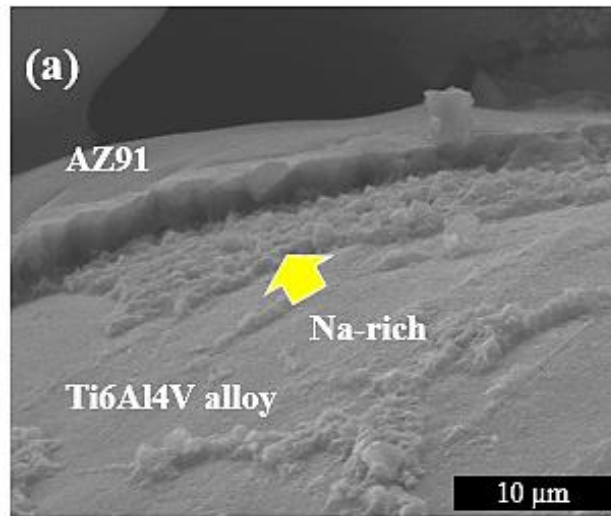


Figure 4.47. (a) Fractured surface of Ti6Al4V-Na-AZ91 composites and EDS analysis taken from the different regions. (b) EDS analysis of regions shown in (a).

4.3 Corrosion Properties

This section consists of three main parts, in which corrosion behaviors of bulk Mg/Mg-alloys, and Ti6Al4V-Mg/Mg-alloy composites with and without Na-rich coating have been investigated separately in SBF through the use of non-electrochemical and electrochemical tests. Degradation behavior of bulk Mg/Mg-alloys was examined by considering the quantity, amount and distribution of the second phases in the initial microstructures. Following that, the influence of coupling of Ti-alloy with unalloyed Mg, AZ91 and WE43 alloys on the galvanic corrosion of composites was discussed. In addition, the effect of interface formation between Ti6Al4V and Mg/Mg-alloys on the corrosion rates of the composites have been also investigated.

4.3.1 As-cast bulk Mg/Mg-alloy

4.3.1.1 Structure and chemical analysis

Figure 4.48(a-b) shows the optical microscope images of starting as-cast unalloyed magnesium. The microstructure contains only α -phase, Figure 4.48(c), with an average grain size of around 400 μm . The formation of deformation twins inside the grains of α -phase (shown by arrows) was attributed to pressure applied during sample preparation steps.

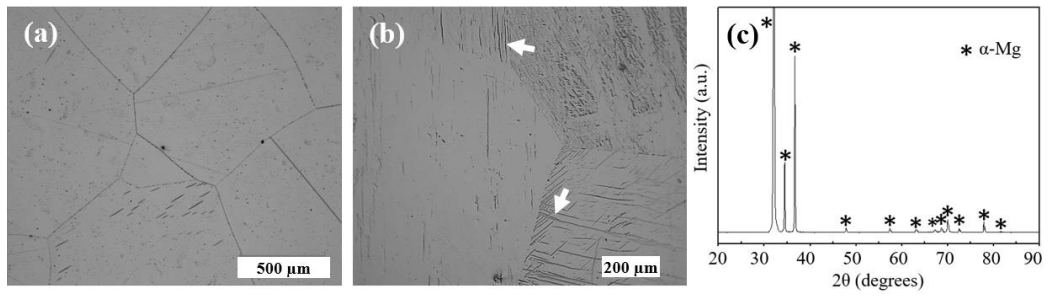


Figure 4.48. (a-b) The starting microstructure and (c) XRD of unalloyed Mg.

The microstructure of bulk as-cast AZ91 alloy was composed of α -Mg matrix and homogeneously distributed secondary phase particles along the grain boundaries, Figure 4.49(a). The enlarged SEM images in Figure 4.49(b-c) showed that the secondary gray particles were surrounded by eutectic phase mixture. EDS analysis taken from the gray secondary particles revealed 58.4 at. % Mg and 40.0 at. % Al with a small amount of Zn (1.6 at. %), Table 4.5, which was defined as the $Mg_{17}Al_{12}$ phase by XRD analysis, Figure 4.51(a). Besides, the eutectic phase mixture possessed a lamellar structure, including alternating layers of α -Mg and β - $Mg_{17}Al_{12}$ intermetallic phases.

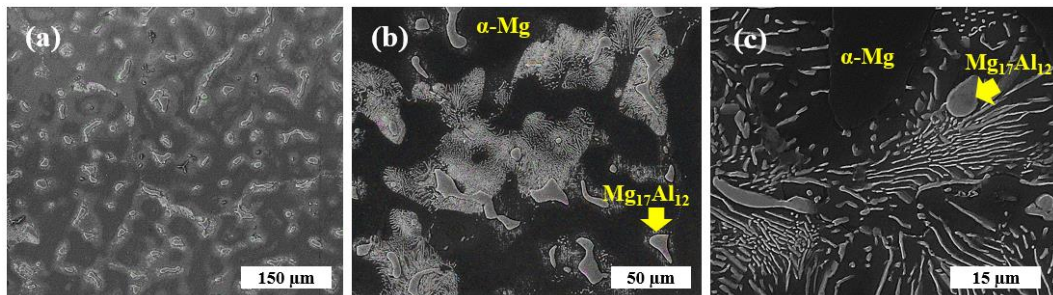


Figure 4.49. The starting microstructure of as-cast AZ91 alloy.

Figure 4.50 presents the microstructure of bulk as-cast WE43 alloy. Intermetallic compounds were randomly distributed around the α -Mg grains. The lamellar type eutectic phase mixture, Figure 4.50(a-b), were detected both on grain boundaries and

at triple junctions. In addition, small white cubic particles with sizes around 2-4 μm , Figure 4.50(c), have been observed to precipitate at the grain boundaries. Table 4.5 shows the EDS analysis results taken from each phases. The white regions in the eutectic mixture contained 4.7 at. % Nd and 4.7 at. % Y and they were identified as $\text{Mg}_{41}\text{Nd}_5$ intermetallic phases by XRD analysis, Figure 4.51(b). On the other hand, the yttrium rich small cubic particles, Table 4.5, were found to be Mg_{24}Y_5 intermetallic phase by XRD analysis, Figure 4.51(b).

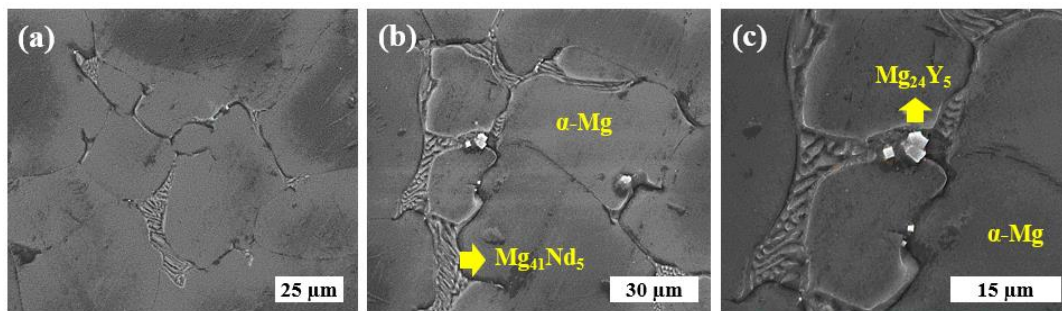


Figure 4.50. The starting microstructure of as-cast WE43 alloy.

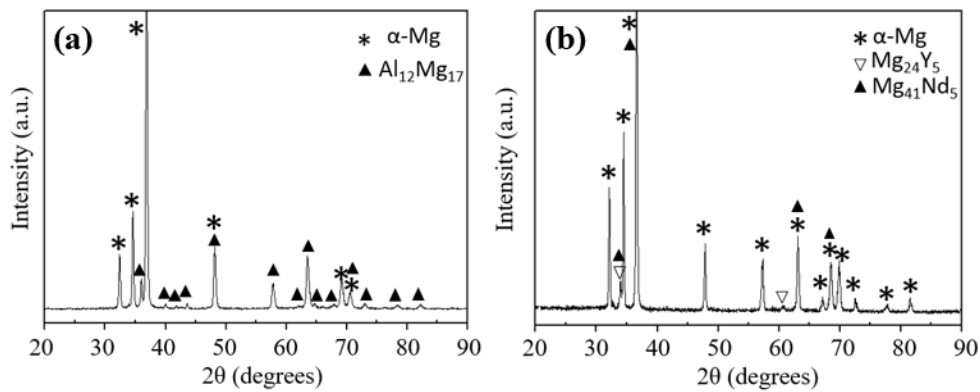


Figure 4.51. XRD results of as-cast (a) AZ91 and (b) WE43 alloys.

Table 4.5 EDS results of various phases in the starting microstructure of as-cast AZ91 and WE43 alloys.

Sample		Elemental composition (at. %)				
		Al	Zn	Nd	Y	Mg
AZ91 Alloy	α -Mg matrix	9.7 \pm 0.2		-	-	balance
	Eutectic mixture	13.8 \pm 2.4		-	-	balance
	Second Phase	40.0 \pm 2.1	1.6 \pm 0.2	-	-	balance
WE43 Alloy	α -Mg matrix	-	-		2.1 \pm 0.6	balance
	Eutectic mixture	-	-	4.7 \pm 0.3	4.7 \pm 0.3	balance
	Cubic phase	-	-	4.6 \pm 0.1	61.4 \pm 8.8	balance

4.3.1.2 Corrosion behaviors

The corrosion behaviors of unalloyed Mg, AZ91, and WE43 alloys have been evaluated by immersion of samples in SBF for short (1-24 hours) and long (1-20 days) immersion times. Corrosion and degradation behaviors of Mg/Mg-alloys have been investigated by various techniques, namely; corrosion product examination, weight loss measurement, hydrogen evolution, potentiodynamic polarization, and electrochemical impedance spectroscopy (EIS) tests. According to results obtained by various tests, corrosion mechanisms were also proposed for each kind of bulk sample.

4.3.1.2.1 Short-term degradation characteristics

In this section, the results of corrosion responses of bulk unalloyed Mg, AZ91, and WE43 alloys have been presented when they are immersed in SBF for 1, 2, 4, 8, and 24 hours. The degradation behaviors of the samples were characterized by

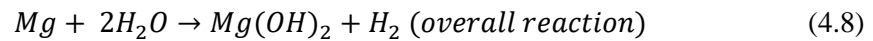
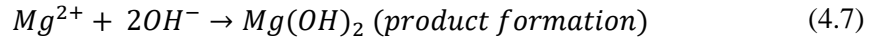
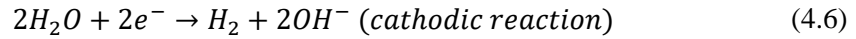
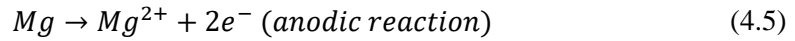
examination of the changes in the microstructure, thickness of corrosion product, ion concentration in the SBF solution, and pH of the electrolyte (SBF).

4.3.1.2.1.1 Microstructural changes

As-cast unalloyed Mg, AZ91, and WE43 alloys samples (Mg/Mg-alloy) have exhibited different interactions and surface morphology changes in the first 24 hours of immersion test. Figure 4.52 shows the surface morphology changes of unalloyed Mg for various times of in-vitro tests. After one hour of immersion, the formation of a small number of craters with a diameter of about 100 μm was detected on the corroded magnesium surfaces in addition to small white particles, Figure 4.52(1h). It was believed that these craters were the gas evolution sites formed after reaction of magnesium with water molecules. Ascencio et al. [61] have found similar holes suggesting the gas evolution sites on the corroded surfaces of WE43 alloy.

It is known that commercially pure magnesium contains impurities such as Fe, Cu, Ni, and also defects like grain boundaries, dislocations, and twins [197]. When magnesium and its alloys are exposed to aqueous environments, micro-galvanic cell forms between the anodic α -Mg matrix and the cathodic impurities or second phases/intermetallics. Magnesium dissolution occurs at the anodic site; at the same time, hydrogen gas evolution takes place at the cathode. The subsequent electrochemical reactions, Eqs. (4.5) and (4.6), are expected to occur at the anodic

and cathodic sites, respectively, and product formation and overall reactions are described according to Eqs. (4.7) and (4.8) [65,74];



In the present study, the corrosion of as-cast unalloyed Mg was attributed to micro galvanic corrosion between α -Mg matrix and impurities found in the starting samples (Fe (0.0176 wt. %), Cu (0.035 wt. %) and Ni (0.35 wt. %), Table 3.2.), while they have not been detected in the microstructural examination. Therefore, craters on the corroded surface, Figure 4.52(1h), were thought to be because of hydrogen gas evolution, implying the presence of cathodic regions in the microstructure.

Figure 4.52(2h) shows the significant changes in the magnesium surfaces after two hours of immersion. The corroded surfaces contained mainly two different regions, namely, cracked corrosion layers and volcano-like structures. Small H₂ gas evolution sites after one-hour immersion converted into volcano-like structures of different sizes, and some parts of them collapsed when samples were kept in SBF for two hours. In the volcano-like structure, corrosion products with 9.9 % Ca, 11.5 % P, 45.3 % O, and 33.3 % Mg (in at. %) accumulated around the central hole. On the other hand, the cracked regions formed after severe corrosion of the α -Mg matrix and contained lower amounts of Ca and P elements, Table 4.6, as expected.

After four hours of immersion, the magnesium surface was corroded drastically, and most of the previously formed volcano-like structure collapsed and replaced with

larger holes, Figure 4.52(4h). At the end of eight hours, the entire surfaces have been observed to be covered with a thick corrosion layer, while some areas were dissolved after 24 hours. XRD analysis, Figure 4.55(a), revealed that the main corrosion product was magnesium hydroxide, $Mg(OH)_2$. Although EDS analysis, Table 4.6, showed the presence of Ca and P elements (with higher contents around the holes in volcano-like structures), they could not be detected by XRD analysis mainly because of their relatively low amounts on the corroded surfaces.

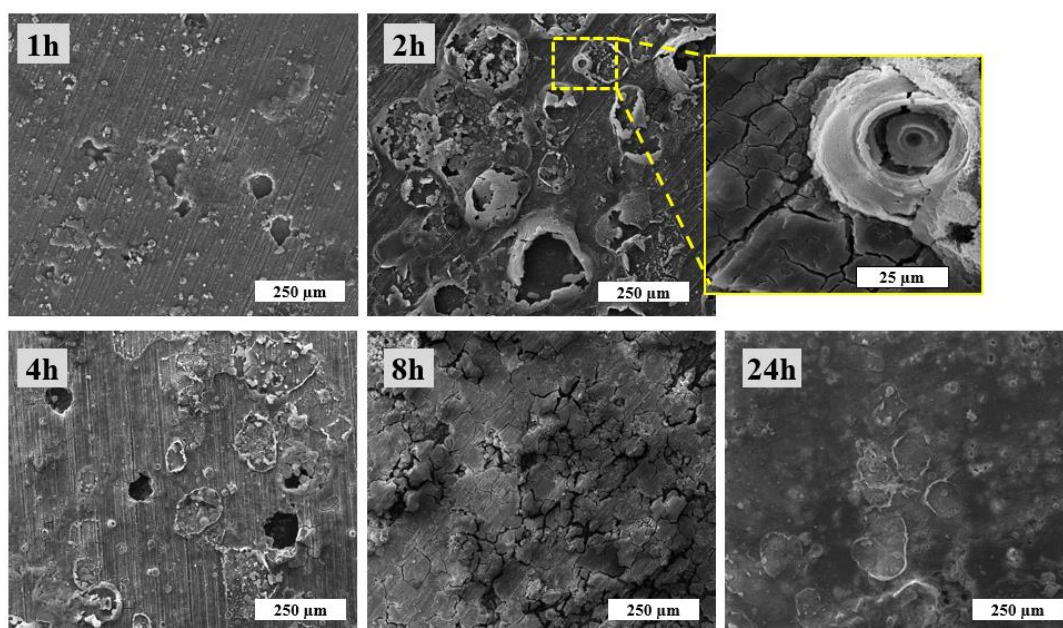


Figure 4.52. Surface morphology change of unalloyed Mg after various immersion time in SBF.

Figure 4.53 presents the surface morphology change of as-cast AZ91 alloy after immersion in SBF. At the initial immersion time, volcano-like structures with different dimensions began to form on the AZ91 alloy's surface. Then, similar to unalloyed magnesium their number increased after two hours of immersion, Figure

4.53 (2h). The formation of volcano-like structures was due to hydrogen gas evolution, which took place at the cathodic $\beta\text{-Mg}_{17}\text{Al}_{12}$ intermetallic sites [72,198,199], which was observed as the gray phase in the starting microstructure of AZ91 alloy, Figure 4.49.

EDS analysis revealed that the chemical composition of the product accumulated around the holes in the volcano-like structures corresponded to 12.8 % Ca, 13.2 % P, 1.9 % Al, 49.7 % O (in at. %) balance with Mg. On the contrary, the corroded area with heavily cracked regions next to the volcano-like structures contained a relatively lower amount of Ca and P elements, Table 4.6, implying that corrosion occurred at the anodic $\alpha\text{-Mg}$ matrix. At the end of the 24 hours, almost all of the volcano-like structures severely collapsed, Figure 4.53(24h) and the corroded surface of AZ91 alloy was covered with a thick corrosion product rich in Ca, P and O, Table 4.6.

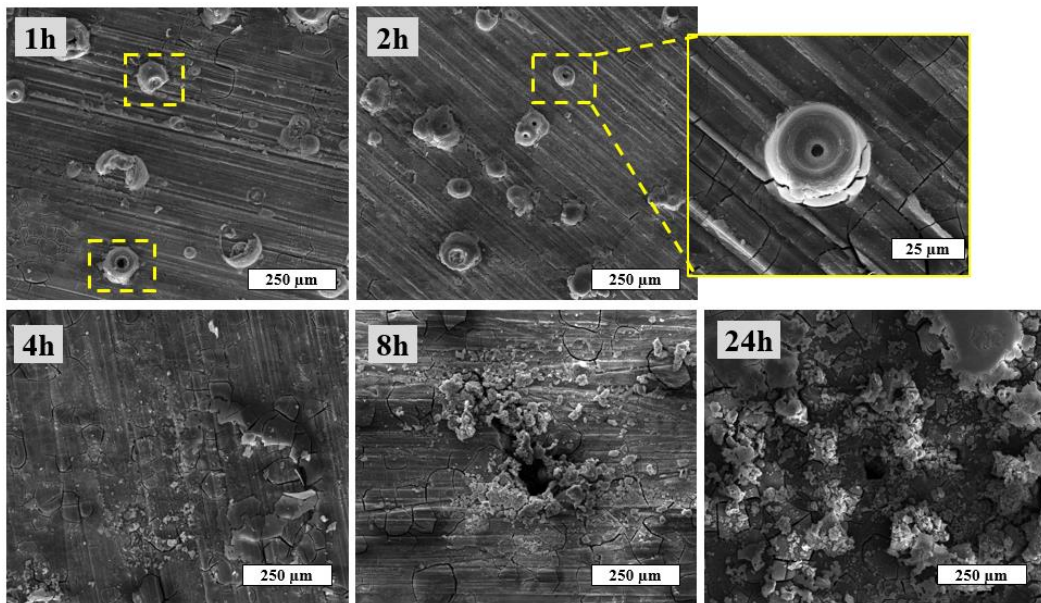


Figure 4.53. Surface morphology change of AZ91 alloy after various immersion time in SBF.

Figure 4.54 displays the SEM images of the degraded surface of WE43 alloy at different time intervals of 24 hours immersion. As expected, volcano-like structures seen around H₂ gas evolution sites started to form at the first immersion time, just like those seen in unalloyed Mg and AZ91 alloy. Subsequently, the number of volcano-like structure increased as corrosion proceeded, Figure 4.54(2h). In addition, the corroded surface was covered with a cracked layer, as observed in unalloyed magnesium and AZ91 alloy. However, at the end of the four hours, the surface was severely damaged with the formation of plenty of cracks so that volcano-like structures could not be detected.

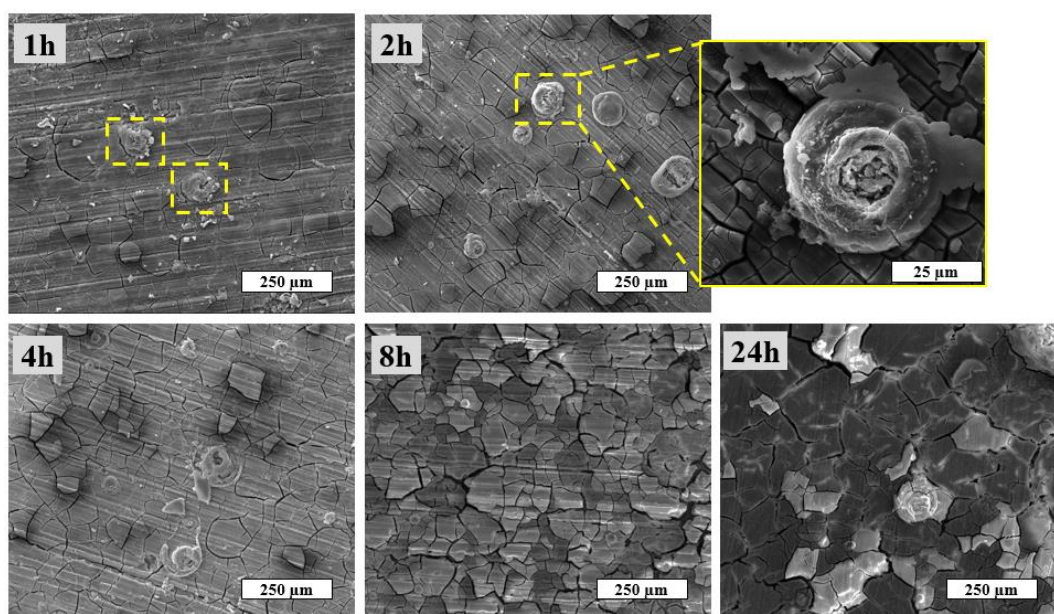


Figure 4.54. Surface morphology change of WE43 alloy after various immersion time in SBF.

Although the corroded cathodic regions of all samples consisted of primarily Mg in addition to alloying elements (Al and Zn elements in AZ91, and Nd and Y elements in WE43 alloy), Ca, P, and O elements were the main constituents of the volcano-

like structure, Table 4.6. While the cracked corrosion layers had Ca/P ratio changing between 0.4-0.9, the volcano-like structure displayed significantly higher Ca contents. In addition, cracks were observed in the corrosion regions because of the dehydration of the surfaces during the drying process.

Besides, $Mg(OH)_2$ was the main corrosion product detected on the surfaces of both unalloyed Mg and WE43 alloy even after four hours of immersion, Figure 4.55(a) and (c). The reason of detection of such phase could be due to the high degradation rate of Mg and WE43 alloy in SBF. On the other hand, XRD analysis of AZ91 alloy did not reveal any corrosion products in the form of $Mg(OH)_2$, Figure 4.55(b), possibly due to relatively thin layer of $Mg(OH)_2$ phase.

Table 4.6 EDS analysis of unalloyed Mg, AZ91, and WE43 alloys after two hours of immersion in SBF.

		Element (at. %)						
Sample	Region	Ca	P	Al	Y	Nd	O	Mg
Mg-2h	Volcano-like	9.9 ± 2.2	11.4 ± 1.7	-	-	-	45.3 ± 2.1	balance
	Cracked region	1.9 ± 0.8	4.9 ± 1.9	-	-	-	27.9 ± 6.4	balance
AZ91-2h	Volcano-like	12.8 ± 0.7	13.2 ± 0.7	1.9 ± 0.4	-	-	49.7 ± 1.0	balance
	Cracked region	1.6 ± 0.3	5.3 ± 1.4	16.0 ± 3.2	-	-	23.7 ± 1.9	balance
WE43-2h	Volcano-like	15.4 ± 2.7	9.7 ± 1.6	-	1.2 ± 0.7	0.1 ± 0.7	29.4 ± 2.0	balance
	Cracked region	2.9 ± 1.2	7.9 ± 1.1	-	2.6 ± 1.3	0.5 ± 0.9	49.7 ± 2.0	balance

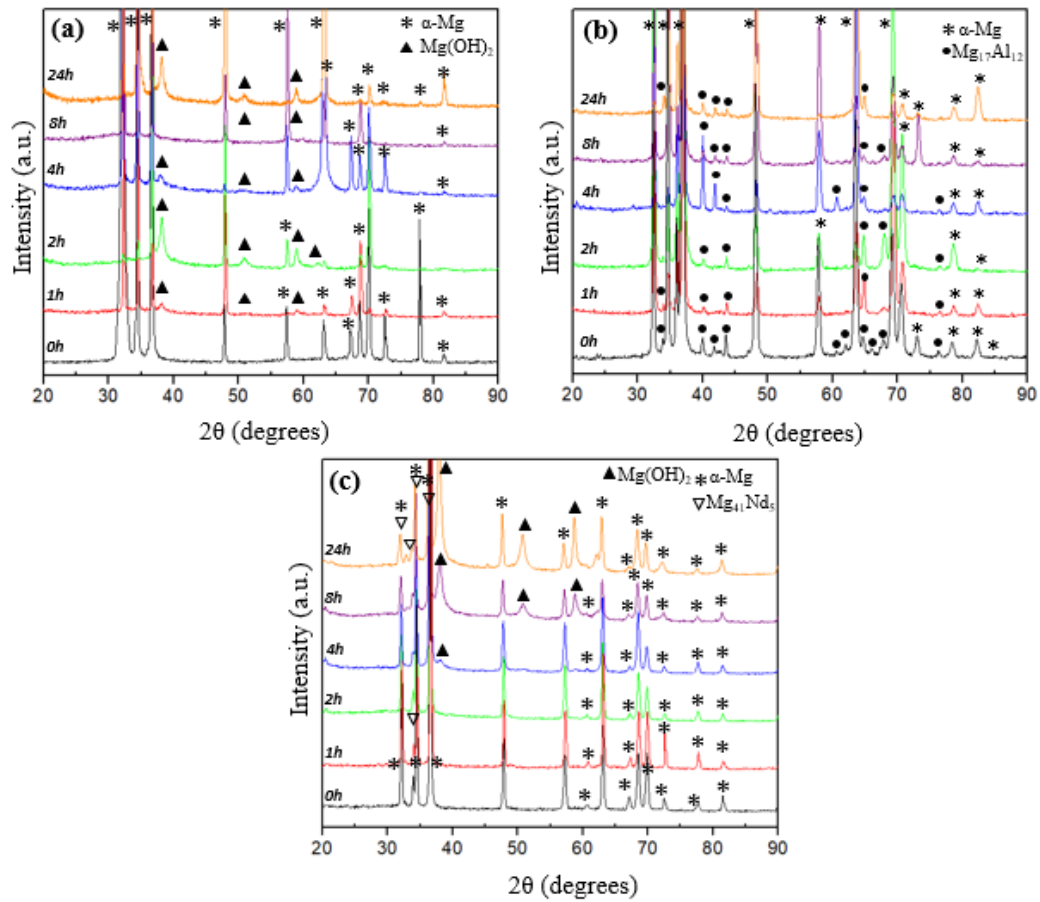


Figure 4.55. XRD results of (a) unalloyed Mg, (b) AZ91, and (c) WE43 alloys after various immersion times. 0h indicates starting as-cast samples.

4.3.1.2.1.2 Cross-sectional examination

Figure 4.56 shows the cross-section of as-polished unalloyed Mg, AZ91, and WE43 alloy surfaces after immersion in SBF for various time. Similar to the microstructural changes, the change in the thickness of the corrosion layers was observed to be different for Mg/Mg-alloys. As expected, increased immersion time resulted in thickening of the corrosion layer. The measured thickness of the corrosion layer was higher for unalloyed Mg so that a higher amount of corrosion products accumulated

on the surface owing to the relatively higher degradation rate of Mg. For instance, the thickness of the corrosion layer reached around 55 μm after 24 h, while it was around 9 μm in the first hour of immersion. Although the initial corrosion layer thickness (around 6.5 μm) in WE43 alloy was lower compared to Mg, it reached approximately 56.5 μm at the end of the immersion experiment, which was close to the measured layer thickness of Mg in the same time interval, Figure 4.56. On the contrary, relatively thinner corrosion layers were observed in AZ91 alloy, possibly due to its lower corrosion rate. For example, the highest thickness of the corrosion layer in AZ91 alloy after 24 h was measured around 34 μm , well below the thickness of the corrosion layer measured for unalloyed Mg and WE43 alloy in the same interval, Figure 4.56.

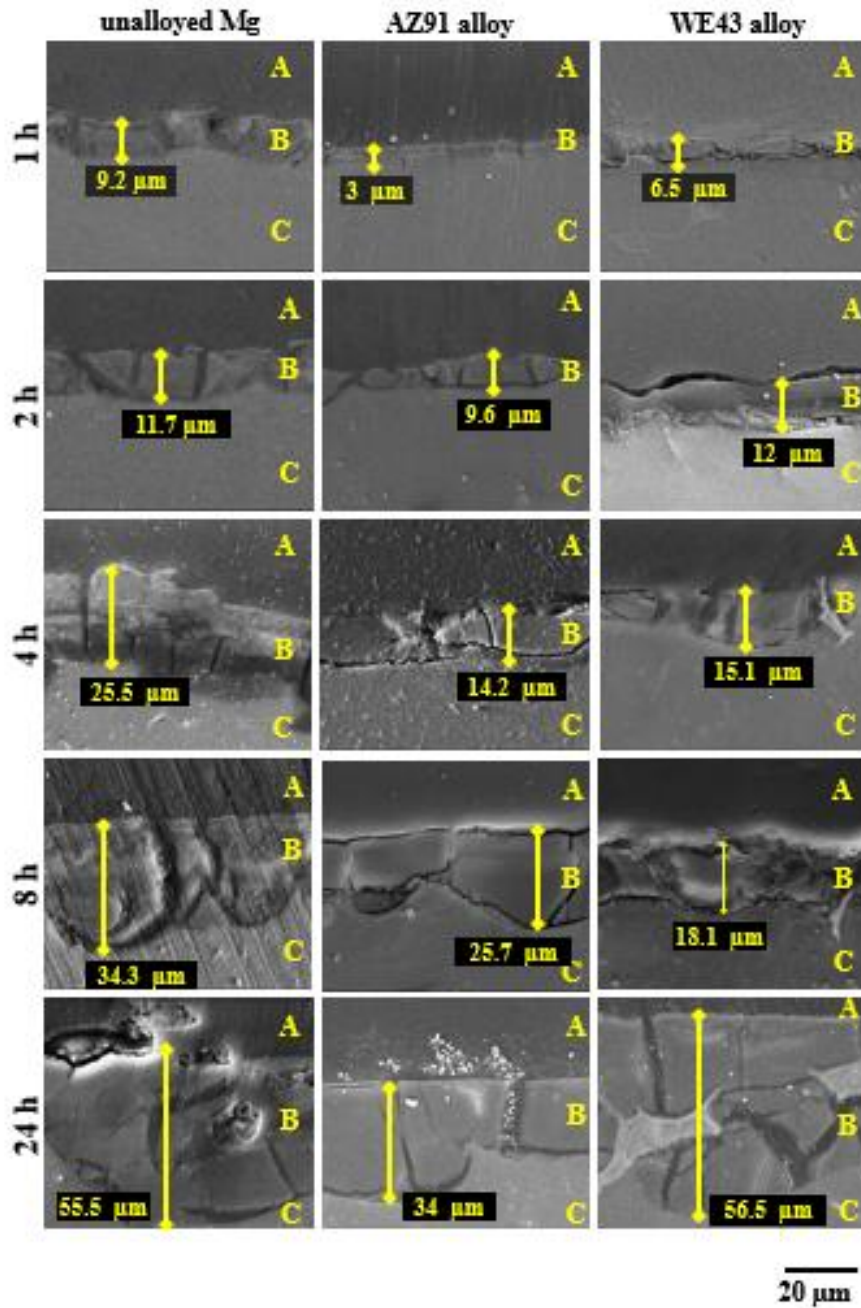


Figure 4.56. Cross-section analysis of Mg/Mg-alloys after various times of immersion. A: Epoxy resin, B: Corrosion layer, C: Mg/Mg-alloys substrate.

4.3.1.2.1.3 Electrolyte analysis and pH change of SBF

Analysis of SBF chemical composition at various stages of in-vitro tests is another effective way to understand the relative corrosion rates of Mg/Mg alloys as well as the precipitation rates of Ca and P elements on the corroded surfaces. Figure 4.57(a-c) shows the variations in the concentrations of Mg, Ca, and P elements after soaking the samples in SBF for 1, 8, and 24 h. As-prepared SBF was reference solution containing an initial concentration of ions presented in Table 3.3 and it was marked as “0”. It is seen that the ion concentration of dissolved magnesium in SBF exhibited a rapid increase in the first hour for all Mg/Mg-alloys samples due to the immediate reaction of magnesium with water molecules. After one hour, the measured Mg ion concentration continued to rise rapidly until eight hours. However, the Mg dissolution rate slowed down, and considerably lower amount of Mg dissolution was observed at the end of 24 hours, Figure 4.57(a-c). The thickening and improvement of protective ability of the $Mg(OH)_2$ corrosion product can cause a decrease in the dissolution rate because $Mg(OH)_2$ layer inhibits the transition of water molecules to the underlying magnesium substrate [61,129,200]. Accordingly, the magnesium dissolution rate was progressively slowed down.

Electrolyte analysis about corrosion of samples was similar to those found in the cross-sectional examination of samples shown in Figure 4.56. For example, according to cross-sectional examination, corrosion thickness was the smallest for the AZ91 alloy displaying the lowest corrosion in the alloy. Likewise, analysis of electrolyte of AZ91 alloy revealed the lowest corrosion with the lowest amount of Mg detected in SBF for each interval of immersion in SBF, Figure 4.57(b). On the other hand, corrosion of unalloyed Mg sample was the highest as observed in cross-sectional examinations and Mg ion concentration in the SBF was the highest throughout the immersion in SBF, Figure 4.57(a). In addition, the measured Mg ion

concentration in the SBF of WE43 alloy, Figure 4.57(c), was between the values measured values of unalloyed Mg and AZ91 alloy samples as expected.

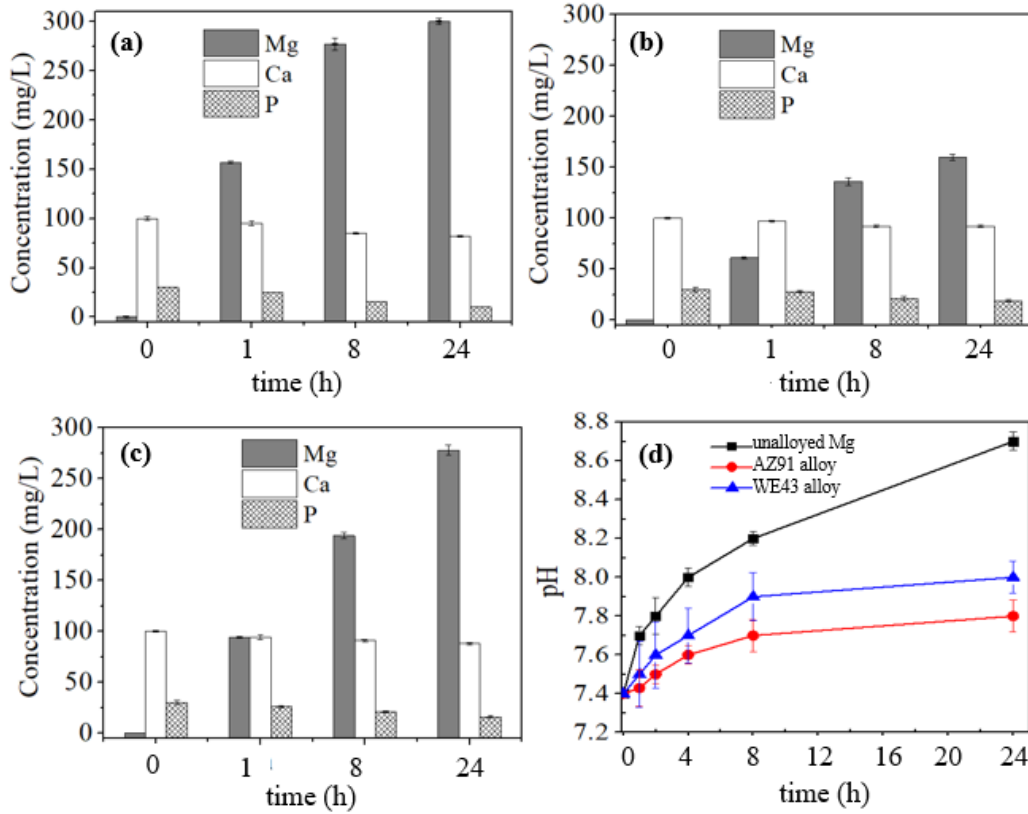


Figure 4.57. ICP-OES analysis of SBF solution for (a) unalloyed Mg, (b) AZ91, and (c) WE43 alloys after 1, 8, and 24 h, and (d) change in pH of the SBF solution during first 24 h.

In contrast to Mg ion concentration, the variation of Ca and P ions in SBF exhibited a gradual decrease for all of the magnesium samples, Figure 4.57(a-c). As the Ca and P rich phases precipitated on the corrosion layers, Figure 4.56, their concentrations in SBF drastically decreased, Figure 4.57(a-c). Ascencio et al. [61] found similar

results and stated that increasing soaking time resulted in reducing the ion concentration of Ca and P in SBF due to the accumulation of an insoluble Ca and P rich protective layer on the substrate surfaces. In the solution of unalloyed Mg, Figure 4.57(a), there was about 14% and 60% change in the concentration of Ca and P ions, respectively. Although small changes were detected in the concentration of Ca ion of AZ91 and WE43 alloy (approximately 5 %), Figure 4.57(b-c), there was an observable change in the phosphate concentration, which was 32% and 38% for both AZ91 and WE43 alloy, respectively.

The monitoring of the pH variation gives also information about corrosion and may be used for supporting the results of ion concentration measurements as well as the examination of the corrosion layer. Figure 4.57(d) displays the variation of pH of the SBF solution during the in-vitro test up to 24 h. During the first two hours, there was an increase in the pH values of SBF containing different samples, while the accelerated increase was observed for unalloyed magnesium. In magnesium and magnesium alloys, as a result of the immediate reaction of magnesium with aqueous SBF solution, the hydrogen gas evolution occurs at the cathodic sites by water reduction, as stated in Eq. (4.6) so that the release of hydroxide, OH^- , ions can cause an increase in the solution pH.

The rate of increase in pH value diminished after two hours, Figure 4.57(d), which was the indication of change in the dissolution rate of magnesium and its alloys. It is known that anodic and cathodic reactions, Eqs. (4.5) and (4.6) can cause the formation of protective $\text{Mg}(\text{OH})_2$ film on the substrate surface. Therefore, magnesium ions release rate decrease and the solution pH increase rate diminishes [16]. At the end of the immersion experiments, the solution pH of unalloyed magnesium increased from 7.4 to 8.7. However, the pH values remained at lower levels of 8.0 and 7.8 for AZ91 and WE43 alloys, respectively. Additionally, the pH values of both AZ91 and WE43 alloys increased at a comparatively lower rate than

that of unalloyed Mg because of the relatively lower degradation rate of magnesium alloys.

4.3.1.2.2 Long-term degradation characteristics

This part presents the results of long-term immersion tests, which were conducted to understand the corrosion mechanism of bulk Mg/Mg-alloy samples. Also, the corrosion rate of Mg/Mg-alloys has been compared extensively by weight loss measurement, hydrogen (H₂) gas evolution, and potentiodynamic polarization test, as well as the EIS test.

4.3.1.2.2.1 Macro-structural change

Figure 4.58 shows the corroded surfaces of unalloyed Mg, AZ91, and WE43 alloys after immersion in SBF for various times (1-20 days). Whitish corrosion products accumulated on the corroded surfaces, especially in unalloyed Mg and WE43 alloys, even after one day of immersion. According to XRD results, Figure 4.59(a) and (c), these white corrosion products were identified as magnesium hydroxide, Mg(OH)₂, which was considerably thick and were able to be observed by naked eye. On the other hand, relatively thinner dark grey corrosion layers were detected on the AZ91 alloy's surfaces, Figure 4.58(b). XRD analysis revealed that the main corrosion product was the calcium carbonate phase, CaCO₃, formed by the precipitation of Ca and O ions on AZ91 alloy surfaces, Figure 4.59(b). Moreover, Ascencio et al. [61] stated that the formation of the carbonate phase on the magnesium surfaces improves the passivation and inhibits the further corrosion of magnesium alloys. Therefore, the relatively higher corrosion resistance of AZ91 alloy can be explained by the formation of CaCO₃ layer on its surface. Besides, corrosion pits initially began to form at the edge of the AZ91 alloy's surfaces, Figure 4.58, but they homogeneously

distributed on the surface at the end of the experiment in the form of shallow groves in contrast to other samples in which severe pits were observed.

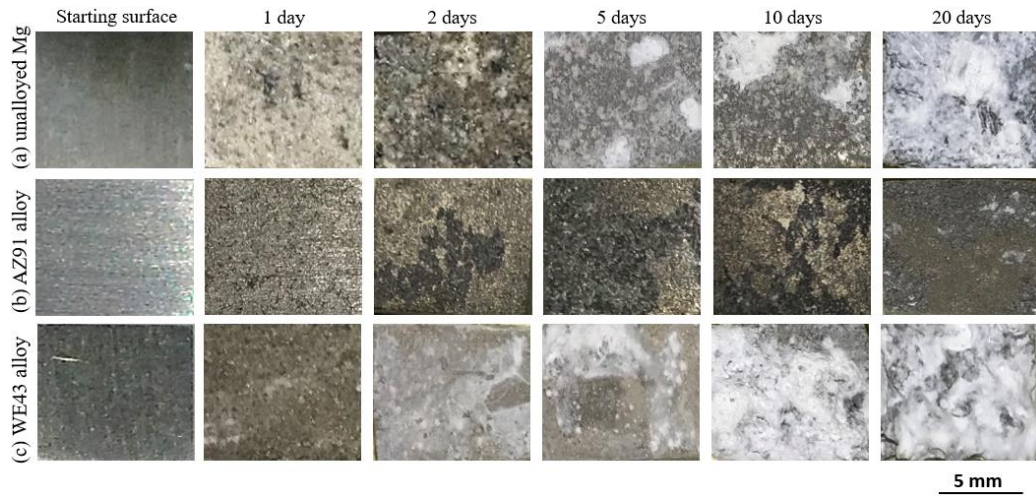


Figure 4.58. Macro images of the corroded surfaces of Mg/Mg-alloys after different time intervals in SBF.

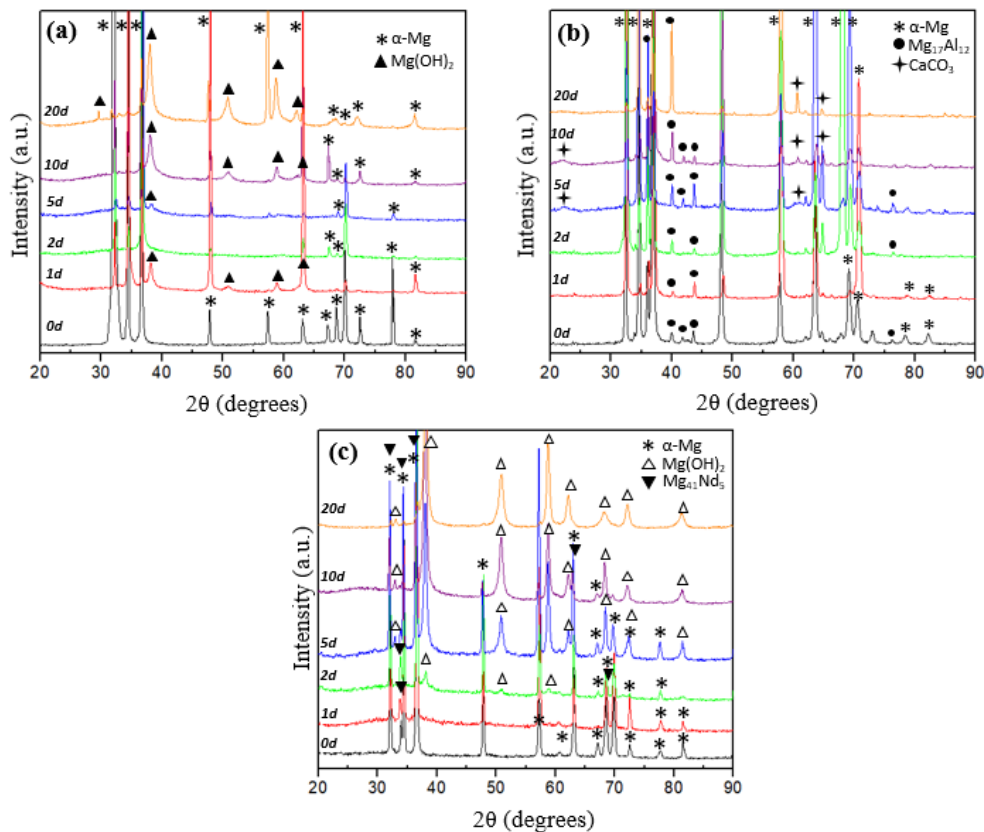


Figure 4.59. XRD results of (a) unalloyed Mg, (b) AZ91, and (c) WE43 alloys after various time intervals in SBF. 0d indicates the XRD of uncorroded as-cast samples.

Figure 4.60 shows the macro-structural change of the sample surfaces after removing the corrosion products by use of CrO₃ solution to see the extent of corrosion clearly. Corrosion started to form especially at the edges and corners of the unalloyed Mg and AZ91 alloy after two days of immersion, while uniform corrosion was detected on the surface of WE43 alloy in the same time interval. However, severe corrosion initiated at the surface of WE43 alloy after five days with the formation of deep pits. Then, localized corrosion caused the growth of the deeper pits within ten days so that WE43 alloy did not preserve its starting rectangular shape, Figure 4.60.

Shallow corrosion pits were distributed homogeneously throughout the surface of the AZ91 alloy; therefore, localized corrosion was not as severe as seen in WE43 alloy. Although a similar tendency was detected in unalloyed magnesium, like AZ91 alloy, considerable shape change was observed after twenty days, possibly because of relatively higher localized corrosion in some regions compared to AZ91 alloy.



Figure 4.60. Macro-structural changes of Mg/Mg-alloys after immersion in SBF.

4.3.1.2.2 Microgalvanic effect

After investigation of corrosion products formed on the magnesium surfaces for long-term in-vitro experiments, backscattered electron (BSE) SEM images have been taken to reveal the effect of micro-galvanic corrosion. Before inspecting the surfaces, the corrosion products on the surfaces were cleaned with CrO_3 solution.

Figure 4.61 displays the representative BSE images of Mg/Mg-alloys' surfaces after immersion in SBF for two days. The surface of unalloyed magnesium, had randomly

distributed deep corrosion pits, Figure 4.61(a) and (d). It is known that Mg and Mg alloys exhibit micro galvanic corrosion due to the presence of cathodic centers (impurities or second phases), which are less active than anodic magnesium matrix [201]. For magnesium, cathodic sites are thought to be the regions rich in impurity elements (Fe, Cu, and Ni). In the present study, on the other hand, no preferential corrosion was observed either along grain boundaries or inside the grains of unalloyed magnesium. However, ICP-OES spectroscopy measurements, Table 3.2, revealed that unalloyed Mg contained about 0.0176 % Fe, 0.0356 % Cu, and 0.072 % Ni (in wt. %). While Cu concentration was in the acceptable range, as stated in [202], the amount of Fe and Ni was higher than the critical levels above which degradation rate of magnesium was expected to increase gradually due to micro galvanic effect.

On the other hand, magnesium alloy samples displayed different corrosion characteristics, probably due to the existence of the intermetallic and secondary phases. Figure 4.61(b) shows the corroded AZ91 alloy surfaces. In the starting microstructure of AZ91 alloy, Figure 4.49, β -Mg₁₇Al₁₂ intermetallics had interconnected network structure and homogeneously distributed throughout the microstructure. Also, the amount of intermetallics was higher than that of the α -Mg matrix. Song et al. [65] found that the micro galvanic corrosion takes place between anodic α -matrix and cathodic β -Mg₁₇Al₁₂ intermetallics in AZ91 alloys because of the electrochemical potential differences between two phases. When the amount of β -Mg₁₇Al₁₂ intermetallics having a uniform distribution is higher than that of α -Mg matrix, preferential corrosion attack starts at α -Mg matrix close to intermetallics for AZ91 alloy [67,203]. Likewise, in the present study, subsequent immersion in SBF caused the preferential dissolution of α -Mg close to intermetallics so that cathodic β -Mg₁₇Al₁₂ intermetallics (indicated by yellow arrows in Figure 4.61(b) and (e)) remained in the microstructure.

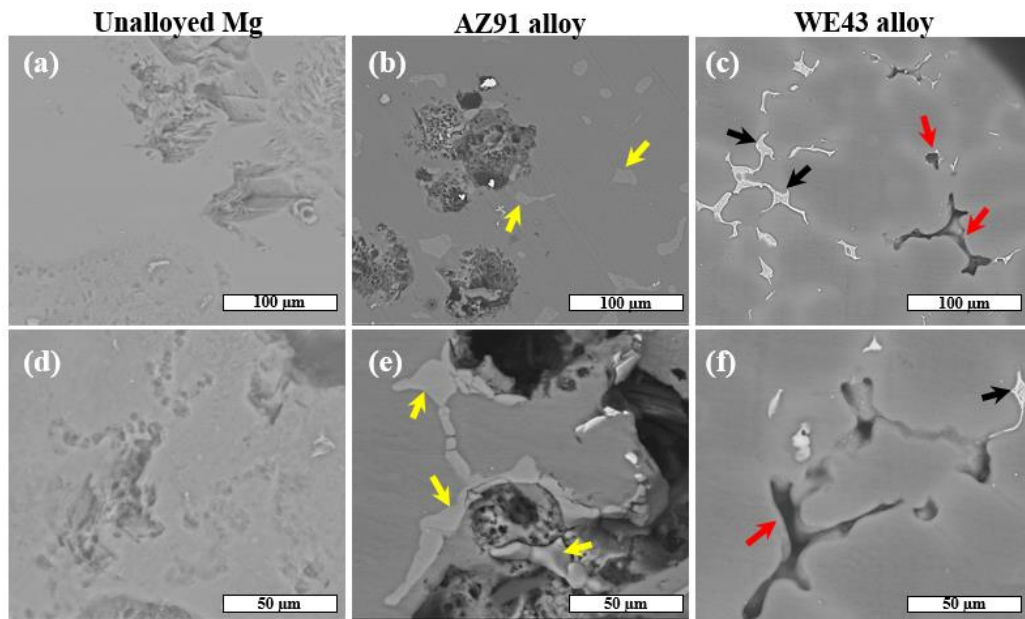


Figure 4.61. BSE images of (a–d) unalloyed Mg, (b–e) AZ91 and (c–f) WE43 alloys after two days of immersion.

After immersion of WE43 alloy for two days, some Nd and Y-rich intermetallics, Table 4.7, shown by black arrows, fell out by the corrosion of the anodic α -Mg matrix (red arrows, Figure 4.61(c-f)). According to the particle undermining model [65], the cathodic secondary phases are expected to fall out (undermine) by the corrosion of nearby anodic Mg matrix due to their non-uniform distribution as well as their relatively lower amount in the microstructure [72,199]. Therefore, in the present study, the degradation rate of WE43 alloy was expected to be affected by the undermining of secondary phase particles. As a result, the corrosion rate of WE43 alloy drastically increased due to the undermining of the Nd and Y rich intermetallic phases.

Table 4.7 EDS analysis of the regions shown by yellow, black, and red arrows in Figure 4.61.

Sample	Investigated region	Element (at. %)			
		Al	Nd	Y	Mg
AZ91 alloy	Yellow arrow	37.9 ± 1.3	-	-	60.7 ± 1.4
WE43 alloy	Black arrow	-	4.8 ± 0.4	3.4 ± 0.6	91.7 ± 0.5
	Red arrow	-	3.7 ± 1.6	1.7 ± 0.5	95.4 ± 2.8

It is stated that the improved corrosion resistance of AZ91 alloy is explained by the electrochemically passive intermetallic network layer. Intermetallic compounds, like $Mg_{17}Al_{12}$, are continuously formed at the grain boundary in as-cast condition, which turn out to be a barrier against corrosion and propagation of corrosion pits [204]. Similarly, in the present study, homogenous distribution and network layer of $Mg_{17}Al_{12}$ intermetallics acted as passive precipitates. They remained in the microstructure corrosion proceeded by preferential dissolution of α -Mg matrix. Therefore, their relative amount stayed nearly constant in the microstructure during the in-vitro test, Figure 4.62.

Nakatsugawa et al. [204] stated that RE-containing magnesium alloys exhibited relatively good corrosion resistance because of the formation of less cathodic intermetallics such as $Mg_{12}Nd$, $Mg_{24}Y_5$, or $Mg_{12}NdY$. In the study of Narayanan [205], they found that the formation of continuous network of passive $Mg_{41}Nd_5$ intermetallic at grain boundaries was responsible for the improved corrosion behavior of rare-earth containing magnesium alloy [205]. Also, Song et al. [206] stated that the formation of stable and passive intermetallics results in noble corrosion potential and higher corrosion resistance. On the other hand, Ambat et al. [207] believed that when the interparticle distance between the second phases is very high, undermining of β - $Mg_{17}Al_{12}$ phases caused an increase in the corrosion rate of ingot cast AZ91 alloy. Similarly, in the present study, although, $Mg_{41}Nd_5$, and

Mg₂₄Y₅ intermetallics found at the grain boundaries were passive, inhomogeneous and discontinuous distribution cause falling out of intermetallics from the corroded surface. Additionally, quantitative analysis of second phases showed that the undermining of intermetallics from the corroded surface caused decrease in the quantity of intermetallic phase during in-vitro test, Figure 4.62. Therefore, corrosion rate of WE43 alloy increased. Zucchi et al. [208] also observed undermining of the second phases by preferential dissolution of α -Mg matrix in WE43 alloy which was immersed in concentrated NaCl solution.

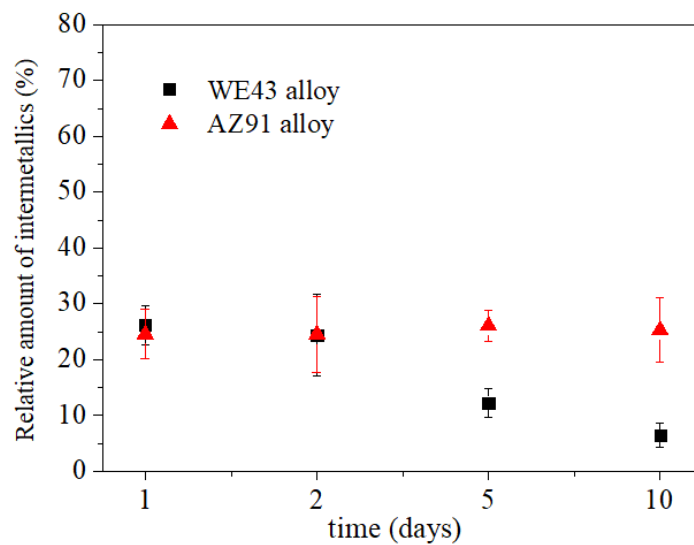


Figure 4.62. Relative amount of the intermetallics in the AZ91 and WE43 alloys during in-vitro test.

Although the high corrosion rate of the as-cast magnesium alloy was attributed to micro galvanic corrosion between intermetallics and α -Mg matrix, heat treatment also alters the corrosion rate of magnesium alloys. For example, the ageing heat treatment decreases the corrosion resistance of AZ91 alloy because of the precipitation of β phase with the ageing, which intensifies the micro galvanic effect

[209]. On the other hand, solutionizing heat treatment leads to the dissolution and redistribution of intermetallics in the α -Mg matrix, so the corrosion resistance of the alloy is increased [210]. Guo et al. [209] found that homogenization treatment improves the corrosion resistance of the AZ91D alloy. Also, Chu et al. [211] stated that solution-treated RE containing magnesium alloy exhibited lower degradation rate compared to that of as-cast WE43 alloy.

4.3.1.2.2.3 Weight loss measurement

After microstructural characterization of the corroded surface, it was seen that each sample displayed different corrosion characteristics in SBF due to different chemical compositions and microstructure. Because of the formation of the pits, corrosion was not homogenous in the samples.

Figure 4.63(a) shows the time-dependent change of weight loss percentage of the Mg/Mg-alloys after the removal of the corrosion products by CrO_3 solution. Both unalloyed Mg and AZ91 alloy displayed nearly similar corrosion behaviour, where a steady-state increase was detected in weight loss during the experiment. However, AZ91 alloy exhibited relatively lower weight loss throughout the test, Figure 4.60. Although the weight loss percentage of WE43 alloy exhibited a similar continuous increase similar to unalloyed magnesium and AZ91 alloy within two days, it displayed a sudden increase in weight loss percentage after five days, Figure 4.63(a). The observed sharp change was attributed to the undermining of intermetallics, Figure 4.61(c), and (f), which resulted in a rapid decrease in the weight of the samples due to the loss of intermetallic particles. Besides, the nonhomogeneous distribution of relatively larger pits at both edges and corners, Figure 4.60, was another reason for the sudden increase in the weight loss percentage of WE43 alloy, Figure 4.63(a).

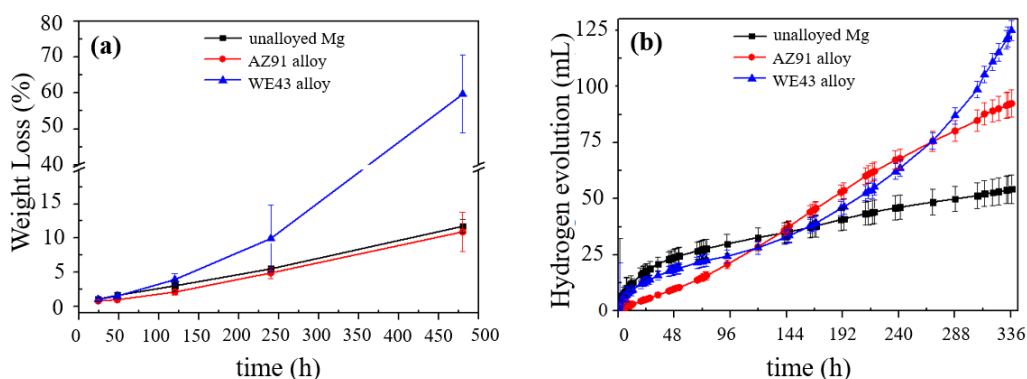


Figure 4.63. (a) Weight loss percentage and (b) cumulative hydrogen gas produced during the in-vitro test in SBF.

4.3.1.2.2.4 Hydrogen evolution

The quantity of H_2 gas produced was utilized to compare the corrosion rates of Mg/Mg-alloys because hydrogen gas is a corrosion by-product of the cathodic reaction, Eq. (4.6). Figure 4.63(b) showed that each magnesium samples exhibited different hydrogen evolution rates (HER) at different time intervals of the SBF test. For unalloyed magnesium, initially, hydrogen evolution increased rapidly, which subsequently became sluggish at the end of ten days (240 hours). On the other hand, three different regions were detected in the HER of AZ91 alloy, Figure 4.63(b). Until around 90 hours, hydrogen production decreased continuously after an initial small increase, possibly because of the formation of a protective layer. However, the HER increased at the end of the nine days of immersion. The main reason was thought to be the partial loss in the protectiveness of the surface and penetration of water molecules to the magnesium surface, causing the evolution of hydrogen gas. In the remaining period of the experiment, HER again slowed down. Because the protective corrosion layer, $Mg(OH)_2$, started to thicken at the initial stages of corrosion and did not permit additional water access into the surface layer as immersion time increases. In the final stage, HER continued to decrease because of the reduction of corrosion

rate. It was also believed that the additional calcium carbonate in the later stages, Figure 4.59(b), hindered the further corrosion of the AZ91 alloy's surface.

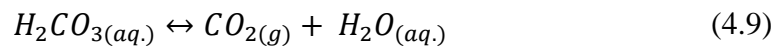
On the other hand, different hydrogen evolution regions were observed in WE43 alloy. Until 96 h (four days), just like unalloyed magnesium, the HER decreased after an initial instant increase; however, a lower amount of hydrogen was generated compared to Mg within the same period. In contrast to other samples, the first region in WE43 alloy was followed by a sudden exponential rise in the HER after five days. Therefore, the corrosion rate increased rapidly, which was also seen in weight loss tests, Figure 4.63(a). In addition, macro-structural examination revealed sudden pit growth at the end of the five days, Figure 4.60. Similarly, Ascencio et al. [59] stated that increasing pit formation leads to a higher amount of gas evolution from the surface. Also, Song et al. [212] noted that breaking of protective $Mg(OH)_2$ film due to pit formation caused the increase in corrosion rate together with more hydrogen gas evolution. Therefore, it can be concluded that WE43 alloy exhibited the highest corrosion rate compared to investigated Mg and Mg alloys.

4.3.1.2.2.5 pH change of SBF solution

Figure 4.64 shows the pH variations of the SBF solution during the in-vitro test conducted for 20 days. In order to stabilize the ion concentration, SBF was refreshed every three days, indicated with the arrows on the graph. With the beginning of the in-vitro tests, the pH of the solutions increased continuously and reached their maximum values of 9.5 (for AZ91 alloy) and 10.5 (for unalloyed Mg and WE43 alloys) at the end of the four days and remained nearly constant for the remaining period. The results obtained from pH change of AZ91 alloy solution were compatible with results obtained from hydrogen evolution results. The hydrogen evolution rate in AZ91 alloy was reduced till three days after an initial increase, and subsequently, the evolution rate increased for the remaining days implying a decrease and an

increase in the corrosion rates for the first three days and remaining period, respectively.

Likewise, pH measurements of the AZ91 alloy solution displayed a constant pH around 8.5 till three days after the initial increase in the first 24 h, which was followed by a sudden increase of pH up to 9.5 in the remaining period. The pH change of unalloyed Mg and WE43 alloy was also compatible with the hydrogen evolution results such that pH values increased up to their maximum values in a shorter time like the evolution of a higher amount of hydrogen in a short time for both samples. The sudden increase of the pH was explained by the generation of the alkaline environment owing to hydroxyl ions, Eq. (4.6) [59,61,129]. Another reason for the immediate increase was the creation of insoluble precipitates containing Ca, P, and O elements on the surface of the Mg and Mg-alloys and subsequent consumption of the elements in the solution, Figure 4.57(a-c). Moreover, it is believed that a reduction in the concentration of carbonate species in SBF, can also cause pH increase because of the release of CO₂ to the atmosphere, Eq. (4.9) [59]. As a result, the combined effect of magnesium corrosion reactions and CO₂ release caused the increase in pH of the solution. For the remaining period of in vitro tests, the pH of all SBF solutions was stabilized around 9.6, Figure 4.64.



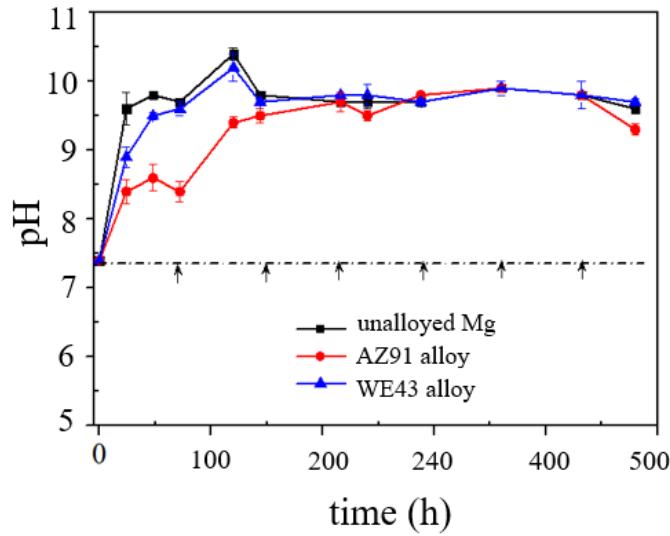


Figure 4.64. pH change measurement of Mg/Mg-alloys during the in-vitro test in SBF.

Moreover, the fluctuation of the pH of the solution was affected by the refreshment of SBF. For instance, the pH was quickly decreased to 7.4 (not shown in Figure 4.64) and then gradually increased until the following renewal time. The decrease in pH of the solution caused the partial dissolution of the $Mg(OH)_2$ corrosion layer, according to Eq. (4.10) [59]. Although the corrosion layer's protective ability was lessened at each refreshment time due to the partial dissolution of the hydroxide layer, the corrosion layer thickness again increased until the next renewal time.

$$\log[Mg^{2+}] = 16.95 - 2pH \quad (4.10)$$

4.3.1.2.3 Electrochemical tests

The potentiodynamic polarization and EIS tests have been conducted so as to obtain a quantitative analysis of the corrosion rates.

4.3.1.2.3.1 Potentiodynamic polarization test

Figure 4.65 presents the electrochemical polarization curves of unalloyed Mg, AZ91, and WE43 alloys. The corrosion potential (E_{corr}) and the corrosion current density (i_{corr}) values of each sample were obtained by the Tafel extrapolation method, Table 4.8. Corrosion rates (CR) of bulk alloy samples were determined according to ASTM G102 standard, Eq. (3.3) [183].

The polarization curves of the Mg/Mg-alloys showed different behaviors. In contrast to alloys, unalloyed Mg exhibited passivation characteristics in the anodic branch due to formation of the $\text{Mg}(\text{OH})_2$ on the surface, Figure 4.59(a). However, AZ91 alloy possessed lower i_{corr} value compared to unalloyed Mg, Table 4.8. Because, the addition of Al and Zn alloying elements improved the corrosion resistance of magnesium by shifting the corrosion current density to lower i_{corr} direction, Figure 4.65. In addition, homogenous distribution and relatively higher amount of β - $\text{Mg}_{17}\text{Al}_{12}$ intermetallics compared to the α -Mg matrix in AZ91 alloy inhibited further dissolution by acting as a corrosion barrier as observed in the previous studies conducted on AZ91 alloys [62,129]. However, the WE43 alloy possessed the highest i_{corr} value because micro galvanic corrosion accelerated the dissolution of the alloy in SBF, Table 4.8. As a result, AZ91 alloy displayed the highest corrosion resistance in SBF; while, the corrosion rate of WE43 alloy was higher than that of unalloyed Mg. The results obtained by the electrochemical polarization curve were in agreement with that of weight loss and H_2 evolution experiments, where WE43 alloy displayed accelerated corrosion after a certain time, and its corrosion rate was the highest among the bulk samples.

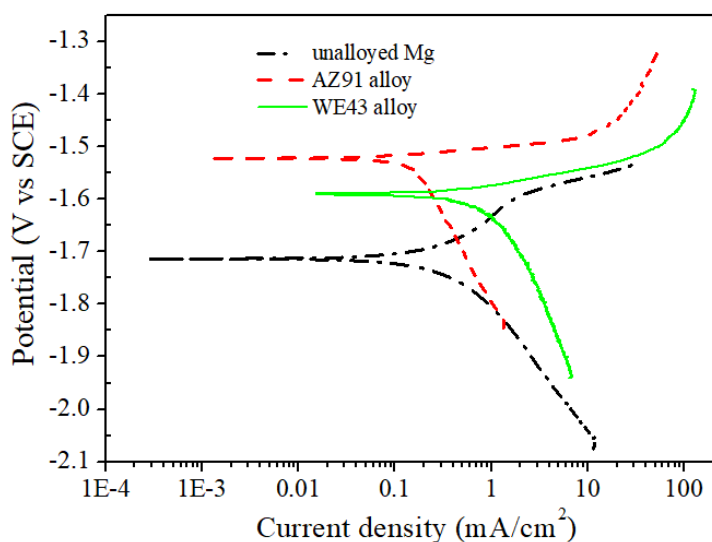


Figure 4.65. Polarization curves of as-cast unalloyed Mg, AZ91 and WE43 alloys in SBF at 37 °C.

Table 4.8 Corrosion parameters measured from polarization curves of Mg/Mg alloys.

Sample	E_{corr} (V vs SCE)	i_{corr} ($\mu\text{A}/\text{cm}^2$)	CR (mm/year)
Unalloyed Mg	-1.71	0.35	7.91
AZ91 alloy	-1.52	0.13	2.72
WE43 alloy	-1.59	0.77	17.61

4.3.1.2.3.2 Electrochemical Impedance Spectroscopy (EIS) test

Figure 4.66 presents the Nyquist diagram of Mg/Mg-alloys in SBF after 1, 2, and 4 hours. All of the Nyquist plots belonging to unalloyed Mg, AZ91, and WE43 alloy had a similar behavior that was characterized by two well-defined loops with two-

time constants. Figure 4.66(d) shows an equivalent circuit, $R_s(CPE_1R_1)(CPE_2R_2)$, obtained by Nyquist plots. In this circuit, R_s represents the solution resistance, R_1 and R_2 are the charge transfer resistance and resistance of the corrosion product layer, respectively. In addition, CPE_1 and CPE_2 are constant phase elements.

The first time constant (CPE_1R_1) at the high-frequency loop was associated with the charge transfer resistance at the interface of magnesium substrate and electrolyte. On the other hand, the second time constant (CPE_2R_2) at intermediate frequency was relevant to the diffusion of Mg^{2+} species through the corrosion layer. Wu et al. [213] also stated two-time constants for Mg-3Nd-0.2Zn-0.4Zr after subjecting to SBF at various time intervals. In the study of Jamesh et al. [62], they reported two-time constants for WE43 alloy as well when soaked in Ringer's solution and SBF.

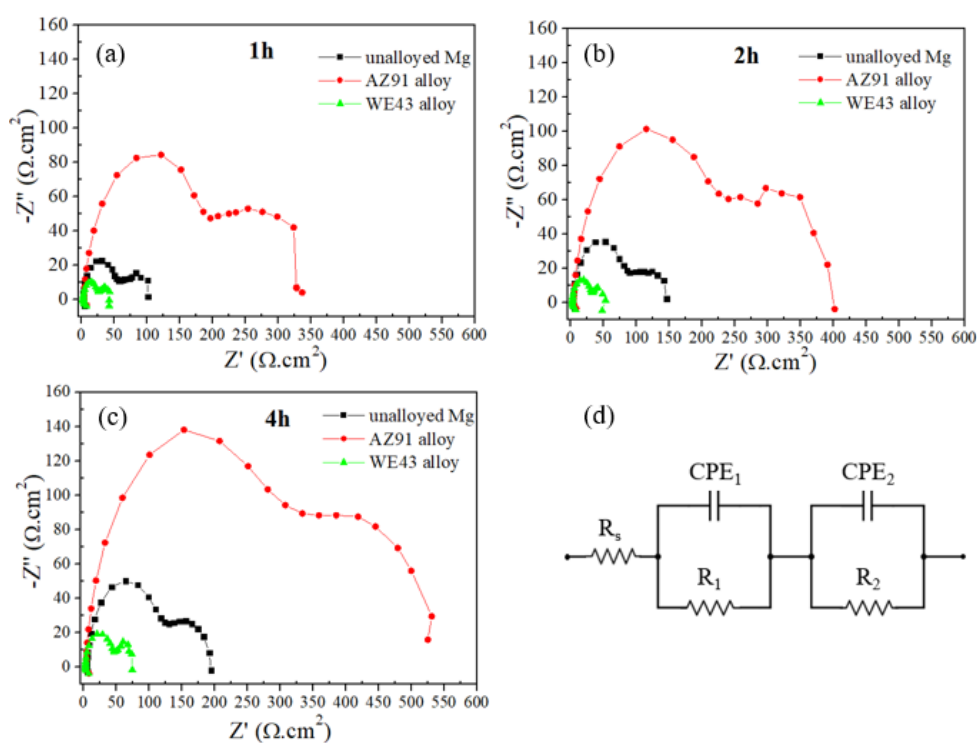


Figure 4.66. Nyquist diagrams of Mg/Mg-alloys for (a) 1, (b) 2, and (c) 4 h, and (d) equivalent circuit for EIS data fitting.

The diameter and shape of the semicircles provide information about the corrosion mechanism of magnesium. If the semicircles have similar characteristics, corrosion mechanisms of the samples are assumed to be the same. On the other hand, the diameter of the loop gives information about the corrosion rate of the samples [62,122,200]. Therefore, in the current study, all Mg/Mg-alloys exhibited the same corrosion mechanisms but different corrosion rates. WE43 alloy had the smallest loop diameter, while the largest loop diameter belonged to the AZ91 alloy, Figure 4.66. Therefore, corrosion resistance, in the decreasing order, was found to be as AZ91 alloy, unalloyed Mg, and WE43 alloy.

Table 4.9 presents the various EIS parameters derived by curve fitting method. The R_1 value of AZ91 alloy was the highest compared to those of found for unalloyed Mg and WE43 alloy. Thus, AZ91 alloy exhibited the highest corrosion resistance among the investigated Mg samples. On the other hand, a larger R_2 value represents the formation of more compact corrosion products [200]. R_2 of WE43 alloy was the highest among all samples because corrosion film on WE43 alloy had less ability to protect the alloy further from corrosion. As a result, EIS experiments were also agreement with immersion experiments (hydrogen evolution, weight loss, and pH tests) and the potentiodynamic polarization tests by presenting similar conclusions about the corrosion rates of the samples.

Table 4.9 Fitting parameters of Mg/Mg-alloys in SBF for after 1, 2, and 4 h.

Sample	time (h)	R_s ($\Omega \text{ cm}^2$)	R_1 ($\Omega \text{ cm}^2$)	CPE_1 ($F \text{ cm}^{-2}$)	n_1	R_2 ($\Omega \text{ cm}^2$)	CPE_2 ($F \text{ cm}^{-2}$)	n_2
unalloyed Mg	1	7.83	151.34	1.28E-03	0.75	156.55	5.21E-06	1.02
	2	9.68	203.67	1.04E-03	0.75	255.08	7.69E-06	0.95
	4	14.66	255.14	7.66E-04	0.78	370.07	8.19E-06	0.92
AZ91 alloy	1	13.80	584.50	2.66E-06	0.97	469.94	2.07E-04	0.86
	2	15.93	694.72	3.40E-06	0.96	550.10	1.91E-04	0.87
	4	12.47	912.15	3.76E-06	0.96	784.23	1.74E-04	0.85
WE43 alloy	1	8.76	71.51	2.02E-03	0.75	68.37	7.14E-06	1.03
	2	8.14	75.55	1.53E-03	0.85	90.75	8.80E-06	1.02
	4	8.96	109.79	1.51E-03	0.82	131.36	1.05E-05	1.00

4.3.1.2.3.3 Proposed corrosion mechanism

The following corrosion mechanisms were proposed for unalloyed magnesium, AZ91, and WE43 alloys by using the information gathered from literature and the results obtained from the short and long-term immersion experiments of the current study.

Stage 1: When the surface of the Mg/Mg-alloys was exposed to the SBF solution, micro galvanic corrosion occurs, and Mg dissolution starts, Figure 4.67(a). Then, all Mg/Mg-alloy samples experience an electrochemical reaction with the release of Mg^{2+} and OH^- ions. The anodic reaction occurs at the α -Mg matrix where Mg^{2+} ions releases for all samples. On the other hand, cathodic regions are impurities in unalloyed Mg and intermetallics/secondary phases in AZ91 and WE43 alloys, in which hydrogen gas evolution is observed.

Stage 2: At the same time, the continuous dissolution of Mg^{2+} and the increase in OH^- ions induce the H_2 gas evolution and $Mg(OH)_2$ formation, Figure 4.67(b) according to Eqs. 4.4 and 4.5. Subsequently, the pH of the solution increases, Figure 4.57(d), because of the fast production of OH^- ions [59]. Accordingly, the volcano-like deposits occur on the surface of Mg/Mg alloys at the cathodic sites (intermetallics or impurities), Figure 4.67(b).

Stage 3: The growth of the $Mg(OH)_2$ layer on the surface is enhanced by a dissolution-precipitation mechanism [50]. The formation and re-dissolution process of the $Mg(OH)_2$ continue as a dynamic process during in-vitro test, Figure 4.67 (c). In addition, $Mg(OH)_2$ layer can act as a nucleation site for Ca-P rich phases, which starts the precipitation of Ca-P rich phases by consuming the Ca^{2+} and PO_4^{3-} ions from the SBF, Figure 4.57.

Stage 4: After two days, pit formation on the surfaces of unalloyed Mg, AZ91, and WE43 alloys, Figure 4.60, becomes visible. Especially for WE43 alloy samples, severe pitting formation accompanies higher hydrogen gas formation, Figure 4.67 (d). As a result, the structural integrity of WE43 alloy is lost due to increased pit density on the surface at the end of ten days.

Stage 5: The final stage of the corrosion, Figure 4.67(d), is different for all of the samples. Although pH values increase with the growth of $Mg(OH)_2$ in unalloyed Mg and WE43 alloy samples, $CaCO_3$ layers form on the corroded surfaces of AZ91 alloy samples, Figure 4.67(c). As immersion time increases, the diffusion of water molecules through the magnesium substrate becomes more difficult since the corrosion products on the surface become a thicker, Figure 4.67(e). Therefore, the corrosion resistance of the samples is improved. Since the improvement in the corrosion layer protective properties is related to an increase in the corrosion layer diffusion resistance (R_2 , Table 4.9), AZ91 alloy possesses the lowest degradation rate compared to unalloyed Mg and WE43 alloy.

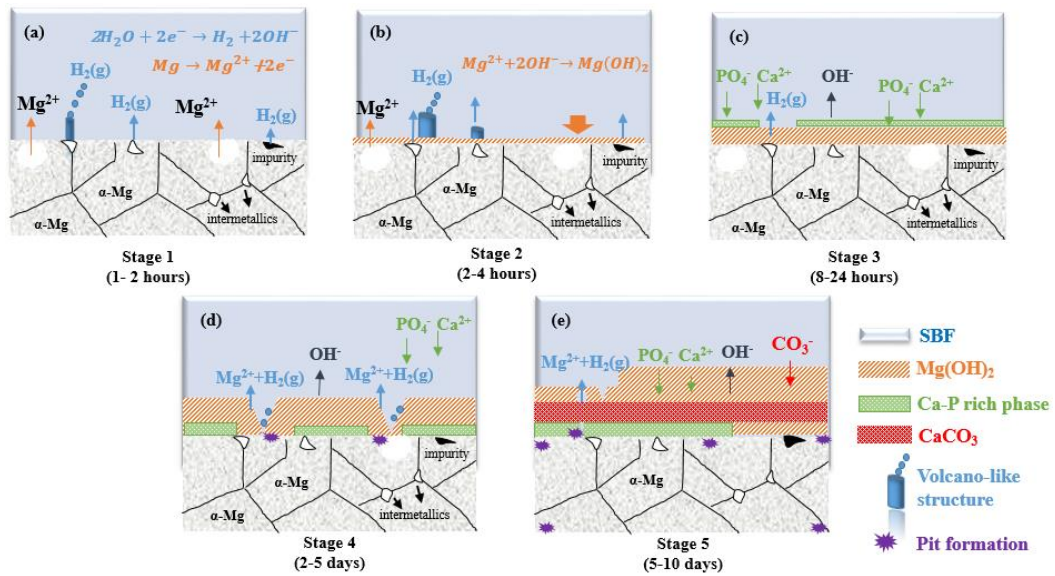


Figure 4.67. Schematic corrosion mechanism of bulk Mg/Mg-alloys.

4.3.2 Composites

4.3.2.1 Macro-structural examination

Figure 4.68 shows the macro images of the Ti6Al4V-Mg/AZ91/WE43 composites at different time intervals of the in-vitro test. Among the composites, observable macroscopic changes were detected for Ti6Al4V-Mg composites. Even after one day of immersion in SBF, corrosion of magnesium in Ti6Al4V-Mg composite was so heavy that the composites were not able to preserve their mechanical integrities. High pressure generated by the sudden formation of hydrogen gas overcame the local strength of sintering necks of the Ti6Al4V alloy structure so that Ti6Al4V-Mg composites fractured and could not maintain their mechanical integrities.

On the other hand, the corrosion rate of WE43 alloy containing composite was relatively slower at the initial stage, and they were able to maintain their mechanical integrities partially until the end of five days of immersion. The small number of fragments, formed by fracturing of the samples at their surfaces, was found, Figure 4.68. After ten days, similar to the Ti6Al4V-Mg composites, the composite lost its mechanical integrity entirely.

Among the composite samples, Ti6Al4V-AZ91 composites did not fracture during ten days of in-vitro experiments and preserved their integrity throughout the test, Figure 4.68. AZ91 alloy in the Ti6Al4V-AZ91 composite degraded over time by leaving the pores behind it without disrupting the composite's mechanical integrity. After ten days, most of the AZ91 alloy in the composite degraded and the peak strength of the Ti6Al4V-AZ91 composite reduced to 365 ± 30 MPa, which was lower than that of Ti6Al4V-AZ91 composite (470 MPa) prior to immersion test, Table 4.2; however, it was high enough for maintaining the mechanical integrity. Likewise, yield strength and elastic modulus of the composite decreased and found to be 6.45 ± 0.5 GPa and 150 ± 20 MPa, respectively.

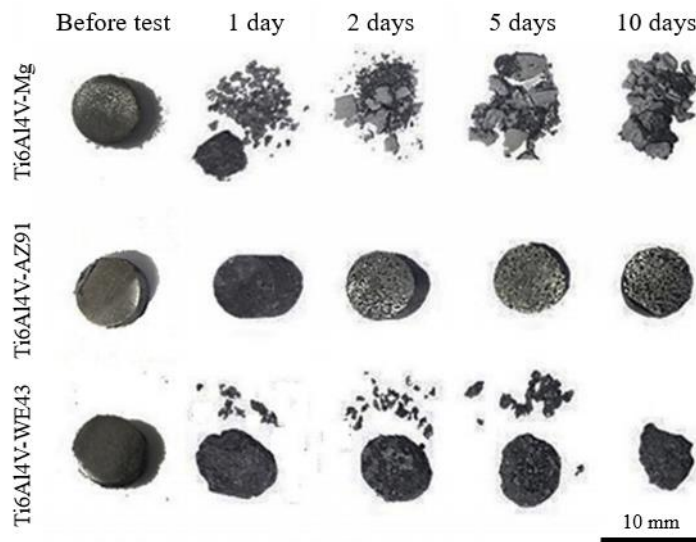


Figure 4.68. Macro-structural changes of composites during in-vitro tests [195].

4.3.2.2 Microstructural changes

Figure 4.69 and 4.70 display the morphological changes detected on the surfaces at the microscale for two different time intervals, which are 1-24 hours and 1-10 days. In the Ti6Al4V-Mg composite, magnesium regions were selectively degraded because of the galvanic corrosion occurred between unalloyed Mg and Ti6Al4V alloy. At the first two hours, swelling observed in the form of blistering shown by yellow arrows in Figure 4.69. Subsequently, magnesium sites of the composites began to corrode while swelled regions were still observed at the end of the four hours. Then, microcracks formed at the interface regions of partially sintered Ti6Al4V alloy powders (shown by blue arrows) and infiltrated Mg after eight hours. Finally, after 24 hours, intensified microcracks caused the composites to lose their mechanical integrity and fracture. The formation of microcracks between two metals generated fresh magnesium surfaces available for further corrosion, which caused catastrophic failure through the sintering necks of Ti6Al4V alloy powders due to increased hydrogen gas formation at fresh surfaces. In Figure 4.70, fractured neck regions of partially sintered Ti6Al4V alloy powders are shown by white arrows in the Ti6Al4V-Mg composite after 1, 2, 5, and 10 days. As previously stated, hydrogen gas pressure in the composite exceeded the strength of porous Ti6Al4V alloy (57 MPa, Table 4.2), and caused the composite failure after one day.

Unlike Ti6Al4V-Mg composite, severe degradation was not detected in the composite containing AZ91 alloy. Similarly, due to galvanic corrosion, AZ91 alloy was selectively corroded and caused blistering in AZ91 alloy regions up to 24 hours (white arrows in Figure 4.69). On the other hand, there were no microcracks detected in the Ti6Al4V-AZ91 composite. Instead, AZ91 corroded uniformly and slowly, and prior AZ91 regions became empty at the end of ten days of immersion test by leaving pores behind it (region B), Figure 4.70. Moreover, the formation of white precipitates on Ti6Al4V alloy powders was also observed after five days, Figure 4.70(region A).

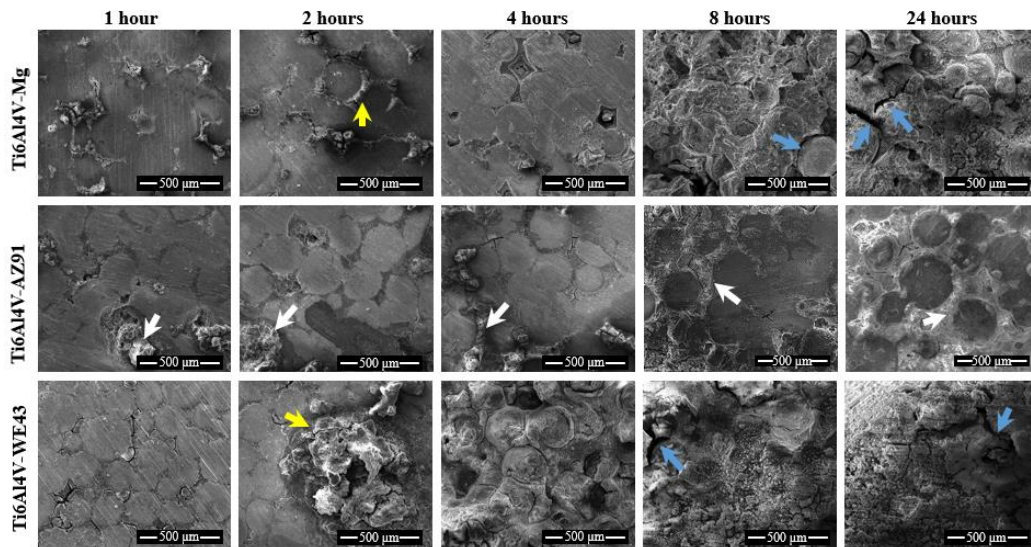


Figure 4.69. SEM images of corroded surfaces in composites in SBF for various immersion times [195].

The swelling of magnesium sites was also detected in the Ti6Al4V-WE43 composites. In the first two hours of immersion, more significant local swelled regions were observed (shown by yellow arrows in Figure 4.69). The composite displayed corrosion behavior similar to that of Ti6Al4V-Mg composite in which preferential degradation began at prior Mg-rich regions after four hours. In addition, small microcracks (blue arrows) formed between Ti6Al4V alloy and WE43 alloy after eight hours, Figure 4.69. At the end of the ten days, on the other hand, WE43 alloy containing composite lost almost all its mechanical integrity. Apart from the other composites, after eight hours, the surface of the Ti6Al4V-WE43 composite was covered with a thick whitish corrosion product, which remained on the surface throughout the in-vitro test, Figure 4.70.

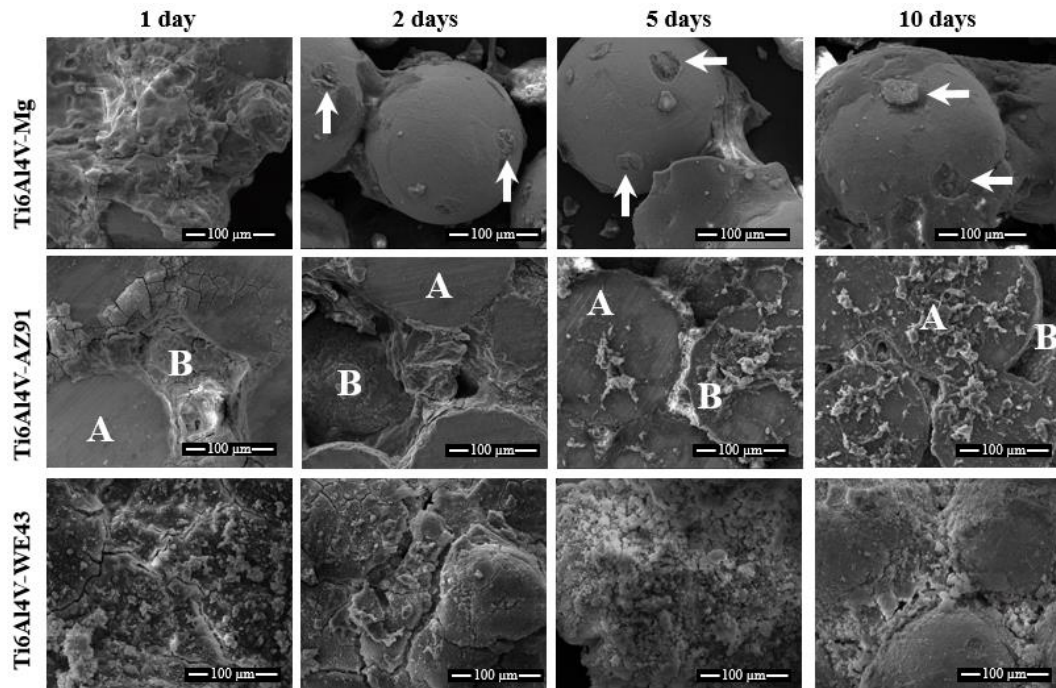


Figure 4.70. SEM images of corroded surfaces in composites for various immersion times in SBF (A: Ti6Al4V powder, B: prior Mg/Mg-alloy regions) [195].

4.3.2.2.1 Cross-sectional examination

The depth of the corrosion layer from the surface to interior sections of the Ti6Al4V-Mg/AZ91/WE43 composites was also investigated in the first 24 hours. The region between the yellow dashed lines was the maximum depth of corroded magnesium layers, Figure 4.71. As expected, the thickness of the corroded region showed a gradual increase with time. Moreover, the change of the corrosion depth with time was approximately well matched with the macro and microstructural variations in the composites' surfaces observed in Figure 4.68 and 4.69. While the measured corrosion depth for Ti6Al4V-Mg composites was relatively lower for the first four hours, then it passed the corrosion depths detected in Ti6Al4V-AZ91 and WE43

composites, Figure 4.72. Comparatively lower corrosion depths were observed in AZ91 containing composites throughout the test, which were agreement with the corrosion behavior seen in Figure 4.68-69-70.

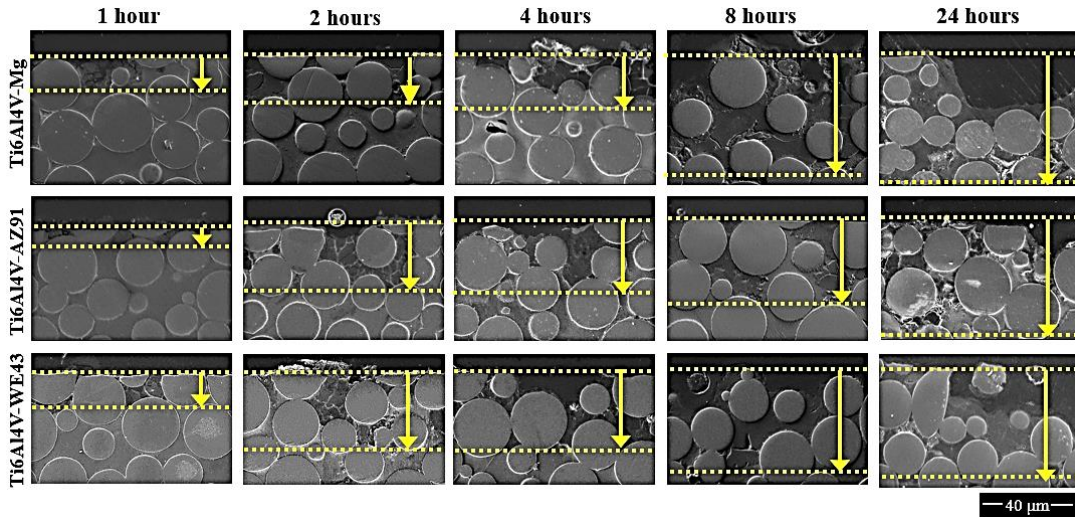


Figure 4.71. Cross-sections of the polished surface of Ti6Al4V-Mg/AZ91/WE43 composites showing corrosion depth at different time intervals of immersion in SBF [195].

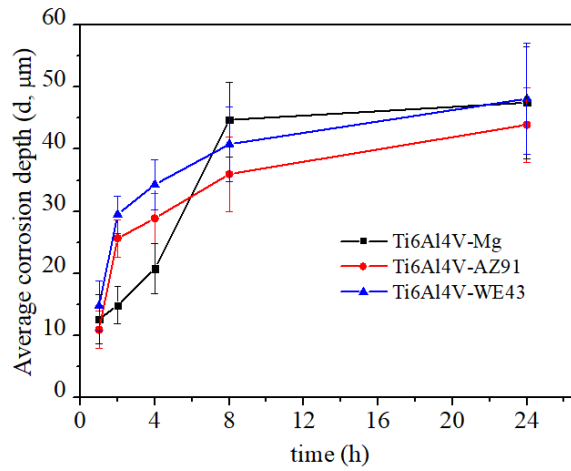


Figure 4.72. The change of average corrosion depths of Ti6Al4V-Mg/Mg-alloy composites with time.

4.3.2.2.2 Corrosion products

Ti6Al4V-Mg/AZ91/WE43 composites exhibited different corrosion response compared to bulk as-cast Mg, AZ91, and WE43 alloys. Severe galvanic corrosion was seen at the interface region of Ti6Al4V and Mg/Mg-alloys. Since the corrosion products severely accumulated at the interface region and on the surfaces, the presence of micro galvanic corrosion in magnesium regions could not be detected in composites. Figure 4.73(a-c) show the initial stage (after one hour) of corrosion in Ti6Al4-Mg composite. Volcano-like structures seen in as-cast unalloyed magnesium were also seen in the composites. However, volcanos formed only on Ti6Al4V regions (shown by yellow arrows in Figure 4.73(a) and (b), which were thought to be cathodic centers. On the other hand, magnesium, region B, became anodic sites with cracked and swelled corrosion layers. In addition to Ti and Mg elements, either volcano-like structure or magnesium regions consisted of O, Ca, P and Na elements, Table 4.10. However, a relatively higher amount of Ca-P precipitation was detected on volcano-like structures (Ca/P:0.96), while Ca/P ratio was found to be 0.83 on magnesium regions.

In AZ91 alloy containing composites, two different morphologies were observed on the corroded magnesium regions, which are swelling in the form of blistering (point A in Figure 4.73(d)), and some corroded regions (point B in Figure 4.73(e)). Compared to unalloyed Mg containing composites, volcano-like structures were not detected on the titanium alloy regions; instead, small holes were observed close to AZ91-Ti6Al4V alloy interfaces, shown by white arrows in Figure 4.73(f). Blistered regions were found to be rich in Mg and O, Table 4.10, possibly due to the rapid formation of $Mg(OH)_2$. On the other hand, corroded Mg regions contained Ca and P elements having a Ca/P ratio of 1.4, which was close to atomic ratio of $Ca_3(PO_4)_2$ phase.

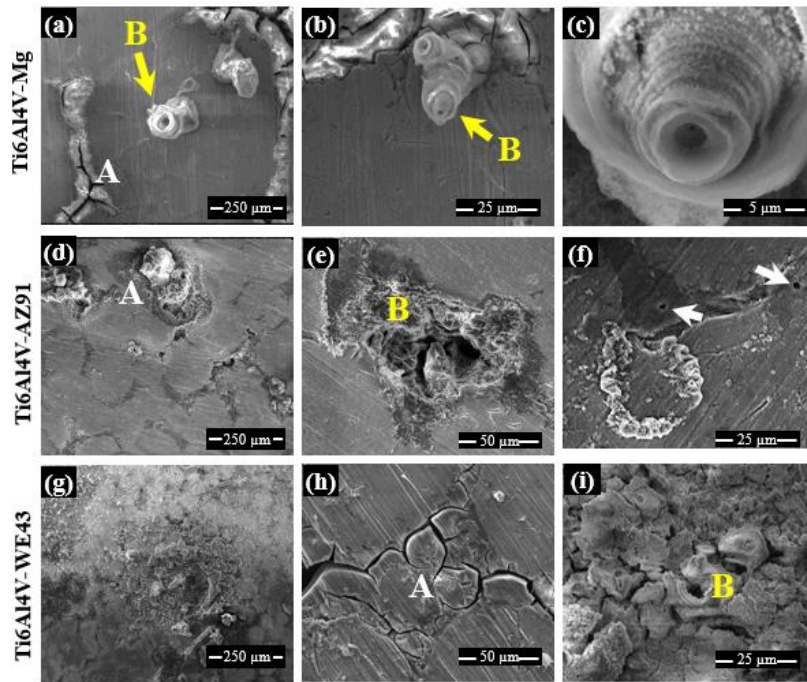


Figure 4.73. SEM images of corroded surfaces of (a-c) Ti6Al4V-Mg, (d-f) Ti6Al4V-AZ91, and (g-i) Ti6Al4V-WE43 composites after one hour of immersion in SBF [195].

In the Ti6Al4V-WE43 alloy composites, the corrosion of the magnesium sites was not homogenous in which blistered magnesium regions with volcano-like structures and cracked areas were seen at the same time, Figure 4.73(g-i). The EDS analysis, Table 4.10, taken from the cracked region (point A, Figure 4.73(h), showed the existence of Ca and P elements with a Ca/P ratio of 0.72. Yet, volcano-like structures were thought to be in highly corroded regions; therefore, the origin of the volcano-like structure formation points could not be distinguished clearly. In addition to the small amount of Na and Cl, the volcano-like structures consisted of mainly Mg and O elements, Table 4.10.

Table 4.10 EDS analysis of composites taken from different regions labeled in Figure 4.73.

Sample	Region	Elements (in wt. %)									
		O	Mg	Al	Na	Y	Nd	P	Ca	Cl	Ti
Ti6Al4V-Mg	A	42.0	25.7					15.7	12.9		3.7
	B	43.5	21.6		11.5			10.3	10.0	-	3.0
Ti6Al4V-AZ91	A	51.5	42.9	-	-	-	-	-	-	2.3	3.3
	B	45.1	18.3	8.1	9.7	-	-	5.4	7.6	-	5.8
Ti6Al4V-WE43	A	29.2	11.3	2.5	8.0	6.4	4.7	4.5	3.3	0.6	29.3
	B	38.6	40.2	-	6.1	-	-	-	-	6.7	8.5

Since the corrosion layers at the initial stages were not thick enough, XRD analysis was not conducted for samples for the first 24 h immersion. Figure 4.74 shows XRD analysis, performed on the corroded composite samples' surfaces exposed to SBF for 1-10 days. Mg(OH)₂ phase was detected in all corroded composites' surfaces since the degradation of Mg and the formation of Mg(OH)₂ occurred simultaneously. While EDS analysis, Table 4.10, revealed Ca and P elements close to volcano-like structures, Ca and P rich phases could not be detected by XRD analysis because of dominance of thick Mg(OH)₂ phase. Sodium chloride phase, NaCl, which possibly precipitated from SBF on the Ti6Al4V-Mg composites' surface during immersion, was also detected in some samples. It remained even after the cleaning process with DI water.

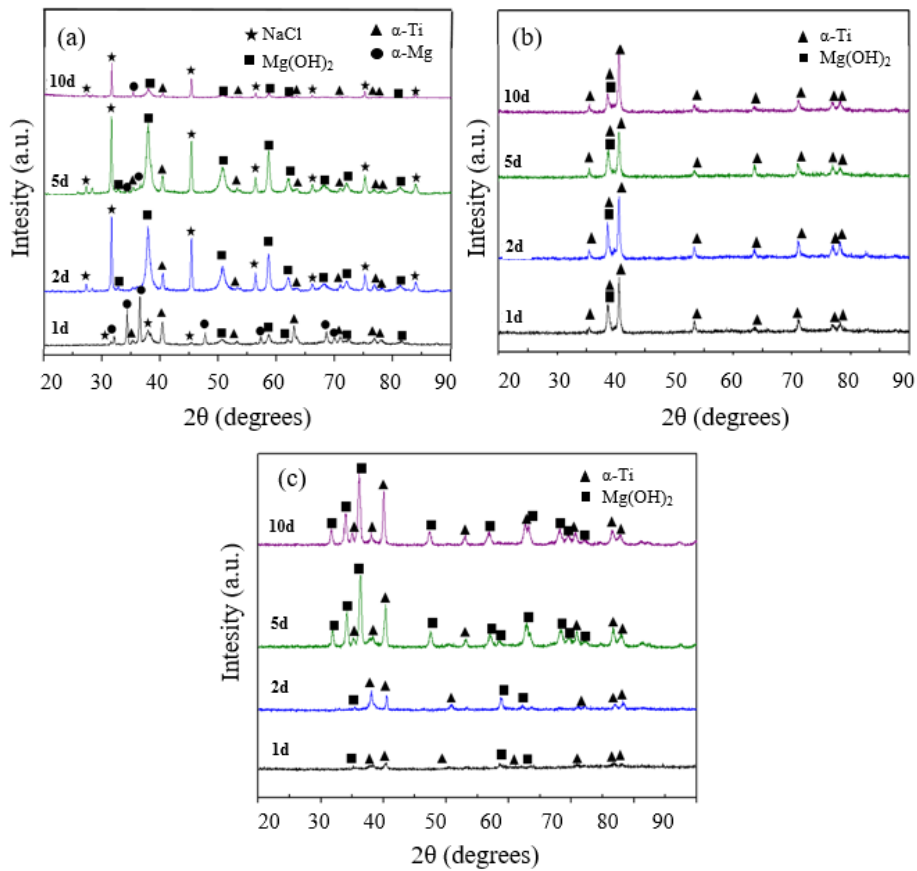


Figure 4.74. XRD of (a) Ti6Al4V-Mg, (b) Ti6Al4V-AZ91, and (c) Ti6Al4V-WE43 composites after 1, 2, 5, and 10 days of immersion in SBF [195].

Besides, closer investigation of cracked regions around the volcano-like structures contained rod-like structures, Figure 4.75(a-c), with a high content of Mg and Cl (Table 4.11). This rod-like morphology was also found in previous studies conducted on the corrosion of magnesium [214]. It is believed that Mg and its alloys can be passivated in the basic environment ($\text{pH} > 7.0$) by the formation of $\text{Mg}(\text{OH})_2$ corrosion layer. However, hydroxide phases are not stable in the long immersion times because they are soluble in aqueous environments. The existence of chlorate, sulfate, bromide, and chloride cause distortion of passive films [202]. When the

concentration of chloride is above 0.15 M, and the pH of the solution is between 6.8-7.4, $Mg(OH)_2$ can be partly converted into more soluble magnesium chloride, $MgCl_2$, according to Eq. (4.11) [15].

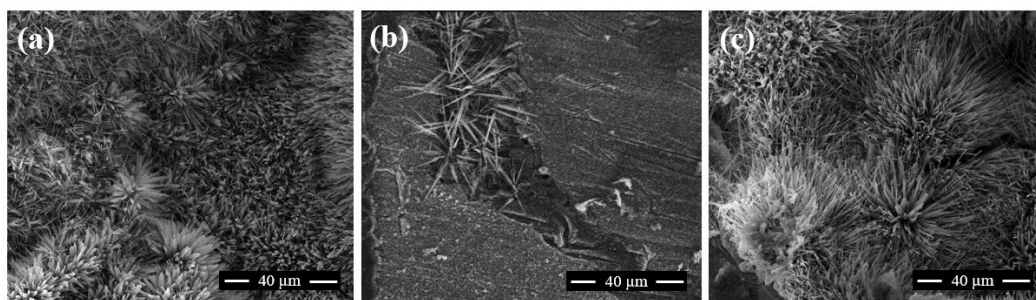
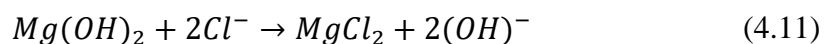


Figure 4.75. SEM images of the corroded surface of (a) Ti6Al4V-Mg, (b) Ti6Al4V-AZ91, and (c) Ti6Al4V-WE43 composites showing Cl rich rod-like structure [195].

Table 4.11 EDS analysis taken from the rod-like structures seen in Figure 4.75.

	Elements (in wt. %)					
	O	Na	Mg	P	Cl	Ti
(a) Ti6Al4V-Mg	40.8	-	35.4	-	20.6	3.1
(b) Ti6Al4V-AZ91	41.8	1.8	39.5	1.2	13.3	2.4
(c) Ti6Al4V-WE43	35.4	-	40.9	-	23.8	-

4.3.2.3 Hydrogen evolution

Figure 4.76 shows the cumulative hydrogen gas produced during the corrosion of the composite samples. In all composite samples, the high hydrogen production in the first two hours was followed by a steady decrease until the end of the experiments. During the initial immersion times, possibly the porous corrosion layer allowed water penetration through the underlying fresh substrate surface. On the other hand, as immersion time increased, the thickening of the protective layer made it difficult to access water to the substrate surface so that the hydrogen evolution rate decreased.

The fastest and the highest hydrogen gas evolution was observed in the Ti6Al4V-Mg composite. A possible explanation was the creation of fresh magnesium surfaces available for corrosion as a result of microcrack formation between Ti6Al4V and unalloyed Mg in the first eight hours, Figure 4.69. These microcracks created new magnesium surfaces available for water reduction and magnesium dissolution. Nearly half of the total hydrogen gas evolved in the early 24 hours, and it caused fracturing of the composites severely through the necks between sintered Ti6Al4V alloy powders. Therefore, in addition to micro-crack formation, after 24 hours, catastrophic fracture also increased the new magnesium surface area formation available for corrosion. Besides, hydrogen evolution in the Ti6Al4V-Mg composites ended after three days showing that almost all of the magnesium corroded and no magnesium remained in the composite, Figure 4.76.

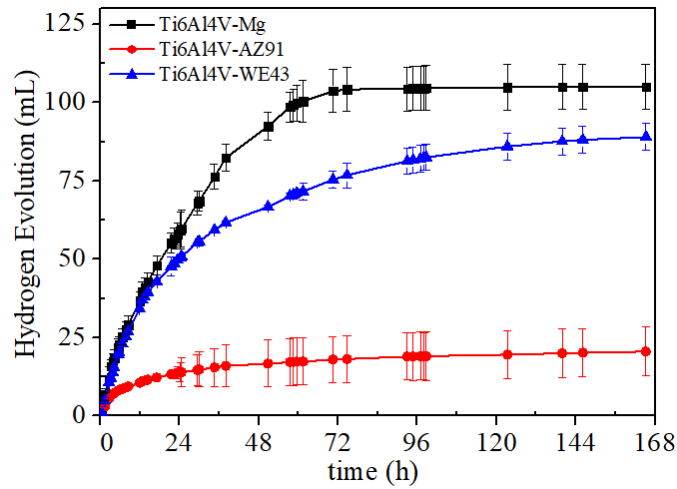


Figure 4.76. Cumulative hydrogens produced the Ti6Al4V-Mg/AZ91/WE43 composites during the in-vitro test [195].

For WE43 alloy containing composites, the initial hydrogen evolution rate was similar to that of Ti6Al4V-Mg composites for the first eight hours. Although hydrogen evolution decreased over time, hydrogen evolution continued to take place slowly even after seven days. It has been observed that the use of alloyed Mg, i.e., WE43 alloy, instead of unalloyed Mg in composites, reduced the galvanic corrosion. The effect of Mg-alloy coupling with Ti-alloy on galvanic corrosion is more obvious in Ti6Al4V-AZ91 composites. The rate of hydrogen evolution in the Ti6Al4V-AZ91 composite was the lowest among the composite samples. Even in the early stage of immersion, the hydrogen gas evolution rate began to decrease and subsequently became very slow after 120 h (five days). Cumulative hydrogen gas produced in the composite at the end of the immersion experiment was about 75% and 80% lower than those measured in Ti6Al4V-WE43 and Ti6Al4V-Mg composites, respectively. With relatively lower amount of hydrogen gas generated, Ti6Al4V-AZ91 composites had the highest corrosion resistance and did not lose their mechanical

integrity, Figure 4.68, because the hydrogen gas pressure was not sufficient to overcome the strength of the sintering necks of Ti6Al4V powders.

4.3.2.4 pH change of SBF solution

Figure 4.77 shows the variations in the pH of the SBF solution during the in-vitro test. The pH change behavior of the solutions was approximately the same in all Ti6Al4V-Mg composites. However, the pH of the Ti6Al4V-AZ91 solution was slightly lower than the others, as observed in as-cast bulk AZ91 alloy. Initially, the pH of the solution raised to around 10 in the first two days; then, it continuously decreased to around 8 at the end of ten days. Similar to that of bulk as-cast Mg/Mg-alloy samples, Figure 4.64, an increase in the pH was attributed to both the dissolution of Mg and the increase of OH⁻ ions in the SBF [17]. On the other hand, the solution renewal at every three days (shown by arrows in Figure 4.77) decreased the pH of the solutions as corrosion products were removed from the solution. However, this sudden decrease in pH values was not shown in the figure. It is known that a decrease in pH of the solution reduces the protection ability of the Mg(OH)₂ corrosion layer because the equilibrium concentration of Mg²⁺ in the solution increased at each renewal time according to Eq. (4.10) [215]. As stated in the study of Ascencio et al. [59], a decrease in solution pH and attack of chloride ions caused the partial dissolution and an increase in the porosity level of the corrosion layer.

Apart from sudden pH decrease at renewal times, the pH of all solutions has been observed to decrease gradually after the first three days of immersion. The decrease in the pH value was more evident in the solution containing Ti6Al4V-AZ91 composites. All of the magnesium alloy degraded and almost all of its corrosion products were thrown away during the third refreshment. Subsequently, the measured pH value of the solution after ten days decreased dramatically and reached to around 7.6.

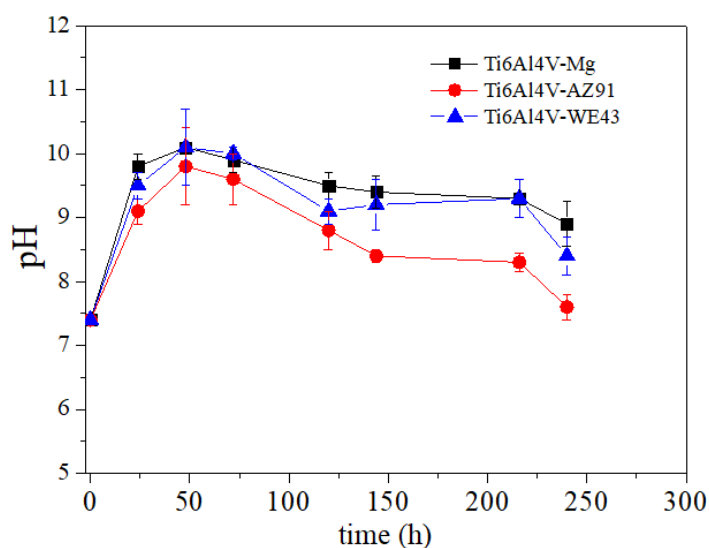


Figure 4.77. pH change of the SBF solution containing Ti6Al4V-Mg/AZ91/WE43 composites [195].

4.3.2.5 Electrochemical tests

4.3.2.5.1 Galvanic Corrosion

Prior to potentiodynamic polarization experiments of Ti6Al4V-Mg/Mg-alloy composites, galvanic corrosion between Ti6Al4V alloy and Mg/Mg-alloys was quantitatively investigated by galvanic experiments. Figure 4.78 shows the change in the potential and current density measured for the couples of the Ti6Al4V-unalloyed Mg, Ti6Al4V-AZ91, and Ti6Al4V-WE43 alloys in SBF. The galvanic current density for the couple containing AZ91 alloy was the lowest among all of the couples, Figure 4.78(b). Moreover, WE43 alloy exhibited the highest current density when it was coupled with Ti6Al4V alloy. Since galvanic current related to the corrosion rate, it was suggested that WE43 alloy was more susceptible to galvanic corrosion than unalloyed Mg, and AZ91 when coupled with Ti6Al4V alloy. Similar

results were also found in the previous corrosion test results conducted on bulk Mg/Mg-alloys.

In addition, the fluctuations were observed in the galvanic corrosion potential and current density graphs, especially in WE43 alloy, Figure 4.78. Sakairi et al. [216] stated that the current and potential fluctuation is observed in the presence of localized or pitting corrosion. Moreover, Al-Mazeedi et al. [217] found that larger fluctuations are the indication of a more localized process in magnesium alloy. In the current study, localized corrosion was observed in the corroded surfaces of WE43 alloy by the formation of deep pits, Figure 4.60, which accelerated the corrosion rate of the alloy. Similarly, the formation of corrosion pits on the surface of WE43 alloy caused the fluctuations in the galvanic potential and current densities when coupled with Ti6Al4V alloy. On the other hand, the amplitude of the current fluctuations in unalloyed Mg and AZ91 alloy was relatively smaller than that of the WE43 alloy, Figure 4.78.

Table 4.12 lists the galvanic corrosion parameter calculated by a statistical approach. It is known that the inverse of R_g is proportional to the corrosion rate [218]. Therefore, the samples having the highest R_g values possessed the lowest degradation rate. According to calculated corrosion parameters, AZ91 alloy exhibited the highest galvanic resistance, R_g , among the investigated Mg/Mg-alloys. Besides, unalloyed Mg had a comparatively higher degradation rate with respect to the AZ91 alloy. On the other hand, the most severe galvanic corrosion was observed in WE43 alloy.

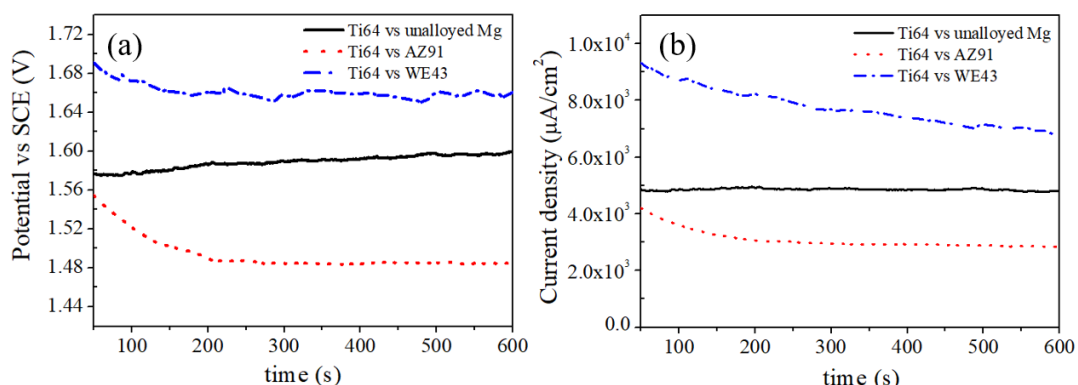


Figure 4.78. The change in (a) potential and (b) current density of Mg/Mg-alloys coupled with Ti6Al4V alloy.

Table 4.12 Galvanic corrosion parameter of unalloyed Mg, AZ91, and WE43 alloys.

	Mean E_{corr} (V vs. SCE)	Mean I_{corr} (mA / cm ²)	Std. Dev. E, σ_E	Std. Dev. I, σ_I	Galvanic resistance, R_g (Ω)
Ti64 vs. unalloyed Mg	1.59	1.16	1.02E-03	1.76E-05	58.01
Ti64 vs. AZ91 alloy	1.49	0.82	9.79E-04	1.57E-05	62.45
Ti64 vs. WE43 alloy	1.66	1.74	2.25E-03	9.29E-05	24.23

4.3.2.5.2 Potentiodynamic polarization tests

The potentiodynamic polarization graphs have been used to understand the relationship between the corrosion rate calculated by corrosion current with those examined by direct measurements, namely, corrosion depth analysis and hydrogen evolution tests. Figure 4.79 displays the electrochemical corrosion behavior of Ti6Al4V-Mg, Ti6Al4V-AZ91, and Ti6Al4V-WE43 composites. Compared to

results of as-cast bulk Mg/Mg-alloy counterparts, Table 4.8, composites manufactured using infiltration of Mg/Mg-alloy into porous Ti6Al4V structure exhibited relatively lower corrosion resistance. Since the galvanic corrosion occurred between two dissimilar metals of Mg and Ti6Al4V alloy, i_{corr} and CR of composites were higher by around 1.5 and 9 times than that of bulk Mg alloys, respectively, Table 4.13.

However, combining of porous Ti6Al4V structure with alloys of AZ91 and WE43 instead of unalloyed magnesium decreased i_{corr} and CR values in composites by around 15% and 20%, respectively. As it is known that alloying magnesium alleviates the galvanic effect [219], similarly, corrosion resistance of composite was improved by the addition of alloying elements to Mg. On the other hand, AZ91 alloy was found to be a more suitable coupling alloy with Ti-alloy with reduced galvanic corrosion as found in the galvanic corrosion test in Figure 4.78. The presence of a secondary phase region by the formation of the TiAl_3 phase at the interface region of Ti6Al4V and AZ91 alloy, Figure 4.26, can also be effective in lessening the galvanic effect.

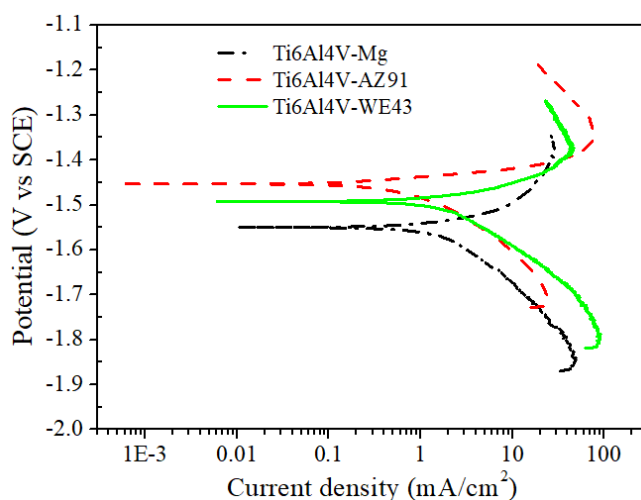


Figure 4.79. Polarization curves of Ti6Al4V-Mg/Mg-alloy composites in SBF at 37 °C [195].

Table 4.13 Corrosion parameters obtained from the polarization curves of the composites [195].

Sample	E_{corr} (V vs. SCE)	i_{corr} ($\mu\text{A}/\text{cm}^2$)	CR (mm/year)
Ti6Al4V-Mg	-1.55	1.76	25.22
Ti6Al4V-AZ91	-1.45	0.78	10.19
Ti6Al4V-WE43	-1.49	1.50	19.73

In contrast to Ti6Al4V-WE43 composites, Ti6Al4V-Mg composites displayed lower corrosion resistance. The i_{corr} and CR values of Ti6Al4V-Mg composites were found to be higher than the values calculated for Ti6Al4V-WE43 composite by around 10 % and 18 %, respectively, Table 4.13. In composite samples, the CR results obtained from potentiodynamic polarization tests were different from those found in as-cast bulk Mg/Mg-alloys, which indicated that the bulk WE43 alloy had the highest corrosion rate among all of the as-cast samples due to micro galvanic corrosion. However, the galvanic corrosion test has been revealed that WE43 alloy was more susceptible to galvanic corrosion when coupled with Ti6Al4V alloy, Figure 4.78. Moreover, in composite samples, galvanic corrosion between Ti6Al4V and WE43 alloy was observed to be more dominant compared to micro galvanic corrosion seen in as-cast WE43 alloy. Therefore, the corrosion resistance of Ti6Al4V-WE43 composites was found to be higher than that of Ti6Al4V-Mg composite, Table 4.13. Corrosion rates of the composite samples calculated from polarization curves were similar to those measured by hydrogen evolution tests. The lowest and the highest CR values were obtained for AZ91, and unalloyed Mg containing composites, respectively.

4.3.2.5.3 Electrochemical Impedance Spectroscopy (EIS) tests

Figure 4.80 demonstrates the Nyquist plots of the composites immersed in SBF for different times (1, 2, 4 and 6 hours). The EIS diagram of both Ti6Al4V-Mg and Ti6Al4V-WE43 composites, Figure 4.80(a) and (e), showed a single capacitive loop, which indicated that the corrosion mechanism of composites was primarily controlled by a charge transfer process from the surface to the electrolyte through the electrochemical double-layer [220,221]. Moreover, Wu et al. [59] stated that the EIS diagram of as-cast Mg-Ca-Al alloy also exhibited one well defined capacitive loop, showing that the charge transfer process is the main corrosion mechanism. In the present study, Nyquist plots of Ti6Al4V-Mg and Ti6Al4V-WE43 composites, which had a single capacitive loop, were fitted based on the equivalent circuit as $R_s(CPE_1R_1)$, Figure 4.80(b) and (f). In this circuit, R_s , R_1 , and CPE_1 indicate the solution resistance, charge transfer resistance, and constant phase element at the interface, respectively. The CPE_1 is commonly determined by n value, which is a dimensionless constant in the range of -1 to 1. When n is identical to 1, CPE is equal to a capacitor [59]. In the present study, n values were smaller than 1, Table 4.14.

The Nyquist plots of the Ti6Al4V-AZ91 composite were described by a large well-defined capacitive loop at high frequency followed by an inductive loop at low frequency, Figure 4.80(c). Inductive semicircle was thought to form during the relaxation process by the absorption of Mg^+ intermediate species at the anode. The formation of metastable Mg^+ ion related to one-electron transfer kinetics has also been observed by Jamesh et al. [129]. The inductive loop was disappeared as immersion time increased, Figure 4.80(c). EIS curves of Ti6Al4V-AZ91 composites were fitted via an equivalent circuit, $R_s(CPE_1R_1(LR_L))$, Figure 4.80(d). CPE_1 , R_1 , and R_s represent the notations presented previously, while L and R_L show the inductance and inductive resistance, respectively. Wu et al. [222] found that extruded Mg-2Ca-

2Al alloy exhibited one well defined capacitive loop with an inductive loop when exposed to an aqueous NaCl solution.

Different EIS parameters were derived by curve fitting method and given in Table 4.14. R_1 values of AZ91 containing composite were observed to be the highest compared to those of Ti6Al4V-Mg and Ti6Al4V-WE43 composites. Since the high value of R_1 implied the lower degradation rate of samples, the Ti6Al4V-AZ91 composite possessed the highest corrosion resistance among the composites. When composites were immersed in the SBF solution, Mg^{2+} and OH^- ions released and pH of the solution increased, Figure 4.77, followed by the formation of $Mg(OH)_2$ on the surfaces.

Furthermore, composites containing unalloyed Mg and WE43 exhibited an increase in R_1 between 1 h to 6 h, possibly because of the thickening of the $Mg(OH)_2$ layer, Figure 4.74. Also, Ti6Al4V-Mg composite had smaller corrosion resistance compared to that of Ti6Al4V-WE43 composite, which was related to the lower R_1 value, Table 4.14. On the other hand, as stated previously, the Ti6Al4V-AZ91 composite had the highest corrosion resistance (R_1 , Table 4.14). One of the possible reasons for high corrosion resistance is the formation of $TiAl_3$ phase at the interface between Ti6Al4V and AZ91 alloys.

The diameter of capacitive loops in the Nyquist plot was associated with the corrosion rate. Ti6Al4V-Mg and Ti6Al4V-WE43 composite exhibited the same corrosion behavior as their capacitive loops had similar shape. Nonetheless, their corrosion rate was dissimilar because of their different loop diameters, Figure 4.80. The largest loop diameter was detected in the Ti6Al4V-AZ91 composite, showing the best corrosion resistance among the produced composites.

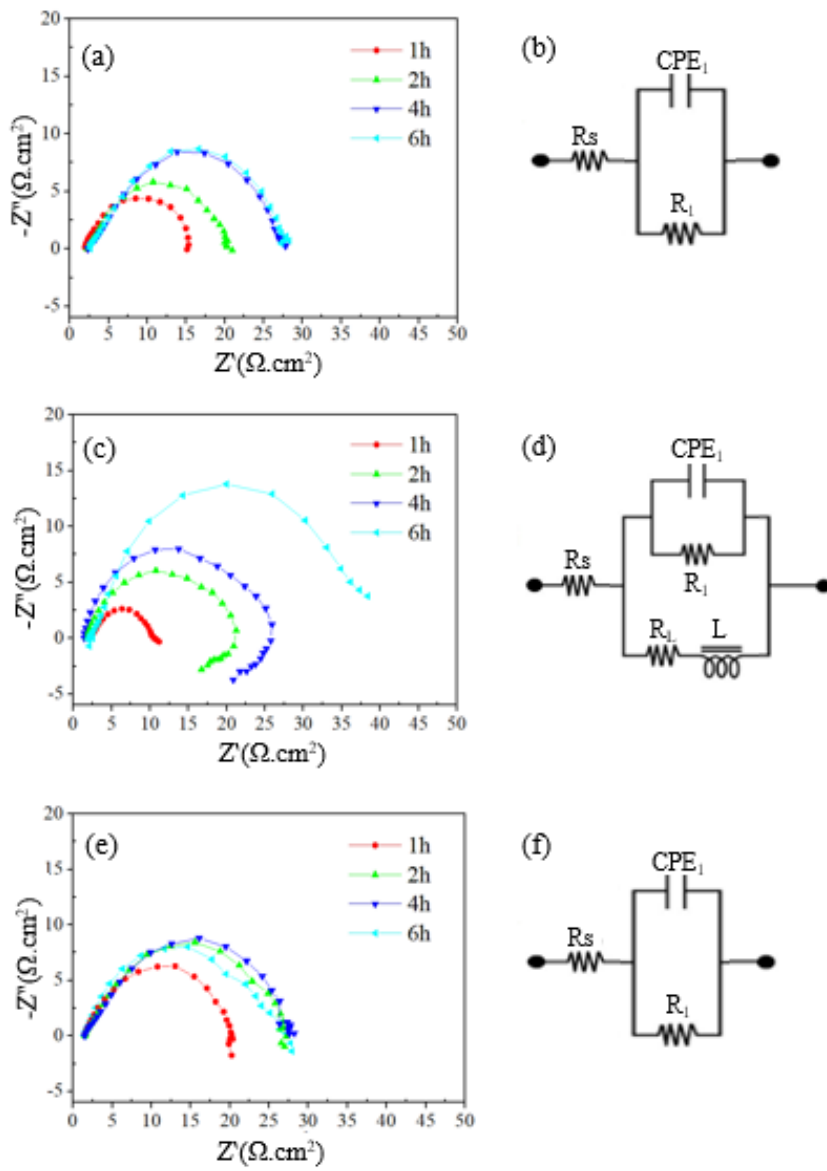


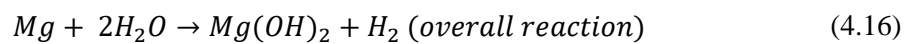
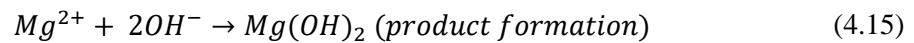
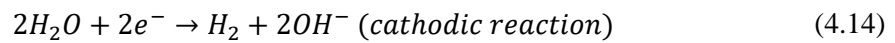
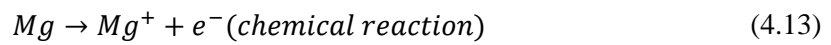
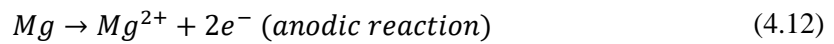
Figure 4.80 Nyquist diagrams and corresponding equivalent circuits of (a-b) Ti6Al4V-Mg, (c-d) Ti6Al4V-AZ91, (e-f) Ti6Al4V-WE43 composites.

Table 4.14 Fitting parameters of composites in SBF solution for 1, 2, 4, and 6 hours [195].

Samples	time (h)	Rs ($\Omega \text{ cm}^2$)	R ₁ ($\Omega \text{ cm}^2$)	CPE ₁ (F cm ⁻²)	n ₁	R _L ($\Omega \text{ cm}^2$)	L ₁ ($\Omega \text{ s cm}^2$)
Ti6Al4V-Mg	1	1.90	13.80	3.96E-04	0.74		
	2	2.33	18.47	9.17E-04	0.68		
	4	2.57	26.53	1.47E-03	0.66		
	6	2.67	26.39	1.36E-03	0.69		
Ti6Al4V-AZ91	1	2.21	50.03	3.43E-03	0.66	21.11	0.46
	2	1.49	56.78	8.55E-05	0.86	22.72	20.32
	4	1.78	64.83	2.62E-04	0.75	19.06	6.56
	6	2.32	82.70	1.92E-03	0.69	9.11	0.15
Ti6Al4V-WE43	1	1.56	23.19	3.86E-04	0.79		
	2	1.56	18.51	4.81E-04	0.76		
	4	1.56	26.11	9.10E-04	0.70		
	6	1.59	26.94	9.82E-04	0.68		

4.3.2.6 Proposed corrosion mechanism

Figure 4.81 shows the possible corrosion mechanisms for Ti6Al4V-Mg/AZ91/WE43 composites, which was proposed based on the corrosion experimental results. During explaining the mechanisms and corrosion product formation, the following equations are used:



Stage 1: The immediate reaction of magnesium and water molecules causes the release of Mg^{2+} and OH^- ions according to anodic and cathodic reactions, Eqs. (4.12) and (4.14). Following this, H_2 gas evolves from the cathodic Ti6Al4V alloy regions, and Mg sites act as anodic sites, and they are preferentially dissolved, Figure 4.81(a). Volcano-like structures are observed at the cathodic sites especially for unalloyed Mg containing composites for 1 hour of immersion in SBF, Figure 4.73(a-c).

Stage 2: At the end of the 24 hours, pH of all composites increase to around 10. The pH increase can be referred to formation of OH^- ions as a result of the corrosion process. Ascencio et al. [61] stated that rise in pH value leads to the precipitation of $Mg(OH)_2$ phase above a pH of about 10. Similarly, in the present study, the $Mg(OH)_2$ phase is detected on the composites' surfaces, Eq. (4.15), which can partially protect the surface of composites. Because of the severe galvanic corrosion between Ti6Al4V and Mg-alloy, it is hard to detect the volcano-like structure on the surfaces of the composites. In addition, the formation of metastable Mg^+ ion, Eq. (4.13), has also been found by Jamesh et al. [129]. The appearance of low frequency inductance loop in the Nyquist plots of AZ91 alloy after 2 hours, Figure 4.80(c), is due to the existence of Mg^+ ions, which is easily oxidized and transform to Mg^{2+} .

Stage 3: The presence of Cl^- ions in the SBF causes the dissolution of $Mg(OH)_2$ by reacting with Mg^{2+} and produces highly soluble $MgCl_2$ having the rod-like shape, Figure 4.75. Similarly, Jamesh et al. [129] have been reported that higher concentration of Cl^- ions can transform $Mg(OH)_2$ to soluble $MgCl_2$. Since $Mg(OH)_2$ protectiveness disappears partly, the degradation continue, Figure 4.81(c). At the same time, Ca-P rich phases precipitation occur on the corroded surfaces. As proposed in the corrosion of as-cast bulk Mg/Mg-alloys, Ca-P rich phase continues to grow by consuming more Ca^{2+} and PO_4^{3-} ions in the solution.

Stage 4: In the final stage of corrosion, Figure 4.81(d), an increase in pH values indicate the re-precipitation of $Mg(OH)_2$ for all composite samples. Besides, the

micro-crack formation, Figure 4.81(d), is observed through the sintering necks of Ti6Al4V alloy powders. Microcracks due to pressure created by hydrogen gas cause the formation of fresh magnesium surface available for corrosion. Therefore, the corrosion rate is gradually increased and subsequently result in the catastrophic failure of both Ti6Al4V-Mg and Ti6Al4V-WE43 composites, Figure 4.68. Interestingly, there are no microcracks detected on the surface AZ91 containing composites.

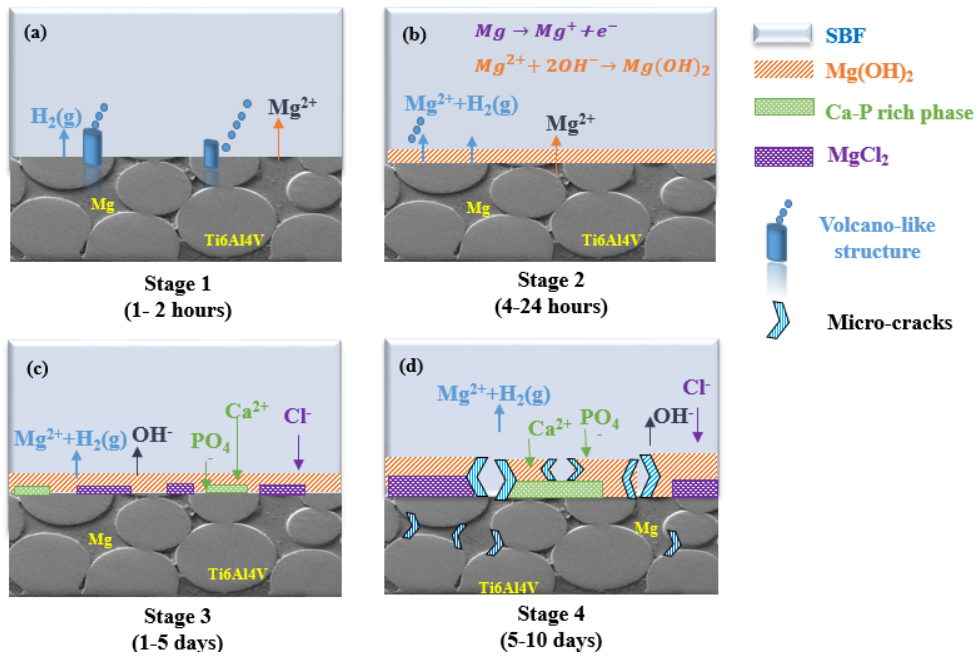


Figure 4.81 Schematic representation of corrosion mechanism for composite samples.

4.3.3 Composites containing Na-rich coating

In this part of the study, the effect of interface formation between Ti6Al4V and Mg/Mg-alloys on the corrosion rate of the Ti6Al4V-Mg/Mg-alloys composites have been investigated. As found in the previous section, galvanic corrosion between Ti6Al4V alloy and magnesium caused the dissolution of unalloyed Mg, AZ91, and WE43 alloys in the composites. Therefore, unalloyed magnesium and AZ91 alloy were infiltrated to the Na-coated porous Ti6Al4V structures to determine the effect of coating at two extreme conditions. Moreover, the relative change of the corrosion rates of the composites containing Na-rich coating, namely, Ti6Al4V-Na-Mg and Ti6Al4V-Na-AZ91, have been investigated using hydrogen evolution and electrochemical tests including galvanic corrosion and potentiodynamic polarization tests.

4.3.3.1 Microstructural changes

Figure 4.82 displays the variations in the surface structures of Ti6Al4V-Na-Mg composites after 1, 2, 4, 8, and 24 hours of immersion in SBF. The starting surface structures of the composites, Figure 4.82(0h), have been found to change entirely after immersion in the SBF solution. At the initial soaking times, magnesium regions were selectively corroded as in the composites without Na-rich interlayer. However, the effect of galvanic corrosion was lessened when there was Na-rich interlayer between Ti6Al4V and Mg. Although the dissolution of the magnesium region continued and blistering formed at the Mg sites at the end of the four days, severe degradation was started after eight hours. After 24 hours, new phase precipitation accompanied magnesium corrosion. The corroded surface of the Ti6Al4V-Na-Mg

composite was found to be covered with a corrosion product rich in Ca, P, and O element, Table 4.15.

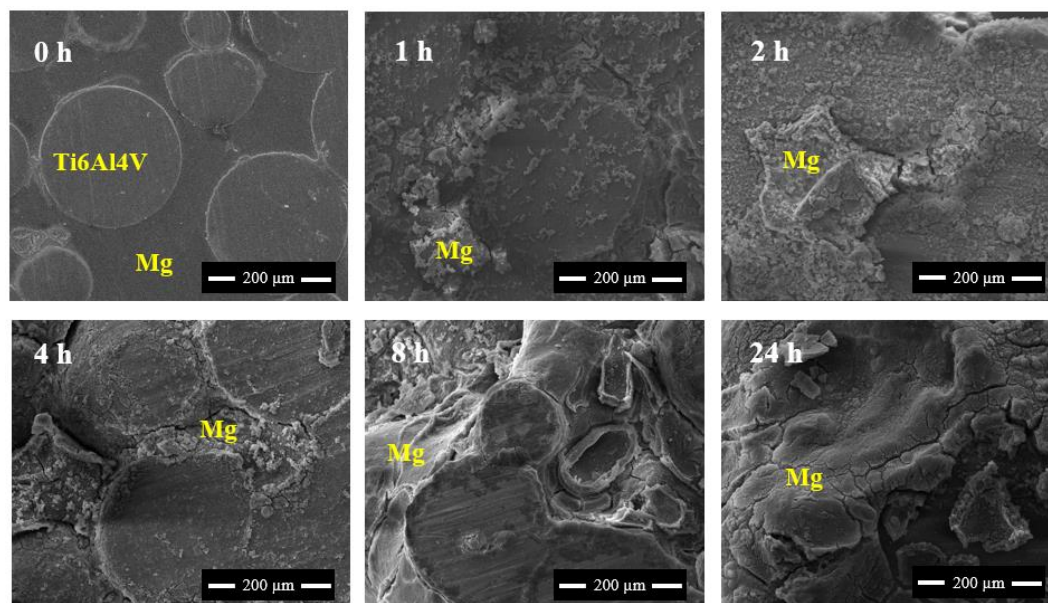


Figure 4.82 Surface morphological changes of Ti6Al4V-Na-Mg composites after immersion in SBF for 1-24 h.

The same dissolution characteristics was observed in the composite containing AZ91 alloy (Ti6Al4V-Na-AZ91) as well. As shown in Figure 4.83, magnesium selectively dissolved and blistering was seen at the magnesium sites, similar to Ti6Al4V-Na-Mg composites. On the contrary, the dissolution of magnesium alloy was slower than that of Ti6Al4V-Na-Mg composite. The relatively lower corrosion rate of the composite containing AZ91 was attributed to alloying elements (Al and Zn), which allowed the formation of intermetallic phases in the microstructure. Since the intermetallic phases act as a cathodic barrier, the corrosion resistance of AZ91 alloy was observed to increase.

Additionally, as observed in the corroded surfaces of bulk Mg/Mg-alloy samples, at cathodic sites, the volcano-like structures (Figure 4.83(2h)) rich in Ca and P elements

(Table 4.15) was detected on the corroded surfaces of Ti6Al4V-Na-AZ91 composites. On the other hand, the volcano-like structure could not be detected on the surface of the TiAl4V-AZ91 composite (without Na-rich interface) possibly due to rapid swelling in magnesium regions, which distorted the potential volcano-like structure nucleation regions. Especially after 8h, the magnesium regions of the composites was slightly degraded and at the end of the 24 hours, corroded surfaces of composites were composed of mainly Ca, P, Mg, and O elements, Table 4.15.

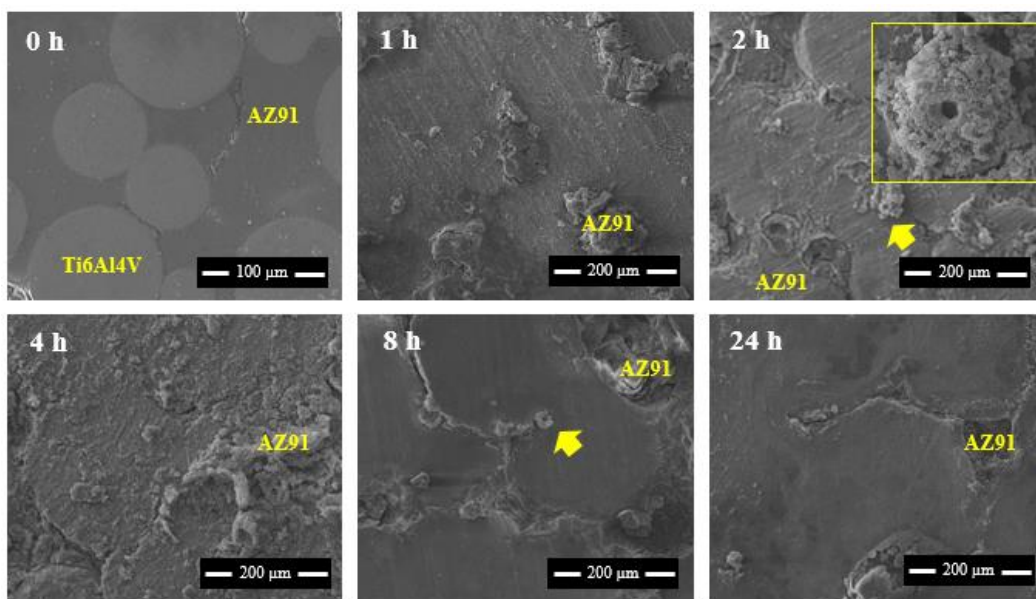


Figure 4.83 Surface morphological changes of Ti6Al4V-Na-AZ91 composites after immersion in SBF for 1-24 h.

Table 4.15 EDS analysis taken from the corroded Mg regions in Figure 4.82 and Figure 4.83.

		Element (wt. %)								
		O	Na	Mg	Al	P	Cl	Ca	Ti	V
	time (hour)									
(a)Ti6Al4V- Na-Mg	1	23.09	0.67	23.52	1.42	1.61	5.4	0.91	41.12	2.25
	2	31.43		36.34	-	12.9	5.39	11.83	1.6	0.5
	4	23.51	0.42	20.65	-	24.95	1.73	28.75	-	-
	8	27.4	1.66	55.02	-	7.39	5.92	2.62	-	-
	24	33.16	1.08	45.45	-	8.12	8.69	8.69	3.5	-
(b) Ti6Al4V- Na-AZ91	1	31.38	0.88	33.88	2.9	11.49	-	7.39	10.65	1.43
	2	31.55	1.23	57.76	1.26	3.2	-	1.44	2.23	1.33
	4	36.62	1.32	43.51	-	6.06	-	2.69	8.59	1.29
	8	18.38	6.56	10.21	7.82	11.99	-	11.02	32.32	1.69
	24	24.85	1.25	17.72	1.67	18.43	2.69	18.88	13.78	0.73

Figure 4.84 shows closer image of the interface region between Ti6Al4V powders and AZ91 alloy after two hours of corrosion for both the Ti6Al4V-AZ91 composite with and without interface. Although galvanic corrosion took place in both Ti6Al4V-AZ91 and Ti6Al4V-Na-AZ91 composites, the corrosion rate in Ti6Al4V-AZ91 composite was slightly higher because of the direct contact of the AZ91 and Ti6Al4V alloys. In the Ti6Al4V-Na-AZ91 composite having Na-rich interface, on the other hand, Ti6Al4V and AZ91 alloy did not directly contact each other due to the existence of sodium-rich layer. However, since the continuity of the coating layer was not preserved due to peeling (Figure 4.46), the coating didn't efficiently act as corrosion barrier. Despite the discontinuity of the coating layer, degradation of the

Mg-alloy regions were not as severe as Ti6Al4V-AZ91 (with no coating) in which deep cracks was formed, Figure 4.84(a).

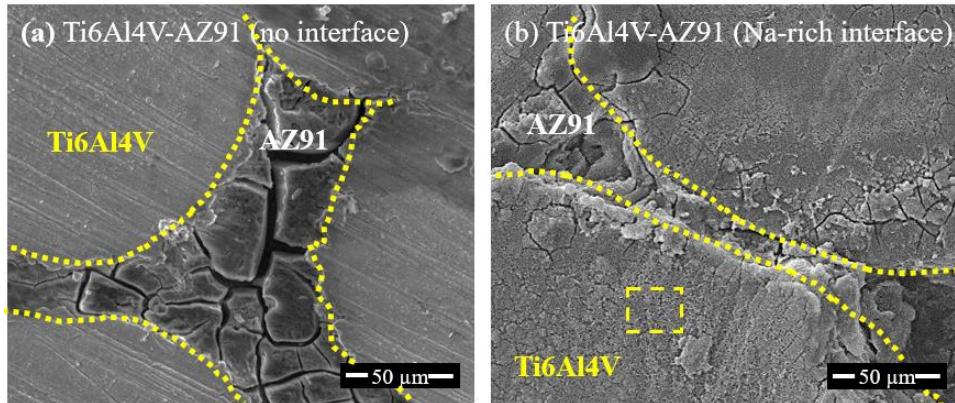


Figure 4.84 Microstructure showing the region between Ti6Al4V powder and AZ91 alloy of (a) Ti6Al4V-AZ91 and (b) Ti6Al4V-Na-AZ91 composites after immersion in SBF for two hours.

Figure 4.85 shows the morphological changes of the Na-containing composites during 1-10 days. In the Ti6Al4V-Na-Mg composites, Figure 4.85(a), significant changes occurred by selective dissolution of magnesium regions and precipitation of Ca and P rich agglomerates even after 2 days, Table 4.16. At the end of the five days, due to high pressure created by the H₂ gas, fracture occurred at neck regions of Ti-alloy as shown by white arrows in Figure 4.85(a). On the other hand, in the Ti6Al4V-Mg composites without Na-rich interface, relatively higher corrosion rate resulted in the loss of mechanical integrity totally after two days of immersion. However, complete degradation of mechanical integrity in the Ti6Al4V-Na-Mg composite (with interface) was observed after five days. On the other hand, presence of Na-rich layer was not altered the type of main corrosion products. In both types of Mg containing composites, with and without Na-rich interlayer, the main corrosion product was the magnesium hydroxide, Mg(OH)₂ phase, Figure 4.86. In some of the

composites, NaCl phase (coming from SBF) was detected even after they were cleaned with DI water, Figure 4.86(a).

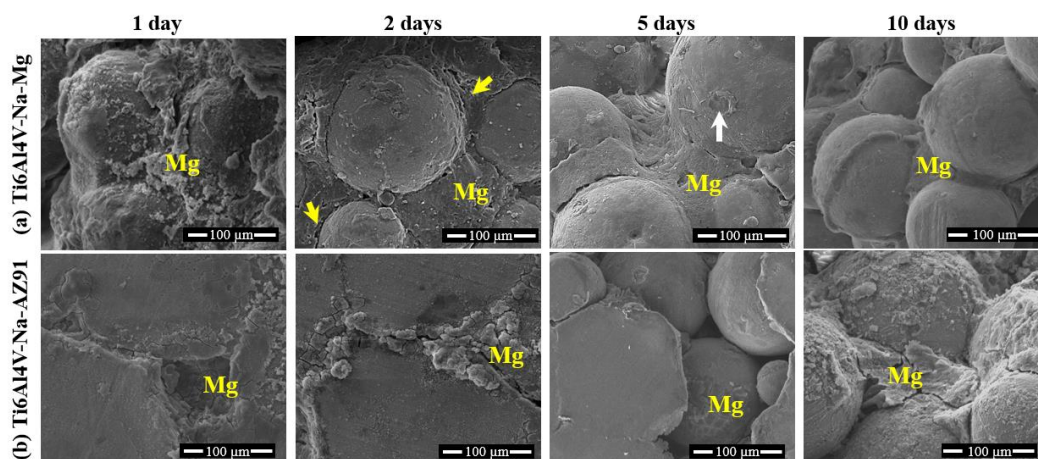


Figure 4.85 Surface morphological changes after immersion in SBF for 1-10 days
(a) Ti6Al4V-Na-Mg, (b) Ti6Al4V-Na-AZ91 composites.

In the Ti6Al4V-Na-AZ91 composites, for the first 2 days, Figure 4.85(b), the extensive swelling of the surface was detected on the AZ91 alloy sites in the form of blistering, similar to the Ti6Al4V-AZ91 composite without interface layer. Besides, Ca, P, Mg, and O rich agglomerates were detected on the corroded surfaces in the same period of immersion, Table 4.16. After five days, almost all of the magnesium alloy in the Ti6Al4V-Na-AZ91 composite corroded and dissolved in SBF. Accordingly, prior magnesium alloy sites became empty and left pores behind it, Figure 4.85(b). The complete removal of magnesium alloy in the Ti6Al4V-AZ91 composite (without interface) occurred between 2 and 5 days. On the other hand, in the composite with Na-rich interlayer, the time needed for complete dissolution of magnesium alloy was extended to five days. After ten days, pores left due to dissolution of magnesium alloy were observed to be refilled with Ca and P-rich phases with a Ca/P ratio of 0.80, Table 4.16 and Figure 4.85. Since Ca-rich phases

precipitated as a thin layer, they could not be detected by the XRD analysis. Only corrosion product of $\text{Mg}(\text{OH})_2$ was detected, Figure 4.86.

Table 4.16 EDS analysis taken from the Mg region in Figure 4.85.

		Element (wt. %)								
		O	Na	Mg	Al	P	Cl	Ca	Ti	V
(a)	1	33.16	1.08	45.45	-	8.12	8.69	8.69	3.5	-
	2	36.01	3.43	46.5	-	3.66	5.35	2.55	2.51	-
	5	33.15	1.75	53.05	2.37	2.37	5.47	1.56	2.66	-
	10	4.18	0.2	4.9	4.78	-	-	--	77.22	1.8
(b)	1	24.85	1.25	17.72	1.67	18.43	2.69	18.88	13.78	0.73
	2	20.12	1.23	17.51	1.89	16.82	-	16.41	3.5	0.94
	5	19.08	-	7.3	14.51	9.33	-	8.49	41.27	-
	10	24.55	-	10.56	10.21	13.92	-	14.39	26.37	-

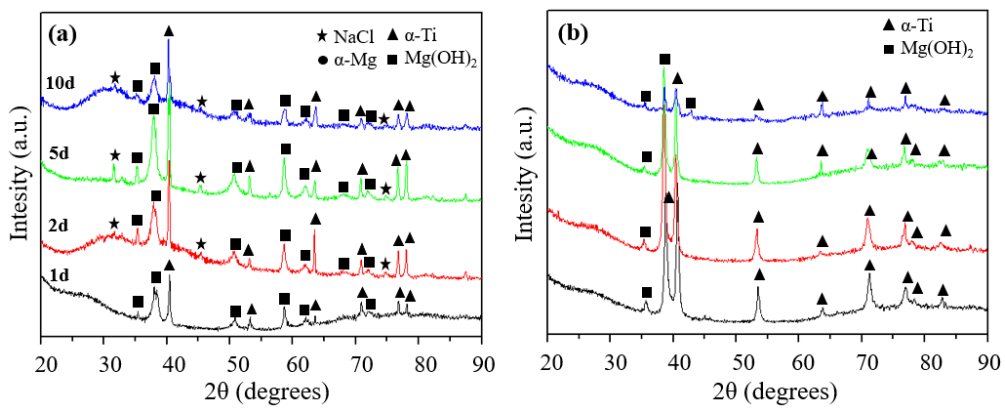


Figure 4.86 XRD analysis of (a) Ti6A4V-Na-Mg and (b) Ti6A14V-Na-AZ91 composites after immersion in SBF for 1- 10 days.

Figure 4.87 shows the variation of Ca/P ratios in all of the composites (with or without interface) during the in-vitro experiments (1-240 hours). All composites exhibited different Ca/P ratios after being exposed to SBF possibly due to non-homogenous precipitation of Ca-P rich phases. For the Ti6Al4V-Mg and Ti6Al4V-Na-Mg composites, the Ca/P ratio as high as 1.4 and 1.2, respectively, was detected. At some instant of the immersion test, a sudden decrease was detected in the Ca/P ratio for both composites. Although Ca/P ratio dropped to nearly zero after 8 h for Ti6Al4V-Mg, it took 240 h in Ti6Al4V-Na-Mg composites. The reason for the difference in disappearance time of Ca-P phase in two different composites was attributed to corrosion rates and bioactivities of the composites. Since the corrosion rate Ti6Al4V-Mg composite is relatively higher, the composite degraded too quickly by loss of its mechanical integrity due to sudden formation of thick Mg(OH)₂ layer and its subsequent dissolution in the solution. Accordingly, Ca-P phases didn't precipitate on Ti6Al4V powders left in the structure by sudden degradation of Mg. On the other hand, Ca-P phases found time to precipitate on Mg sites since its degradation was relatively slower in the presence of Na-rich coating. Moreover, Ca-P phases were able to precipitate even after complete dissolution of Mg in Ti6Al4V-Na-Mg composites possibly because of bioactive Na-rich coating layer on Ti6Al4V alloy powders. Similar tendency was also observed in Ti6Al4V-AZ91 composites with and without Na-rich interlayer. Although the Ca/P ratio never dropped to zero, possibly due to relatively higher corrosion resistance when AZ91 replaced with Mg in the composite, the Ca/P ratio became relatively higher in the composite with Na-rich layer especially after 24 h (Figure 4.87(b) and Table 4.16) at which magnesium alloy started degradation and underlying bioactive Na-rich coating started interaction with SBF.

Therefore, it can be concluded that, the presence of the Na-rich layer in the composites not only improves the corrosion by lessening the galvanic effect but also

enhances the bioactivity of the composites by allowing precipitation of Ca-P phases, which may be precursors for apatite nucleation.

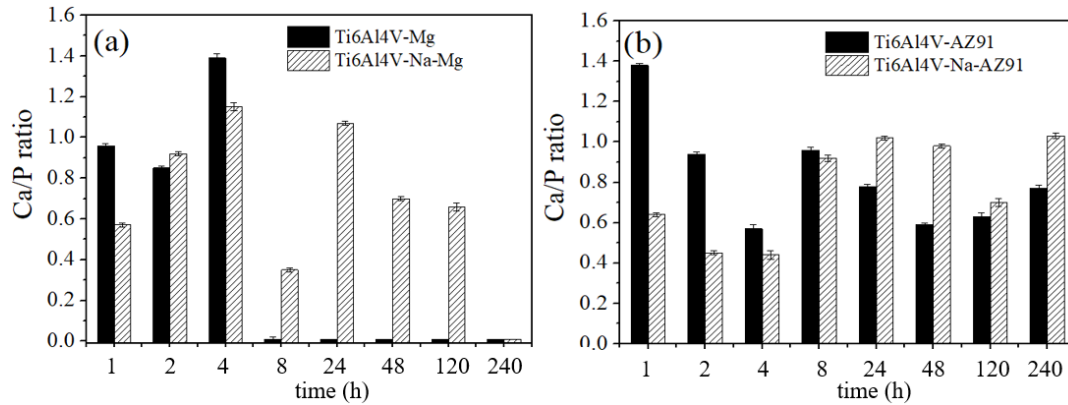


Figure 4.87 Ca/P ratio of the corroded surface in all the composites after immersion in SBF for 1, 2, 5, and 10 days.

4.3.3.2 pH change of SBF solution

The measurement of the pH gives information about the existence of various ions in the solution. Figure 4.88 shows pH changes of SBF solution in all composite samples (with and without Na-rich interface) during the in-vitro test. Observable changes were detected in the pH values of the SBF solutions at the end of the ten days. At the initial immersion times (up to two days), all composites performed similar tendency and pH reached around 9.8 and 9.2 for Ti6Al4V-Mg and Ti6Al4V-AZ91 (with and without interface) composites, respectively. It is known that the reason for the increase in pH is the dissolution reaction of Mg and the release of OH⁻ ion in the SBF solution. The rise in pH in the Mg containing composites was higher compared to AZ91 containing composites due to the higher degradation rate of Mg.

At the end of the three days, the composites with and without interface displayed different characteristics. The sudden decrease was observed in the both Mg and AZ91 containing composites, while pH was gradually raised to 10 and 9.8 for interface containing composites of Ti6Al4V-Mg and Ti6Al4V-AZ91, respectively. The reason may be attributed to a relatively higher amount of Ca^{2+} and PO_4^- ions precipitation from SBF, Table 4.16. The Na-rich coating layer enhanced the formation of Ca and P rich phases on the composites' surface [162,165], especially for Ti6Al4V-Na-Mg because no Ca and P rich phases were detected on the Ti6Al4V-Mg composite's surface. After six days, a similar trend was observed for all composites because of the solution renewal. For instance, pH stayed constant up to nine days and followed by a decrease around 9 for Ti6Al4V-Mg, Ti6Al4V-Na-Mg, and Ti6Al4V-Na-AZ91 composites and about 7.6 for Ti6Al4V-AZ91 composite. The apparent decrease can be explained by the fact that only porous Ti6Al4V remained in the structure.

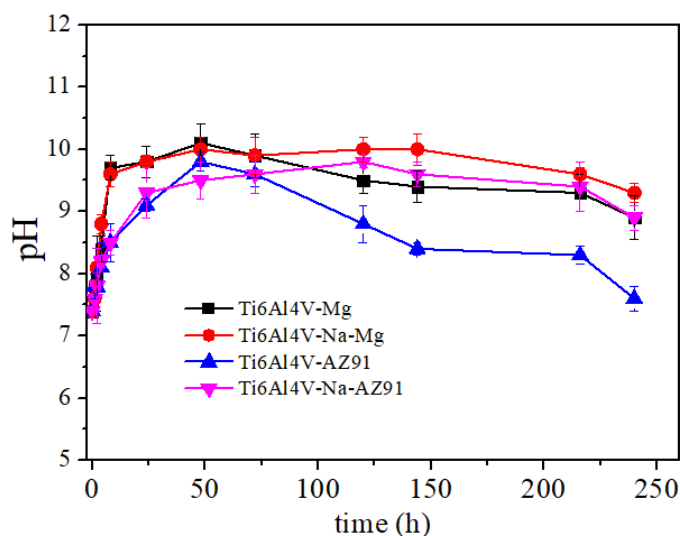


Figure 4.88 pH variations of composites during in-vitro tests.

4.3.3.3 Hydrogen evolution

The hydrogen evolution tests have been performed to determine the corrosion behavior of both Ti6Al4V-Na-Mg and Ti6Al4V-Na-AZ91 composites with respect to their counterparts without Na-rich interface. Since the hydrogen gas is a by-product of magnesium corrosion, its quantity is expected to be high when the corrosion rate is high.

Figure 4.89 displays the cumulative hydrogen volume in the composites with and without Na-rich interface. In Ti6Al4V-Mg composites, the presence of Na-rich interface significantly decreased the amount of cumulative hydrogen gas evolved during in-vitro tests. Na-rich coating lessened the galvanic corrosion and the composite with the Na-rich interface (Ti6Al4V-Na-Mg) possessed a significantly lower dissolution rate as revealed by the lower amount of hydrogen gas. In both Ti6Al4V-Mg and Ti6Al4V-Na-Mg composites, in the first two hours, hydrogen gas evolution rate was high. However, the rate of evolution reduced significantly in Na-rich interface containing composite, while the amount of hydrogen gas reached its maximum in Ti6Al4V-Mg (without interface) and remained constant until the end of experiment, Figure 4.89 (a). The hydrogen gas evolution rate was constant since all of the magnesium was consumed due to rapid corrosion and no fresh magnesium was left for further generation of hydrogen gas.

The influence of Na-rich coating on the hydrogen evolution in Ti6Al4V-AZ91 composites was different from Ti6Al4V-AZ91 composites, Figure 4.89(b). The rate of evolution was more or less the same for composites with and without coating and the hydrogen evolution behavior of both composites exhibited similar characteristics. At the initial immersion time (24 hours), the hydrogen evolution rate rapidly increased, and subsequently, the evolution rate become very small and a nearly constant rate was observed. That is to say, the effect of Na-rich coating was

not considerable in Ti6Al4V-AZ91 composites. As discussed in the previous chapters, combining AZ91 alloy with Ti6Al4V resulted in the formation of TiAl₃ phase as a result of reaction between liquid Mg-alloy and solid Ti-alloy which was also observed in composites containing Na-rich coating. TiAl₃ was shown to be possible interface compound which reduces the galvanic effect in Ti6Al4V-AZ91 composites. Possibly, the effect of additional Na-rich interface formation in the Ti6Al4V-AZ91 composites couldn't be detected since TiAl₃ was dominant in alleviating the galvanic corrosion. Although Na-rich coating layer had no detectable influence on corrosion rate, it increases the bioactivity of the composites by allowing precipitation of higher amount of Ca-P phases as shown in Figure 4.87(b).

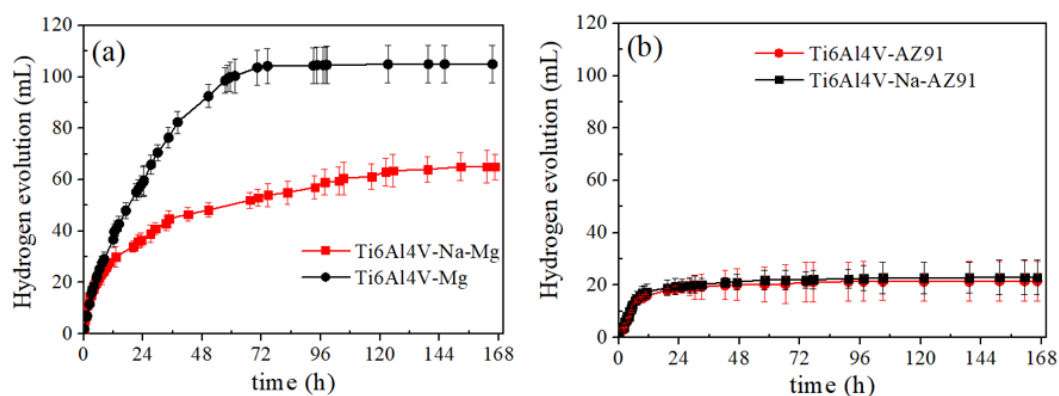


Figure 4.89 The comparison of hydrogen evolution of two different composite couples; (a) Ti6Al4V-Mg and Ti6Al4V-Na-Mg, and (b) Ti6Al4V-AZ91 and Ti6Al4V-Na-AZ91 composites.

4.3.3.4 Electrochemical tests

4.3.3.4.1 Galvanic corrosion test

The galvanic corrosion of as-cast unalloyed Mg and AZ91 alloy coupled with Na-coated Ti6Al4V alloy was investigated in order to see the influence of the presence of Na-rich coating on galvanic corrosion in coated Ti6Al4V alloy and Mg/Mg-alloy couples.

Figure 4.90 shows the change in galvanic corrosion potential and current density of unalloyed Mg and AZ91 alloy when coupled with both uncoated and coated Ti6Al4V alloy samples. It was clearly seen that the formation of the Na-rich phase on the Ti6Al4V lessened the galvanic effect between Ti6Al4V and Mg/Mg-alloys. For both of unalloyed Mg and AZ91 alloy, the corrosion current densities, which is directly proportional to degradation rate, decreased when they were coupled with Na-coated Ti6Al4V alloy.

Table 4.17 summarizes the galvanic corrosion parameters calculated by a statistical approach. After the formation of the Na-rich layer on the Ti6Al4V alloy, the galvanic resistance, R_g , of unalloyed Mg was increased from 58.01 to 69.58 Ω . Moreover, a significant change was detected on the R_g values of AZ91 coupled with Na-coated Ti6Al4V alloy, and about %50 increment was detected in R_g values, Table 4.17.

Therefore, the Na-rich layer alleviated the galvanic effect by decreasing the electrochemical difference between Ti6Al4V alloy and Mg/Mg-alloys. Although porous Ti6Al4V surfaces have a more complex surface structure, it is foreseen that galvanic corrosion between Ti and Mg will be minimized by the presence of biocompatible Na-rich interface.

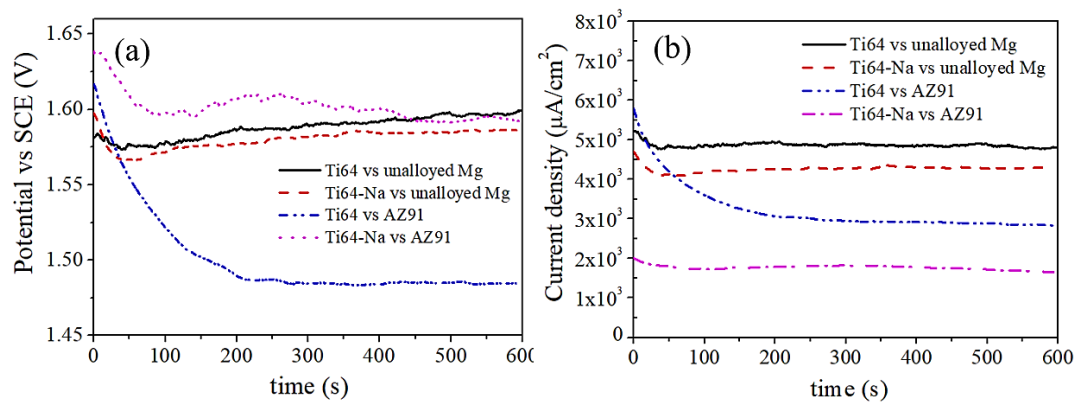


Figure 4.90 The change in (a) potential and (b) current density of Mg/Mg-alloys coupled with uncoated and Na-coated Ti6Al4V alloy.

Table 4.17 Galvanic corrosion parameters of unalloyed Mg, AZ91 coupled with uncoated and Na-coated Ti6Al4V alloy.

	Mean E_{corr} (V vs. SCE)	Mean I_{corr} (mA / cm ²)	Std. Dev. E, σ_E	Std. Dev. I, σ_I	Galvanic resistance, R_g (Ω)
Ti64 vs. unalloyed Mg	1.59	1.16	1.02E-03	1.76E-05	58.01
Ti64-Na vs. unalloyed Mg					
Mg	1.58	4.26	9.75E-04	1.40E-05	69.58
Ti64 vs. AZ91 alloy	1.49	0.82	9.79E-04	1.57E-05	62.45
Ti64-Na vs. AZ91 alloy	1.61	1.79	1.09E-03	1.19E-05	91.52

4.3.3.4.2 Potentiodynamic polarization test

In this part, the potentiodynamic polarization test has been conducted in order to understand how the corrosion rate of the Ti6Al4V-Mg and Ti6Al4V-AZ91 composites changed after Na-rich interface formation. Figure 4.91 shows the polarization curves of Ti6Al4V-Mg, Ti6Al4V-Na-Mg, Ti6Al4V-AZ91, and

Ti6Al4V-Na-AZ91 composites. Similar to the previous polarization experiments, the Tafel extrapolation method was used to obtain the corrosion potential (E_{corr}) and the current density (i_{corr}) of each sample, Table 4.18. Besides, corrosion rates (CR) of the composites, calculated according to ASTM G102 standard [183], were also given in Table 4.18.

Unlike to AZ91 containing composites, Ti6Al4V-Mg, and Ti6Al4V-Na-Mg composites displayed passivation characteristics in the anodic region due to the formation of $\text{Mg}(\text{OH})_2$ on the corroded surfaces, Figure 4.85(a). On the other hand, Ti6Al4V-AZ91 composites (with or without interface) had lower i_{corr} value compared to unalloyed Mg containing composites, Table 4.18, because of the enhanced the corrosion resistance as a result of coupling of Ti-alloy with AZ91 instead of pure Mg. Although Ti6Al4V-Mg composite possessed the highest i_{corr} value because of the galvanic corrosion between titanium and magnesium, the presence of Na-rich interface lessened the galvanic effect and both i_{corr} values and the corrosion rates of the composites reduced by 50%, Table 4.18.

The electrochemical polarization test revealed that the corrosion potential (E_{corr}) of the Ti6Al4V-AZ91 composite shifted towards a nobler direction from -1.55 to -1.53 mV by the creation of sodium-rich interface layer (Ti6Al4V-Na-AZ91), Figure 4.91. On the other hand, there was a little change observed in the i_{corr} and CR values of AZ91 containing composite, Table 4.18. Similar to hydrogen evolution tests, the presence of Na-rich interface in Ti6Al4V-AZ91 composites was found to be insignificant according to potentiodynamic polarization tests. However, Na-rich coating increases the bioactivity as discussed previously.

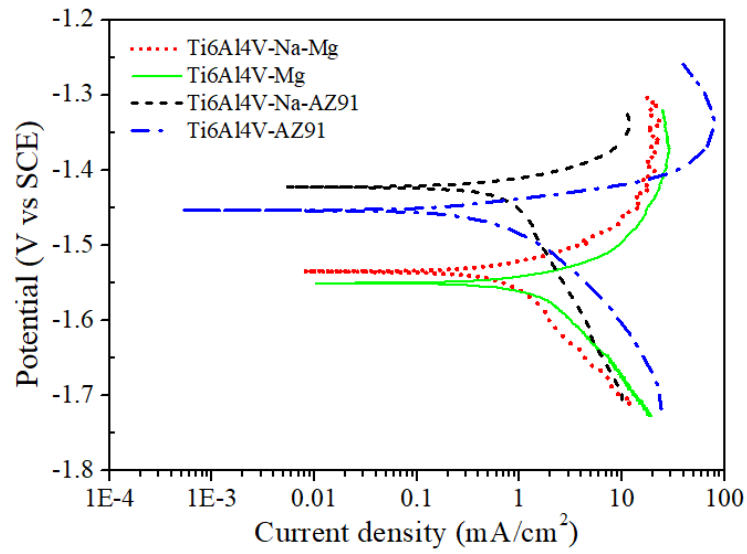


Figure 4.91 Polarization curves of composites in SBF at 37 °C.

Table 4.18 Corrosion parameters obtained from polarization curves of the composites.

Sample	E_{corr} (V vs SCE)	i_{corr} ($\mu\text{A}/\text{cm}^2$)	CR (mm/year)
Ti6Al4V-Mg	-1.55	1.76	25.22
Ti6Al4V-Na-Mg	-1.53	0.87	12.47
Ti6Al4V-AZ91	-1.45	0.78	10.19
Ti6Al4V-Na-AZ91	-1.42	0.81	10.58

CHAPTER 5

CONCLUSION

The most obvious findings and conclusions of the present study were presented in two main groups. Conclusions of the wetting tests, which were crucial in composite production, were given initially. Next, important findings about corrosion tests were listed by emphasizing the corrosion behaviors of bulk Mg/Mg-alloy, composites, and composites containing Na-rich interface.

1. The wetting angle between liquid magnesium and solid Ti6Al4V alloy was measured to be 12° at the end of the wetting test carried out at 800°C . Exactly the same angle was measured for liquid AZ91 alloy; however, the diameter of the melt pool of AZ91 alloy was observed to decrease during the test. The decrease in the dimension of melt pool was attributed to the Zn element, which is known to sublime due to its high vapor pressure, thereby causing significant evaporation of Mg. On the other hand, the wetting of liquid WE43 alloy was not as good as Mg and AZ91 alloy, and the contact angle was measured to be 25° .
2. The reaction between liquid Mg/Mg-alloy and Ti6Al4V and the oxide formation over liquid melt was observed to be dominant in the melting and wetting of Mg/Mg-alloy. For example, MgO formation by reduction of TiO_2 in unalloyed Mg tests retarded the spread of molten Mg over Ti-alloy. Moreover, MgO formation over the melt pool encapsulated liquid and prevented its wetting for a while. Likewise, reaction products across the interfaces of liquid Mg-alloy and Ti6Al4V were detected, which were mainly TiAl_3 and Y_2O_3 and Nd_2O_3 for AZ91 and WE43 alloys, respectively.

3. The presence of Na-rich coating over the solid Ti6Al4V alloy decreased the wettability of liquid Mg, and AZ91 alloy and the measured wetting angles for Mg and AZ91 alloy were around 25° and 35° , respectively. In addition to the reaction as revealed by the presence of MgO across the interface, the highly porous surface of the coating made the flow of liquid difficult.
4. For all as-cast bulk Mg/Mg-alloy samples, micro galvanic corrosion took place between anodic α -Mg matrix, where severe corrosion occurred, and the cathodic impurities/intermetallics, at which H_2 gas bubbles evolved.
5. The high volume fraction and homogenous distribution of $Mg_{17}Al_{12}$ intermetallics slowed down the corrosion of bulk AZ91 alloy by acting as a cathodic barrier. On the other hand, the corrosion accelerated in bulk WE43 by the undermining of cathodic $Mg_{24}Nd_5$ intermetallics due to corrosion of nearby anodic Mg matrix.
6. While unalloyed bulk Mg exhibited a higher degradation rate in a short time interval, the corrosion rate of WE43 alloy surpassed all of the magnesium samples because of the increase in the number of corrosion pits and localized corrosion by undermining of intermetallics.
7. The highest corrosion resistance of AZ91 alloy was attributed to the formation of a protective $CaCO_3$ phase on the surface as well as the presence of high volume fraction and homogenous distribution of $Mg_{17}Al_{12}$ cathodic intermetallics.
8. Among the composite samples, Ti6Al4V-Mg composites displayed the worst corrosion resistance. Relatively higher amount of hydrogen gas evolved at the interface region of dissimilar metals causes microcracks and final failure at sintering necks of Ti6Al4V alloy powders. As a result, the samples could not preserve their mechanical integrities even after 24 h of immersion.

9. AZ91 alloy infiltrated composites possessed the highest corrosion resistance, which was attributed to the formation of the TiAl_3 phase at the interface.
10. Although the galvanic coupling test revealed that WE43 alloy was more susceptible to galvanic corrosion when it was coupled with Ti6Al4V alloy, WE43 alloy infiltrated composites exhibited lower degradation rate compared to that of Ti6Al4V-Mg possibly because of secondary phases formed across the interface region.
11. The Na-rich coating, which was applied to minimize the galvanic effect, was observed to coat the surface of Ti6Al4V alloy homogeneously and had an average thickness of 500 nm. The EDS analysis of the coating revealed mainly Na, O, and Ti elements similar to the bioactive sodium titanate phase.
12. Although Na-rich coating covered the surfaces Ti6Al4V-Mg composites more homogeneously, severely cracked regions were detected in Ti6Al4V-AZ91 composite, possibly due to differences in surface chemistry and thermal expansion coefficients of Mg/Mg-alloys.
13. Potentiodynamic tests carried out on Na-coating Ti6Al4V-Mg, and Ti6Al4V-AZ91 composites displayed significant differences in corrosion rates. While the application of Na-rich coating in Ti6Al4V-Mg composites reduced the corrosion rate of the samples by 50%, nearly no changes in corrosion rates of Ti6Al4V-AZ91 composites when they contained Na-rich coating.
14. $\text{Mg}(\text{OH})_2$ phase was found as the main corrosion product in all corroded composites with and without coating because the degradation of Mg and the formation of $\text{Mg}(\text{OH})_2$ occurred simultaneously. Also, the precipitated phase containing Ca and P elements, referred to $\text{Ca}_3(\text{PO}_4)_2$ phase, was found to be common in the Ti6Al4V-AZ91 composite.
15. As the corrosion mechanism was not investigated in coated samples, the electrochemical impedance spectroscopy (EIS) test is recommended as a

future study to understand the operating corrosion mechanism of Ti6Al4V-Na-Mg/AZ91 composites in SBF.

REFERENCES

- [1] J. Park, R.S. Lakes, *Biomaterials*, 3rd ed., CRC Press, 2007.
- [2] X.-N. Gu, Y.-F. Zheng, A review on magnesium alloys as biodegradable materials, *Front. Mater. Sci. China*. 4 (2010) 111–115. doi:10.1007/s11706-010-0024-1.
- [3] J.B. Brunski, *Biomaterials and biomechanics in dental implant design.*, *Int. J. Oral Maxillofac. Implants*. 3 (1988) 85–97.
- [4] F. Witte, Reprint of: The history of biodegradable magnesium implants: A review, *Acta Biomater*. 23 (2015) S28–S40.
- [5] I. Kulinets, *Biomaterial applications in medicine*, Woodhead Publishing Limited, 2015. doi:10.1533/9780857099204.1.
- [6] B.D. Ratner, A.S. Hoffman, F.J. Schoen, J.E. Lemons, *Biomaterials Science : An Evolving , Multidisciplinary Endeavor*, Third Edit, Elsevier, 2013. doi:10.1016/B978-0-08-087780-8.00153-4.
- [7] B.M. Wroblewski, Professor Sir John Charnley (1911-1982), *Rheumatology*. 41 (2002) 824–825. doi:10.1093/rheumatology/41.7.824.
- [8] R.B. Smith, Arthur B. Voorhees, Jr.: Pioneer vascular surgeon, *J. Vasc. Surg*. 18 (1993) 341–348. doi:10.1016/0741-5214(93)90250-P.
- [9] I. Davis, B.H. Corp, Willem Kolff: Honoring a pioneer of modern dialysis, *ASN Kidney News*. (2009) 2009.
- [10] H.C. Lawson, P. Sampath, E. Bohan, M.C. Park, N. Hussain, A. Olivi, J. Weingart, L. Kleinberg, H. Bren, Interstitial chemotherapy for malignant gliomas: The Johns Hop- kins experience, *J Neurooncol*. 83 (2007) 61–70.

- [11] B.D. Ratner, A.S. Hoffman, F.J. Schoen, J.E. Lemons, *Biomaterials Science*, 1996. doi:10.1016/b978-012582460-6/50002-5.
- [12] L.L. Hench, I. Thompson, Twenty-first century challenges for biomaterials, *J. R. Soc. Interface*. 7 (2010). doi:10.1098/rsif.2010.0151.focus.
- [13] K. Prasad, O. Bazaka, M. Chua, M. Rochford, L. Fedrick, J. Spoor, R. Symes, M. Tieppo, C. Collins, A. Cao, D. Markwell, K. Ostrikov, K. Bazaka, *Metallic biomaterials: Current challenges and opportunities*, *Materials (Basel)*. 10 (2017). doi:10.3390/ma10080884.
- [14] N. Hort, Y. Huang, D. Fechner, M. Störmer, C. Blawert, F. Witte, C. Vogt, H. Drücker, R. Willumeit, K.U. Kainer, F. Feyerabend, Magnesium alloys as implant materials-Principles of property design for Mg-RE alloys, *Acta Biomater*. 6 (2010) 1714–1725. doi:10.1016/j.actbio.2009.09.010.
- [15] F. Witte, N. Hort, C. Vogt, S. Cohen, K.U. Kainer, R. Willumeit, F. Feyerabend, Degradable biomaterials based on magnesium corrosion, *Curr. Opin. Solid State Mater. Sci*. 12 (2008) 63–72.
- [16] M.P. Staiger, A.M. Pietak, J. Huadmai, G. Dias, Magnesium and its alloys as orthopedic biomaterials: A review, *Biomaterials*. 27 (2006) 1728–1734. doi:10.1016/j.biomaterials.2005.10.003.
- [17] M. Bornapour, M. Celikin, M. Cerruti, M. Pekguleryuz, Magnesium implant alloy with low levels of strontium and calcium : The third element effect and phase selection improve bio-corrosion resistance and mechanical performance, *Mater. Sci. Eng. C*. 35 (2014) 267–282.
- [18] A. Nouri, P.D. Hodgson, C. Wen, Biomimetic Porous Titanium Scaffolds for Orthopedic and Dental Applications, in: A. Mukherjee (Ed.), *Biomimetics Learn. From Nat.*, 2010: pp. 415–451.

- [19] M. Peuster, C. Fink, P. Wohlsein, M. Bruegmann, A. Günther, V. Kaese, M. Niemeyer, H. Haferkamp, C. V. Schnakenburg, Degradation of tungsten coils implanted into the subclavian artery of New Zealand white rabbits is not associated with local or systemic toxicity, *Biomaterials*. 24 (2003) 393–399. doi:10.1016/S0142-9612(02)00352-6.
- [20] H. Hermawan, D. Dubé, D. Mantovani, Degradable metallic biomaterials: Design and development of Fe-Mn alloys for stents, *J. Biomed. Mater. Res. - Part A*. 93 (2010) 1–11. doi:10.1002/jbm.a.32224.
- [21] S. Bose, A. Bandyopadhyay, *Characterization of Biomaterials*, 2013.
- [22] S. D'Souza, G. Ferrante, P. Tyczynski, C. Di Mario, Biodegradable Stents – A New Era?, *Eur. Cardiol. Rev.* 4 (2008) 82. doi:10.15420/ecr.2008.4.2.82.
- [23] I. Galaev, B. Mattiasson, Smart polymers and what they could do in biotechnology and medicine, *Trends Biotechnol.* 17 (1999) 335–340.
- [24] B.D. Ulery, L.S. Nair, C.T. Laurencin, Biomedical applications of biodegradable polymers, *J. Polym. Sci. Part B Polym. Phys.* 49 (2011) 832–864. doi:10.1002/polb.22259.
- [25] G. Heness, B. Ben-Nissan, Innovative bioceramics, *Mater. Forum*. 27 (2004) 104–114.
- [26] A. Pasđnldđ, R.S. Aksoy, Yapay Kemik Uygulamaları İçin Hidroksiapatit Hydroxyapatite For Artificial Bone Applications, 2010 (2010) 41–51.
- [27] T. V. Thamaraiselvi, S. Rajeswar, Biological evaluation of bioceramic materials-a review, *Carbon N. Y.* 24 (2004) 172.
- [28] J. Yang, J.L. Guo, A.G. Mikos, H. Chunyan, G. Cheng, Material Processing and Design of Biodegradable Metal Matrix Composites for Biomedical Applications, *Ann. Biomed. Eng.* 46 (2018) 1229–1240. doi:10.1007/s10439-

018-2058-y.

- [29] P. Feng, J. He, S. Peng, C. Gao, Z. Zhao, S. Xiong, C. Shuai, Characterizations and interfacial reinforcement mechanisms of multicomponent biopolymer based scaffold, *Mater. Sci. Eng. C*. 100 (2019) 809–825.
- [30] İ. Yavuz, *Orthodontics - Teeth*, (2015).
- [31] Y.F. Zheng, X.N. Gu, F. Witte, Biodegradable metals, *Mater. Sci. Eng. R Reports*. 77 (2014) 1–34. doi:10.1016/j.mser.2014.01.001.
- [32] Y.M. Wang, F.H. Wang, M.J. Xu, B. Zhao, L.X. Guo, J.H. Ouyang, Microstructure and corrosion behavior of coated AZ91 alloy by microarc oxidation for biomedical application, *Appl. Surf. Sci.* 255 (2009) 9124–9131. doi:10.1016/j.apsusc.2009.06.116.
- [33] Y. Pan, S. He, D. Wang, D. Huang, T. Zheng, S. Wang, P. Dong, C. Chen, In vitro degradation and electrochemical corrosion evaluations of microarc oxidized pure Mg, Mg-Ca and Mg-Ca-Zn alloys for biomedical applications, *Mater. Sci. Eng. C*. 47 (2015) 85–96. doi:10.1016/j.msec.2014.11.048.
- [34] S. V. Dorozhkin, Calcium orthophosphate coatings on magnesium and its biodegradable alloys, *Acta Biomater.* 10 (2014) 2919–2934. doi:10.1016/j.actbio.2014.02.026.
- [35] G. Sahu, A Brief Review on MG Alloys Their Properties and Application, *Int. J. Adv. Res. Sci. Eng.* 8354 (2015) 65–71.
- [36] J.E.G. González, J.C. Mirza-Rosca, Study of the corrosion behavior of titanium and some of its alloys for biomedical and dental implant applications, *J. Electroanal. Chem.* 471 (1999) 109–115. doi:10.1016/S0022-0728(99)00260-0.
- [37] K. Gusieva, C.H.J. Davies, J.R. Scully, N. Birbilis, Corrosion of magnesium

- alloys: the role of alloying, *Int. Mater. Rev.* 60 (2015) 169–194. doi:10.1179/1743280414Y.00000000046.
- [38] P.G. Laing, *Clinical Experience With Prosthetic Materials: Historical Perspectives, Current Problems, And Future Directions*, in: *Int Symp Corros Degrad. Implant Mater*, Kansas City, 1979: pp. 199–211.
- [39] R. Waksman, R. Pakala, R. Baffour, R. Seabron, D. Hellinga, F.O. Tio, Short-term effects of biocorrosible iron stents in porcine coronary arteries, *J. Interv. Cardiol.* 21 (2008) 15–20. doi:10.1111/j.1540-8183.2007.00319.x.
- [40] M. Schinhammer, P. Steiger, F. Moszner, J.F. Löffler, P.J. Uggowitzer, Degradation performance of biodegradable FeMnC(Pd) alloys, *Mater. Sci. Eng. C.* 33 (2013) 1882–1893. doi:10.1016/j.msec.2012.10.013.
- [41] S. Zhu, N. Huang, L. Xu, Y. Zhang, H. Liu, Y. Lei, H. Sun, Y. Yao, Biocompatibility of Fe-O films synthesized by plasma immersion ion implantation and deposition, *Surf. Coatings Technol.* 203 (2009) 1523–1529. doi:10.1016/j.surfcoat.2008.11.033.
- [42] S. Hiromoto, A. Yamamoto, Control of degradation rate of bioabsorbable magnesium by anodization and steam treatment, *Mater. Sci. Eng. C.* 30 (2010) 1085–1093. doi:10.1016/j.msec.2010.06.001.
- [43] J.R.P.D. Hendra Hermawan, Dadan Ramdan, Metals for biomedical applications, *Biomed. Eng. - From Theory to Appl.* (2011) 411–430. doi:10.5772/2629.
- [44] V. Jokanović, M. Vilotijević, B. Jokanović, M. Jenko, I. Anžel, D. Stamenković, V. Lazic, R. Rudolf, Investigations of corrosion on the surface of titanium substrate caused by combined alkaline and heat treatment, *Corros. Sci.* 82 (2014) 180–190. doi:10.1016/j.corsci.2014.01.014.

- [45] Y. Xie, L. Zhao, Z. Zhang, X. Wang, R. Wang, C. Cui, Fabrication and properties of porous Zn-Ag alloy scaffolds as biodegradable materials, *Mater. Chem. Phys.* 219 (2018) 433–443. doi:10.1016/j.matchemphys.2018.08.023.
- [46] P. Wen, M. Voshage, L. Jauer, Y. Chen, Y. Qin, R. Poprawe, J.H. Schleifenbaum, Laser additive manufacturing of Zn metal parts for biodegradable applications: Processing, formation quality and mechanical properties, *Mater. Des.* 155 (2018) 36–45. doi:10.1016/j.matdes.2018.05.057.
- [47] T.J. Butler, R.W. Jackson, J.Y. Robson, R.J.T. Owen, H.T. Delves, C.E. Sieniawska, J.D.G. Rose, In vivo degradation of tungsten embolisation coils, *Br. J. Radiol.* 73 (2000) 601–603. doi:10.1259/bjr.73.870.10911782.
- [48] D. Humphry, XXIII. Electro-chemical researches, on the decomposition of the earths; with observations on the metals obtained from the alkaline earths, and on the amalgam procured from ammonia, *R. Soc.* 98 (1808).
- [49] J. Geng, M.F. Chisholm, R.K. Mishra, K.S. Kumar, An electron microscopy study of dislocation structures in Mg single crystals compressed along [0 0 0 1] at room temperature, *Philos. Mag.* 95 (2015) 3910–3932. doi:10.1080/14786435.2015.1108531.
- [50] M. Bornapour, Investigation of New Biodegradable Magnesium Alloy with Improved Biocorrosion, Biocompatibility and Mechanical Properties For Use In Temporary Cardiovascular Stents, 2014.
- [51] L.W. Evans, Metal Production: Electrometallurgy, *Encycl. Mater. Sci. Technol.* (Second Ed. (2003) 1–12.
- [52] Q. Chen, G. a. Thouas, Metallic implant biomaterials, *Mater. Sci. Eng. R Reports.* 87 (2015) 1–57. doi:10.1016/j.mser.2014.10.001.
- [53] A. Atrens, G.-L. Song, M. Liu, Z. Shi, F. Cao, M.S. Dargusch, Review of

- Recent Developments in the Field of Magnesium Corrosion, *Adv. Eng. Mater.* 17 (2015) 400–453. doi:10.1002/adem.201400434.
- [54] M. Esmaily, J.E. Svensson, S. Fajardo, N. Birbilis, G.S. Frankel, S. Virtanen, R. Arrabal, S. Thomas, L.G. Johansson, Fundamentals and advances in magnesium alloy corrosion, *Prog. Mater. Sci.* 89 (2017) 92–193. doi:10.1016/j.pmatsci.2017.04.011.
- [55] J. Walker, S. Shadanbaz, T.B.F. Woodfield, M.P. Staiger, G.J. Dias, Review Article Magnesium biomaterials for orthopedic application : A review from a biological perspective, (2014) 1316–1331. doi:10.1002/jbm.b.33113.
- [56] M.S. Uddin, C. Hall, P. Murphy, Surface treatments for controlling corrosion rate of biodegradable Mg and Mg-based alloy implants, *Sci. Technol. Adv. Mater.* 16 (2015) 053501. doi:10.1088/1468-6996/16/5/053501.
- [57] B.J.C. Luthringer, F. Feyerabend, R. Willumeit-römer, Magnesium-based implants : a mini-review, *Magnes. Res.* 27 (2014) 142–54.
- [58] H. Eggebrecht, J. Rodermann, P. Hunold, A. Schmermund, Images in Cardiovascular Medicine Novel Magnetic Resonance – Compatible Coronary Stent, *Images Cardiovasc. Med.* 112 (2005) 303–304.
- [59] M. Ascencio, M. Pekguleryuz, S. Omanovic, An investigation of the corrosion mechanisms of WE43Mg alloy in a modified simulated body fluid solution: The effect of electrolyte renewal, *Corros. Sci.* 91 (2015) 297–310. doi:10.1016/j.corsci.2014.11.034.
- [60] D. Paramitha, M.F. Ulum, A. Purnama, Monitoring degradation products and metal ions in vivo, 2016. doi:10.1016/B978-0-08-100603-0.00002-X.
- [61] M. Ascencio, M. Pekguleryuz, S. Omanovic, An investigation of the corrosion mechanisms of WE43 Mg alloy in a modified simulated body fluid solution :

- The influence of immersion time, *Corros. Sci.* 87 (2014) 489–503. doi:10.1016/j.corosci.2014.07.015.
- [62] M.I. Jamesh, G. Wu, Y. Zhao, D.R. McKenzie, M.M.M. Bilek, P.K. Chu, Electrochemical corrosion behavior of biodegradable Mg-Y-RE and Mg-Zn-Zr alloys in Ringer's solution and simulated body fluid, *Corros. Sci.* 91 (2015) 160–184. doi:10.1016/j.corosci.2014.11.015.
- [63] R.-C. Zeng, Z.-Z. Yin, X.-B. Chen, D.-K. Xu, Corrosion Types of Magnesium Alloys, in: *Magnes. Alloy. - Sel. Issue*, IntechOpen, 2018.
- [64] ASTM F3044-14, Standard Test Method for Evaluating the Potential for Galvanic Corrosion for Medical Implants, 2014. doi:10.1520/F3044-14.N.
- [65] G.L. Song, A. Atrens, Corrosion Mechanisms of Magnesium Alloys, *Adv. Eng. Mater.* 1 (1999) 11–33.
- [66] S. Yan, G. Song, Z. Li, H. Wang, D. Zheng, A state-of-the-art review on passivation and biofouling of Ti and its alloys in marine environments *Journal of Materials Science & Technology* A state-of-the-art review on passivation and biofouling of Ti and its alloys in marine environments, *J. Mater. Sci. Technol.* 34 (2017) 421–435. doi:10.1016/j.jmst.2017.11.021.
- [67] M.C. Zhao, M. Liu, G. Song, A. Atrens, Influence of the β -phase morphology on the corrosion of the Mg alloy AZ91, *Corros. Sci.* 50 (2008) 1939–1953. doi:10.1016/j.corosci.2008.04.010.
- [68] W. Zhou, T. Shen, N.N. Aung, Effect of heat treatment on corrosion behaviour of magnesium alloy AZ91D in simulated body fluid, *Corros. Sci.* 52 (2010) 1035–1041. doi:10.1016/j.corosci.2009.11.030.
- [69] O. Lunder, J.. Lein, T. Kr Aune, K. Nisancioglu, The Role of Mg₁₇Al₁₂ Phase in the Corrosion of Mg Alloy AZ91, *Corrosion.* 45 (1989) 741–745.

- [70] A.E. Coy, F. Viejo, P. Skeldon, G.E. Thompson, Susceptibility of rare-earth-magnesium alloys to micro-galvanic corrosion, Elsevier Ltd, 2010. doi:10.1016/j.corsci.2010.08.006.
- [71] R. Zeng, W. Dietzel, F. Witte, N. Hort, C. Blawert, Progress and challenge for magnesium alloys as biomaterials, *Adv. Eng. Mater.* 10 (2008) 3–14. doi:10.1002/adem.200800035.
- [72] N. Winzer, A. Atrens, G. Song, E. Ghali, W. Dietzel, K.U. Kainer, N. Hort, C. Blawert, A critical review of the Stress Corrosion Cracking (SCC) of magnesium alloys, *Adv. Eng. Mater.* 7 (2005) 659–693. doi:10.1002/adem.200500071.
- [73] Y. Yang, F. Scenini, M. Curioni, A study on magnesium corrosion by real-time imaging and electrochemical methods: Relationship between local processes and hydrogen evolution, *Electrochim. Acta.* 198 (2016) 174–184. doi:10.1016/j.electacta.2016.03.043.
- [74] M. Peron, J. Torgersen, F. Berto, Mg and Its Alloys for Biomedical Applications: Exploring Corrosion and Its Interplay with Mechanical Failure, *Metals (Basel)*. 7 (2017) 252. doi:10.3390/met7070252.
- [75] G.L. Maker, J. Kruger, Corrosion Studies of Rapidly Solidified Magnesium Alloys, 137 (1990) 414–421.
- [76] J. Chen, J. Dong, J. Wang, E. Han, W. Ke, Effect of magnesium hydride on the corrosion behavior of an AZ91 magnesium alloy in sodium chloride solution, *Corros. Sci.* 50 (2008) 3610–3614. doi:10.1016/j.corsci.2008.09.013.
- [77] T. Zhang, Y. Li, F. Wang, Roles of b phase in the corrosion process of AZ91D magnesium alloy, 48 (2006) 1249–1264. doi:10.1016/j.corsci.2005.05.011.

- [78] J. Hanawalt, C. Nelson, J. Peloubet, Corrosion studies of magnesium and its alloy, *Trans AIME*. 147 (1942) 273–99.
- [79] W.S. Loose, *Corrosion and Protection of magnesium*, ASM Int. Materials Park, 1946.
- [80] G.M. Naik, N. Sannayellappa, S.S. Kumar, Review article Corrosion of ECAPed magnesium alloys and its background : A Review, 29 (2019) 1–20. doi:10.14456/jmmm.2019.13.
- [81] H.Q. Ang, *Mechanical Properties and Deformation Behaviour of High-Pressure Die-Cast Magnesium-Aluminium Based Alloys*, 2017. doi:10.13140/RG.2.2.25893.81127.
- [82] G. Song, a. Atrens, X. Wu, B. Zhang, Corrosion behaviour of az10\ az490 and az80 in sodium chloride, *Corros. Sci.* 40 (1998) 1769–1791.
- [83] S. Mathieu, C. Rapin, J. Steinmetz, P. Steinmetz, A corrosion study of the main constituent phases of AZ91 magnesium alloys, *Corros. Sci.* 45 (2003) 2741–2755. doi:10.1016/S0010-938X(03)00109-4.
- [84] Z.Z. Zhou, W. Yang, S.H. Chen, H. Yu, Z.F. Xu, Combined effect of non-equilibrium solidification and thermal annealing on microstructure evolution and hardness behavior of AZ91 magnesium alloy, *Phys. B Condens. Matter.* 443 (2014) 35–42. doi:10.1016/j.physb.2014.02.052.
- [85] S. Verdier, N. Van Der Laak, S. Delalande, J. Metson, F. Dalard, The surface reactivity of a magnesium-aluminium alloy in acidic fluoride solutions studied by electrochemical techniques and XPS, *Appl. Surf. Sci.* 235 (2004) 513–524. doi:10.1016/j.apsusc.2004.03.250.
- [86] J. Liao, M. Hotta, N. Yamamoto, Corrosion behavior of fine-grained AZ31B magnesium alloy, *Corros. Sci.* 61 (2012) 208–214.

- [87] E. Bütev Öcal, Z. Esen, K. Aydınol, A.F. Dericioglu, Comparison of the short and long-term degradation behaviors of as-cast pure Mg , AZ91 and WE43 alloys, *Mater. Chem. Phys.* 241 (2020). doi:10.1016/j.matchemphys.2019.122350.
- [88] M. Esmaily, D.B. Blücher, J.E. Svensson, M. Halvarsson, L.G. Johansson, New insights into the corrosion of magnesium alloys — The role of aluminum, *Scr. Mater.* 115 (2016) 91–95.
- [89] O. Lunder, J.E. Lein, S.M. Hesjevik, T.K. Aune, K. Nişancıoğlu, Corrosion morphologies on magnesium alloy AZ 91, *Mater. Corros.* 45 (1994).
- [90] S. Cai, T. Lei, N. Li, F. Feng, Effects of Zn on microstructure , mechanical properties and corrosion behavior of Mg – Zn alloys, *Mater. Sci. Eng. C.* 32 (2012) 2570–2577. doi:10.1016/j.msec.2012.07.042.
- [91] Y. Chen, Z. Xu, C. Smith, J. Sankar, Recent advances on the development of magnesium alloys for biodegradable implants, *Acta Biomater.* 10 (2014) 4561–4573. doi:10.1016/j.actbio.2014.07.005.
- [92] Z. Xin, Z. Kui, L.I. Xinggang, D. Xia, L.I. Yongjun, Effect of solid-solution treatment on corrosion and electrochemical behaviors of Mg-15Y alloy in 3 . 5 wt .% NaCl solution, *J. Rare Earths.* 30 (2012) 1158–1167. doi:10.1016/S1002-0721(12)60198-7.
- [93] F. Feyerabend, J. Fischer, J. Holtz, F. Witte, R. Willumeit, H. Drücker, C. Vogt, N. Hort, Evaluation of short-term effects of rare earth and other elements used in magnesium alloys on primary cells and cell lines q, *Acta Biomater.* 6 (2010) 1834–1842. doi:10.1016/j.actbio.2009.09.024.
- [94] Y. Chino, M. Kado, M. Mabuchi, Enhancement of tensile ductility and stretch formability of magnesium by, 494 (2008) 343–349.

- [95] E. Willbold, X. Gu, D. Albert, K. Kalla, K. Bobe, M. Brauneis, C. Janning, J. Nellesen, W. Czayka, W. Tillmann, Y. Zheng, F. Witte, *Acta Biomaterialia* Effect of the addition of low rare earth elements (lanthanum , neodymium , cerium) on the biodegradation and biocompatibility of magnesium, *ACTA Biomater.* (2014). doi:10.1016/j.actbio.2014.09.041.
- [96] J. Niu, M. Xiong, X. Guan, J. Zhang, H. Huang, J. Pei, G. Yuan, The in vivo degradation and bone-implant interface of Mg-Nd-Zn-Zr alloy screws: 18 months post-operation results, *Eval. Program Plann.* (2016) 1–5. doi:10.1016/j.corsci.2016.10.009.
- [97] G. Cao, D. Zhang, W. Zhang, W. Zhang, In Vitro Corrosion Study of Friction Stir Processed WE43 Magnesium Alloy in a Simulated Body Fluid, (2016). doi:10.3390/ma9070542.
- [98] N.T. Kirkland, N. Birbilis, M.P. Staiger, Assessing the corrosion of biodegradable magnesium implants: A critical review of current methodologies and their limitations, *Acta Biomater.* 8 (2012) 925–936. doi:10.1016/j.actbio.2011.11.014.
- [99] S. Zhang, X. Zhang, C. Zhao, J. Li, Y. Song, C. Xie, H. Tao, Y. Zhang, Y. He, Y. Jiang, Y. Bian, Research on an Mg-Zn alloy as a degradable biomaterial, *Acta Biomater.* 6 (2010) 626–640. doi:10.1016/j.actbio.2009.06.028.
- [100] J. Wang, C.E. Smith, J. Sankar, Y. Yun, N. Huang, Absorbable magnesium-based stent: physiological factors to consider for in vitro degradation assessments., *Regen. Biomater.* 2 (2015) 59–69. doi:10.1093/rb/rbu015.
- [101] Y. Sasikumar, M.M. Solomon, L.O. Olasunkanmi, E.E. Ebenso, Effect of surface treatment on the bioactivity and electrochemical behavior of magnesium alloys in simulated body fluid, *Mater. Corros.* 68 (2017) 776–790.

- [102] eta B. and S.F. Batlle, V.B. and S.F.B. Maria C. Delgado, Federico R. García-Galvan, A Measuring Approach to Assess the Corrosion Rate of A Measuring Approach to Assess the Corrosion Rate of Magnesium Alloys Using Electrochemical Impedance Spectroscopy Magnesium Alloys Using Electrochemical Impedance Spectroscopy, (n.d.). doi:10.5772/65018.
- [103] Y. Guo, W. Liu, S. Ma, J. Wang, J. Zou, Z. Liu, J. Zhao, Y. Zhou, A preliminary study for novel use of two Mg alloys (WE43 and Mg3Gd), *J. Mater. Sci. Mater. Med.* 27 (2016) 1–14. doi:10.1007/s10856-016-5691-8.
- [104] ASTM G31 – 72, Standard Practice for Laboratory Immersion Corrosion Testing of Metals1, 2012. doi:10.1520/G0031-72R04.2.
- [105] Q. Li, G. Jiang, C. Wang, J. Dong, G. He, Mechanical degradation of porous titanium with entangled structure filled with biodegradable magnesium in Hanks' solution, *Mater. Sci. Eng. C.* 57 (2015) 349–354. doi:10.1016/j.msec.2015.08.008.
- [106] S.Z. Khalajabadi, N. Ahmad, S. Izman, A. Bin Haji Abu, W. Haider, M.R. Abdul Kadir, In-vitro biodegradation, electrochemical corrosion evaluations and mechanical properties of an Mg/HA/TiO₂ nanocomposite for biomedical applications, *J. Alloys Compd.* 696 (2017) 768–781. doi:10.1016/j.jallcom.2016.11.106.
- [107] S. Thomas, N. V. Medhekar, G.S. Frankel, N. Birbilis, Corrosion mechanism and hydrogen evolution on Mg, *Curr. Opin. Solid State Mater. Sci.* 19 (2015) 85–94. doi:10.1016/j.cossms.2014.09.005.
- [108] S. Johnston, Z. Shi, M.S. Dargusch, A. Atrens, Influence of surface condition on the corrosion of ultra-high-purity Mg alloy wire, *Corros. Sci.* 108 (2016) 66–75. doi:10.1016/j.corsci.2016.03.007.

- [109] G. Song, A. Atrens, D. SUohn, An Hydrogen Evolution Method for the Estimation of the Corrosion Rate of Magnesium Alloys, in: S.N. Mathaudhu, A.A. Luo, N.R. Neelameggham, E.A. Nyberg, W.H. Sillekens (Eds.), *Essent. Readings Magnes. Technol.*, The Minerals, Metals & Materials Society, John Wiley&Sons, 2014: pp. 565–572.
- [110] S.M. Kim, J.H. Jo, S.M. Lee, M.H. Kang, H.E. Kim, Y. Estrin, J.H. Lee, J.W. Lee, Y.H. Koh, Hydroxyapatite-coated magnesium implants with improved in vitro and in vivo biocorrosion, biocompatibility, and bone response, *J. Biomed. Mater. Res. - Part A*. 102 (2014) 429–441. doi:10.1002/jbm.a.34718.
- [111] L. Xu, E. Zhang, K. Yang, Phosphating treatment and corrosion properties of Mg-Mn-Zn alloy for biomedical application, *J. Mater. Sci. Mater. Med.* 20 (2009) 859–867. doi:10.1007/s10856-008-3648-2.
- [112] M. Sophocleous, J.K. Atkinson, *Sensors and Actuators A : Physical* A review of screen-printed silver / silver chloride (Ag / AgCl) reference electrodes potentially suitable for environmental potentiometric sensors, *Sensors Actuators A. Phys.* 267 (2017) 106–120. doi:10.1016/j.sna.2017.10.013.
- [113] H.A.G. Stern, D.R. Sadoway, J.W. Tester, Copper sulfate reference electrode, *J. Electroanal. Chem.* 659 (2011) 143–150.
- [114] G. Baril, G. Galicia, C. Deslouis, N. Pébère, B. Tribollet, V. Vivier, An impedance investigation of the mechanism of pure magnesium corrosion in sodium sulfate solutions, *J. Electrochem. Soc.* 154 (2007) 108–113. doi:10.1149/1.2401056.
- [115] G.-L. Song, Z. Xu, The surface, microstructure and corrosion of magnesium alloy AZ31 sheet, *Electrochim. Acta.* 55 (2010) 4148–4161. doi:10.1016/j.electacta.2010.02.068.

- [116] B.H. Lee, Y. Do Kim, K.H. Lee, XPS study of bioactive graded layer in Ti–In–Nb–Ta alloy prepared by alkali and heat treatments, *Biomaterials*. 24 (2003) 2257–2266. doi:10.1016/S0142-9612(03)00034-6.
- [117] P. Tian, X. Liu, Surface modification of biodegradable magnesium and its alloys for biomedical applications, *Regen. Biomater.* (2015) 135–151. doi:10.1093/rb/rbu013.
- [118] D.G. Enos, L.L. Scribner, The Potentiodynamic Polarization Scan The Potentiodynamic Polarization Scan Technical Report 33, (n.d.).
- [119] R. Baboian, Electrochemical Test, in: *Corros. Tests Stand. Appl. Interpret.*, 2nd ed., ASTM Internationa, 2005.
- [120] Z. Li, G.-L. Song, S. Song, Effect of bicarbonate on biodegradation behaviour of pure magnesium in a simulated body fluid, *Electrochim. Acta*. 115 (2014) 56–65. doi:10.1016/j.electacta.2013.10.131.
- [121] M. Liu, P. Schmutz, P.J. Uggowitzer, G. Song, A. Atrens, The influence of yttrium (Y) on the corrosion of Mg-Y binary alloys, *Corros. Sci.* 52 (2010) 3687–3701. doi:10.1016/j.corsci.2010.07.019.
- [122] I.B. Singh, M. Singh, S. Das, A comparative corrosion behavior of Mg, AZ31 and AZ91 alloys in 3.5% NaCl solution, *J. Magnes. Alloy*. 3 (2015) 142–148. doi:10.1016/j.jma.2015.02.004.
- [123] X. Yunchang, L. Chenglong, Z. Xinmeng, T. Guoyi, T. Xiubo, K.C. Paul, Corrosion behavior of biomedical AZ91 magnesium alloy in simulated body fluids, *J. Mater. Res.* 22 (2007). doi:10.1557/JMR.2007.0233.
- [124] A.A.N.E. Metrohm, *Electrochemical Impedance Spectroscopy (EIS) (EIS Part 1 – Basic Principles)*, 2011.
- [125] F. Mansfeld, *An Introduction to Electrochemical Impedance Measurement*,

Anal. Interpret. EIS Data Met. Alloy. (1999).

- [126] A. Lasia, *Electrochemical Impedance Spectroscopy and its Applications*, Springer Science+Business Media New York, 2014. doi:10.1007/978-1-4614-8933-7.
- [127] T. Tanski, W. Borek, M. Krol, *Magnesium Alloys-selected issue*, IntechOpen, 2018.
- [128] W. Choi, H.-C. Shin, J.M. Kim, J.-Y. Choi, W.-S. Yoon, Modeling and Applications of Electrochemical Impedance Spectroscopy (EIS) for Lithium-ion Batteries, *J. Electrochem. Sci. Technol.* 11 (2020) 1–13. doi:10.33961/jecst.2019.00528.
- [129] M. Jamesh, S. Kumar, T.S.N.S. Narayanan, T.S.N. Sankara Narayanan, Corrosion behavior of commercially pure Mg and ZM21 Mg alloy in Ringer’s solution – Long term evaluation by EIS, *Corros. Sci.* 53 (2011) 645–654. doi:10.1016/j.corsci.2010.10.011.
- [130] B. Mei, J. Lau, T. Lin, S.H. Tolbert, B.S. Dunn, L. Pilon, Physical Interpretations of Electrochemical Impedance Spectroscopy of Redox Active Electrodes for Electrical Energy Storage, *J. Phys. Chem. C.* 122 (2018) 24499–24511. doi:10.1021/acs.jpcc.8b05241.
- [131] M. Geetha, a. K. Singh, R. Asokamani, a. K. Gogia, Ti based biomaterials, the ultimate choice for orthopaedic implants – A review, *Prog. Mater. Sci.* 54 (2009) 397–425. doi:10.1016/j.pmatsci.2008.06.004.
- [132] J.R. Davis, *Stainless Steels*. ASM Specialty Handbook, Materials Park, OH: ASM International, 1994.
- [133] A. Bekmurzayeva, W.J. Duncanson, H.S. Azevedo, D. Kanayeva, Surface modification of stainless steel for biomedical applications: Revisiting a

- century-old material, *Mater. Sci. Eng. C.* 93 (2018) 1073–1089. doi:10.1016/j.msec.2018.08.049.
- [134] M. Niinomi, M. Nakai, J. Hieda, Development of new metallic alloys for biomedical applications., *Acta Biomater.* 8 (2012) 3888–903. doi:10.1016/j.actbio.2012.06.037.
- [135] H. Cheng, M. Xu, H. Zhang, W. Wu, M. Zheng, X. Li, Cyclic Fatigue Properties of Cobalt-Chromium Alloy Clasps for Partial Removable Dental Protheses, *J. Prosthet. Dent.* 104 (2010) 389–396.
- [136] H. Walia, W.A. Brantley, H. Gerstein, An Initial Investigation of the Bending and Torsional Properties of Nitinol Root Canal Files, *J Endod.* 14 (1988) 346–351.
- [137] K. Ahmad, O. Arafa, Comparing the effects of titanium alloy and chrome cobalt in removable partial denture connectors on tooth mobility , bone loss and tissue reaction, *Saudi J. Dent. Res.* 7 (2016) 112–117. doi:10.1016/j.sjdr.2016.01.001.
- [138] M. Long, H.J. Rack, Titanium alloys in total joint replacement -- a materials science perspective, *Biomaterials.* 19 (1998) 1621–1639. doi:10.1016/S0142.
- [139] M. Alvarez-Lopez, M.D. Pereda, J.A. Del Valle, M. Fernandez-Lorenzo, M.C. Garcia-Alonso, O.A. Ruano, M.L. Escudero, Corrosion behaviour of AZ31 magnesium alloy with different grain sizes in simulated biological fluids, *Acta Biomater.* 6 (2010) 1763–1771.
- [140] M. Niinomi, Mechanical properties of biomedical titanium alloys, *Mater. Sci. Eng. A.* 243 (1998) 231–236. doi:10.1016/S0921-5093(97)00806-X.
- [141] H. Li, S.M. Oppenheimer, S.I. Stupp, D.C. Dunand, L.C. Brinson, Effects of Pore Morphology and Bone Ingrowth on Mechanical Properties of

- Microporous Titanium as an Orthopaedic Implant Material, *Mater. Trans.* 45 (2004) 1124–1131. doi:10.2320/matertrans.45.1124.
- [142] S.M. Kalantari, H. Arabi, S. Mirdamadi, S.A. Mirsalehi, Biocompatibility and compressive properties of Ti-6Al-4V scaffolds having Mg element., *J. Mech. Behav. Biomed. Mater.* 48 (2015) 183–91. doi:10.1016/j.jmbbm.2015.04.015.
- [143] J. Li, L. SH, K. de Groot, P. Layrolle, Preparation and characterization of porous titanium, *Key Eng. Mater.* 218 (2002) 51–54.
- [144] Z. Esen, Production and characterization of porous titanium alloys, Middle East Technical university, 2007.
- [145] Z. Esen, Ş. Bor, Characterization of Ti–6Al–4V alloy foams synthesized by space holder technique, *Mater. Sci. Eng. A.* 528 (2011) 3200–3209. doi:10.1016/j.msea.2011.01.008.
- [146] D.C. Dunand, Processing of Titanium Foams, *Adv. Eng. Mater.* 6 (2004) 369–376. doi:10.1002/adem.200405576.
- [147] G. Ryan, A. Pandit, D.P. Apatsidis, Fabrication methods of porous metals for use in orthopaedic applications., *Biomaterials.* 27 (2006) 2651–70. doi:10.1016/j.biomaterials.2005.12.002.
- [148] A. Kennedy, Porous Metals and Metal Foams Made from Powders, in: K. Kondoh (Ed.), *Powder Metall., InTech*, 2012.
- [149] L.J. Gibson, M.F. Ashby, *Cellular Solids: structures and properties*, second edi, Cambridge University Press, 1997.
- [150] J. Banhart, Manufacture, characterisation and application of cellular metals and metal foams, *Prog. Mater. Sci.* 46 (2001) 559–632. doi:10.1016/S0079-6425(00)00002-5.

- [151] R.L. Martin, US Patent 5, 564, 064, 1996.
- [152] M. Bram, C. Stiller, H.P. Buchkremer, D. Stöver, H. Baur, High-Porosity Titanium, Stainless Steel, and Superalloy Parts, *Adv. Eng. Mater.* 2 (2000) 196–199. doi:10.1002/(SICI)1527-2648(200004)2:4<196::AID-ADEM196>3.0.CO;2-K.
- [153] G. Kotan, a Ş. Bor, Production and Characterization of High Porosity Ti-6Al-4V Foam by Space Holder Technique in Powder Metallurgy., *Turkish J. Eng. Environ. Sci.* 31 (2007) 149–156. <http://search.ebscohost.com/login.aspx?direct=true&db=a9h&AN=26215344&lang=es&site=ehost-live>.
- [154] Z. Esen, E. Tarhan Bor, Ş. Bor, Characterization of loose powder sintered porous titanium and Ti6Al4V alloy, *Turkish J. Eng. Environ. Sci.* 33 (2009) 207–219. doi:10.3906/muh-0906-41.
- [155] G. Rausch, J. Banhart, Making cellular metals from metals other than aluminum, in: B. Kriszt, H.-P. Degischer (Eds.), *Handb. Cell. Met.*, Weinheim: Wiley-VCH Verlag, 2002.
- [156] I. Oh, N. Nomura, N. Masahashi, S. Hanada, Mechanical properties of porous titanium compacts prepared by powder sintering, *Scr. Mater.* 49 (2003) 1197–1202.
- [157] O. Lame, D. Bellet, M. Di Michiel, D. Bouvard, In Situ Microtomography Study of Metallic Powder Sintering, in: *Eur. Mater. Res. Soc.*, 2002.
- [158] J.L. Cabezas-Villa, J. Lemus-Ruiz, D. Bouvard, O. Jiménez, H.J. Vergara-Hernández, L. Olmos, Sintering study of Ti6Al4V powders with different particle sizes and their mechanical properties, *Int. J. Miner. Metall. Mater.* 25 (2018) 1389–1401. doi:10.1007/s12613-018-1693-5.

- [159] H.H.M. Kim, M. F., T. Kokubo, N. T., F. Miyaji, T. Kokubo, T. Nakamura, Preparation of bioactive Ti and its alloys via simple chemical surface treatment, *Biomed. Mater. Res.* 32 (1996) 409–417.
- [160] J. Sharan, S. V. Lale, V. Koul, M. Mishra, O.P. Kharbanda, An overview of surface modifications of titanium and its alloys for biomedical applications, *Trends Biomater. Artif. Organs.* 29 (2015) 176–187.
- [161] X. Liu, R.W.. Poon, S.C.. Kwok, P.K. Chu, C. Ding, Plasma surface modification of titanium for hard tissue replacements, *Surf. Coatings Technol.* 186 (2004) 227–233. doi:10.1016/j.surfcoat.2004.02.045.
- [162] H. Takadama, H.M. Kim, T. Kokubo, T. Nakamura, TEM-EDX study of mechanism of bonelike apatite formation on bioactive titanium metal in simulated body fluid., *J. Biomed. Mater. Res.* 57 (2001) 441–8. <http://www.ncbi.nlm.nih.gov/pubmed/11523039>.
- [163] T. Kokubo, S. Yamaguchi, Novel Bioactive Titanate Layers Formed on Ti Metal and Its Alloys by Chemical Treatments, *Materials (Basel).* 3 (2009) 48–63. doi:10.3390/ma3010048.
- [164] M. Wei, H.M. Kim, T. Kokubo, J.H. Evans, Optimising the bioactivity of alkaline-treated titanium alloy, *Mater. Sci. Eng. C.* 20 (2002) 125–134. doi:10.1016/S0928-4931(02)00022-X.
- [165] T. Kizuki, H. Takadama, T. Matsushita, T. Nakamura, T. Kokubo, Preparation of bioactive Ti metal surface enriched with calcium ions by chemical treatment., *Acta Biomater.* 6 (2010) 2836–42. doi:10.1016/j.actbio.2010.01.007.
- [166] D.K. Pattanayak, A. Fukuda, T. Matsushita, M. Takemoto, S. Fujibayashi, K. Sasaki, N. Nishida, T. Nakamura, T. Kokubo, Bioactive Ti metal analogous

- to human cancellous bone: Fabrication by selective laser melting and chemical treatments, *Acta Biomater.* 7 (2011) 1398–406. doi:10.1016/j.actbio.2010.09.034.
- [167] C. Migliaresi, L. Nicolais, Composite materials for biomedical applications, *Int. J. Artif. Organs.* 3 (1980) 114–118. doi:10.1177/039139888000300213.
- [168] M. Razavi, M.H. Fathi, M. Meratian, Microstructure, mechanical properties and bio-corrosion evaluation of biodegradable AZ91-FA nanocomposites for biomedical applications, *Mater. Sci. Eng. A.* 527 (2010) 6938–6944. doi:10.1016/j.msea.2010.07.063.
- [169] E. Salernitano, C. Migliaresi, Composite materials for biomedical applications: a review, *J. Appl. Biomater. Biomech.* 1 (2003) 3–18.
- [170] T.M. Cornsweet, Advanced composite materials., *Science.* 168 (1970) 433–438. doi:10.1126/science.168.3930.433.
- [171] C. Gao, M. Yao, S. Li, P. Feng, S. Peng, C. Shuai, Highly biodegradable and bioactive Fe-Pd-bredigite biocomposites prepared by selective laser melting, *J. Adv. Res.* 20 (2019) 91–104. doi:10.1016/j.jare.2019.06.001.
- [172] P.-C. Chang, B.-Y. Liu, C.-M. Liu, H.-H. Chou, M.-H. Ho, H.-C. Liu, D.-M. Wang, L.-T. Hou, Bone tissue engineering with novel rhBMP2-PLLA composite scaffolds., *J. Biomed. Mater. Res. A.* 81 (2007) 771–780. doi:10.1002/jbm.a.
- [173] J.W. Leenslag, A.J. Pennings, R.R.M. Bos, F.R. Rozema, G. Boering, Resorbable materials of poly(l-lactide). VI. Plates and screws for internal fracture fixation, *Biomaterials.* 8 (1987) 70–73.
- [174] B.O. M., M.D. Helsenki, Absorbable implants for the fixation of fractures, *J. Bone Jt. Surg.* 73 (1991) 148–153.

- [175] M. Alizadeh-Osgouei, Y. Li, C. Wen, A comprehensive review of biodegradable synthetic polymer-ceramic composites and their manufacture for biomedical applications, *Bioact. Mater.* 4 (2019) 22–36. doi:10.1016/j.bioactmat.2018.11.003.
- [176] A. Iftekhhar, Source: STANDARD HANDBOOK OF BIOMEDICAL ENGINEERING AND DESIGN CHAPTER 12, *Stand. Handb. Biomed. Eng. Des.* (2004) 1–17.
- [177] T. Nonami, A. Kamiya, K. Naganuma, T. Kameyana, Implantation of hydroxyapatite granules into superplastic titanium alloy for biomaterials, *Mater. Sci. Eng.* (1998) 281–4.
- [178] S.N. Dezfuli, Z. Huan, A. Mol, S. Leeflang, J. Chang, J. Zhou, Advanced bredigite-containing magnesium-matrix composites for biodegradable bone implant applications, *Mater. Sci. Eng. C.* 79 (2017) 647–660. doi:10.1016/j.msec.2017.05.021.
- [179] G. Jiang, C. Wang, Q. Li, J. Dong, G. He, Porous titanium with entangled structure filled with biodegradable magnesium for potential biomedical applications, *Mater. Sci. Eng. C.* 47 (2015) 142–149. doi:10.1016/j.msec.2014.11.014.
- [180] M. Balog, M. Snajdar, P. Krizik, Z. Schauperl, Z. Stanec, A. Catic, Titanium-Magnesium Composite for Dental Implants (BIACOM), in: *TMS 2017 146th Annu. Meet. & Exhib. Suppl. Proc.*, 2017: pp. 105–116. doi:10.1007/978-3-319-51493-2.
- [181] ASTM F1580-01, Standard Specification for Titanium and Titanium-6 Aluminum-4 Vanadium Alloy Powders for Coatings of Surgical Implants 1, 2006.

- [182] T. Kokubo, H. Takadama, How useful is SBF in predicting in vivo bone bioactivity?, *Biomaterials*. 27 (2006) 2907–15.
- [183] ASTM G102-89, Standard Practice for Calculation of Corrosion Rates and Related Information from Electrochemical Measurements, 2018. doi:10.1520/G0102-89R10.2.
- [184] ASTM E9-89a, Standard Test Methods of Compression Testing of Metallic Materials at Room Temperature, (2000) 1–9. doi:10.1520/E0009-09.2.
- [185] N.V.R. Kumar, J.J. Blandin, M. Su, E. Grosjean, Effect of alloying elements on the ignition resistance of magnesium alloys, 49 (2003) 225–230. doi:10.1016/S1359-6462(03)00263-X.
- [186] K. Kondoh, M. Kawakami, H. Imai, J. Umeda, H. Fujii, Wettability of pure Ti by molten pure Mg droplets, *Acta Mater.* 58 (2010) 606–614. doi:10.1016/j.actamat.2009.09.039.
- [187] D. Muscat, R.A.L. Drew, Modeling the infiltration kinetics of molten aluminum into porous titanium carbide, *Metall. Mater. Trans. A*. 25 (1994) 2357–2370. doi:10.1007/BF02648856.
- [188] S. Bao, K. Tang, A. Kvithyld, T. Engh, M. Tangstad, Wetting of pure aluminium on graphite, SiC and Al₂O₃ in aluminium filtration, *Trans. Nonferrous Met. Soc. China (English Ed.* 22 (2012) 1930–1938. doi:10.1016/S1003-6326(11)61410-6.
- [189] Q. Tan, A. Atrens, N. Mo, M.X. Zhang, Oxidation of magnesium alloys at elevated temperatures in air: A review, *Corros. Sci.* 112 (2016) 734–759. doi:10.1016/j.corsci.2016.06.018.
- [190] A. Skolakova, J. Leitner, P. Salvetr, P. Novak, D. Deduytsche, J. Kopecek, C. Detavernier, D. Vojtech, Kinetic and thermodynamic description of

intermediary phases formation in Ti-Al system during reactive sintering, *Mater. Chem. Phys.* 230 (2019) 122–130.

- [191] N. Eustathopoulos, *Wetting by Liquid Metals—Application in Materials Processing: The Contribution of the Grenoble Group*, Metals (Basel). 5 (2015) 350–370. doi:10.3390/met5010350.
- [192] A.W. Adamson, A. Gast, *Physical Chemistry of Surfaces*, 1997.
- [193] L. Yin, B.T. Murray, S. Su, Y. Sun, Y. Efrain, H. Taitelbaum, T.J. Singler, Reactive wetting in metal-metal systems, *J. Phys. Condens. Matter.* 21 (2009) 11. doi:10.1088/0953-8984/21/46/464130.
- [194] M. Sujata, S. Bhargava, S. Sangal, On the formation of TiAl₃ during reaction between solid Ti and liquid Al, *J. Mater. Sci. Lett.* 16 (1997) 1175–1178. doi:10.1007/bf02765402.
- [195] Z. Esen, E. Bütev, A. Akkaya, B. Gürçay, C. Özcan, B. Aslı, Ö. Duygulu, A.F. Derioglu, Corrosion behaviours of Ti6Al4V-Mg / Mg-Alloy composites, *Corros. Sci.* (2020) 108470. doi:10.1016/j.corsci.2020.108470.
- [196] A. Rakngarm, Y. Miyashita, Y. Mutoh, Formation of hydroxyapatite layer on bioactive Ti and Ti-6Al-4V by simple chemical technique., *J. Mater. Sci. Mater. Med.* 19 (2008) 1953–61. doi:10.1007/s10856-007-3285-1.
- [197] G.B. Ferraz, R.E. Pereira, J.F.C. Lins, F.C. Ferraz, Microstructural Analysis of Commercially Pure Magnesium Processed by ECAP at Room Temperature, *Int. J. Eng. Trends Appl.* 4 (2017) 1–5.
- [198] A. Atrens, R. Xu, J.-X. Tao, C. Gao, L. Liu, M.-C. Zhao, Y.-C. Zhao, C. Shuai, Formation and characteristic corrosion behavior of alternately lamellar arranged α and β in as-cast AZ91 Mg alloy, *J. Alloys Compd.* 770 (2018) 549–558. doi:10.1016/j.jallcom.2018.08.103.

- [199] G.-L. Song, A. Atrens, D. StJohn, J. NAIRN, Y. Li, Mg and Its Alloys for Biomedical Applications: Exploring Corrosion and Its Interplay with Mechanical Failure, *Metals* (Basel). 103 (2017) 778. doi:10.3390/met8100778.
- [200] J.H. Dong, L.L. Tan, Y. Bin Ren, K. Yang, Effect of Microstructure on Corrosion Behavior of Mg–Sr Alloy in Hank’s Solution, *Acta Metall. Sin. (English Lett.* 32 (2019) 305–320. doi:10.1007/s40195-018-0750-4.
- [201] H. Kalb, B. Rzany, B. Hensel, Impact of microgalvanic corrosion on the degradation morphology of WE43 and pure magnesium under exposure to simulated body fluid, *Corros. Sci.* 57 (2012) 122–130.
- [202] S.D. Cramer, B.S. Covino, Corrosion Fundamentals, Testing and Protection, in: *ASM Handb.*, Metals Park, Ohio:ASM International, 2003: pp. 692–696.
- [203] H. Feng, S. Liu, Y. Du, T. Lei, R. Zeng, T. Yuan, Effect of the second phases on corrosion behavior of the Mg-Al-Zn alloys, *J. Alloys Compd.* 695 (2017) 2330–2338. doi:10.1016/j.jallcom.2016.11.100.
- [204] I. Nakatsugawa, S. Kamado, Y. Kojima, R. Ninomiya, K. Kubota, Corrosion of magnesium alloys containing rare earth elements, *Corros. Rev.* 16 (1998) 139–157. doi:10.1515/CORRREV.1998.16.1-2.139.
- [205] T.S.N. Sankara Narayanan, I.S. Park, M.H. Lee, Surface modification of magnesium and its alloys for biomedical applications: Opportunities and challenges, Elsevier Ltd, 2015. doi:10.1016/B978-1-78242-077-4.00002-4.
- [206] Y. Song, Z. Wang, Y. Liu, M. Yang, Q. Qu, Influence of erbium, cerium on the stress corrosion cracking behavior of AZ91 alloy in humid atmosphere, *Adv. Eng. Mater.* 19 (2017).
- [207] R. Ambat, N.N. Aung, W. Zhou, Evaluation of microstructural effects on

- corrosion behaviour of AZ91D magnesium alloy, *Corros. Sci.* 42 (2000) 1433–1455. doi:10.1016/S0010-938X(99)00143-2.
- [208] F. Zucchi, V. Grassi, A. Frignani, C. Monticelli, G. Trabanelli, Electrochemical behaviour of a magnesium alloy containing rare earth elements, *J. Appl. Electrochem.* 36 (2006) 195–204. doi:10.1007/s10800-005-9053-3.
- [209] X.W. Guo, W.J. Ding, L.M. Peng, P.H. Fu, J.W. Chang, Effect of Heat Treatment on Corrosion and Electrochemical Behaviors of Mg-3Nd-0.2Zn (wt.%) Magnesium Alloy, *Mater. Sci. Forum.* 546–549 (2009) 559–562. doi:10.4028/www.scientific.net/msf.546-549.559.
- [210] L.M. Peng, J.W. Chang, X.W. Guo, A. Atrens, W.J. Ding, Y.H. Peng, Influence of heat treatment and microstructure on the corrosion of magnesium alloy Mg-10Gd-3Y-0.4Zr, *J. Appl. Electrochem.* 39 (2009) 913–920. doi:10.1007/s10800-008-9739-4.
- [211] P.W. Chu, E.A. Marquis, Linking the microstructure of a heat-treated WE43 Mg alloy with its corrosion behavior, *Corros. Sci.* 101 (2015) 94–104. doi:10.1016/j.corsci.2015.09.005.
- [212] G. Song, Recent progress in corrosion and protection of magnesium alloys, *Adv. Eng. Mater.* 7 (2005) 563–586. doi:10.1002/adem.200500013.
- [213] G. Wu, K. Feng, A. Shanaghi, Y. Zhao, R. Xu, G. Yuan, P.K. Chu, Effects of surface alloying on electrochemical corrosion behavior of oxygen-plasma-modified biomedical magnesium alloy, *Surf. Coatings Technol.* 206 (2012) 3186–3195. doi:10.1016/j.surfcoat.2012.01.001.
- [214] Z. Esen, E. Bütev, M.S. Karakaş, A comparative study on biodegradation and mechanical properties of pressureless infiltrated Ti/Ti6Al4V-Mg composites,

- J. Mech. Behav. Biomed. Mater. 63 (2016) 273–286.
- [215] G.G. Perrault, The potential-pH diagram of the magnesium water systems, J. Electroanal. Chem. Interfacial Electrochem. 51 (1974) 107–119.
- [216] M. SAKAIRI, Y. SHIMOYAMA, H. TAKAHASHI, Electrochemical Noise Analysis of Galvanic Corrosion of Anodized Aluminum in Chloride Environments, Electrochemistry. 6 (2006) 458–462.
- [217] H.A.A. Al-Mazeedi, R.A. Cottis, A practical evaluation of electrochemical noise parameters as indicators of corrosion type, Electrochim. Acta. 49 (2004) 2787–2793. doi:10.1016/j.electacta.2004.01.040.
- [218] X.P. Zhang, Z.P. Zhao, F.M. Wu, Y.L. Wang, J. Wu, Corrosion and wear resistance of AZ91D magnesium alloy with and without microarc oxidation coating in Hank's solution, J. Mater. Sci. 42 (2007) 8523–8528. doi:10.1007/s10853-007-1738-z.
- [219] G. Song, B. Johannesson, S. Hapugoda, D. StJohn, Galvanic corrosion of magnesium alloy AZ91D in contact with an aluminium alloy, steel and zinc, Corros. Sci. 46 (2004) 955–977. doi:10.1016/S0010-938X(03)00190-2.
- [220] L.-X. Wang, R.-B. Song, C.-H. Cai, J.-Y. Li, Enhanced Strength and Corrosion Resistance of Mg–2Zn–0.6Zr Alloy with Extrusion, Acta Metall. Sin. (English Lett. 32 (2019) 10–22. doi:10.1007/s40195-018-0793-6.
- [221] J.C. Valle-Quitana, G.F. Dominguez-Patiño, J.G. Gonzalez-Rodriguez, Corrosion Inhibition of Carbon Steel in 0.5 M H₂SO₄ by Phtalocyanine Blue, ISRN Corros. 2014 (2014) 1–8. doi:10.1155/2014/945645.
- [222] P. Wu, F. Xu, K. Deng, F. Han, Z. Zhang, R. Gao, Effect of extrusion on corrosion properties of Mg-2Ca- xAl (x=0 , 2 , 3 , 5) alloys, Corros. Sci. 127 (2017) 280–290. doi:10.1016/j.corsci.2017.08.014.

APPENDICES

A. PERMISSON LICENCES

28.05.2020

Rightslink® by Copyright Clearance Center



RightsLink®



Home



Help



Email Support



Sign in



Create Account



Comparison of the short and long-term degradation behaviors of as-cast pure Mg, AZ91 and WE43 alloys

Author: Ezgi Bütev Öcal, Ziya Esen, Kadri Aydınol, Arcan F. Dericioğlu

Publication: Materials Chemistry and Physics

Publisher: Elsevier

Date: 1 February 2020

© 2019 Elsevier B.V. All rights reserved.

Please note that, as the author of this Elsevier article, you retain the right to include it in a thesis or dissertation, provided it is not published commercially. Permission is not required, but please ensure that you reference the journal as the original source. For more information on this and on your other retained rights, please visit: <https://www.elsevier.com/about/our-business/policies/copyright#Author-rights>

BACK

CLOSE WINDOW

© 2020 Copyright - All Rights Reserved | Copyright Clearance Center, Inc. | [Privacy statement](#) | [Terms and Conditions](#)
Comments? We would like to hear from you. E-mail us at customercare@copyright.com



RightsLink®



Home



Help



Email Support



Sign in



Create Account



Corrosion behaviours of Ti6Al4V-Mg/Mg-Alloy composites

Author:

Ziya Esen, Ezgi Bütev Öcal, Aslı Akkaya, Benu Gürçay, Ceren Özcan, Burcu Aslı Özgümüş, Özgür Duygulu, Arcan F. Dericioğlu

Publication: Corrosion Science

Publisher: Elsevier

Date: 15 April 2020

© 2020 Elsevier Ltd. All rights reserved.

Please note that, as the author of this Elsevier article, you retain the right to include it in a thesis or dissertation, provided it is not published commercially. Permission is not required, but please ensure that you reference the journal as the original source. For more information on this and on your other retained rights, please visit: <https://www.elsevier.com/about/our-business/policies/copyright#Author-rights>

BACK

CLOSE WINDOW

CIRRICULUM VITAE

PERSONAL INFORMATION

Surname, Name: Büttev Öcal, Ezgi
Nationality: Turkish (TC)
Date and Place of Birth: 13 October 1989, Ankara
Marital Status: Married
Phone: +90 505 962 36 13
email: butevezgi@gmail.com

EDUCATION

Degree	Institution	Year of Graduation
MS	METU Metallurgical and Materials Engineering	2015
BS	METU Metallurgical and Materials Engineering	2012
High School	Gazi Anadolu High School, Ankara	2007

WORK EXPERIENCE

Year	Place	Enrollment
2013-Present	Çankaya University	Lecturer
2011 July	TAI	Intern Eng. Student
2010 August	ERDEMİR	Intern Eng. Student

FOREIGN LANGUAGES

Advanced English

PUBLICATIONS

1. Büttev Öcal E., Esen Z., Aydınol K., Dericioğlu A. F. “Comparison of the short and long-term degradation behaviors of as-cast pure Mg, AZ91 and WE43 alloys”, *Materials Chemistry and Physics*, 241, 122350 (2010).
2. Esen Z., Büttev Öcal E., Akkaya A., Gürçay B., Özcan C., Özgümüş B. A., Duygulu Ö., Dericioğlu A. F. “Corrosion behaviours of Ti6Al4V-Mg/Mg-Alloy composites”, *Corrosion Science*, 166, 108470 (2020).
3. Koroglu L., Butev E., Esen Z., Ayas E. “A Novel Approach for Synthesis of Monticellite Based Bioactive Ceramic Powders from Boron Derivative Waste”, *Materials Letters*, 209, 315–318 (2017).
4. Esen Z., Büttev Öcal E. “Surface Characteristic and in-vitro behavior of hydrothermally treated bulk Ti6Al7Nb alloys”, *Surface and Coatings Technology*, 309, 829-839, 12 (2017).
5. Esen Z., Büttev E., Karakaş M. S. “A comparative study on biodegradation and mechanical properties of pressureless infiltrated Ti/Ti6Al4V-Mg composites”, *Journal of the Mechanical Behavior of Biomedical Materials*, 63, 273-286 (2016).
6. Büttev E., Esen Z., Bor Ş. “Characterization of Ti6Al7Nb alloy foams surface treated in aqueous NaOH and CaCl₂ solutions”, *Journal of the Mechanical Behaviour of Biomedical Materials*, 60, 127-138 (2016).
7. Büttev E., Esen Z., Bor Ş. “In vitro bioactivity investigation of alkali treated Ti6Al7Nb alloy foams”, *Applied Surface Science*, 327, 437–443 (2015).